

# Coherent structures and transport in drift wave plasma turbulence

**Korsholm, Søren Bang**

*Publication date:*
2002

*Document Version*
Publisher's PDF, also known as Version of record

# Coherent structures and transport in drift wave plasma turbulence

Risø-R-Report

Søren Bang Korsholm
Report number Risø-R-1337 (rev. ed.) (EN)
Publication date December 2011

Risø DTU
National Laboratory for Sustainable Energy

**Author:** Søren Bang Korsholm
**Title:** Coherent structures and transport in drift wave plasma turbulence
**Division:** Plasma Physics and Technology Programme

**Report number Risø-R-1337 (rev. ed.) (EN)**
**Publication date December 2011**

**Abstract (max. 2000 char.)**:
Fusion energy research aims at developing fusion power plants providing safe and clean energy with abundant fuels. Plasma turbulence induced transport of energy and particles is a performance limiting factor for fusion devices. Hence the understanding of plasma turbulence is important for optimization. The present work is a part of the puzzle to understand the basic physics of transport induced by drift wave turbulence in the edge region of a plasma. The basis for the study is the Hasegawa-Wakatani model. Simulation results for 3D periodic and non-periodic geometries are presented. The Hasegawa-Wakatani model is further expanded to include ion temperature effects. Another expansion of the model is derived from the Braginskii electron temperature equation. The result is a self-consistent set of equations describing the dynamical evolution of the drift wave fluctuations of the electron density, electron temperature and the potential in the presence of density and temperature gradients. 3D simulation results of the models are presented.
Finally, the construction and first results from the MAST fluctuation reflectometer is described. The results demonstrate how L- to H-mode transitions as well as edge-localized-modes can be detected by the relatively simple diagnostic system.

The present Risø report is a slightly updated version of my original PhD report which was submitted in April 2002 and defended in August 2002.

**ISSN 0106-2840**
**ISBN 87-550-3047-5 (Internet)**
**ISBN 87-550-3046-7 (Printed)**

**Pages: 151**
**References: 105**

Information Service Department
Risø National Laboratory for Sustainable Energy
Technical University of Denmark
P.O.Box 49
DK-4000 Roskilde
Denmark
Telephone +45 46774005
bibl@risoe.dtu.dk
Fax +45 46774013
www.risoe.dtu.dk

# Dansk resumé

Udnyttelse af fusionsenergi til energiproduktion vil kunne løse flere af de miljømæssige problemer, vi kender fra energiproduktionen i dag, samt sikre os ubegrænsede brændstofressourcer. Der er ingen $CO_2$-udslip ved fusionsenergiproduktion, der er en meget begrænset transport af brændstof, og selvom fusionsenergien produceres ved kerneprocesser er der en begrænset mængde mellem-langlivet (∼100 år) radioaktivt affald. Brændslet til fusionsenergiproduktionen består af to hydrogen isotoper, deuterium (D) og tritium (T). D findes i rigelige mængder i havvand, og T produceres i forbindelse med selve reaktoren ved brug af lithium (Li).
Ved en fusionsproces mellem D og T dannes helium ($^4$He) og en neutron, samt en frigiven energi på 17,6 MeV. Den energimængde, der produceres af 1 kg D-T brændsel, svarer til energimængden i 7600 ton olie. For at muliggøre fusion skal blandingen af D og T opvarmes til godt 100 millioner grader Kelvin. Ved så høje temperaturer er atomerne ioniserede, og blandingen er nu en ladet gas af elektroner og positive ioner. Denne tilstandsform kaldes et plasma.
I fusionsplasmaeksperimenter holdes plasmaet indesluttet af et stærkt magnetfelt, idet direkte kontakt mellem det varme plasma og beholdervægge er umulig. En nødvendig betingelse for udnyttelse af fusionsenergi er, at energien og partiklerne i plasmaet indesluttes så længe, at tilstrækkelig mange fusionsprocesser kan finde sted. Denne indeslutningstid begrænses af en transport af energi og partikler ud af plasmaet, og det er eksperimentelt bestemt at transporten er forårsaget af turbulens i plasmaet. Det er vigtigt at lære fysikken bag denne transport at kende, så transporten kan begrænses i fremtidige fusionsreaktorer.
Det er almindeligt antaget at elektrostatiske fluktuationer, og herunder driftsbølgeturbulens, i høj grad kan forklare den turbulente transport, og idet driftsbølger er lineært ustabile i de fleste plasmakonfigurationer vil de næsten altid vil være til stede og forårsage tab af energi og partikler.

I dette projekt undersøger vi dels driftsbølgeturbulens numerisk og analytisk, dels turbulens i UKAEA Culham Science Centre's MAST eksperiment v.h.a. reflektometri. Rapporten indledes med en gennemgang af baggrunden for fusionsforskningen og for den specielle interesse i turbulent transport. Dernæst præsenteres kort forskellige tilgange til turbulensmodeller og -simuleringer, og centrale begreber der bruges i rapporten beskrives.
De numeriske undersøgelser tager udgangspunkt i Hasegawa-Wakatani

modellen for driftsbølgeturbulens i et magnetiseret resistivt plasma (A. Hasegawa and M. Wakatani, Phys. Rev. Lett. **50** (1983) pp. 682–686). Modellen kan udtrykkes i to partielle differentialligninger i perturbationerne af tætheden, $n$, og det elektrostatiske potentiale, $\phi$, og energien til turbulensen kommer fra en konstant tæthedsgradient. Vi gennemgår først udledningen af Hasegawa-Wakatani modellen og resultater af simuleringer for at have et anerkendt sammenligningsgrundlag, når vi i de følgende kapitler modificerer eller udvider modellen med flere fysiske effekter.

Den generelle opførsel af Hasegawa-Wakatani systemet kan opsummeres således: De lineært ustabile driftsbølger vokser op fra meget små perturbationer af $n$ og $\phi$. Driftsbølgerne eksiterer via ikke-lineær kobling konvektive celler, der er kohærente strukturer uden variation (i $n$ og $\phi$) parallelt med magnetfeltet. Ikke-lineære processer mellem driftsbølgerne og de konvektive celler dominerer dynamikken gennem en turbulent tilstand, der afsluttes ved, at et poloidalt flow opbygges, og forhindrer tilførslen af energi til driftsbølgerne. Dermed stabiliseres systemet, og hovedparten af energien overføres til store konvektive celler.

Ved den første modifikation af Hasegawa-Wakatani modellen inkluderer vi effekter af en endelig men lille iontemperatur. Vi ser at for nogle parametervalg bliver dynamikken af systemet påvirket, mens den generelle opførsel af den iontemperatur-modificerede Hasegawa-Wakatani model minder meget om den oprindelige models.

Vi udleder dernæst en model vi kalder $n\phi T_e$-modellen, som tager udgangspunkt i Hasegawa-Wakatani modellens driftsbølgebillede, men tillige medtager perturbationer i elektrontemperaturen $T_e$ og effekter af en konstant elektrontemperaturgradient. Ved denne udvidelse er det nu muligt at beregne både partikel- og varmefluxen, samt estimere fluxen af energi ud af plasmaet. Vi ser at systemet for nogle parametervalg udvikler sig som Hasegawa-Wakatani systemet (for de sammenlignelige størrelser), men finder samtidig at dynamikken bliver væsentligt påvirket af den relative størrelse af tætheds- og elektrontemperaturgradienterne.

De ovennævnte simulationer blev alle udført i en tredimensional periodisk geometri. Anvendelsen af denne geometri er ikke altid hensigtsmæssig, så i det efterfølgende kapitel behandler vi resultaterne af simuleringer af Hasegawa-Wakatani modellen i en ikke-periodisk geometri. Vi ser her blandt andet hvordan perturbationerne i tætheden selvorganiserer sig til at modvirke den påtrykte konstante tæthedsgradient. Vi diskuterer også det såkaldte Reynolds stress, der udtrykker i hvilken grad turbulensen selvgenererer et *shear flow*. Vi undersøger endvidere validiteten af et foreslået pseudo-Reynolds stress, der i givet fald vil være nemmere at bestemme eksperimentelt end det virkelige Reynolds stress. Endelig gennemgår vi lidt af systemets parametriske afhængighed, og ser på effekten af at inkludere et eksternt påtrykt shear flow.

En del af projektet blev udført på UKAEA Culham Science Centre, hvor reflektometriundersøgelser af turbulens i MAST plasmaet blev udført. Efter en generel beskrivelse af reflektometri og af MAST eksperimentet, bliver disse undersøgelser gennemgået. De mest interessante resultater

er opnået ved målinger af såkaldte *H-modes* i MAST, en tilstand hvor indeslutningstiden af partiklerne er høj og den turbulente transport bliver reduceret. Vi ser tydelige signaturer af H-modes, og ser også tidlige tegn på korte turbulente hændelser (*ELMs*) og afslutningen af H-mode tilstanden.
Sidst giver vi en kort beskrivelse af et interessant fænomen observeret i MAST, hvor elektrontemperaturprofilerne i nogle tilfælde viste sig at være kraftigt inverterede, d.v.s. den centrale temperatur var meget lavere end den maximale temperatur i plasmaet.
Slutteligt opsummerer vi resultaterne af projektets undersøgelser.

Dette projekts titel er *"Kohærente strukturer og transport i driftsbølge-plasmaturbulens"*. Projektet er udført ved Institut for Fysik, Danmarks Tekniske Universitet, i samarbejde med Afdelingen for Optik og Fluid Dynamik, Forskningscenter Risø, hvor arbejdet konkret fandt sted. Projektet blev financieret af Forskerakademiet (nu Forskeruddannelsesrådet) i samarbejde med Forskningscenter Risø.

| | |
|---|---|
| Vejledere på projektet var: | Dr. Poul K. Michelsen, Risø |
| | Dr. Jens Juul Rasmussen, Risø |
| | Dr. Erik Mosekilde, DTU |
| Projektet er udført i perioden: | 1. maj 1998 – 14. april 2002 |
| Projektet er udført af: | Søren B. Korsholm<br>P928781 |
| Dato: | 14. april 2002 |

Projektet er afleveret til opnåelse af ph.d. graden ved DTU.

# Contents

# Preface

The subject of this thesis is: *"Coherent structures and transport in drift wave plasma turbulence"* and it is submitted to the Department of Physics at the Technical University of Denmark (DTU) in order to obtain a PhD degree. The work for the thesis was performed in the Plasma and Fluid Dynamics group at the Optics and Fluid Dynamics Department at Risø National Laboratory, Denmark, from May 1998 till April 2002. The work has primarily contained numerical and theoretical studies of drift wave turbulence and turbulent transport, but in the period $7^{th}$ of February till $29^{th}$ of July 2000 I worked at UKAEA-Fusion at Culham Science Centre near Abingdon, Oxfordshire, England. The main objective of the stay was to get experience with experimental plasma physics, preferably, with connection to the theoretical and numerical parts of the present thesis. Hence, I was involved in setting up and running the MAST fluctuation reflectometer.

The thesis is initiated by two introductory chapters: In Chapter 1 I motivate the development of fusion energy, and throw a brief look onto fusion research in general. I include this rather broad introduction to the field of fusion research since it is an important motivation for me to see my work as a part (although tiny) of the joint research programme towards the development of fusion energy as a power source. As such Chapter 1 puts the rest of the thesis into a context. Furthermore, I have spend a part of the time informing high school and university students, other physicists, and politicians about fusion energy and fusion research. The second introductory chapter, Chapter 2, describes some of the concepts of turbulence and anomalous transport and set the frame for the models investigated in the following chapters.

The Hasegawa-Wakatani model forms the basis for the models being investigated in this thesis. The model and simulation results are reviewed in Chapter 3. In Chapter 4 a Hasegawa-Wakatani type model with finite ion temperature effects is presented and tested by simulations. The Hasegawa-Wakatani system is expanded by including electron temperature fluctuations and a constant electron temperature gradient in the $n\phi T_e$ model being derived in Chapter 5, where also results of simulations are presented. As a final chapter on simulations Chapter 6 contains results of simulations of the Hasegawa-Wakatani model performed in a non-periodic geometry. Chapter 6 further treats the Reynolds stress in connection with flow generation, and the recently introduced concept of a pseudo-Reynolds stress is discussed.

The work on reflectometry measurements at the MAST tokamak at Culham Science Centre is presented in Chapter 7. In the last part of my stay

at Culham, I was involved in the initial work of finding an explanation for hollows in the electron temperature profiles observed by the Thomson Scattering system. This is briefly described in Chapter 8.
Finally, the results of the thesis are summarised in Chapter 9.
In Appendix A the chaotic behaviour of the Hasegawa-Wakatani system is briefly described, and by the end of the thesis in Appendix B a list of symbols used in the thesis is presented.

| | |
|---|---|
| The supervisors on the project were: | Dr. Poul K. Michelsen, Risø |
| | Dr. Jens Juul Rasmussen, Risø |
| | Dr. Erik Mosekilde, DTU |
| The project took place from: | May 1998 to April 2002 |
| The project was performed by: | Søren B. Korsholm |
| Date | $14^{th}$ of April 2002 |

# Acknowledgements

This project was financed by Risø National Laboratory and the Danish Research Academy (now the Danish Research Training Council) who's support is gratefully acknowledged. I stayed half a year at Culham Science Centre, Abingdon, UK, working on the MAST project, which is funded by the UK Department of Trade and Industry and EURATOM.
I would like to thank everyone in the Plasma and Fluid Dynamics group in the Optics and Fluid Dynamics Department at Risø National Laboratory for providing a pleasant atmosphere and for their kind help whenever a problem occurred. Not the least, my wife Camilla and I are grateful for the remarkable understanding of the situation concerning the illness of our son, Jonathan. In particular, I would like to thank my supervisors Dr. P. K. Michelsen and Dr. J. Juul Rasmussen for inspiration and enlightening conversations, Dr. V. Naulin for guidance and many inspirational inputs, and Dr. A. H. Nielsen for help on numerical challenges. Furthermore, I would like to express my gratitude to the secretaries of the department: Lone Astradsson, Heidi D. Carlsen, and Bitten Skaarup, for their kind and professional help on administrative issues. I am also grateful to Dr. V. O. Jensen for many interesting discussions on fusion, physics, and the world of today and yesterday.
I also want to thank my supervisor at DTU Dr. E. Mosekilde for the interest shown in the project and for helpful comments.
The collaboration with the whole MAST team at UKAEA Fusion, Culham Science Centre is gratefully acknowledged. In particular, I would like to thank Dr. G. Cunningham for patient supervision of a theoretist going experimental. Special thanks go to the so-called Ghetto-people who made the stay in Oxford memorable for more than a work experience for Camilla and me.
I would also like to express my gratitude towards Dr. H. Pécseli, University of Oslo, Dr. A. Thyagaraja, Culham Science Centre, and Dr. L. Garcia, Universidad Carlos III, Madrid, for fruitful discussions and collaboration on the subjects of the ion temperature modified Hasegawa-Wakatani model, the hollow profiles in MAST, and the pseudo-Reynolds stress, respectively.
I wish to thank my family for never failing support, and finally, I would like to thank Camilla for taking a large part of the responsibility for Jonathan during this difficult period.

Søren B. Korsholm, April 2002

# Chapter 1

# The development of fusion energy production

In the present chapter we present a motivation for the research effort in fusion energy, the different paths of fusion research, the status of fusion research - technically as well as politically, and the future prospects of fusion research.

## 1.1 Motivation for developing fusion energy

Since Newcomens and Watts invention of the "manual" and the "automatic" steam engines in 1769 and the following industrialisation, the consumption of energy for production, transport and domestic purposes has been the basis for the prosperity of the so-called industrialised countries. Today, energy supplies are so crucial for the world that the possession of large supplies and fuel reserves is an important political power factor. In a Green Paper from November 2000 the EU-commission estimated the prospects for European import of energy fuel to reach 70% by the year 2030, as opposed to the current 50%, and conclude that this constitutes a problem for the EU that calls for action [1].
The fuel used for energy production by the first steam engines was coal. Today, more than 200 years later, one of the major fuels is still coal, which combined with oil and natural gas provides approximately 85% of the supplies. The remaining energy supplies are provided by nuclear fission ($\sim 7\%$), hydro power ($\sim 7\%$) and renewables like wind power, photo voltaic cells, etc. producing $\sim 1\%$ [2].
Since the industrialisation the energy consumption[1] has been ever increasing, and due to the use of fossil fuels the emission of $CO_2$ has increased dramatically (see Figure 1.1). Over the last 250 years the $CO_2$ content in the atmosphere has increased by nearly 25% [3]. It seems unlikely that the increase is just a natural variation, not least when it is correlated to the $CO_2$ emissions after the industrialisation. The increased $CO_2$ content in the atmosphere is expected to be causing the so-called greenhouse effect, in which

[1] The current annual global energy consumption is estimated to be 10 Gtoe (giga tonnes oil equivalent), and it is expected to triple over the next 50 years.

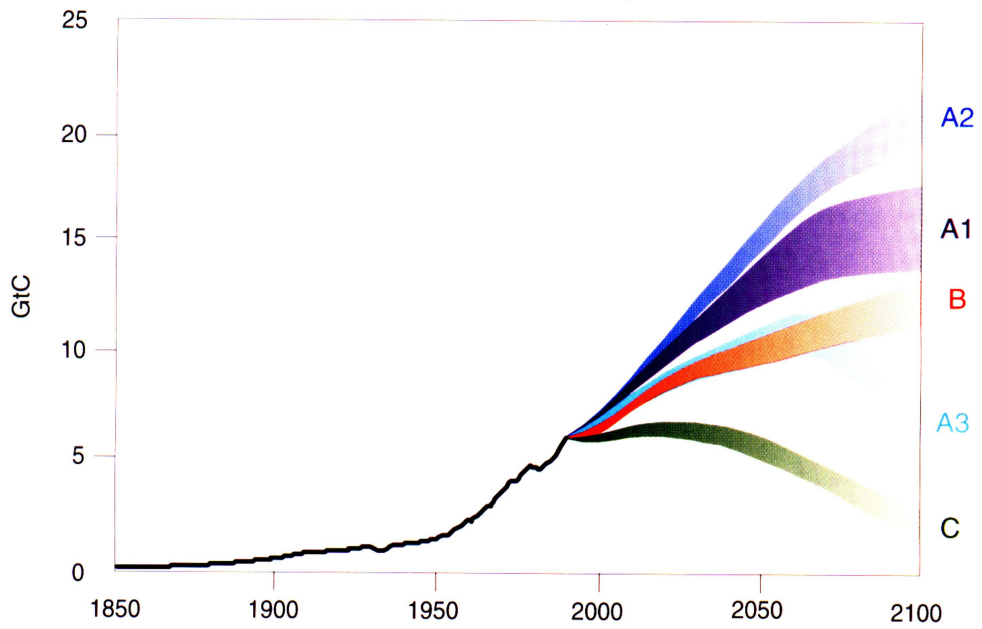


Figure 1.1: The evolution of global carbon emissions under different scenarios. Scenario A "High Growth" is divided into A1 oil and gas-based, A2 too little oil and a massive return to coal and A3 evolution of nuclear and renewable energy technologies and phase out of fossil fuels. Scenario B "Middle Course" and Scenario C "Ecologically Driven". GtC is giga tonnes of carbon per year. (From: *Global Energy Perspectives to 2050 and Beyond*, WEC/IIASA, 1995.)

the $CO_2$ creates an insulating layer in the atmosphere inhibiting outward radiation and thus causing the mean temperature at Earth to increase resulting in ecological changes. The sketched causal relations is widely agreed on by researchers in the field of climate change, and it is the basis for the UN climate change meetings - one of which lead to the Kyoto protocol in 1997 - setting standards for emission of $CO_2$. It should be mentioned, though, that the ability of nature to absorb $CO_2$ (in the oceans), the full effect of $CO_2$ in the atmosphere, and the cause of the observed temperature increases have not been scientifically proven, although most evidence and correlations support the theory sketched above. One point is certain, however, that the pace at which fossil fuels are burned is in the order of a million times the regeneration time, i.e. the $CO_2$ is released a million times faster than it was accumulated in the coal and oil. The uncertainty of the effect of $CO_2$ release could lead one to claim that we are at present performing a large scale experiment with our global environment. A comprehensive guide to the subject of global warming and climate change is found in [4].
Besides the potential problems of emissions from burning of fossil fuels, great uncertainty about the reserves of fossil fuels exist. The present estimates are that coal reserves last for approximately 200 years at the present rate of consumption, whereas the corresponding estimates for gas and oil are in the

order of 50 years [2].
In the light of the above, one of the major tasks for mankind in the near future should be to find ways of producing energy while limiting the use of fossil fuels. There is no simple answer on how to tackle the future energy supply problems, but there is several possible paths, e.g., through a wide range of renewables, fission energy in the form of breeder reactors, and development of fusion energy. Probably none of the options may solve the energy problems by itself, since any technology has advantages and disadvantages: for the fission breeder reactor the technology is ready, but it produces long-lived radioactive waste, the renewables are relatively clean technologies, but all of them are intermittent in power level and the power density is generally relatively low[2], and finally we have fusion:

- the fuel is abundant[3]
- the fuel is evenly distributed among nations
- transport of fuel is negligible[4]
- no transport of radioactive materials
- no $CO_2$ release[5]
- no long-lived radioactivity (reactor radioactive for 100-200 years, only)
- inherently safe
  - no chain reactions
  - only fuel for a few seconds burn in reactor
  - irregularities in operation causes burning conditions to disappear

The disadvantages of fusion are primarily that we are not yet able to construct the first fusion power plant, and that the expected size of power plant units is rather large.

## 1.2 Paths of fusion research

The nuclear fusion process of Deuterium (D) and Tritium (T) forming Helium and a neutron is the one with largest cross-section, i.e. the one easiest to obtain. The energy yield for the D-T fusion process is 17.6 MeV. The difficulty in promoting the process is to bring the nuclei sufficiently close to fuse,

[2] A 1000 MW solar power plant need about 100 $km^2$ photo-voltaic panels in Middle Europe [2]

[3] Deuterium is extracted from sea water and Tritium is produced at the power plant from Lithium.

[4] A 1000 MW coal power plant has a fuel consumption of 2.7 million tonnes of coal. The equivalent for a fusion power plant would be 100 kg Deuterium and 150 kg Tritium [2], the latter being transported in the form of approximately 350 kg Lithium.

[5] The waste of a fusion reaction between Deuterium and Tritium is Helium accompanied by a neutron which is absorbed in the reactor structure

since they are repelled from each other due to the Coulomb force. Different ways to overcome or circumvent the coulomb force are being attempted, and among these are: Muon catalyzed fusion [5], inertial confinement fusion (laser fusion) [6], and magnetic confinement fusion. I will only focus on the latter where the fuel is heated to form a plasma in which the thermal energy is sufficient for the particles to overcome the Coulomb force. The hot plasma (100-200 million degrees) can only be contained in a magnetic field, and a number of different configurations for magnetically confining a fusion plasma exist. The common feature of the configurations is a toroidally shaped vessel, but the magnetic configuration varies significantly. The Russian invented Tokamak is the leading concept (e.g., the joint European JET in England, JT-60U in Japan, DIII-D in the USA, and ASDEX Upgrade in Germany), while research is also conducted for concepts like the Stellarator (e.g., Wendelstein 7-AS in Germany and the Large Helical Device (LHD) in Japan) and the Spherical Tokamak (e.g., MAST in England and NSTX in the USA).

## 1.3 Present status of fusion research

Todays leading tokamak experiment is the Joint European Torus (JET) located in Oxfordshire in England. It was build from 1979 to 1983, and its performance has by far exceeded the original objectives. Since 1988 an international consortium consisting of Japan, the European Union, Russia and the United States of America has been designing the next major step towards a fusion reactor, namely the International Thermonuclear Experimental Reactor (ITER). The first ITER design was ready in 1998, but it was decided to redesign and downsize ITER. Currently, the new design is almost finished and the ITER parties - now including Canada, but excluding the USA - are negotiating the legal agreement, the financing, and the location of ITER. When a consensus on ITER is achieved (planned to occur in 2002), it will take approximately 8 years to build ITER at a cost currently estimated to be 4 billion Euros[6].
ITER will be approximately twice the size of JET (plasma volume of more than 800m$^3$), and as the first experimental fusion reactor it is projected to produce more power by fusion reactions than the power used to heat the plasma (up to a factor of 10 more). This energy, however, will not be harnessed, since ITER will be an experimental engineering and physics project testing various components and scenarios for a future reactor. The most probable course after an ITER success will be the construction of a demonstration power plant (DEMO), followed by prototypes and commercial power plants by the middle of the $21^{st}$ century.
The basic principles founding the footing for a fusion power plant are understood, but a number of tasks still remain to be solved before an efficient

[6]2011 update: In June 2005, it was decided to built ITER in Cadarache in Southern France. The ITER partners consist of EU, Japan, China, India, Russia, South Korea, and the USA. The cost is estimated to 15 billion Euros, and the first plasma is scheduled for 2020.

exploitation of fusion power can become a reality. On the engineering side the major tasks are materials testing and production of the huge fusion reactor construction, e.g., ITER's 12 T superconducting coils weighing approximately 840 tonnes. On the physics side the major task is to obtain better plasma control, specifically to improve the confinement of the plasma particles and energy, and integrated into this, to obtain a better understanding of the nature of plasma instabilities, turbulence and transport of plasma.
Transport of energy and particles across the magnetic field confinement is inevitable, and fusion energy is only feasible if this transport is limited. Therefore, a large effort experimentally, theoretically, and numerically is put into improving the understanding of the nature of the turbulence and the plasma transport it causes. The effort is intended to assist the design of more efficient fusion power plants, and may even be responsible for the feasibility of fusion power.
The present thesis should be regarded as a small paving stone on the road to a better understanding of the nature of the fundamental processes causing turbulent transport.

# Chapter 2

# Drift waves and turbulent transport in plasmas

As described in the previous chapter, one of the major tasks on the way to realising a fusion reactor is obtaining control of the particle and energy transport out the fusion plasma. The major transport mechanism is the so-called anomalous transport, which is transport caused by turbulence. During the last decades numerous models of turbulence have been proposed and investigated analytically and numerically in order to obtain a better understanding of the nature of the plasma turbulence.
In the following, different approaches to turbulence simulations are mentioned, succeeded by a description of the electrostatic drift wave models being treated in this thesis. Lastly, we briefly discuss the influence of shear flows on turbulent transport. Please note that the present chapter is only intended to give the reader a brief introduction to the field. It is thus not meant as a review of the broad field of plasma turbulence models and simulations, but rather as an appetizer. For a further review of plasma turbulence and plasma transport one may suggest [7–11].

## 2.1 Turbulence simulations

The nature of plasma turbulence is immensely complex. A comprehensive description would include interaction between numerous turbulent fluctuating fields, such as the density, potential, electron temperature, ion temperature, parallel currents, parallel velocities, magnetic field fluctuations, etc. Furthermore, the fluctuating fields interact with and influence background "equilibrium" quantities and are confined by complex magnetic fields with shear and curvature. Therefore, when attempting to reveal the secrets of nature by plasma turbulence simulations, one has to identify the objective and limit the problem size. One may roughly divide the models of plasma turbulence into two: 1) Simplified models focusing on a few physical mechanisms (e.g., the interaction of two turbulent fields and a background gradient) and using a simple geometry and 2) Complex models trying to approach the physics and the geometries of real experiments. Both approaches have advantages

and disadvantages: The simplified models are more transparent concerning the physics involved, and specific physical effects are more easily identified. However, important physical and geometrical effects may be missed. The more complex models, on the other hand, may produce results which are qualitatively and quantitatively close to experiments. This is an important step (towards, e.g., a numerical tokamak[1]), however, a clear distinction of the individual physical and geometrical effects is difficult. Furthermore, the aspect of computation time sets some limits on the extensiveness of models, but this limitation is less significant today with the increased powers of computers.

Turbulence and transport models can also be divided into fluid and kinetic models where the latter concerns the distribution functions of the particles, whereas the former treats the plasma as a macroscopic continuum. One can make a further division into gyrofluid (e.g., [12]) and gyrokinetic models (e.g., [13]). We will only consider fluid turbulence in the following.

Having established the fluid equations for a plasma one further distinguishes between magnetohydrodynamic (MHD) instabilities and drift order microinstabilities [14], where the spatial scales of microturbulence are much smaller than the scales of the MHD equilibrium and MHD instabilities. Generally, the growth rate for MHD instabilities is much larger than for drift order microinstabilities. Owing to the high standard of today's plasma experiments the dynamics is rarely influenced by MHD instabilities, which would occur on a much faster time-scale than that observed [15]. In other words the experimental plasmas are generally MHD stable and the time scale of the observed turbulence is of drift ordering, i.e. $\omega_t \ll \omega_{ci}$, where $\omega_t$ is a typical frequency of the turbulence and $\omega_{ci} = eB/m_i$ is the ion cyclotron frequency. For microturbulence one typically assumes presence of macroscopic sources of free energy, e.g., the density gradient that are supplied by a (MHD stable) global MHD equilibrium being constant in time [10].

We are considering drift order microturbulence, and having narrowed down this far we may further split up into models including electromagnetic fluctuations and models with a static magnetic field, i.e. electromagnetic and electrostatic models. Some important dynamics are lost by choosing an electrostatic model, like, e.g., coupling to Alfvén waves (drift Alfvén turbulence is described in, e.g., [16]). However, various experimental results, e.g., [17, 18], point to electrostatic turbulence being responsible for a major part of the turbulent transport. Using an electrostatic model as opposed to an electromagnetic does also simplify the model, enabling more clarity of some physical effects as discussed above. Note additionally that an electrostatic model may still contain a complicated magnetic field geometry, e.g., with shear and/or curvature.

A wide variety of geometries of the simulation domains exist. These can be slab, cylindrical or toroidal, with one or more boundaries being periodic

[1] An aim for some researchers is to construct codes and computers sufficiently powerful to simulate the turbulent transport performance of fusion devices before they are build. See, e.g., the Numerical Tokamak Turbulence Project on http://www.acl.lanl.gov/GrandChal/Tok/tokamak.html

in one, two or three dimensions. Two considerations are important when choosing the geometry: the geometry should be suitable for the problem considered, and at the same time the geometry and the model should be sufficiently simple to evaluate in a finite time. Hence, the preferred geometries, until recently, have been doubly/triply periodic slab or cylindrical [19], whereas more and more toroidal codes have emerged over the last few years. The models treated in this thesis are electrostatic drift wave models, and with reference to the above division of models into simplified and complex, we should state that the models treated in this thesis should be considered to be among the simplified models.

## 2.2 Electrostatic drift wave models

"Drift waves occur universally in magnetized plasmas producing the dominant mechanism for the transport of particles, energy and momentum across magnetic field lines" [9]. The phenomenological picture of resistive drift waves has often been explained (see, e.g., [20–22]), thus it suffices to mention that the drift wave instability occurs as a result of the plasma resistivity disabling the electrons to instantaneously respond to the ion motion. This results in a linear instability of the drift waves that grow exponentially by extracting free energy from the background gradients.
In 1983 Hasegawa and Wakatani proposed a self-consistent three-dimensional (3D) two-field model describing resistive drift waves [23]. Historically the model may be viewed as a further development of the two-dimensional (2D) one-field Hasegawa-Mima model from 1978 of resistive drift waves assuming Boltzmann distributed electrons [24]. The Hasegawa-Mima equation corresponds to the Charney equation for Rossby waves in standard (nonmagnetised) fluid turbulence (see, e.g., [25,26]). Since 1983, the Hasegawa-Wakatani model has been cited more than 80 times and is probably the most successful model in the field of drift wave turbulence studies.
The Hasegawa-Wakatani model consists of two coupled nonlinear partial differential equations in the perturbations of the density and the electrostatic potential. The model has mainly been studied in a 2D reduction due to limited computer power. The reduction seemed to be well justified since the turbulence dynamics is mainly two-dimensional (perpendicular to the magnetic field). Hence, the parallel dynamics was assumed to interact through only one parallel mode. This mode has been chosen in two different ways, but in [27] it was concluded that the method of the choice of the parallel mode strongly affected the results and therefore fully three-dimensional simulations are necessary.
The first results of three-dimensional simulations of the Hasegawa-Wakatani model were presented by Biskamp and Zeiler in 1995 in [28]. Further studies of the three-dimensional model were presented in [22, 29, 30]. The results are significantly different from those of the 2D simulations and emphasise the need for 3D simulations, although some similarities could be found. The most important difference between the two approaches is that in the 3D for-

mulation the drift waves may couple to convective cells, which are nonlinear mode structures having $k_\parallel = 0$, while drift waves have finite $k_\parallel$, where $k_\parallel$ is the wave number along the magnetic field.
The Hasegawa-Wakatani model forms the basis for the models investigated in this thesis. The model is thus reviewed in the next chapter and is further studied in a three-dimensional non-periodic geometry in Chapter 6.

## 2.3 Shear flows and transport

Transport fluxes of particles, heat and energy are some of the major quantities sought to be investigated by the numerous plasma turbulence models mentioned above. These are interesting measures, since mitigation (and ultimately control) of turbulent transport may be a prerequisite for an efficient future fusion reactor as discussed in Chapter 1. One objective of numerical modeling is therefore to investigate how the turbulence and turbulent transport evolve and interact with different inhibiting mechanisms.
In experiments one has obtained confinement regimes, such as H-mode confinement that shows a drastically reduced radial transport[2] [31]. The generation of H-mode confinement regimes seems to be closely related to poloidal shear flows[3] in the edge region of the plasma (see [11] and references therein). Generally, it is observed experimentally and in numerical models that shear flows in plasmas suppress turbulence and transport. It is also the case for the so-called internal transport barriers (ITB) that occur in regions with strong flow shear [11]. Thus, the physics of the turbulence-flow interaction and the generation mechanism of these flows are of great interest.
A property of many turbulent systems is *self-organisation*, by which large scale structures in the turbulence are created by the turbulent field itself. As it will be shown in this thesis, large scale structures such as vortices and flows are created as a result of self-organisation of the drift wave turbulence described by the Hasegawa-Wakatani model.
In the view of turbulence self-organising into, e.g., a shear flow, one may say that shear flow suppression of turbulence is a matter of energy redistribution from the turbulence to the flows. However, shear flows may be applied externally (this is discussed in Section 6.4.4), and the direct effect from the shear flow upon the turbulence is of interest regardless of how the shear flow was generated. In [11] a list of criteria for shear flow suppression of turbulence is advanced: 1) the shearing rate of the shear flow should exceed the eddy turnover rate, 2) the shear flow must be stable, 3) the turbulence should stay in the region of shear flow longer than the eddy turnover time, and 4) the dynamics should be two-dimensional. Regarding 1) we define the shearing rate as $\tau^{-1} = \frac{\partial v_y}{\partial x}$ and the eddy turnover rate is the inverse of the eddy turnover time or eddy lifetime defined by the time the fluid parcels of an eddy structure remain coherent. Regarding 2) the requirement of the shear flow being stable is often not met in nonionised fluids, where shear flows with

[2] H-modes will be further discussed in Section 7.4.3.
[3] We understand a shear flow as a flow with shear in the velocity profile.

$\frac{\partial^2 v}{\partial x^2} \neq 0$ will be Kelvin-Helmholtz unstable and lead to instabilities rather than suppression of turbulence. Nevertheless, even the unstable shear flows may change the unstable wavenumber regimes [32]. In the case of fusion plasmas, however, the requirement of a stable shear flow is routinely met, since it is believed that magnetic shear stabilises the Kelvin-Helmholtz instability. Regarding 4) the strong magnetic field in fusion plasmas cause the dynamics of the turbulence to be effectively two-dimensional perpendicular to the magnetic field. However, note that despite the two-dimensionality of the turbulent dynamics, three-dimensional effects are important as discussed in Section 2.2.

The physical effects of a stable shear flow on fluctuations and transport can be divided into four distinct categories [11]: "1) the fundamental process of direct reduction of scales and amplitude in turbulence, 2) the stabilisation of collective modes that are otherwise linearly unstable, 3) the disruption of correlation between the fluctuations of an advectant and the advecting flow, resulting in a reduction of transport far beyond that accounted for by decreased fluctuation amplitudes, and 4) the disruption of the extended correlation of large-scale avalanchelike transport events." For a thorough treatment of shear flow suppression of turbulence and transport, please refer to [11].

# Chapter 3

# The Hasegawa-Wakatani model

The most successful basic description of electrostatic drift wave turbulence in a plasma is the Hasegawa-Wakatani model [23] from 1983. Simulations with the model was first performed in a two-dimensional geometry, but from the last part of the 1990's simulations in a full three-dimensional geometry were presented [28, 30]. The Hasegawa-Wakatani model was extensively treated in a three-dimensional periodic geometry in the authors Master's thesis [22]. We will, however, start with a review of the derivation of the Hasegawa-Wakatani equations, and also briefly review the results of the simulations with the model found in [22], since the Hasegawa-Wakatani model is the basis for the models and simulations described in this thesis.
The contents of this chapter were in part described in [29, 30] and naturally also in [22].

## 3.1 A review of the derivation of the Hasegawa-Wakatani model

The Hasegawa-Wakatani model is based on these equations:

- The ion vorticity equation
- The electron continuity equation
- The generalised Ohm's law for the parallel electron dynamics

Below, we derive the Hasegawa-Wakatani equations after a presentation of the most basic assumptions[1]. The remaining assumptions will be presented appropriately as they are used. For a more detailed description of the derivation of the equations, please refer to [22].

[1] 2011 update: The present derivation of the Hasegawa-Wakatani model is inspired by the original derivation by Hasegawa and Wakatani [23]. An opponent at the thesis defence pointed out that their derivation is not particularly clear. Furthermore, the number of assumptions were criticised. I agree that some assumptions in the text are really corollaries of other assumptions like the case of Assumption 8 that follow from Assumption 7. By this comment we point the readers attention to this fact, and have chosen not to alter the original derivation and assumptions.

### 3.1.1 Fundamental assumptions

Drift waves are localised to the edge region of a plasma since a density gradient is required. The temperature in the edge region is relatively low, and we consider a plasma with warm electrons having a temperature $T_e$, and cold ions having a temperature $T_i$.

**Assumption 1** $\frac{T_i}{T_e} \ll 1$

Due to this assumption, inclusion of effects of finite ion temperature will only give rise to higher order terms, and these are neglected in the Hasegawa-Wakatani model. A modified model including finite ion temperature effects is derived in Chapter 4.
Electron temperature gradient effects are neglected. This is due to the assumption that the relative electron temperature gradient is much smaller than the relative density gradient

**Assumption 2** $\frac{\nabla_\perp \ln(T_e)}{\nabla_\perp \ln(n_0)} \ll 1$

where $n_0$ is the background number density. Hence the electron temperature $T_e$ is assumed to be constant. The assumption may be valid in the edge region of a tokamak as indicated in Figure 3.1. The effects of including an electron temperature gradient and temperature perturbations are described in Chapter 5.

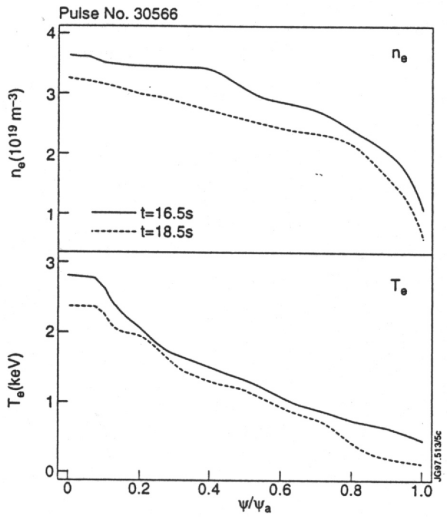


Figure 3.1: The electron temperature and density gradients for a JET pulse at two time slices. The abscissa $\psi/\psi_a$ ranges from 0 at the center of the plasma to 1 at the edge. Taken from [33].

A fusion plasma is configured in a sheared and curved magnetic field. To avoid the complicated geometrical effects we make a local approximation and assume

**Assumption 3** *The geometry is a slab.*

i.e. the domain is chosen sufficiently small to neglect the geometrical variations of the magnetic field. The magnetic field lines of the unperturbed constant magnetic field are straight and are assumed to be in the direction of the $z$-axis of the slab:

**Assumption 4** $\mathbf{B} = B_0 \mathbf{e}_z$

The directions perpendicular to $\mathbf{B}$ are chosen so that the background density is varying in the $x$-direction, corresponding to the radial direction in a toroidal device, and the $y$-direction then corresponds to the poloidal direction in a toroidal device. We assume that the plasma is a low $\beta$ plasma, i.e. that the magnetic field pressure is much larger than the particle pressure:

**Assumption 5** $\beta = \frac{n_e T_e}{B^2/2\mu_0} \ll 1$

where $\mu_0$ is the vacuum permeability and $n_e$ is the electron number density. Perturbations in density and potential of the plasma also generate perturbations in the magnetic field. It is, however, a reasonable approximation to neglect these perturbations, since the magnetic field is very strong (Assumption 5). This means $\partial B/\partial t = 0$ and Faraday's law leads to the electrostatic approximation

**Assumption 6** $\mathbf{E} = -\nabla\phi$

where $\phi$ is the electrostatic potential.
If the wave numbers fulfill

**Assumption 7** $k^2 \ll \frac{1}{\lambda_D^2}$

where $\lambda_D$ is the Debye length, then it can be assumed that

**Assumption 8** $n_e \approx n_i$

This is called the quasi-neutrality condition. It follows from the fact that a plasma can be assumed to be quasi-neutral over distances larger than the Debye length [34]. The electron and ion number densities can be written as

$$n_e = n_i = n = n_0 + n_1 \quad ,$$

where $n_1$ is the density perturbation.

### 3.1.2 The ion vorticity equation

The ion fluid equation describes momentum conservation for ions, and is the basis for the derivation of the ion vorticity equation. In [8] for example, it is given by

$$\frac{\partial \mathbf{v}_i}{\partial t} + (\mathbf{v}_i \cdot \nabla)\mathbf{v}_i = \frac{e}{m_i}(\mathbf{E} + \mathbf{v}_i \times \mathbf{B}) - \frac{\nabla p_i}{n_i m_i} + \mathbf{g} \tag{3.1}$$

where $\mathbf{v}_i$ is the ion velocity, $m_i$ is the ion mass, $p_i$ is the isotropic ion pressure, and $\mathbf{g}$ is a gravitational force on the ions included for generality.
Before proceeding, the following assumptions about $\mathbf{v}_i$ are stated. Since $m_i \gg m_e$ we may assume that the ion inertia fixes the ions in the parallel direction. Furthermore, the ion thermal velocity is neglected due to Assumption 1. Hence the ion motion parallel to the magnetic field is zero:

**Assumption 9** $\mathbf{v}_i \cdot \mathbf{e}_z = 0$

We want to describe the motion of the ions in the drift order approximation. Hence, we assume that the time-scale of the drift motion is much larger than the time-scale of the gyro motion of the ions around the magnetic field lines:

**Assumption 10** $\omega_t \ll \omega_{ci}$

where $\omega_t$ is a typical frequency of the turbulence observed, and $\omega_{ci}$ is the ion cyclotron frequency given by: $\omega_{ci} = eB/m_i$, $\boldsymbol{\omega}_{ci} = \omega_{ci}\mathbf{e}_z$. From Assumption 10 follows that the $\mathbf{E}\times\mathbf{B}$-drift is dominant to the polarisation drift [8]. We may thus express the velocities of the ions and electrons perpendicular to the magnetic field by

$$\mathbf{v}_{i\perp} = \mathbf{v}_{e\perp} = \mathbf{v}_E = \frac{\mathbf{E}\times\mathbf{B}}{B^2} = \frac{-\nabla\phi\times\mathbf{e}_z}{B_0} = \frac{1}{B_0}\begin{bmatrix} -\frac{\partial\phi}{\partial y} \\ \frac{\partial\phi}{\partial x} \\ 0 \end{bmatrix} \tag{3.2}$$

$\mathbf{v}_E$ is the $\mathbf{E}\times\mathbf{B}$-velocity, and we use Assumption 4 and 6 for the second last equality.
We will also assume that the variation of the waves is mainly in the perpendicular plane, so that

**Assumption 11** $k_\parallel \ll k_y \sim k_x$

where $k_\parallel = k_z$ is the wavenumber in the $z$-direction, i.e. parallel to the magnetic field. The assumption is valid for a typical drift wave instability, as it will appear later in the analysis.
We take the curl of (3.1) and obtain

$$\frac{\partial\boldsymbol{\omega}}{\partial t} - \nabla\times(\mathbf{v}_i\times\boldsymbol{\omega}) = -\frac{\partial\boldsymbol{\omega}_{ci}}{\partial t} + \nabla\times(\mathbf{v}_i\times\boldsymbol{\omega}_{ci}) + \frac{1}{n_i^2 m_i}\nabla n_i\times\nabla p_i \tag{3.3}$$

where $\boldsymbol{\omega}$ is the the ion vorticity given by: $\boldsymbol{\omega} = (\nabla\times\mathbf{v}_i)$. On the right hand side Faraday's law has been used. Note that we keep the first term although it is zero according to the electrostatic approximation.
We may find an expression for $\nabla\cdot\mathbf{v}_i$ from the ion continuity equation:

$$\frac{\partial n_i}{\partial t} + \nabla\cdot(n_i\mathbf{v}_i) = 0 \Rightarrow \nabla\cdot\mathbf{v}_i = -(\frac{\partial}{\partial t} + \mathbf{v}_i\cdot\nabla)\ln n_i$$

By using appropriate vector relations (3.3) can be rearranged to the ion vorticity equation, which at this point is an exact derivation from the ion fluid equation

$$(\frac{\partial}{\partial t} + \mathbf{v}_i\cdot\nabla)\ln\left(\frac{\omega+\omega_{ci}}{n_i}\right) = \frac{1}{n_i^2 m_i}\nabla n_i\times\nabla p_i\cdot\mathbf{e}_z \tag{3.4}$$

where we have taken the scalar product with $\mathbf{e}_z$, since the only non-zero component of $\boldsymbol{\omega}$ is the parallel ($z$) component due to Assumption 11.
The parallel component of the ion vorticity, $\omega$, can be expressed as

$$\omega = (\nabla\times\mathbf{v}_i)\cdot\mathbf{e}_z = \frac{-\nabla\times(\nabla\phi\times\mathbf{e}_z)}{B_0}\cdot\mathbf{e}_z = \frac{\nabla_\perp^2\phi}{B_0} \tag{3.5}$$

By Assumption 1 $\nabla p_i = \nabla(n_i T_i)$ and in turn the term on the right hand side of (3.4) vanishes. According to Assumption 9 and (3.2) we may replace $\mathbf{v}_i$ by $\mathbf{v}_E$, and we introduce the convective derivative now defined as:

$$\frac{\mathrm{D}}{\mathrm{D}t} = \frac{\partial}{\partial t} + \mathbf{v}_E \cdot \nabla$$

Since we are interested in weakly nonlinear drift waves, the relative perturbations in number density $n_1$, electrostatic potential $\phi$, and ion vorticity $\omega$ are assumed to be of the same order, $\varepsilon$.

**Assumption 12** $\quad \frac{n_1}{n_0} \sim \frac{e\phi}{T_e} \sim \frac{\omega}{\omega_{ci}} \sim \varepsilon \ll 1$

Using Assumption 12 in (3.4) keeping only first order terms leads to

$$\frac{\mathrm{D}}{\mathrm{D}t}\left(\frac{\omega}{\omega_{ci}} - \ln n_0 - \frac{n_1}{n_0}\right) = 0, \quad \text{since } \frac{\partial B}{\partial t} = 0$$

A viscosity term is normally included [23], and using (3.5) the ion vorticity equation can finally be written as

$$\frac{\mathrm{D}}{\mathrm{D}t}\left(\frac{\nabla_\perp^2 \phi}{\omega_{ci} B_0} - \ln n_0 - \frac{n_1}{n_0}\right) = \frac{\mu}{\omega_{ci} B_0} \nabla_\perp^4 \phi \tag{3.6}$$

where $\mu$ is a viscosity parameter.
We may define a quantity denominated the potential vorticity, $PV$, from the ion vorticity equation:

$$PV = \frac{\omega + \omega_{ci}}{n_i} = \frac{\nabla_\perp^2 \phi}{\omega_{ci} B_0} - \ln n_0 - \frac{n_1}{n_0} \tag{3.7}$$

We will find an expression for $PV$ in dimensionless variables in Section 3.1.5, and further discuss the potential vorticity in Chapter 6.

### 3.1.3 The generalised Ohm's law

The parallel electron dynamics may be described by the parallel component of the generalised Ohm's law. The generalised Ohm's law is a result of ideal or single-fluid magnetohydrodynamics (MHD) [21, 34] . In ideal MHD the plasma is described as a single fluid by assuming quasi-neutrality (Assumption 8), and by the assumption that

**Assumption 13** *electron inertia is neglected*

since $\frac{m_e}{m_i} \ll 1$.
In [21] the generalised Ohm's law is found from the single-fluid *electron* equation of motion. For the first order perturbed quantities it is expressed by

$$\mathbf{E}_1 + \mathbf{v}_1 \times \mathbf{B}_0 = \eta \mathbf{J}_1 + \frac{1}{n_0 e}(\mathbf{J} \times \mathbf{B} - \nabla p_e)_1 \tag{3.8}$$

where $\mathbf{v} \approx \mathbf{v}_i + (m_e/m_i)\mathbf{v}_e$, and $\eta$ is the plasma resistivity and $\mathbf{J}$ is the plasma current density. In the electrostatic approximation (Assumption 6)

we neglect perturbations of the magnetic field, thus $(\mathbf{J}\times\mathbf{B})_1 = \mathbf{J}_1\times\mathbf{B}_0$. This term is perpendicular to the magnetic field and the parallel component of the generalised Ohm's law is then

$$E_\parallel = \eta J_\parallel - \frac{1}{n_0 e}\frac{\partial p_{e1}}{\partial z} \tag{3.9}$$

We assume the electrons to be collisionally damped rather than damped by Landau damping[2]. This is the case if

**Assumption 14** $\quad \frac{\omega_t}{\nu_e} \ll \frac{v_{Te}^2 k_\parallel^2}{\nu_e^2} \lesssim 1$

where $\nu_e$ is the electron collision rate, and $v_{Te}$ is the thermal speed. If this condition is fulfilled, the electrons may be treated as an isothermal fluid so that no temperature gradients in the $z$-direction exist, i.e. $\frac{\partial}{\partial z}\ln T_e \approx 0$ [23]. We deduce from Assumption 14 that $\omega_t \sim \frac{\partial}{\partial t} \sim \varepsilon$.
If we use Assumption 6 and 14, we may rewrite (3.9) as follows:

$$\begin{aligned} -\frac{\partial\phi}{\partial z} &= \eta J_\parallel - \frac{1}{n_0 e}\frac{\partial(n_1 T_e)}{\partial z} \Leftrightarrow \\ J_\parallel &= -\frac{1}{\eta}\left(\frac{\partial\phi}{\partial z} - \frac{T_e}{n_0 e}\frac{\partial n_1}{\partial z}\right) \Leftrightarrow \\ J_\parallel &= -\frac{T_e}{\eta e}\frac{\partial}{\partial z}\left(\frac{e\phi}{T_e} - \frac{n_1}{n_0}\right) \end{aligned} \tag{3.10}$$

### 3.1.4 The electron continuity equation

The electron velocity can be expressed as

$$\mathbf{v}_e = \mathbf{v}_{e\perp} + \mathbf{v}_{e\parallel} = \mathbf{v}_E - \frac{J_\parallel}{e n_e}\mathbf{e}_z$$

according to Assumption 10 and the generalised Ohm's law. This can be inserted in the electron continuity equation to give

$$\frac{\partial n_e}{\partial t} + n_e\nabla\cdot(\mathbf{v}_E - \frac{J_\parallel}{e n_e}\mathbf{e}_z) + (\mathbf{v}_E - \frac{J_\parallel}{e n_e}\mathbf{e}_z)\cdot\nabla n_e = 0 \tag{3.11}$$

Using appropriate vector relations on the $\nabla\cdot(\frac{J_\parallel}{e n_e}\mathbf{e}_z)$-term, and remembering that $\nabla\cdot\mathbf{v}_E = 0$, (3.11) can be rearranged to

$$\begin{aligned} \frac{\mathrm{D}n_e}{\mathrm{D}t} &= n_e\frac{\partial}{\partial z}\left(\frac{J_\parallel}{e n_e}\right) + \frac{J_\parallel}{e n_e}\frac{\partial n_e}{\partial z} \\ &= \frac{n_e}{e}\left(\frac{1}{n_e}\frac{\partial J_\parallel}{\partial z} + J_\parallel\frac{\partial n_e^{-1}}{\partial z}\right) + \frac{J_\parallel}{e n_e}\frac{\partial n_e}{\partial z} \\ &= \frac{n_e}{e}\left(\frac{1}{n_e}\frac{\partial J_\parallel}{\partial z} - \frac{J_\parallel}{n_e^2}\frac{\partial n_e}{\partial z}\right) + \frac{J_\parallel}{e n_e}\frac{\partial n_e}{\partial z} \\ &= \frac{1}{e}\frac{\partial J_\parallel}{\partial z} \end{aligned} \tag{3.12}$$

[2] A description of Landau damping may be found in, e.g., [21].

We divide (3.12) by $n_e$ and use $n_e = n_0 + n_1$ to obtain

$$\frac{\mathrm{D}}{\mathrm{D}t}\ln(n_0+n_1) = \frac{1}{e(n_0+n_1)}\frac{\partial J_\parallel}{\partial z} \tag{3.13}$$

Since $\frac{n_1}{n_0} \ll 1$ (Assumption 12) we may write

$$\frac{1}{n_0+n_1} = \frac{1}{n_0}\frac{1}{1+\frac{n_1}{n_0}} \approx \frac{1}{n_0}(1-\frac{n_1}{n_0})$$

Inserting this in (3.13) we obtain

$$\frac{\mathrm{D}}{\mathrm{D}t}\ln(n_0+n_1) = \frac{1-\frac{n_1}{n_0}}{en_0}\frac{\partial J_\parallel}{\partial z} \tag{3.14}$$

We only want to keep first order terms, and hence the second term on the right hand side can be neglected, since $J_\parallel$ is a first order term as seen from (3.10) and Assumption 12. At the left hand side we use the approximation $\ln(1+\frac{n_1}{n_0}) \approx \frac{n_1}{n_0}$ and finally arrive at

$$\frac{\mathrm{D}}{\mathrm{D}t}\left(\ln n_0 + \frac{n_1}{n_0}\right) = \frac{1}{en_0}\frac{\partial J_\parallel}{\partial z} \tag{3.15}$$

### 3.1.5 The Hasegawa-Wakatani system

We have now obtained the three equations that form the basis for the Hasegawa-Wakatani system and restate them for convenience

$$\frac{\mathrm{D}}{\mathrm{D}t}\left(\frac{\nabla_\perp^2\phi}{\omega_{ci}B_0} - \ln n_0 - \frac{n_1}{n_0}\right) = \frac{\mu}{\omega_{ci}B_0}\nabla_\perp^4\phi \tag{3.6}$$

$$J_\parallel = -\frac{T_e}{\eta e}\frac{\partial}{\partial z}\left(\frac{e\phi}{T_e} - \frac{n_1}{n_0}\right) \tag{3.10}$$

$$\frac{\mathrm{D}}{\mathrm{D}t}\left(\ln n_0 + \frac{n_1}{n_0}\right) = \frac{1}{en_0}\frac{\partial J_\parallel}{\partial z} \tag{3.15}$$

First we eliminate $J_\parallel$ by substituting (3.10) in (3.15):

$$\frac{\mathrm{D}}{\mathrm{D}t}\left(\ln n_0 + \frac{n_1}{n_0}\right) = -\frac{T_e}{\eta e^2 n_0}\frac{\partial^2}{\partial z^2}\left(\frac{e\phi}{T_e} - \frac{n_1}{n_0}\right) \tag{3.16}$$

This equation is commonly simplified by assuming that the relative background density gradient is constant locally in the edge region, i.e. in the domain of the model. This is the case if the background number density is of the form

**Assumption 15** $\quad n_0 = n_0(x) = N_0 e^{-\frac{x}{L_n}}$

where $N_0$ is a constant number density, and $L_n$ is a characteristic length scale for the density gradient. Then the relative background density gradient is

$$\frac{1}{n_0}\frac{\partial n_0}{\partial x} = \frac{\partial \ln(n_0)}{\partial x} = -\frac{1}{L_n}\mathbf{e}_x \tag{3.17}$$

For Assumption 15 to be valid we assume that the length scale of the perturbations fulfills

**Assumption 16** $\quad \frac{1}{L_n} \ll k$

A typical length scale of the perturbations is the ion Larmor radius at the electron temperature $\rho_s$, given by

$$\rho_s = \frac{\sqrt{T_e m_i}}{eB_0}$$

This follows implicitly from the equations, and it may thus be seen that Assumption 16 leads to $\frac{\rho_s}{L_n} \sim \varepsilon \ll 1$.
Using Assumption 15 we can write (3.16) as

$$\frac{\mathrm{D}}{\mathrm{D}t}\left(\frac{n_1}{n_0}\right) + \frac{1}{L_n B_0}\frac{\partial \phi}{\partial y} = -\frac{T_e}{\eta e^2 n_0}\frac{\partial^2}{\partial z^2}\left(\frac{e\phi}{T_e} - \frac{n_1}{n_0}\right) \tag{3.18}$$

since

$$\frac{\mathrm{D}}{\mathrm{D}t}\ln n_0 = (\frac{\partial}{\partial t} + \mathbf{v}_E \cdot \nabla)\ln(N_0 e^{-\frac{x}{L_n}}) = \mathbf{v}_E \cdot (-\frac{1}{L_n}\mathbf{e}_x) = \frac{1}{L_n B_0}\frac{\partial \phi}{\partial y}$$

The partial differential equation (3.18) is the Hasegawa-Wakatani equation for the density perturbation. The corresponding equation for the potential is obtained by substituting (3.16) in (3.6):

$$\frac{\mathrm{D}}{\mathrm{D}t}\left(\frac{\nabla_\perp^2 \phi}{\omega_{ci} B_0}\right) = -\frac{T_e}{\eta e^2 n_0}\frac{\partial^2}{\partial z^2}\left(\frac{e\phi}{T_e} - \frac{n_1}{n_0}\right) + \frac{\mu}{\omega_{ci} B_0}\nabla_\perp^4 \phi \tag{3.19}$$

We have now obtained the Hasegawa-Wakatani equations (3.18) and (3.19). They are a self-consistent set of equations of the order of $\varepsilon^2$. This follows from Assumption 12 and 14, and that $\frac{\rho_s}{L_n} \sim \varepsilon$, provided

$$\frac{T_e}{\eta e^2 n_0} \sim \varepsilon \ll 1$$

is fulfilled.
The Hasegawa-Wakatani equations are commonly re-scaled to the order of unity and simplified by transforming them to dimensionless variables with the following normalisations:

$$\tilde{x} = \frac{x}{\rho_s}, \quad \tilde{y} = \frac{y}{\rho_s}, \quad \tilde{z} = \frac{z}{L_\parallel}, \quad \tilde{t} = t\omega_{ci}\frac{\rho_s}{L_n}, \quad \tilde{\phi} = \frac{e\phi}{T_e}\frac{L_n}{\rho_s}, \quad \tilde{n} = \frac{n_1}{n_0}\frac{L_n}{\rho_s}$$

$L_\parallel$ is a typical parallel scale length. Notice that the normalised quantities are all of the order unity, because of the scaling. The Hasegawa-Wakatani equations are thus, expressed in dimensionless variables:

$$(\frac{\partial}{\partial\tilde{t}} + \tilde{\mathbf{v}}_E \cdot \tilde{\nabla}_\perp)\tilde{n} + \frac{\partial\tilde{\phi}}{\partial\tilde{y}} = \mathcal{C}\frac{\partial^2}{\partial\tilde{z}^2}(\tilde{n} - \tilde{\phi}) \tag{3.20}$$

$$(\frac{\partial}{\partial\tilde{t}} + \tilde{\mathbf{v}}_E \cdot \tilde{\nabla}_\perp)(\tilde{\nabla}_\perp^2\tilde{\phi}) = \mathcal{C}\frac{\partial^2}{\partial\tilde{z}^2}(\tilde{n} - \tilde{\phi}) + \upsilon\tilde{\nabla}_\perp^4\tilde{\phi} \tag{3.21}$$

where $\upsilon = \mu L_n/\rho_s^3$ is a viscosity parameter. The parallel coupling factor, $\mathcal{C}$, is defined by

$$\mathcal{C} \equiv \frac{T_e L_n}{\eta e^2 n_0 \omega_{ci}\rho_s L_\parallel^2} \tag{3.22}$$

Note that $\mathcal{C}$ is consistently of the order of 1, since $L_n/\rho_s$ and $T_e/\eta e^2 n_0$ is of the order of $\varepsilon^{-1}$ and $\varepsilon$ respectively. Unless explicitly expressed otherwise $\mathcal{C} = 1$ in the simulations. The normalisations change (3.5) to

$$\tilde{\omega} = \tilde{\nabla}_\perp^2\tilde{\phi}$$

We use *Fourier spectral methods* and a semi-implicit scheme using the third order Stiffly Stable method [35] for the temporal integration in the numerical simulations of the present work (see Chapter 3 of [22]). These require dissipation of high wave number modes to avoid numerical noise generated by inadequately resolved steep gradients. The effect of the viscous term in (3.21) is insufficient, as the simulations only have a limited spatial resolution. It is thus often replaced by a non-physical *hyperviscosity* term of the form $\nabla_\perp^{2p}$[28,36–38], where $p$ is an integer and $2p$ is denoted as the order of the hyperviscosity. The viscosity parameter, $\nu$, and the order of the hyperviscosity, $2p$, is chosen to ensure sufficient dissipation of the highest modes, while still allowing for a spectral subrange, where the nonlinearity is important and the influence of viscosity is negligible. Emphasis should be placed on the fact that hyperviscosity is applied for numerical reasons only, and is assumed not to influence the physics of the system. The hyperviscosity is only imposed in the perpendicular plane, and simulations have shown this to be adequate. The hyperviscosity term is also added to (3.20), and the final formulation of the equations is thus

$$(\frac{\partial}{\partial t} + \mathbf{v}_E \cdot \nabla_\perp)n + \frac{\partial\phi}{\partial y} = \mathcal{C}\frac{\partial^2}{\partial z^2}(n - \phi) + \nu\mathcal{D}^{2p}n \tag{3.23}$$

$$(\frac{\partial}{\partial t} + \mathbf{v}_E \cdot \nabla_\perp)(\nabla_\perp^2\phi) = \mathcal{C}\frac{\partial^2}{\partial z^2}(n - \phi) + \nu\mathcal{D}^{2p+2}\phi \tag{3.24}$$

$$\mathcal{D}^{2p} \equiv (-1)^{p+1}\nabla_\perp^{2p}$$

The "$\sim$"s are omitted for convenience here and henceforth. For convenience we have chosen to use the same viscosity parameter in both equations.
Finally, we may find a dimensionless form of the expression (3.7) we found in Section 3.1.2 for the potential vorticity, $PV$, using Assumption 15 for $n_0$:

$$PV = \frac{\rho_s}{L_n}\nabla_\perp^2\phi - \ln N_0 + \frac{\rho_s}{L_n}x - \frac{\rho_s}{L_n}n \tag{3.25}$$

## 3.2 A review of the analytical treatment of the Hasegawa-Wakatani model

A full analytical solution of the partial differential equations is not generally possible. However, important properties of the system may be found analytically. In the present section we will analyse the linear instability and derive the temporal derivatives of the energy and the enstrophy, and hereby determine the sources and sinks of the system.

### 3.2.1 Dispersion relation and linear growth rate

The dispersion relation for the linearly unstable waves of the Hasegawa-Wakatani system can be derived from (3.23) and (3.24) by linear stability analysis. We assume that as long as $n$ and $\phi$ are small, they can locally be described as plane waves of the form

$$n = n_a e^{i(\mathbf{k}\cdot\mathbf{r}-\omega_t t)}, \quad \phi = \phi_a e^{i(\mathbf{k}\cdot\mathbf{r}-\omega_t t)}$$

with $n_a$ and $\phi_a$ being small quantities. By inserting these in the Hasegawa-Wakatani equations we deduce the dispersion relation:

$$\omega_t^2 + i\omega_t \left[\mathcal{C}k_\parallel^2\left(1+\frac{1}{k_\perp^2}\right)+2\nu k_\perp^{2p}\right] - \mathcal{C}k_\parallel^2\left[i\frac{k_y}{k_\perp^2}+\frac{\nu^2 k_\perp^{4p}}{\mathcal{C}k_\parallel^2}+\nu k_\perp^{2p}\left(1+\frac{1}{k_\perp^2}\right)\right]=0 \tag{3.26}$$

The Hasegawa-Wakatani system contains the resistive linear instability, and therefore small perturbations will grow. The growth rate can be determined from the non-damped branch of the dispersion relation for the Hasegawa-Wakatani system and it is found to be

$$\omega_t = \omega_r + i\gamma \tag{3.27}$$

with frequency $\omega_r$ and growth rate $\gamma$ which are given by:

$$\omega_r = \frac{\lambda_0}{2\sqrt{2}}\sqrt{\sqrt{1+\frac{16\sigma^2}{\lambda_0^4}}-1} \tag{3.28}$$

$$\gamma = -\frac{\lambda}{2}+\frac{\lambda_0}{2\sqrt{2}}\sqrt{\sqrt{1+\frac{16\sigma^2}{\lambda_0^4}}+1} \tag{3.29}$$

with

$$\lambda = \lambda_0 + \lambda_1 = \mathcal{C}k_\parallel^2\frac{1+k_\perp^2}{k_\perp^2}+2\nu k_\perp^{2p} \qquad \text{and} \qquad \sigma = \mathcal{C}k_\parallel^2\frac{k_y}{k_\perp^2}$$

The linear waves are seen to be dispersive and the dependency of the growth rate on $k_y$ and $k_\parallel$ is presented in Figure 3.2. $\gamma$ has a maximum at $\gamma_{max} \approx \gamma(k_x = 0, k_y = 1, k_\parallel = 0.5) \approx 0.15$ in accordance with [28]. For $p = 3$ and $k$ in the order of one the effect of hyperviscosity on the growth rate becomes significant already for $\nu = 10^{-4}$. All $\mathbf{k}$ with $k_y \gtrsim 3$ is actually damped due to the hyperviscosity.

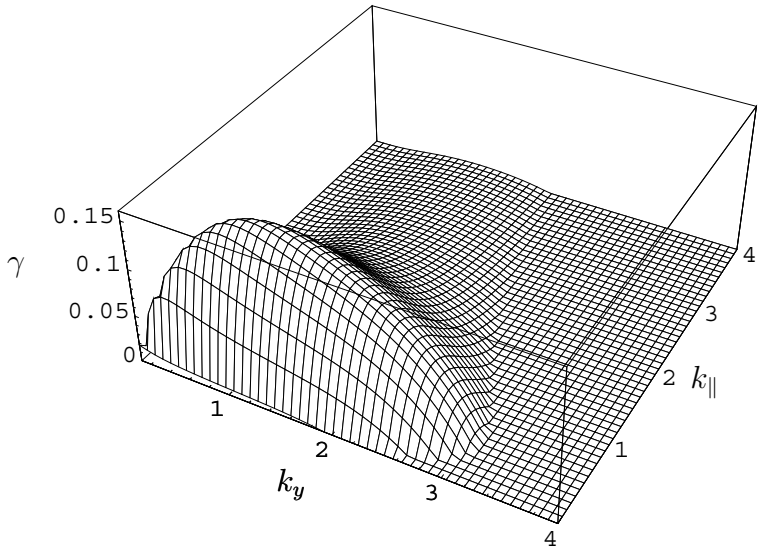


Figure 3.2: The linear growth rate, $\gamma$, as a function of $k_y$ and $k_\parallel$ for $k_x = 0$, $\mathcal{C} = 1$, $\nu = 10^{-4}$ and $2p = 6$. Only positive values of $\gamma$ are shown.

### 3.2.2 Energy and flux

The total energy $\mathcal{E}$, and the generalised enstrophy[3] $\mathcal{W}$, are defined by

$$\mathcal{E} = \mathcal{E}_{kin} + \mathcal{E}_{pot} = \frac{1}{2}\iiint (\nabla_\perp \phi)^2 \,\mathrm{d}x\,\mathrm{d}y\,\mathrm{d}z + \frac{1}{2}\iiint n^2 \,\mathrm{d}x\,\mathrm{d}y\,\mathrm{d}z \tag{3.30}$$

and

$$\mathcal{W} = \frac{1}{2}\iiint (n - (\nabla_\perp^2 \phi))^2 \,\mathrm{d}x\,\mathrm{d}y\,\mathrm{d}z \tag{3.31}$$

Due to the linear instability these quantities are not conserved within the Hasegawa-Wakatani system. Important properties of the system such as sources and sinks might be revealed by deriving the temporal derivatives of the two quantities. By assuming a triply periodic geometry $\frac{\mathrm{d}\mathcal{E}}{\mathrm{d}t}$ and $\frac{\mathrm{d}\mathcal{W}}{\mathrm{d}t}$ are found to be [22]:

$$\frac{\mathrm{d}\mathcal{E}}{\mathrm{d}t} = \iiint \left[ -n\frac{\partial \phi}{\partial y} - \mathcal{C}[\frac{\partial}{\partial z}(n-\phi)]^2 - \nu((\nabla_\perp^{p+1}\,\phi)^2 + (\nabla_\perp^p n)^2) \right] \mathrm{d}x\,\mathrm{d}y\,\mathrm{d}z \tag{3.32}$$

$$\frac{\mathrm{d}\mathcal{W}}{\mathrm{d}t} = \iiint \left[ -n\frac{\partial \phi}{\partial y} - \nu(\nabla_\perp^p (n - \nabla_\perp^2 \phi))^2 \right] \mathrm{d}x\,\mathrm{d}y\,\mathrm{d}z \tag{3.33}$$

From (3.32) and (3.33) it is apparent that only the $n\frac{\partial \phi}{\partial y}$-term may be positive and hence act as a source term of energy and enstrophy. The term may be written as

$$\Gamma_n = \iiint -n\frac{\partial \phi}{\partial y}\,\mathrm{d}x\,\mathrm{d}y\,\mathrm{d}z = \iiint n v_{Ex}\,\mathrm{d}x\,\mathrm{d}y\,\mathrm{d}z \tag{3.34}$$

[3]The generalised enstrophy is a quantity often used in fluid mechanics. For a given energy, a large enstrophy is typically connected to a flow with many small scale structures.

and it is recognised as the turbulent flux in the $x$-direction, i.e. the flux out of the plasma. Since the $\frac{\partial \phi}{\partial y}$-term enters the $\frac{\partial n}{\partial t}$-equation through

$$\frac{\mathrm{D}}{\mathrm{D}t} \ln n_0 = \frac{1}{L_n B_0} \frac{\partial \phi}{\partial y}$$

it is clear that the energy of the turbulence is extracted from the background density gradient. In [37], the term in the two-dimensional formulation of $\frac{\mathrm{d}\mathcal{E}}{\mathrm{d}t}$ analogous to $\mathcal{C}[\frac{\partial}{\partial z}(n-\phi)]^2$ is interpreted as a sink due to resistive dissipation of fluctuation energy. The remaining terms are sinks due to the hyperviscosity.
Note that the nonlinear convective terms, $\mathbf{v}_E \cdot \nabla_\perp(\nabla_\perp^2 \phi)$ and $\mathbf{v}_E \cdot \nabla_\perp n$, do not contribute to $\frac{\mathrm{d}\mathcal{E}}{\mathrm{d}t}$ and $\frac{\mathrm{d}\mathcal{W}}{\mathrm{d}t}$, i.e. the energy and enstrophy are preserved in the nonlinear interactions through these terms.

## 3.3 A review of the simulation results of the Hasegawa-Wakatani model

As written in Section 3.1.5 the equations are solved in a triply periodic geometry using Fourier spectral methods and a semi-implicit scheme using the third order Stiffly Stable method [35] for the temporal integration (see Chapter 3 of [22]). For reasons of comparison the parameters used in the simulation, presented in this section, are identical to those used in [28], i.e. $L_x = L_y = L_z = 12\pi$, $m = n = 96$, $o = 48$, $\nu = 10^{-4}$, and a hyperviscosity of the order $2p = 6$. The time step used was in the order of $10^{-3}$ to keep the simulation within the stability domain of the numerical scheme. The simulation domain is a triply periodic box, and the system is initialised in mode space for all $k_x, k_y, k_\parallel \neq 0$ with low level random noise having amplitudes proportional to $k^{-2}$.
As drift waves have a finite parallel wavenumber, we split the total energy $\mathcal{E}$, into two contributions: the energy of the drift waves $\mathcal{E}(k_\parallel \neq 0)$, and the energy of the flute-like modes $\mathcal{E}(k_\parallel = 0)$. The evolution with time of the total energy and the drift wave energy as well as the turbulent particle flux $\Gamma_n$ as defined by (3.34) are presented in Figure 3.3. These results are very similar to those obtained by an independent code and presented in [28].
The initial state of the system is dominated by growth of the perturbations due to the linear instability. Therefore the total energy grows exponentially in this state, as it may be deduced from the energy plot in Figure 3.3.(a) (note that the ordinate axis is logarithmic).
As shown in the previous section $(k_x, k_y, k_\parallel) \approx (0, 1, 0.5)$ is the most linearly unstable mode. In Figure 3.4.(a) this is supported by the $\mathcal{E}(k_\perp, k_\parallel)$ contour plot at $t = 40$, which is during the state of exponential growth. The reason for $(k_\perp, k_\parallel) = (0.6667, 0.3333)$ and not exactly $(1.0, 0.5)$ being the most energetic mode is the way the system is initialised, with amplitudes scaled by $k^{-2}$.
We present the $\mathcal{E}(k_\parallel)$ spectrum at three instants in Figure 3.5, where $k_\parallel \approx 0.5$ is seen still to be the dominant mode at $t = 60$, i.e. the numerical scheme

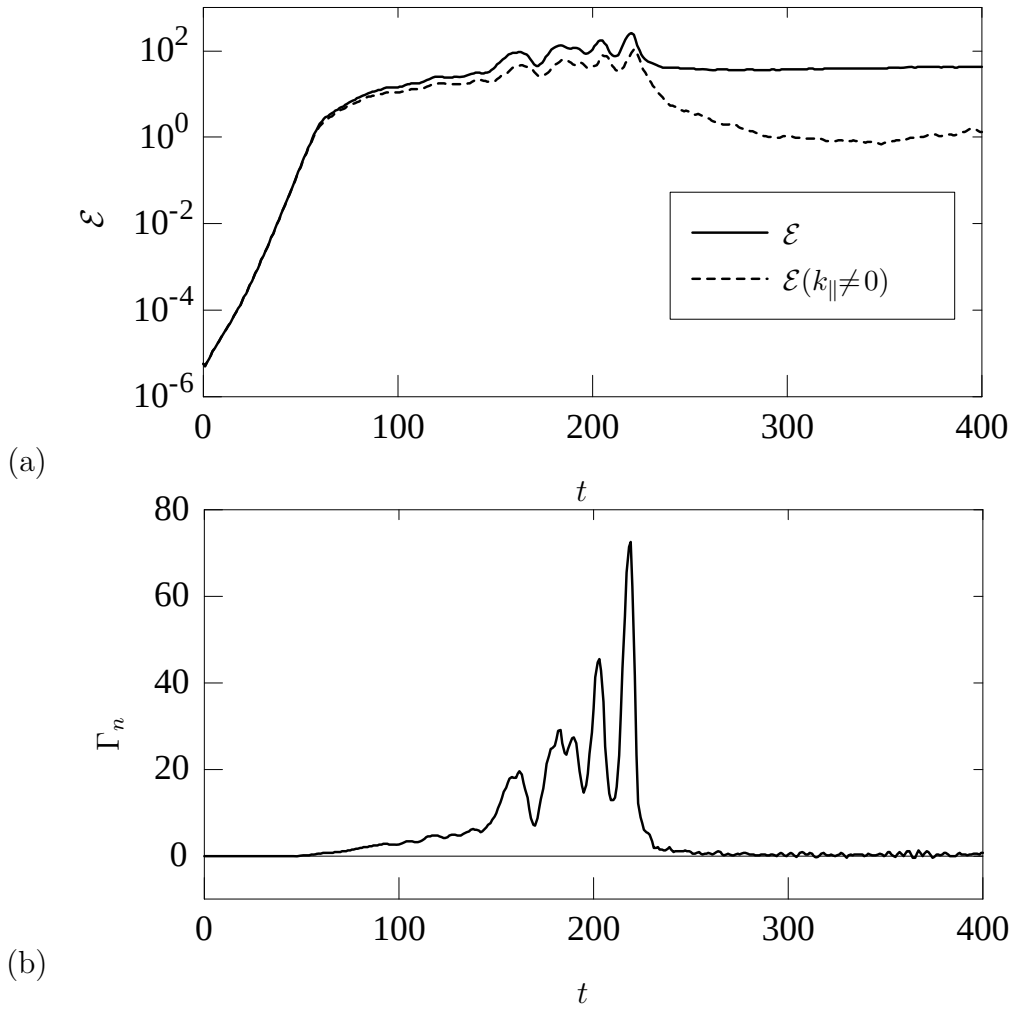


Figure 3.3: The temporal evolution of (a) the total energy and the energy of the drift waves $\mathcal{E}$ and $\mathcal{E}(k_\parallel \neq 0)$, and of (b) the turbulent flux $\Gamma_n$.

reproduces the linear dispersion relation. In Figure 3.3, the growth of the energy reduces at $T \approx 60$ indicating that nonlinear effects begin to be important. In this state energy is cascaded to both higher and lower **k**-values. The cascading includes transfer into the $k_\parallel = 0$ modes, i.e. into flute-like structures – convective cells. The nonlinear interaction between drift waves and convective cells has been described and explained in [39]. Note that the nonlinear interaction is the only way to drive the $k_\parallel = 0$ modes, since these are linearly stable in the Hasegawa-Wakatani system (this may be seen from (3.29)).

Figure 3.5 shows that at $t = 120$ the energy is distributed over the whole $k_\parallel$ spectrum with the $k_\parallel = 0$ modes being most energetic. In this state, dominated by nonlinear coupling, both the drift waves and the convective cells are growing. This growth due to nonlinear processes may be explained by: "Large-scale convective cells drive $k_\parallel = 0$ density fluctuations at broad scales $k_\perp$. These excite $k_\parallel \neq 0$ drift waves (through nonlinear coupling), which in turn reinforce the convective cells" [28]. The convective cells $\phi(k_\parallel = 0)$

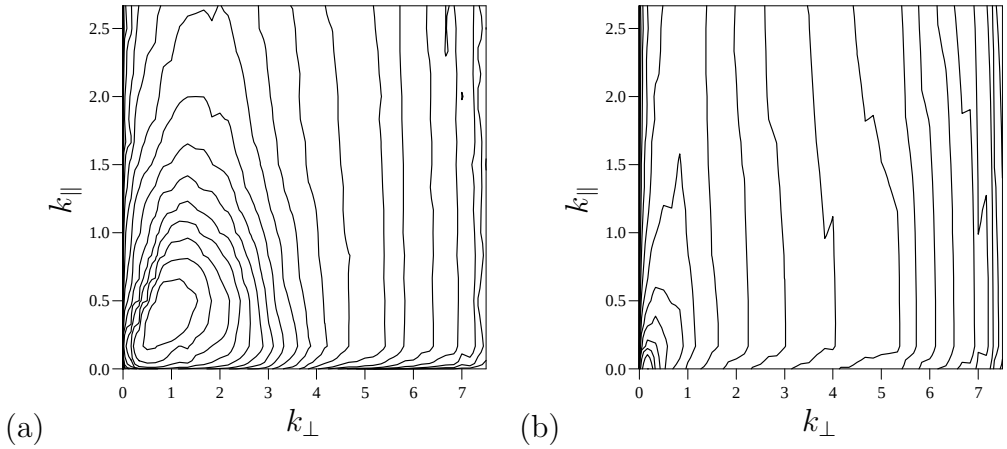


Figure 3.4: Contour plots of the $\mathcal{E}(k_\perp, k_\parallel)$-spectra at (a) the exponential growth state (t=40) and (b) the state of large fluctuations (t=200). The contour levels have a logarithmic spacing of (a) $\Delta \log_{10} \mathcal{E} = 0.52$ and (b) $\Delta \log_{10} \mathcal{E} = 0.38$. The most energetic modes are (a) $(k_\perp, k_\parallel) = (0.6667, 0.3333)$ with $\mathcal{E} = 1.4 \cdot 10^{-4}$ and (b) $(k_\perp, k_\parallel) = (0.1667, 0)$ with $\mathcal{E} = 4.1 \cdot 10^{1}$.

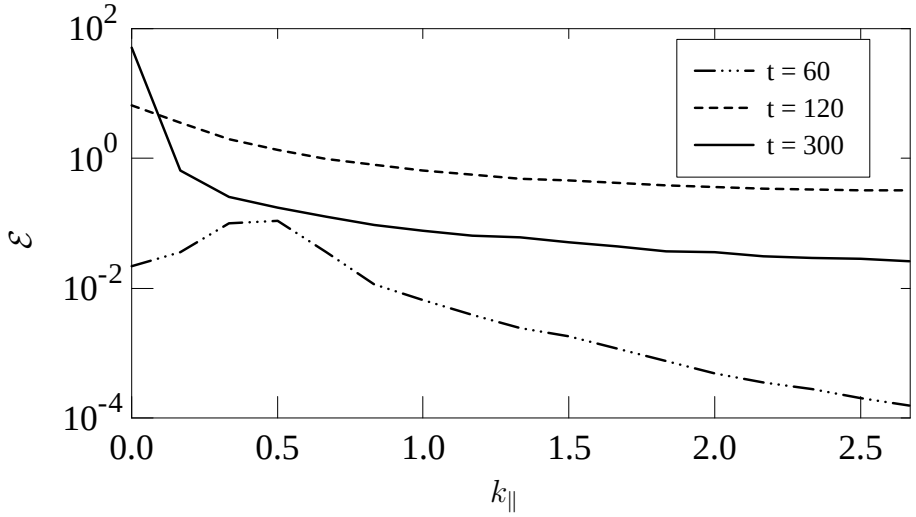


Figure 3.5: The $\mathcal{E}(k_\parallel)$ spectrum at three instants: $t = 60$, $t = 120$, and $t = 300$.

drive the $n(k_\perp, k_\parallel = 0)$ fluctuations through the $\frac{\partial \phi}{\partial y}$-term. In this state the potential energy forms the main part of the total energy, as seen in Figure 3.6.(a).

The state of nonlinear growth is succeeded by a turbulent state ($T \approx 150 - 230$) with large fluctuations in the energy, and growth in the turbulent flux and the enstrophy (see Figures 3.3.(b) and 3.6.(b)). During this state the kinetic energy grows and becomes dominant as the system enters a "final" state ($k_\parallel = 0$ being dominant) where the potential energy drops significantly (see Figure 3.6.(a)). In Figure 3.4.(b) we see that the energy has been transferred to lower **k**-values. The time of the collapse into the

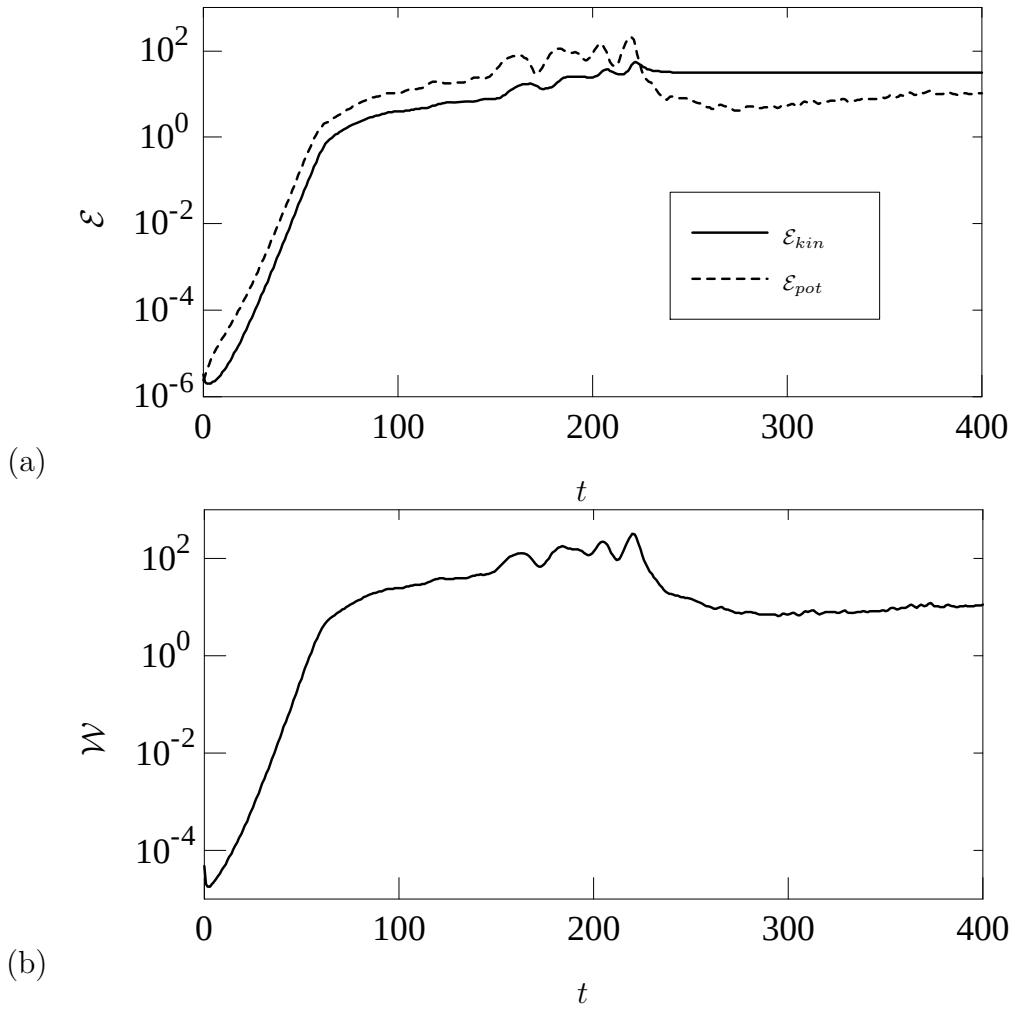


Figure 3.6: The temporal evolution of (a) the kinetic and potential energy, $\mathcal{E}_{kin}$ and $\mathcal{E}_{pot}$, and of (b) the enstrophy $\mathcal{W}$.

$k_\parallel = 0$ mode is nearly the same as that for the large fluctuations.
In the "final" state the system apparently becomes stable and most of the energy is transferred into the convective cells. This is most easily deduced from Figure 3.5, where the energy in the $k_\parallel = 0$ mode at $t = 300$ is two orders of magnitude larger than that in the $k_{\parallel,1}$-mode. The stable state is characterised by energy in very low $\mathbf{k}$-values, which might further be stated from the energy spectra in Figure 3.7. A strong poloidal flow, indicated by $\phi(k_x \approx k_{x,1}, k_y \approx 0, k_\parallel)$, initiates as the system enters the stable state. The flow impedes the drift waves since the turbulent flux driving the drift waves drops (to zero) as a consequence of (3.34):

$$\Gamma_n = \iiint -n\frac{\partial \phi}{\partial y}\,\mathrm{d}x\,\mathrm{d}y\,\mathrm{d}z$$

The consequence is dissipation of the drift waves, causing the nonlinear transfer of energy between $k_\parallel = 0$ and $k_\parallel \neq 0$ to decay. In this stable low $\mathbf{k}$ state, the enstrophy also drops significantly – more than one order of magnitude

(see Figure 3.6.(b)). This is expected from the definition of the generalised enstrophy (3.31), since the average $k_\perp$ for $\phi$ and $n$ becomes very small.
The change from a state dominated by nonlinear coupling between drift waves and convective cells, to a stable state largely dominated by convective cells, is expected from the transfer functions calculated by Biskamp and Zeiler [28]. These show that a dual cascade of energy for the parallel wavenumbers is occurring: The system exhibits a strong tendency to transfer potential energy from $k_\parallel = 0$ to $k_\parallel \neq 0$ modes, and kinetic energy is transfered from high to (very) low $k_\parallel$ modes. In the state of nonlinear coupling between drift waves and convective cells we saw that the potential energy was dominant. During the succeeding state of large fluctuations the kinetic energy rose. Eventually, the tendency to transfer energy to low $k_\parallel$ became dominant, and lead to the "final" stable state with dominant convective cells.
In [23,27,37] angle integrated energy spectra were determined for simulations of the Hasegawa-Wakatani system in a two-dimensional reduction. The corresponding spectra of the three-dimensional fields are calculated in cylindrical coordinates $(k_\perp, \theta, k_\parallel)$ by

$$\mathcal{E}(k_\perp) = \int_0^{k_{\parallel,max}} \int_{\sqrt{k_x^2+k_y^2}=k_\perp} \mathcal{E}(k_x, k_y, k_\parallel) d\theta dk_\parallel \tag{3.35}$$

We also want to obtain spectra for the drift waves only. This is done by

$$\mathcal{E}(k_\perp)_{k_\parallel \neq 0} = \mathcal{E}(k_\perp) - \int_{\sqrt{k_x^2+k_y^2}=k_\perp} \mathcal{E}(k_x, k_y, 0) d\theta \tag{3.36}$$

We may compare the $\mathcal{E}(k_\perp)_{k_\parallel \neq 0}$ spectra obtained in this work to the results of two-dimensional simulations of drift waves. Note, however, that the drift wave energy spectra $\mathcal{E}(k_\perp)_{k_\parallel \neq 0}$ do not correspond fully to spectra obtained by two-dimensional simulations, since a specific choice of $\mathcal{C}$ in the two-dimensional case corresponds to one specific $k_\parallel$ value. Hence an $\mathcal{E}(k_\perp)$ spectrum from two-dimensional simulations corresponds better to the spectrum obtained by cutting the $\mathcal{E}(k_\perp, k_\parallel)$ spectrum perpendicularly to the $k_\parallel$-axis at the relevant $k_\parallel$ value. The angle integrated $\mathcal{E}(k_\perp)$-spectrum for the "final" state (t=400) is shown in Figure 3.7 for both the total energy and the energy of the drift waves ($k_\parallel \neq 0$). For the two-dimensional simulations the $\mathcal{E}(k_\perp)$ spectra were observed to follow $\mathcal{E}(k_\perp) \propto k_\perp^{-\alpha}$ for an intermediate range of $k_\perp$ values, with $\alpha \in [1.6; 4.5]$ dependent on the coupling factor [37]. From Figure 3.7 we find for the energy of the drift waves $\alpha \approx 2.1$, and for the total energy $\alpha \approx 2.4$.
The evolution of the potential perturbation, $\phi$, towards the "final" state is presented in Figure 3.8 by three-dimensional isosurface plots. Note that the values of $\phi$ are indicated by colours at the boundaries. It may be seen from Figure 3.8.(a) that the structures of $\phi$ are well defined during the linear growth state since only a few modes are excited. This is expected since the energy is contained mainly in the linearly unstable modes. At $t = 120$ (Figure 3.8.(b)) the nonlinear effects are dominant and $\phi$ is being more turbulent, and there is an initiating tendency to form flute-like structures. Figure

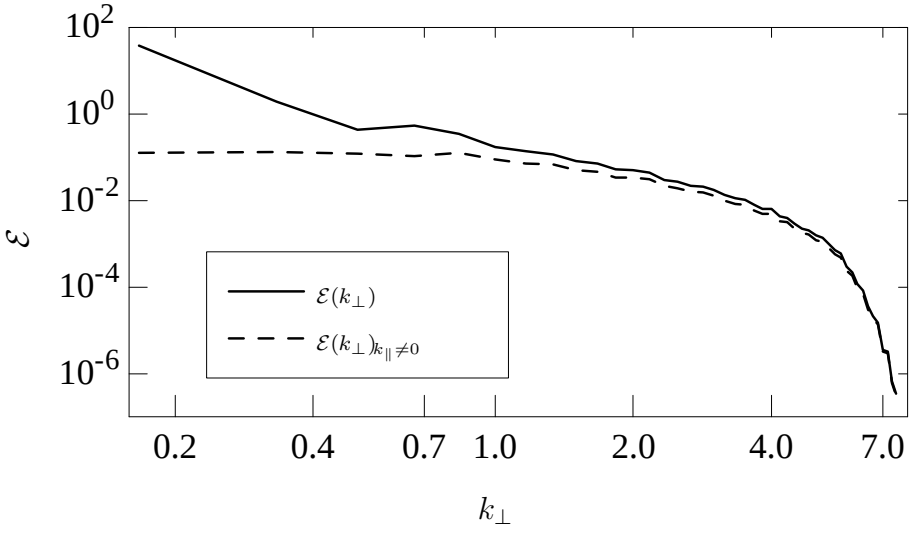


Figure 3.7: $\mathcal{E}(k_\perp)$-spectra at $t = 400$ for all parallel modes (full line) and for the drift wave modes (dashed line).

3.8.(c) shows $\phi$ at $t = 200$ where the self-organisation into coherent structures is apparent, although this is still in the turbulent state. The last plot at $t = 400$ (Figure 3.8.(d)) is in the state dominated by a poloidal flow and large convective cells. In Figure 3.9 the corresponding perturbation in the density, $n$, is depicted for the final state at $t = 400$.
Plots of the drift wave components ($k_\parallel \neq 0$) of $n$ and $\phi$ are presented in Figure 3.10. For the drift waves, the energy is more evenly distributed on the modes (this is also seen in Figure 3.7). However, the perturbations seem to align in the $y$-direction, i.e. they follow the poloidal flow. Some correlation between $n$ and $\phi$ may be seen, although it is not obvious. In order to better illustrate the correlation between the different components (drift and flute) of $n$ and $\phi$ we have calculated the pointwise correlation of the perturbations as a function of $k_\parallel$. The pointwise correlation of $n$ and $\phi$ for time lag zero is defined as

$$\langle n\phi\rangle(k_\parallel) = \frac{\int n(k_\parallel)\phi(k_\parallel)\mathrm{d}x\mathrm{d}y}{\sqrt{\int n(k_\parallel)^2\mathrm{d}x\mathrm{d}y}\sqrt{\int \phi(k_\parallel)^2\mathrm{d}x\mathrm{d}y}}$$

The correlation at $t = 400$ is shown in Figure 3.11. It is clear that the perturbations are adiabatic ($n \approx \phi$) for $k_\parallel \gtrsim 1$. The average correlation including all $k_\parallel$ is -0.47, due to the strong convective cell for which the perturbations are nearly anti-correlated. Notice, however, that calculating the correlation this way (without considering a time lag) would result in zero correlation if $n$ and $\phi$ were 90° out of phase.
The three-dimensional numerical investigations presented here, are of a size which makes it hard to include as many wave numbers as desired with respect to guaranteeing converging solutions. The effect of the limited number of wave numbers has been systematically investigated with variations of the wave numbers included in the simulations [22]. The investigations show a dependency of the wave numbers included on the evolution of the Hasegawa-

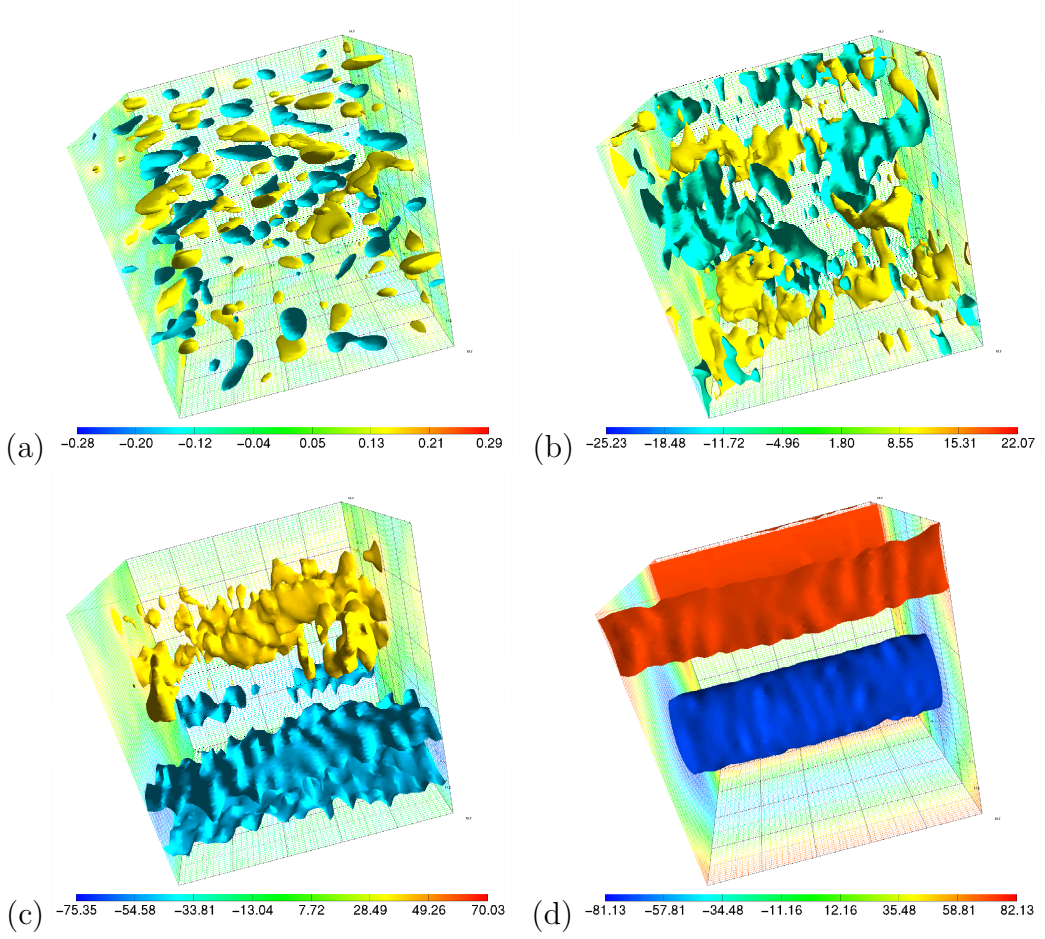


Figure 3.8: Three-dimensional plots of the potential perturbation, $\phi$, at the characteristic states of the Hasegawa-Wakatani system: (a) the linear growth state (t=40), (b) the state of growth during nonlinear interactions (t=120), (c) the state of large fluctuations (t=200), and (d) the stationary state (t=400). The box is viewed along the $x$-direction, $y$ is vertical and $z$ is horizontal.

Wakatani system. Especially variation of the wave numbers included in the parallel direction seems to have an effect. However, the tendency of the system to form large convective cells seems to be a global phenomenon in the wavenumber parameter space. Only the steadiness and the time of occurrence of the "final" state is affected.
The formation of large global structures, however, violates the assumption of the turbulence being microturbulence ($\frac{1}{L_n^2} \ll k^2$ - Assumption 16) which is used to validate the use of periodic boundary conditions. Hence investigations of the system using more physical boundary conditions are necessary. This was treated in [22, 30], and will be further treated in Chapter 6.

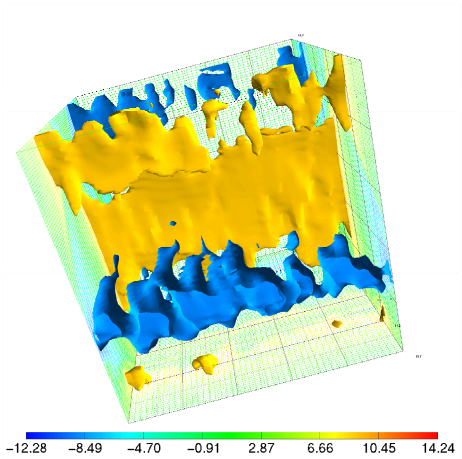


Figure 3.9: Three-dimensional plot of the density perturbation, $n$, at $t = 400$. The box is viewed along the $x$-direction, $y$ is vertical and $z$ is horizontal.

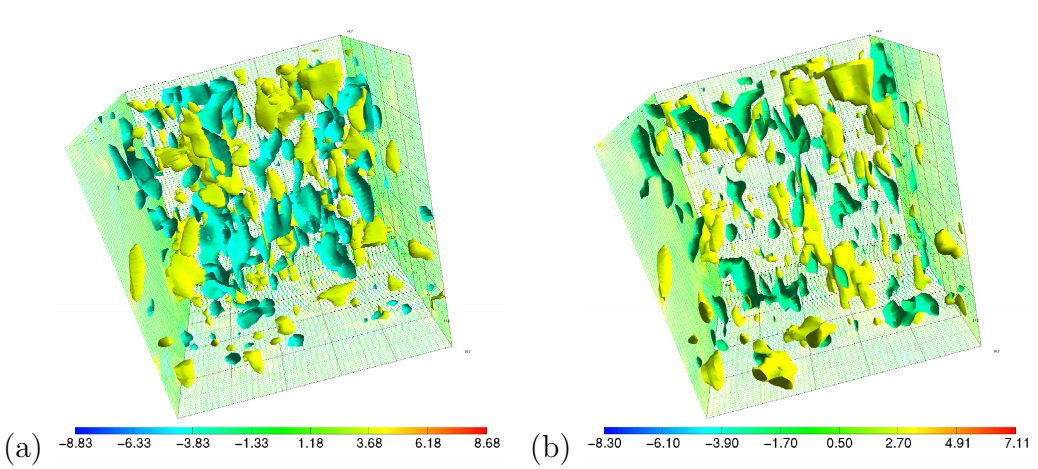


Figure 3.10: The drift wave perturbations at t=400 (a) the perturbation in $n$ and (b) the perturbation in $\phi$. The box is viewed along the $x$-direction, $y$ is vertical and $z$ is horizontal.

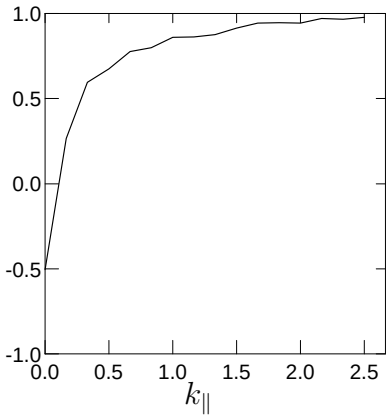


Figure 3.11: The correlation of $n$ and $\phi$ as a function of $k_\parallel$ at $t = 400$.

## 3.4 Condensation and dependence on coupling factor

The tendency of the Hasegawa-Wakatani system to condense most of the energy into convective cells, after a state where drift wave turbulence is dominant, has been illustrated in the preceding section. A hypothesis could be that the coupling and the transfer of energy between drift waves and convective cells are dependent on the drive of the drift wave dynamics, i.e. the phase shift between the density and potential fluctuations, and in turn the resistivity of the plasma.
If the resistivity is very low, the electrons will obey the Boltzmann relation $n = \phi$ (or in non-normalised units $\frac{n_1}{n_0} = \frac{e\phi}{T_e}$), and the fluctuations be adiabatic. In this case of no resistivity the drift wave perturbation is stable and will be a purely oscillatory wave (see, e.g., Section 2.1.1 in [22]). For an increasing resistivity the fluctuations will be non-adiabatic and the drift waves unstable. In this section we investigate how variation of the resistivity, and by this the adiabaticity of $n$ and $\phi$, affect the tendency of the system to condense the energy into convective cells.
Changing the resistivity changes the parallel coupling ($\mathcal{C}k_\parallel^2$ in Fourier space) of the equations according to (3.22). We have determined the time of condensation of the system $t_c$, i.e. the time at which the transition into the convective cell state occurs for a number of simulations. We fixed $L_z = 2\pi$ and varied $\mathcal{C}$. The remaining parameters were $L_x = L_y = 12\pi$, $m = n = o = 96$, $\nu = 10^{-4}$, and a hyperviscosity of the order $2p = 6$. The time step used was $2 \cdot 10^{-3}$.
In Figure 3.12 it is illustrated how $t_c$ is determined, and the results for five simulations are summarised in Figure 3.13. A sixth simulation with $\mathcal{C}^{-1} = 256$ did not yet condense for $t > 1000$, hence the extrapolation. It is seen that the hypothesis of the condensation of the energy into flute modes being dependent on the coupling of the drift wave fluctuations in $n$ and $\phi$, is

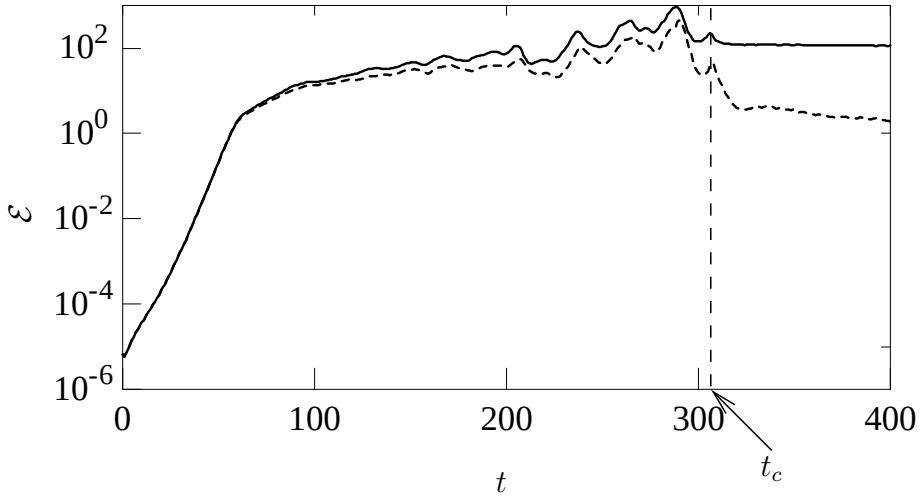


Figure 3.12: The time of condensation $t_c$, for a simulation with $\mathcal{C}^{-1} = 81$.

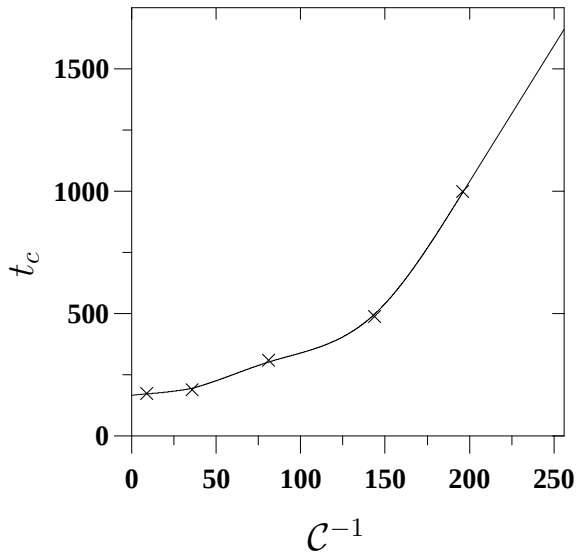


Figure 3.13: The time of condensation as a function of the inverse coupling constant ($\mathcal{C}^{-1}$). The parameters used are $m = n = o = 96$, $L_x = L_y = 12\pi$, $L_z = 2\pi$, $\nu = 10^{-4}$, $2p = 6$, and $dt = 2 \cdot 10^{-3}$. The last part of the curve is extrapolated.

supported, i.e. when the coupling is weak (high resistivity), the drift waves are non-adiabatic and more unstable, resulting in more persistent turbulence and thus a decreased tendency to couple the energy into convective cells, and vice versa.
Finally, it should be noted that due to the immense CPU time usage for these investigations, we have very poor statistics. Nevertheless, the trend is quite significant.

# Chapter 4

# The Ion temperature modified Hasegawa-Wakatani model

A number of assumptions are made in the derivation of the Hasegawa-Wakatani model. One of these is that the ion temperature is assumed to be much smaller than the electron temperature, and effects of finite ion temperature are neglected in order to simplify the equations. The assumption of $T_i = 0$ is clearly not realistic, and Pécseli shows in [40] that the equations actually do not complicate greatly by including effects of finite but small $T_i$

**Assumption 17** *$T_i$ is finite and $\frac{T_i}{T_e} \ll 1$*

which in this chapter replaces Assumption 1. In the following, we determine the correction to the equations for a finite $T_i$ fulfilling this. We will follow a different route but end up with a result similar to the one presented in [40]. Note that we do not include effects of an ion temperature gradient.[1]
The contents of this chapter were in part described in [41, 42].

## 4.1 The model

Compared to the standard Hasegawa-Wakatani model the effects of finite ion temperature only affect the ion vorticity equation. Therefore, we merely re-derive this equation and keep the remaining assumptions and equations of Chapter 3.

[1] 2011 update: At the thesis defence an opponent pointed out that a high order term is being neglected in the derivation of (4.5), even though this high order term is of the same order of magnitude as the non-linear term being added to the ion vorticity equation (4.7). The modeling of the Ion temperature modified Hasegawa-Wakatani model has not been redone. Hence the present derivation of the equations will remain as the original derivation, in order for the equations and the presented modeling results to correspond. However, the missing term will be presented, and the reader's attention is pointed to the fact that the correct addition of the missing term, may to some extent change some of the conclusions of this chapter.

### 4.1.1 The modified ion vorticity equation

Including the anisotropic part of the pressure tensor, the ion fluid equation is expressed as

$$\frac{\partial \mathbf{v}_i}{\partial t} + (\mathbf{v}_i \cdot \nabla)\mathbf{v}_i = \frac{e}{m_i}(\mathbf{E} + \mathbf{v}_i \times \mathbf{B}) - \frac{\nabla \cdot \bar{\bar{\mathrm{P}}}_i}{n_i m_i} + \mathbf{g} \tag{4.1}$$

where $\mathbf{v}_i$ is the ion velocity, $m_i$ is the ion mass, $\mathbf{g}$ is a gravitational force on the ions included for generality, and the pressure tensor is

$$\bar{\bar{\mathrm{P}}}_i \equiv \bar{\bar{\Pi}}_i + p_i \bar{\bar{\mathrm{I}}} \tag{4.2}$$

The tensor $\bar{\bar{\Pi}}_i$ contains the deviations from the isotropic pressure $p_i$. The deviations arise from ion-ion collisions and from finite Larmor radius (FLR) effects. The effects of ion-ion collisions are actually included through the viscosity term applied to (4.7), therefore we will only treat the FLR effects here. For $T_i > 0$ the ions have a finite Larmor (or gyro) radius, and thus their $\mathbf{E} \times \mathbf{B}$ velocity will be modified in a nonuniform electric field, if the scale length of the perturbations in the electric field is of the order of the Larmor radius. An extensive treatment of the pressure tensor is given in [34]. In [40] the FLR components of $\bar{\bar{\Pi}}_i$ are given as

$$\begin{aligned}
\Pi_{xx} &= -\Pi_{yy} = -\frac{1}{2}\frac{n_i T_i}{\omega_{ci}}\left(\frac{\partial v_y}{\partial x} + \frac{\partial v_x}{\partial y}\right) = -\frac{1}{2}\frac{n_i T_i}{B_0 \omega_{ci}}\left(\frac{\partial^2 \phi}{\partial x^2} - \frac{\partial^2 \phi}{\partial y^2}\right) \\
\Pi_{xy} &= \Pi_{yx} = \frac{1}{2}\frac{n_i T_i}{\omega_{ci}}\left(\frac{\partial v_x}{\partial x} - \frac{\partial v_y}{\partial y}\right) = \frac{1}{2}\frac{n_i T_i}{B_0 \omega_{ci}}\left(-2\frac{\partial^2 \phi}{\partial x \partial y}\right)
\end{aligned}$$

where ion motion parallel to the magnetic field has been neglected (see Assumption 9). The derivation becomes more clear if we define a tensor $\bar{\bar{\mathrm{Q}}}$ by

$$\bar{\bar{\Pi}}_i = \frac{n_i T_i}{2 B_0 \omega_{ci}} \bar{\bar{\mathrm{Q}}}$$

Simple tensor algebra leads to

$$\nabla \cdot \bar{\bar{\mathrm{Q}}} = \begin{pmatrix} -\frac{\partial}{\partial x}\left(\frac{\partial^2}{\partial x^2} + \frac{\partial^2}{\partial y^2}\right)\phi \\ -\frac{\partial}{\partial y}\left(\frac{\partial^2}{\partial x^2} + \frac{\partial^2}{\partial y^2}\right)\phi \\ 0 \end{pmatrix} = \begin{pmatrix} -\frac{\partial}{\partial x}\nabla_\perp^2 \phi \\ -\frac{\partial}{\partial y}\nabla_\perp^2 \phi \\ 0 \end{pmatrix}$$

which we will use later.
If we take the curl of (4.1) we may obtain

$$\frac{\partial \boldsymbol{\omega}}{\partial t} - \nabla \times (\mathbf{v}_i \times \boldsymbol{\omega}) = -\frac{\partial \boldsymbol{\omega}_{ci}}{\partial t} + \nabla \times (\mathbf{v}_i \times \boldsymbol{\omega}_{ci}) + \frac{1}{n_i^2 m_i} \nabla n_i \times \nabla \bar{\bar{\mathrm{P}}}_i \tag{4.3}$$

where $\boldsymbol{\omega}$ is the the ion vorticity. On the right hand side Faraday's law has been used. Note that we keep the first term although it is zero, according to the electrostatic approximation Assumption 6.

By using appropriate vector relations and definitions introduced in Section 3.1.2, (4.3) can be rearranged to the modified ion vorticity equation

$$\frac{\mathrm{D}}{\mathrm{D}t}\ln\left(\frac{\omega+\omega_{ci}}{n_i}\right)=\frac{1}{n_i^2 m_i(\omega+\omega_{ci})}\left(\nabla n_i\times\nabla\cdot\bar{\bar{\mathrm{P}}}_i\right)\cdot\mathbf{e}_z \tag{4.4}$$

where we have taken the scalar product with $\mathbf{e}_z$, since the only non-zero component of $\boldsymbol{\omega}$ is the parallel component due to Assumption 11. From Chapter 3 we know that the parallel component of the ion vorticity, $\omega$ is expressed as

$$\omega=(\nabla\times\mathbf{v}_i)\cdot\mathbf{e}_z=\frac{-\nabla\times(\nabla\phi\times\mathbf{e}_z)}{B_0}\cdot\mathbf{e}_z=\frac{\nabla_\perp^2\phi}{B_0} \tag{3.5}$$

The right hand side of (4.4) can be further reduced:

$$\frac{1}{n_i^2 m_i(\omega+\omega_{ci})}\left(\nabla n_i\times\nabla\cdot\bar{\bar{\mathrm{P}}}_i\right)\cdot\mathbf{e}_z=$$

$$\frac{1}{n_i^2 m_i\omega_{ci}}\left(\nabla n_i\times\nabla\cdot(\frac{n_iT_i}{2B_0\omega_{ci}}\bar{\bar{\mathrm{Q}}}+p_i\bar{\bar{\mathrm{I}}})\right)\cdot\mathbf{e}_z$$

using Assumption 12.
The last term is zero since

$$\nabla n_i\times\nabla\cdot p_i\bar{\bar{\mathrm{I}}}=T_i\nabla n_i\times\nabla n_i=0$$

We use the tensor relation

$$\nabla\cdot(n\bar{\bar{\mathrm{Q}}})=(\nabla n)\cdot\bar{\bar{\mathrm{Q}}}+n\nabla\cdot\bar{\bar{\mathrm{Q}}}$$

to obtain

$$\frac{T_i}{n_i^2 m_i 2B_0\omega_{ci}^2}\left(\nabla n_i\times((\nabla n_i)\cdot\bar{\bar{\mathrm{Q}}}+n_i\nabla\cdot\bar{\bar{\mathrm{Q}}})\right)\cdot\mathbf{e}_z=$$

$$\frac{T_i}{n_0 m_i 2B_0\omega_{ci}^2}\left(\nabla n_0\times(\nabla\cdot\bar{\bar{\mathrm{Q}}})\right)\cdot\mathbf{e}_z \tag{4.5}$$

where we insert $n_0+n_1$ for $n_i$ and only keep the lowest order terms[2], i.e. terms containing $n_0$. Using $n_0=n_0(x)$ and substituting $\nabla\cdot\bar{\bar{\mathrm{Q}}}$ reduces (4.5) to

$$\frac{T_i}{n_0 m_i 2B_0\omega_{ci}^2}\frac{\partial n_0}{\partial x}(-\frac{\partial\nabla_\perp^2\phi}{\partial y})=\frac{T_i}{L_n m_i 2B_0\omega_{ci}^2}\frac{\partial\nabla_\perp^2\phi}{\partial y} \tag{4.6}$$

where we use $\frac{1}{n_0}\frac{\partial n_0}{\partial x}=\frac{\partial ln(n_0)}{\partial x}=\frac{-1}{L_n}$ (3.17). By using Assumption 12 we may now write the modified ion vorticity equation in its final form:

$$\frac{\mathrm{D}}{\mathrm{D}t}\left(\frac{\nabla_\perp^2\phi}{\omega_{ci}B_0}-\ln n_0-\frac{n_1}{n_0}\right)=\frac{T_i}{L_n m_i 2B_0\omega_{ci}^2}\frac{\partial\nabla_\perp^2\phi}{\partial y}+\frac{\mu}{\omega_{ci}B_0}\nabla_\perp^4\phi \tag{4.7}$$

[2]In (4.5) a term of the same order as the remaining term has been neglected. The correct form of (4.5) should be:

$$\frac{T_i}{n_0 m_i 2B_0\omega_{ci}^2}\left(\nabla n_0\times(\nabla\cdot\bar{\bar{\mathrm{Q}}})+\nabla n_1\times(\nabla\cdot\bar{\bar{\mathrm{Q}}})\right)\cdot\mathbf{e}_z$$

The term should be included because $\nabla n_0$ and $\nabla n_1$ is of the same order. However, as described in the introduction to this chapter the term is not included in the derivation of the equations.

### 4.1.2 The modified equations

We have now obtained necessary equations that form the basis for the system and restate them for convenience

$$\frac{\mathrm{D}}{\mathrm{D}t}\left(\frac{\nabla_\perp^2\phi}{\omega_{ci}B_0} - \ln n_0 - \frac{n_1}{n_0}\right) = \frac{T_i}{L_n m_i 2B_0\omega_{ci}^2}\frac{\partial\nabla_\perp^2\phi}{\partial y} + \frac{\mu}{\omega_{ci}B_0}\nabla_\perp^4\phi \tag{4.7}$$

$$J_\parallel = -\frac{T_e}{\eta e}\frac{\partial}{\partial z}\left(\frac{e\phi}{T_e} - \frac{n_1}{n_0}\right) \tag{3.10}$$

$$\frac{\mathrm{D}}{\mathrm{D}t}\left(\ln n_0 + \frac{n_1}{n_0}\right) = \frac{1}{en_0}\frac{\partial J_\parallel}{\partial z} \tag{3.15}$$

From these the finite ion temperature modified Hasegawa-Wakatani equations in dimensionless, normalised variables can be derived to be:

$$(\frac{\partial}{\partial t} + \mathbf{v}_E\cdot\nabla_\perp)n + \frac{\partial\phi}{\partial y} = \mathcal{C}\frac{\partial^2}{\partial z^2}(n-\phi) \tag{4.8}$$

$$(\frac{\partial}{\partial t} + \mathbf{v}_E\cdot\nabla_\perp)(\nabla_\perp^2\phi) - \theta\frac{\partial}{\partial y}\nabla_\perp^2\phi = \mathcal{C}\frac{\partial^2}{\partial z^2}(n-\phi) + \upsilon\nabla_\perp^4\phi \tag{4.9}$$

where $\theta = 0.5T_i/T_e$ and the parallel coupling factor is still

$$\mathcal{C} \equiv \frac{T_e L_n}{\eta e^2 n_0 \omega_{ci}\rho_s L_\parallel^2} \tag{3.22}$$

The $\theta$-containing term in (4.9) originates from the fluctuating ion diamagnetic drift at finite ion temperatures, and it is the only difference to the Hasegawa-Wakatani model. Since, the standard set of Hasegawa-Wakatani equations explicitly retains the collisional part of the ion viscosity, it is consistent also to keep other terms which originate from finite ion temperatures as the $\theta$-term in (4.9). The discrepancy between [40] and the equations above is the factor $\frac{1}{2}$ in $\theta$.
For the simulations we include a hyperviscosity term in each of the equations in analogy with the case for the standard Hasegawa–Wakatani equations in Chapter 3. The model equations will thus appear as (3.23) and (3.24) with the addition of the $-\theta\frac{\partial}{\partial y}\nabla_\perp^2\phi$-term to the vorticity equation.

## 4.2 Analytical treatment

### 4.2.1 Dispersion relation and linear growth rate

We may obtain a dispersion relation for the linearly unstable drift waves of the ion temperature modified Hasegawa-Wakatani model by linearising the equations (4.8) and (4.9) and assume plane wave solutions as in Section 3.2.1:

$$\omega^2 + i\omega\left[\mathcal{C}k_\parallel^2\left(1+\frac{1}{k_\perp^2}\right) + \nu k_\perp^2 - i\theta k_y\right] - \mathcal{C}k_\parallel^2\left[ik_y\left(\frac{1}{k_\perp^2} - \theta\right) + \nu k_\perp^2\right] = 0 \tag{4.10}$$

This is how the dispersion relation appear in [41]. If, however, we include the hyperviscosity terms as we do in the simulations the dispersion relation is

$$\begin{aligned} & \omega_t^2 + i\omega_t \left[ \mathcal{C}k_\parallel^2 \left( 1 + \frac{1}{k_\perp^2} \right) + 2\nu k_\perp^{2p} - i\theta k_y \right] \\ - \quad & \mathcal{C}k_\parallel^2 \left[ ik_y \left( \frac{1}{k_\perp^2} - \theta \right) + \frac{\nu k_\perp^{2p}}{\mathcal{C}k_\parallel^2} \left( \nu k_\perp^{2p} - i\theta k_y \right) + \nu k_\perp^{2p} \left( 1 + \frac{1}{k_\perp^2} \right) \right] = 0 \end{aligned} \tag{4.11}$$

From the dispersion relation we may find the linear growth rate $\gamma$, which is dispersive and is plotted in Figure 4.1 as a function of $k_y$ and $k_\parallel$ for $\theta = 0.2$. The maximum growth rate for $\theta = 0.2$ is $\gamma(k_x = 0, k_y = 0.82, k_\parallel = 0.46) \approx 0.147$. For $\theta = 0$ (presented in Figure 4.2) the equations reduce to the standard Hasegawa-Wakatani equations, and the maximum growth rate for $\theta = 0$ is consistently found to be $\gamma(k_x = 0, k_y = 1, k_\parallel = 0.5) \approx 0.150$. Generally, the damping of the higher wave numbers is increased and the maximum growth rate reduced for increasing values of $\theta$, as it may be realised by comparing Figures 4.1 and 4.2. The reason for this effect of the increasing ion temperature could be that when the ion Larmor radius increase, the ions experience larger variations in the nonuniform electric field, if the scale length of the perturbations in the electric field is of the order of the Larmor radius. This in turn affect the ion $\mathbf{E}\times\mathbf{B}$ velocity, and may work as a damping mechanism on especially the fine scale variations of the ion motion, i.e. for high wave numbers.

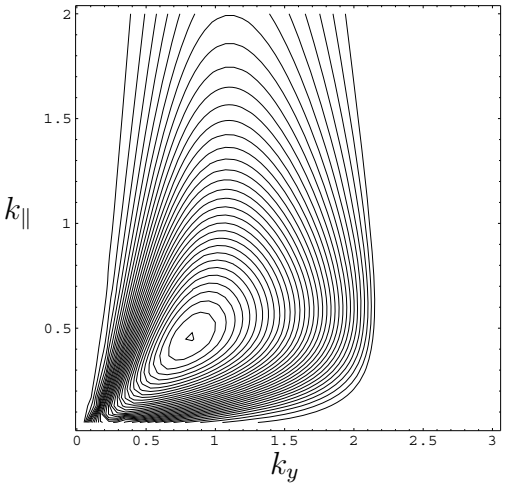


Figure 4.1: The linear growth rate $\gamma$, as a function of $k_y$ and $k_\parallel$, for $k_x = 0$, $\mathcal{C} = 1$, $\theta = 0.2$, $\nu = 10^{-4}$ and $2p = 6$. The contours are equally spaced and only positive values are plotted.

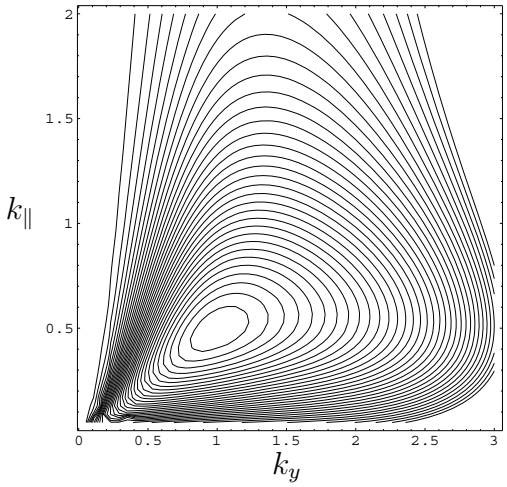


Figure 4.2: The linear growth rate $\gamma$, as a function of $k_y$ and $k_\parallel$, for $k_x = 0$, $\mathcal{C} = 1$, $\theta = 0.0$, $\nu = 10^{-4}$ and $2p = 6$. The contours are equally spaced and only positive values are plotted.

### 4.2.2 Energy and flux

The energy of the system is defined as

$$\mathcal{E} = \mathcal{E}_{kin} + \mathcal{E}_{pot} = \frac{1}{2}\iiint (\nabla_\perp \phi)^2 \,\mathrm{d}x\,\mathrm{d}y\,\mathrm{d}z + \frac{1}{2}\iiint n^2 \,\mathrm{d}x\,\mathrm{d}y\,\mathrm{d}z \qquad (3.30)$$

and by studying the temporal derivative of this, the sources and sinks of the system may be found, as it was done for the Hasegawa-Wakatani system in Chapter 3. It turns out that the $\theta$-containing term does not contribute to $\frac{\mathrm{d}\mathcal{E}}{\mathrm{d}t}$, and does thus only redistribute the energy between modes. As in the case of the Hasegawa-Wakatani system the source is the background density gradient, whereas the losses are due to Ohmic resistivity and hyperviscosity.

## 4.3 Numerical results

The equations are solved in a triply periodic geometry using the same numerical methods as those used in Chapter 3. Below, we present results of two simulations, of which the first was presented in [41].
The parameters for the simulation presented first are a spatial resolution of 96 Fourier modes in each of the perpendicular directions and 48 modes in the parallel, i.e. the $z$-direction, a time step of $2 \cdot 10^{-3}$ normalised time units, a domain size of $L_x = L_y = L_z = 12\pi$, and a hyperviscosity of order $2p = 6$ with a viscosity parameter $\nu = 10^{-4}$ and a temperature ratio of $\theta = 0.05$. The initial conditions are low level random noise with zero mean divided by $k^2$.
Due to the linear instability discussed in Section 4.2.1 the perturbations grow exponentially. Nonlinear coupling starts to have an effect when the perturbations reach a given level (order one, due to the normalisations) and a turbulent state arises. In this state the major direction of energy cascading is towards smaller **k**–values and finally a state dominated by flute–like convective cells with $k_\parallel = 0$ is reached. This is all reflected in Figure 4.3.(a) in which we show the time evolution of the total energy $\mathcal{E}$, and the total drift wave energy $\mathcal{E}(k_\parallel \neq 0)$. The difference between the two curves is thus a measure of the excitation of the convective cells. By comparing the energy evolution in Figure 4.3.(a) to the corresponding plot of the standard Hasegawa-Wakatani system for the same parameters in Figure 3.3.(a), it is seen that the changes are very modest. The flux levels in Figures 4.3.(b) and 3.3.(b), however, seem to be increasing by the introduction of ion temperature effects. This is supported by a simulation with the same parameters, except for an increased ion temperature ($\theta = 0.2$), for which the flux level is even higher.
In Figure 4.4 we give the one-dimensionalised power spectrum of the total energy, $\mathcal{E}(k_\perp)$[3], the kinetic energy and the potential energy at selected time steps: (a) $t = 120$ (weakly turbulent state), (b) $t = 240$ (turbulent state), and (c) $t = 400$ (convective cell dominated final state). Note that the cas-

[3]See (3.35) of Section 3.3 for a definition.

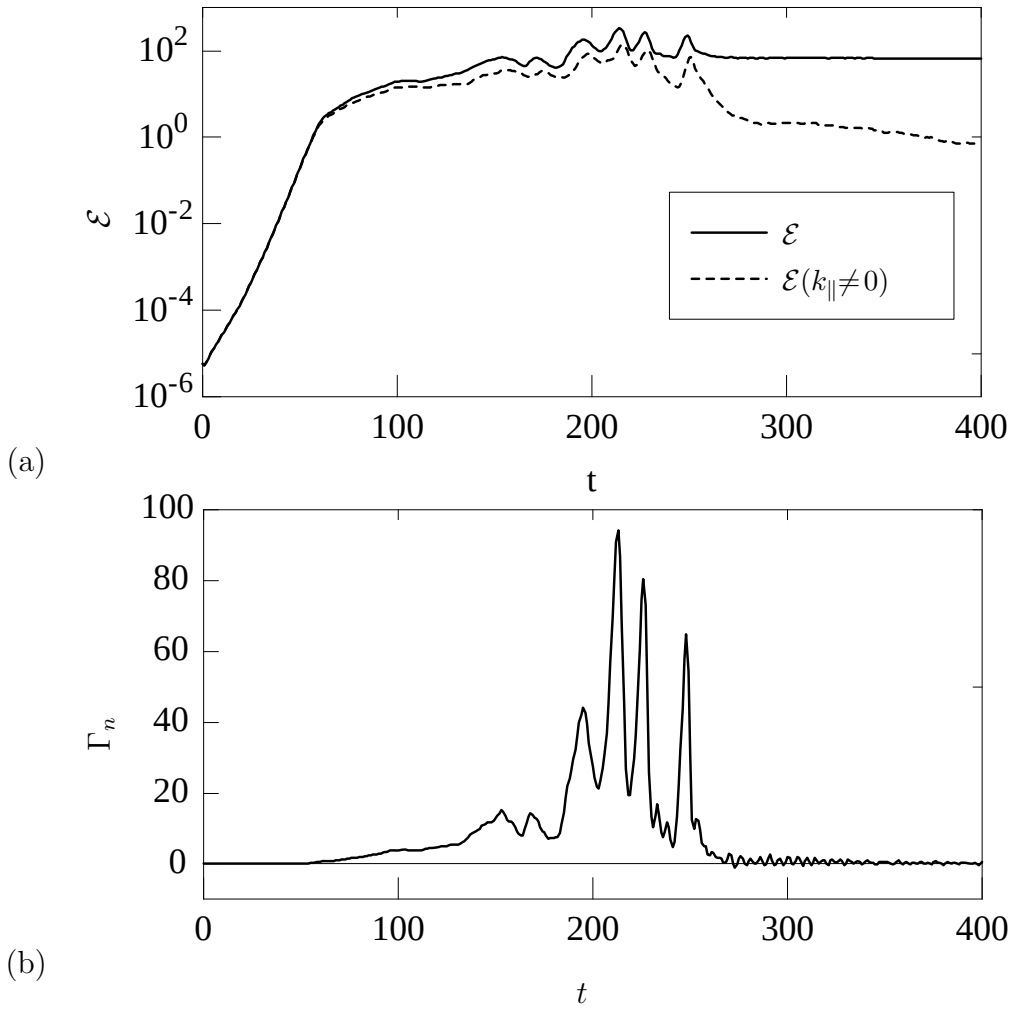


Figure 4.3: Time evolution of (a) the total energy (full line) and the total drift wave energy in the modes except the flute–like modes with $k_\parallel = 0$ (dotted line), and of (b) the turbulent flux $\Gamma_n$.

cading of energy towards longer scales is clear for the total energy and the kinetic energy component, but not for the potential energy component.
In Figure 4.5 the spectral distribution of the total energy is presented in $(k_\perp, k_\parallel)$–space at selected time steps: (a) $t = 40$ (during the exponential growth), (b) $t = 120$, (c) $t = 240$, and (d) $t = 400$. We note the evolution of an enhancement of the levels with $k_\parallel = 0$ at late times. This is the spectral indicator of the formation of flute modes. The spectrum does not contain the information of the relative phases of the modes, which we obtain from the actual realisations. We find that the flute–like modes have the form of a pair of large vortices of opposite polarity, as it was the case for the pure Hasegawa-Wakatani system presented in, e.g., Figure 3.8.(d). As for the Hasegawa-Wakatani system this formation of global structures is intrinsic for the model, and it questions the validity of the use of periodic boundaries. However, as this was discussed in Section 3.3, it will not be treated further here.

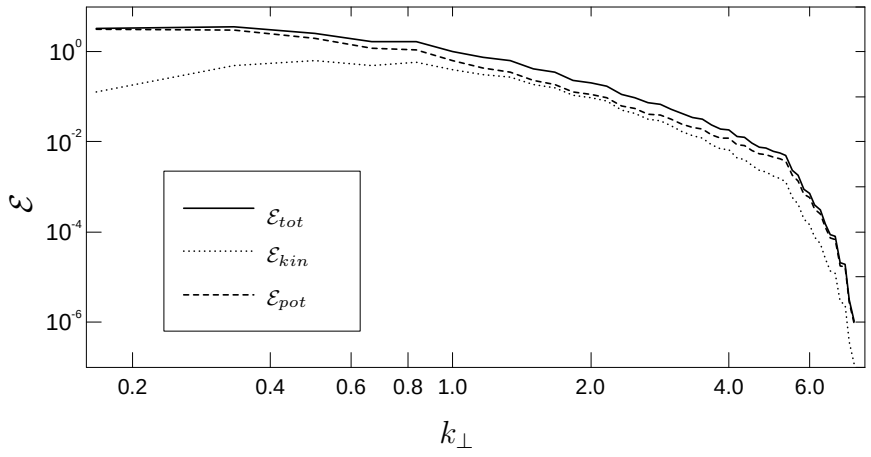


(a)

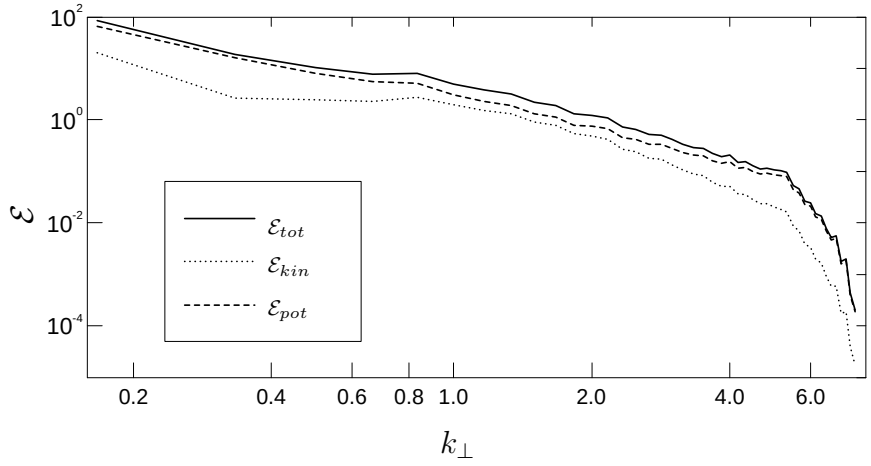


(b)

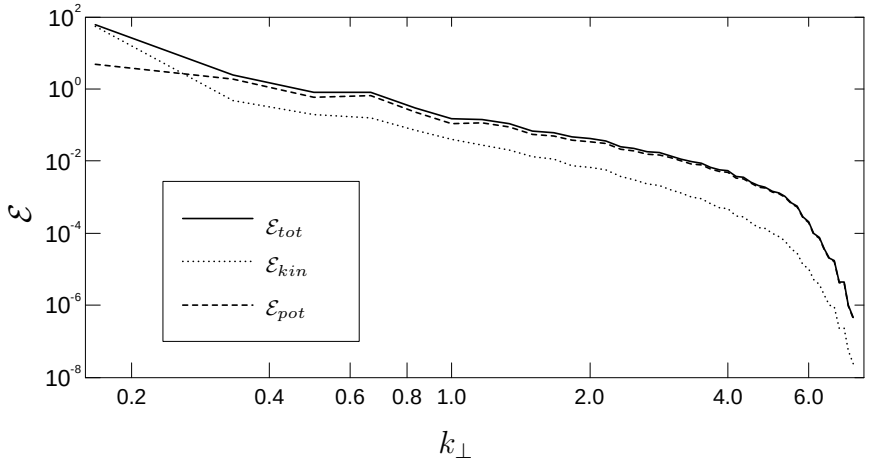


(c)

Figure 4.4: Time evolution of the $\mathcal{E}(k_\perp)$-spectra for the total energy (full line), the kinetic energy (dotted line), and the potential energy (dashed line). (a) $t = 120$ (weakly turbulent state), (b) $t = 240$ (turbulent state), and (c) $t = 400$ (convective cell dominated final state).

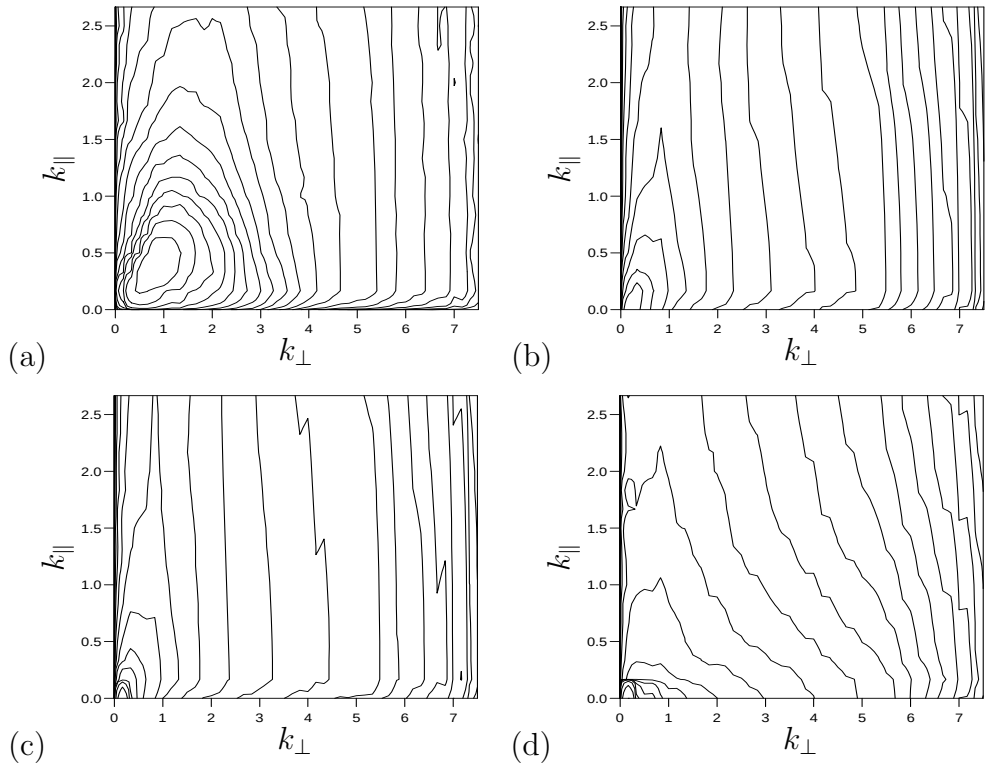


Figure 4.5: Time evolution of the energy power spectrum in $k_\perp, k_\parallel$–space. (a) $t = 40$ (exponential growth state), (b) $t = 120$ (weakly turbulent state), (c) $t = 240$ (turbulent state), and (d) $t = 400$ (convective cell dominated final state).

The evolution of the finite ion temperature modified Hasegawa-Wakatani system is quite similar to that of the standard Hasegawa-Wakatani system (compare to Section 3.3). This is due to the nonlinear effects being dominant from the turbulent state and onwards, where we find that the norm of the nonlinear term is at least an order of magnitude larger than that of the $\theta$-term. However, for some parameters the effect is more pronounced, as it is discussed below.
In order to emphasise the effect of the ion temperature modification a simulation with more extreme parameters is presented. The simulation had a domain size of $L_x = L_y = 12\pi$ and $L_z = 28\pi$, a spatial resolution of $96^3$ Fourier modes, $\mathrm{d}t = 2 \cdot 10^{-3}$, hyperviscosity of the order $2p = 6$ and a viscosity parameter $\nu = 10^{-4}$, and $\theta = 0.2$, i.e. higher $\theta$, more parallel modes and smaller $k_\parallel$ values. The relatively low $k_\parallel$-values cause the coupling to be low, and according to Section 3.4 the Hasegawa-Wakatani system will take longer to condensate the energy into the convective cell dominated state.
The temporal evolution of the energy of the system is presented in Figure 4.6, and in Figure 4.7 we present the corresponding evolution of the standard Hasegawa-Wakatani system for equivalent parameters. It is clear from the figures that the transition into the convective cell dominated state occurs earlier when the ion temperature effects are included. The transition for the

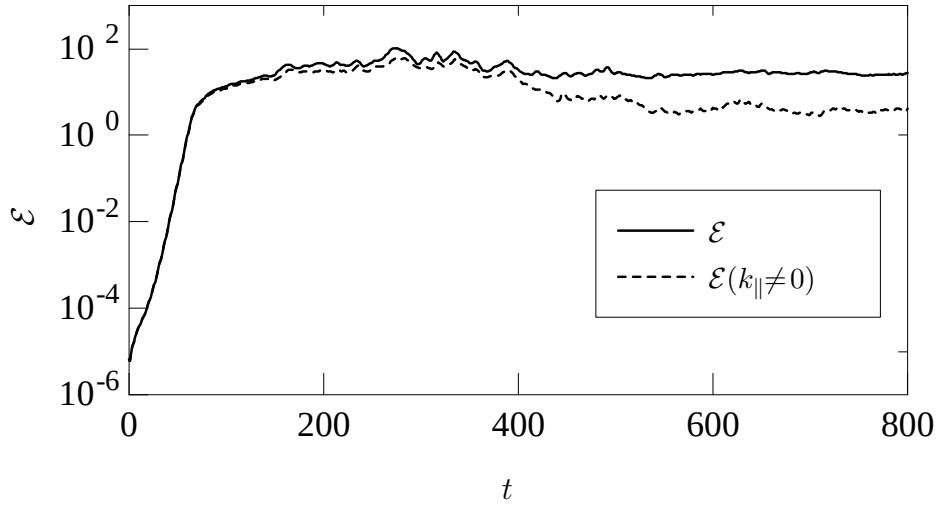


Figure 4.6: The evolution of the total energy $\mathcal{E}$, and the drift wave energy $\mathcal{E}(k_\parallel \neq 0)$, for the ion temperature modified Hasegawa-Wakatani model.

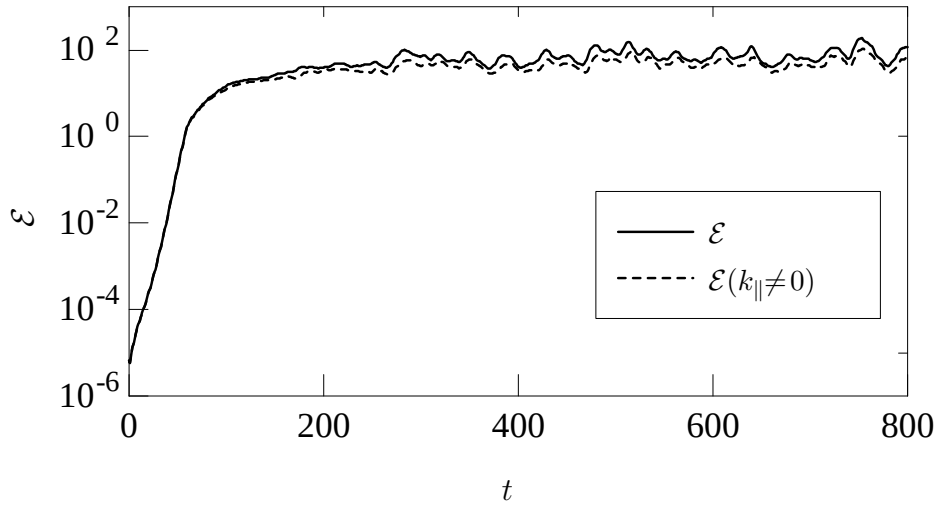


Figure 4.7: The evolution of the total energy $\mathcal{E}$, and the drift wave energy $\mathcal{E}(k_\parallel \neq 0)$, for the standard Hasegawa-Wakatani model.

Hasegawa-Wakatani system is actually happening at the time $t = 1000$. Analysis make probable that the reason for the earlier transition between states in the ion temperature modified case is that the $\theta$-term causes a relatively larger part of the energy to be kinetic energy. Biskamp and Zeiler showed in [28] that the dominant cascading direction of the kinetic energy is from high to low $k_\parallel$-values.

## 4.4 Evaluation of the model

In the present chapter we derived and analysed a model of weakly nonlinear resistive drift waves with a low but finite ion temperature. The equations

of the model are a generalisation of the standard Hasegawa-Wakatani equations, with ion temperature corrections retained to lowest order.
The main results of the simulations with the model can be summarised as follows: Starting with a slightly perturbed initial condition, we first see an exponential growth, which is well described by linear theory. The instability saturates after a turbulent state in a weakly turbulent state, where the dominant features are a pair of large flute-like structures associated with $k_{\|} = 0$, interpreted as electrostatic flute modes. This behaviour is alike that of the Hasegawa-Wakatani system, however, for some parameters the tendency of the system to condensate the energy into the $k_{\|} = 0$-modes, is affected by the finite ion temperature. Furthermore, the level of the turbulent flux is somewhat increased by increasing ion temperature.

# Chapter 5

# Electron temperature variations

The Hasegawa-Wakatani model [23] provides a good first principles view over resistive drift wave dynamics in magnetised plasmas. A natural next step towards a better understanding of the basic properties of the nature of drift waves is to include electron temperature variations. In the Hasegawa-Wakatani model it is assumed that the electron temperature gradient is negligible compared to the density gradient (Assumption 2), and it is assumed likewise that the perturbations in the electron temperature, $T_e$, is negligible to the perturbations in the density, $n$. This is often not fulfilled in experiments (see, e.g., [43]). Hence, we propose a model including the effects of a background electron temperature gradient and a background density gradient, and fluctuations in the density $n$, the electrostatic potential $\phi$, and the electron temperature $T_e$: the $n\phi T_e$ model.
The $n\phi T_e$ model was first derived in the authors Master's thesis [22], and results were presented in [44]. Unfortunately, however, these first results contained an error in the derivation, which is corrected in the present text.
Some publications with similar models exist, e.g., [45–47], though these additionally contain an equation for the ion parallel velocity, and inhomogeneous magnetic fields.

## 5.1 The $n\phi T_e$ model

The model has the same foundation as the Hasegawa-Wakatani model with the addition of an equation for the evolution of the electron temperature fluctuations taken from Braginskii [48]. Thus the assumptions of Chapter 3 are still valid, with the exception of Assumption 2 for obvious reasons. Furthermore, the weak turbulence ordering assumption, Assumption 12, is extended to

**Assumption 18** $\quad \frac{n_1}{n_0} \sim \frac{T_{e1}}{T_{e0}} \sim \frac{e\phi}{T_{e0}} \sim \frac{\omega}{\omega_{ci}} \sim \varepsilon \ll 1$

where $T_e = T_{e0} + T_{e1}$ with $T_{e0}$ being the background temperature and $T_{e1}$ the electron temperature fluctuations.

The ion vorticity equation (3.6) and the electron continuity equation (3.15) are not modified by the introduction of electron temperature effects. Thus only the generalised Ohm's law is re-derived.
As it was the case for the Hasegawa-Wakatani model the $n\phi T_e$ model is derived in a three-dimensional Cartesian geometry.

### 5.1.1 The modified generalised Ohm's law

The parallel electron dynamics may be described by the parallel component of the generalised Ohm's law. The generalised Ohm's law is a result of ideal or single-fluid magnetohydrodynamics [21, 34]. Since the electrons are collisionally damped (according to Assumption 14), the generalised Ohm's law is found from the electron equation of motion, the electron momentum equation, which Braginskii expresses by [48]:

$$\begin{aligned} m_e n_e \frac{\mathrm{D}v_{e,\parallel}}{\mathrm{D}t} =& -\nabla_\parallel p_e - \nabla_\beta \bar{\bar{\Pi}}_{e\parallel\beta} - e n_e \left(E_\parallel + (\mathbf{v}_e \times \mathbf{B})_\parallel\right) \\ &+ \left(\frac{e n_e}{\sigma_\parallel} J_\parallel + \frac{e n_e}{\sigma_\perp} J_\perp - 0.71 n_e \nabla_\parallel T_e - \frac{3}{2}\frac{n_e}{\omega_e \tau_e} \mathbf{e}_\parallel \times \nabla T_e\right)_\parallel \end{aligned} \tag{5.1}$$

where only the parallel components are considered. Since the model is derived in the electrostatic approximation (Assumption 6) no perturbations in the magnetic field exist and since $\mathbf{B} = B_0 \mathbf{e}_\parallel$ (Assumption 4) the $(\mathbf{v}_e \times \mathbf{B})_\parallel$-term is zero. In an electromagnetic picture this term would have given a $\partial\psi/\partial t$-term, where $\psi$ is the magnetic vector potential.
$\bar{\bar{\Pi}}_{e\parallel\beta}$ is the anisotropic part of the electron pressure. The tensor contains terms of the form $\frac{\partial v_{e\alpha}}{\partial x_\beta}$, i.e. the $\nabla_\beta \bar{\bar{\Pi}}_{e\parallel\beta}$-term will include third order derivatives of $\phi$. We will omit the term for simplicity.
Additionally, the second and fourth term in the last parenthesis vanish, since only the parallel components are included. The momentum equation (5.1) is now:

$$m_e n_e \frac{\mathrm{D}v_{e,\parallel}}{\mathrm{D}t} = -\nabla_\parallel p_e - e n_e E_\parallel + \frac{e n_e}{\sigma_\parallel} J_\parallel - 0.71 n_e \nabla_\parallel T_e \tag{5.2}$$

The fluctuation induced parallel current $J_\parallel$ is assumed to be of first order, and thus all terms on the right hand side of (5.2) are of the same order. The term on the left hand side of (5.2) is set to zero since we neglect electron inertia according to Assumption 13, and the terms on the right hand side should balance.
Replacing the inverse of the parallel conductivity $1/\sigma_\parallel$ by the parallel resistivity $\eta$, and $E_\parallel$ by $-\nabla_\parallel \phi$ (Assumption 6) results in

$$-e n_e \eta J_\parallel = -\nabla_\parallel p_e + e n_e \nabla_\parallel \phi - 0.71 n_e \nabla_\parallel T_e \tag{5.3}$$

Inserting now the background and fluctuation parts $n_0 + n_1$ for $n_e$ and $T_{e0} + T_{e1}$ for $T_e$ we obtain:

$$\begin{aligned} -e(n_0 + n_1)\eta J_\parallel \;=\; & -\nabla_\parallel (n_0 T_{e0} + n_0 T_{e1} + n_1 T_{e0} + n_1 T_{e1}) + e(n_0 + n_1)\nabla_\parallel \phi \\ & -0.71(n_0 + n_1)\nabla_\parallel (T_{e0} + T_{e1}) \end{aligned} \tag{5.4}$$

We may now assume the same shape of the background electron temperature gradient as that for the background density (Assumption 15):

**Assumption 19** $T_{e0} = T_{e0}(x) = T_0 e^{-\frac{x}{L_T}}$

where $-1/L_T$ is the relative background electron temperature gradient. In order for Assumption 19 to be valid we have to assume - analogous to Assumption 16 - that

**Assumption 20** $\frac{1}{L_T} \ll k$

where $k$ is a typical length scale of the perturbations.
From Assumptions 15 and 19 follow that the parallel derivatives of the background density and of the background temperature are zero, i.e. $\nabla_\parallel n_0 = 0$ and $\nabla_\parallel T_{e0} = 0$. Using this and neglecting second order terms we may rewrite (5.4) as follows:

$$-en_0\eta J_\parallel = -n_0\nabla_\parallel T_{e1} - T_{e0}\nabla_\parallel n_1 - 0.71 n_0 \nabla_\parallel T_{e1} + en_0\nabla_\parallel\phi \Leftrightarrow$$

$$J_\parallel = -\frac{T_{e0}}{\eta e}\nabla_\parallel\left(\frac{e\phi}{T_{e0}} - \frac{n_1}{n_0} - \hat{\alpha}\frac{T_{e1}}{T_{e0}}\right) \tag{5.5}$$

which is the generalised Ohm's law, where $\hat{\alpha} = 1.71$.

### 5.1.2 The Braginskii electron temperature equation

In order to close the set of equations we need an explicit equation for the electron temperature, and this may be obtained from the Braginskii temperature equation [48]:

$$\frac{3}{2}n_e\frac{\mathrm{D}T_e}{\mathrm{D}t} + v_{e,\parallel}\cdot\nabla T_e + p_e\nabla\cdot\mathbf{v}_e = -\nabla\cdot\mathbf{q}_e + Q_e - \bar{\bar{\Pi}}_{e\alpha\beta}\frac{\partial v_{e\alpha}}{\partial x_\beta} \tag{5.6}$$

where $\mathbf{v}_e = \mathbf{v}_E - \frac{J_\parallel}{en_e}\mathbf{e}_z$ and $\bar{\bar{\Pi}}_{e\alpha\beta}$ is the anisotropic part of the electron pressure. The tensor contains terms of the form $\frac{\partial v_{e\alpha}}{\partial x_\beta}$; Here the terms will be omitted for simplicity.
We derive the equations under the assumption of a strong magnetic field (Assumption 5) and may thus assume that $\omega_{ce}\tau_e \propto eB_0/m_e\nu_e$ is large ($\tau_e$ is the electron collision time and $\nu_e$ is the electron collision rate). We may hence use the expressions for $\mathbf{q}_e$ and $Q_e$ as given in [48]. The electron heat flux, $\mathbf{q}_e$, is

$$\mathbf{q}_e = 0.71 n_e T_e \mathbf{u}_\parallel + \frac{3}{2}\frac{n_e T_e}{\omega_{ce}\tau_e}(\mathbf{e}_z\times\mathbf{u}) - \kappa_\parallel\nabla_\parallel T_e - \kappa_\perp\nabla_\perp T_e - \frac{5}{2}\frac{n_e T_e}{eB_0}(\mathbf{e}_z\times\nabla T_e) \tag{5.7}$$

where $\kappa_\parallel$ and $\kappa_\perp$ are the parallel and perpendicular thermal conductivities, respectively. We will omit the $\kappa_\perp$-term since $\kappa_\perp/\kappa_\parallel \propto (\omega_{ce}\tau_e)^{-2} \ll 1$. $\mathbf{u}$ is the relative velocity of the ions and electrons:

$$\mathbf{u} = (\mathbf{v}_e - \mathbf{v}_i) = (0, 0, \frac{-J_\parallel}{en_e})$$

since $\mathbf{v}_{e\perp} = \mathbf{v}_{i\perp} = \mathbf{v}_E$ and $\mathbf{v}_{i\parallel} = 0$ according to Assumption 9. The heat $Q_e$ generated in the electrons due to collisions with ions is given by

$$Q_e = \frac{J_\parallel^2}{\sigma_\parallel} + \frac{\mathbf{J}_\perp^2}{\sigma_\perp} - \frac{1}{en_e}\mathbf{J}\cdot(0.71 n_e \nabla_\parallel T_e + \frac{3}{2}\frac{n_e}{\omega_{ce}\tau_e}(\mathbf{e}_z \times \nabla T_e)) - 3\frac{m_e n_e}{m_i \tau_e}(T_e - T_i) \tag{5.8}$$

where $\mathbf{J} = -en_e\mathbf{u} \Rightarrow \mathbf{J}_\perp = 0$. We neglect the last term due to the factor $m_e/m_i$ (Assumption 13), and the $J_\parallel^2$-term is of second order and is omitted. This reduces (5.8) to

$$Q_e = -\frac{1}{en_e}\mathbf{J}\cdot(0.71 n_e \nabla_\parallel T_e + \frac{3}{2}\frac{n_e}{\omega_{ce}\tau_e}(\mathbf{e}_z \times \nabla T_e)) \tag{5.9}$$

The last term $\mathbf{J}\cdot(\mathbf{e}_z \times \nabla T_e)$ vanishes since $\mathbf{J} = J_\parallel \mathbf{e}_z$, and the first term is left out as well, because it is of second order

$$J_\parallel \frac{\partial T_e}{\partial z} = J_\parallel \frac{\partial T_{e1}}{\partial z} \text{ , since } \frac{\partial T_{e0}(x)}{\partial z} = 0$$

Hence, there is no contribution from $Q_e$.
Before substituting into (5.6) the expression for $\nabla\cdot\mathbf{q}_e$ is reduced. We substitute the expression for $\mathbf{u}$ and note that the second term in (5.7) vanishes since $\mathbf{u} \parallel \mathbf{e}_z$. We take the divergence and get

$$\nabla\cdot\mathbf{q}_e = -0.71\frac{1}{e}\frac{\partial J_\parallel T_e}{\partial z} - \kappa_\parallel \frac{\partial^2 T_e}{\partial z^2} - \nabla\cdot\left(\frac{5}{2}\frac{n_e T_e}{eB_0}(\mathbf{e}_z \times \nabla T_e)\right) \tag{5.10}$$

The last term vanishes by use of ordinary vector algebra. By inserting $T_e = T_{e,o}(x) + T_{e1}(x,y,z)$, leaving out second order terms and remembering that $\frac{\partial T_{e0}(x)}{\partial z} = 0$ we reduce (5.10) to

$$\nabla\cdot\mathbf{q}_e = -0.71\frac{T_{e0}}{e}\frac{\partial J_\parallel}{\partial z} - \kappa_\parallel \frac{\partial^2 T_{e1}}{\partial z^2} \tag{5.11}$$

The term $v_{e,\parallel}\cdot\nabla T_e$ of (5.6) may be written as:

$$v_{e,\parallel}\cdot\nabla T_e = -\frac{J_\parallel}{en_e}\cdot\nabla_\parallel T_e = -\frac{J_\parallel}{en_e}\cdot(\nabla_\parallel T_{e0} + \nabla_\parallel T_{e1}) = -\frac{J_\parallel}{en_e}\cdot\nabla_\parallel T_{e1}$$

since $\frac{\partial T_{e0}}{\partial z} = 0$, and the term is thus neglected since it is of second order.
Finally, the $p_e\nabla\cdot\mathbf{v}_e$-term may be reduced as follows

$$\begin{aligned} p_e\nabla\cdot\mathbf{v}_e = p_e\nabla\cdot\left(\mathbf{v}_E - \frac{J_\parallel}{en_e}\mathbf{e}_z\right) &= n_e T_e \frac{\partial}{\partial z}\left(\frac{J_\parallel}{en_e}\right) \\ &= \frac{n_e T_e}{e}\left(\frac{1}{n_e}\frac{\partial J_\parallel}{\partial z} + J_\parallel \frac{\partial n_e^{-1}}{\partial z}\right) \\ &= \frac{n_e T_e}{e}\left(\frac{1}{n_e}\frac{\partial J_\parallel}{\partial z} - \frac{J_\parallel}{n_e^2}\frac{\partial n_e}{\partial z}\right) \\ &= \frac{T_{e0}}{e}\frac{\partial J_\parallel}{\partial z} \end{aligned}$$

where we use that $\mathbf{v}_E$ is divergence free, that $\frac{\partial n_0}{\partial z} = 0$, and leave out second order terms.
The temperature equation (5.6) may now be written as

$$\frac{3}{2} n_e \frac{\mathrm{D}}{\mathrm{D}t}(T_{e0} + T_{e1}) = \hat{\alpha} \frac{T_{e0}}{e} \frac{\partial J_\parallel}{\partial z} + \kappa_\parallel \frac{\partial^2 T_{e1}}{\partial z^2} \tag{5.12}$$

where again $\hat{\alpha} = 1.71$.

### 5.1.3 The system of equations

We have now obtained the four equations that form the basis for the system and restate them for convenience

$$\frac{\mathrm{D}}{\mathrm{D}t}\left(\frac{\nabla_\perp^2 \phi}{\omega_{ci} B_0} - \ln n_0 - \frac{n_1}{n_0}\right) = \frac{\mu}{\omega_{ci} B_0} \nabla_\perp^4 \phi \tag{3.6}$$

$$J_\parallel = -\frac{T_{e0}}{\eta e} \frac{\partial}{\partial z}\left(\frac{e\phi}{T_{e0}} - \frac{n_1}{n_0} - \hat{\alpha}\frac{T_{e1}}{T_{e0}}\right) \tag{5.5}$$

$$\frac{\mathrm{D}}{\mathrm{D}t}\left(\ln n_0 + \frac{n_1}{n_0}\right) = \frac{1}{e n_0} \frac{\partial J_\parallel}{\partial z} \tag{3.15}$$

$$\frac{3}{2} n_e \frac{\mathrm{D}}{\mathrm{D}t}(T_{e0} + T_{e1}) = \hat{\alpha} \frac{T_{e0}}{e} \frac{\partial J_\parallel}{\partial z} + \kappa_\parallel \frac{\partial^2 T_{e1}}{\partial z^2} \tag{5.12}$$

First we eliminate $J_\parallel$ by substituting (5.5) in (3.15):

$$\frac{\mathrm{D}}{\mathrm{D}t}\left(\ln n_0 + \frac{n_1}{n_0}\right) = -\frac{T_e 0}{\eta e^2 n_0} \frac{\partial^2}{\partial z^2}\left(\frac{e\phi}{T_{e0}} - \frac{n_1}{n_0} - \hat{\alpha}\frac{T_{e1}}{T_{e0}}\right) \tag{5.13}$$

This equation is commonly simplified by assuming that the relative background density gradient is constant locally in the edge region, i.e. of the domain of the model. This is the case according to Assumptions 15 and 16, and (5.13) can be written as

$$\frac{\mathrm{D}}{\mathrm{D}t}\left(\frac{n_1}{n_0}\right) + \frac{1}{L_n B_0} \frac{\partial \phi}{\partial y} = -\frac{T_{e0}}{\eta e^2 n_0} \frac{\partial^2}{\partial z^2}\left(\frac{e\phi}{T_{e0}} - \frac{n_1}{n_0} - \hat{\alpha}\frac{T_{e1}}{T_{e0}}\right) \tag{5.14}$$

since

$$\frac{\mathrm{D}}{\mathrm{D}t} \ln n_0 = (\frac{\partial}{\partial t} + \mathbf{v}_E \cdot \nabla) \ln(N_0 e^{-\frac{x}{L_n}}) = \mathbf{v}_E \cdot (-\frac{1}{L_n}\mathbf{e}_x) = \frac{1}{L_n B_0} \frac{\partial \phi}{\partial y}$$

The partial differential equation (5.14) is the equation for the density perturbation, and the corresponding equation for the potential is obtained by substituting (5.13) into (3.6):

$$\frac{\mathrm{D}}{\mathrm{D}t}\left(\frac{\nabla_\perp^2 \phi}{\omega_{ci} B_0}\right) = -\frac{T_{e0}}{\eta e^2 n_0} \frac{\partial^2}{\partial z^2}\left(\frac{e\phi}{T_{e0}} - \frac{n_1}{n_0} - \hat{\alpha}\frac{T_{e1}}{T_{e0}}\right) + \frac{\mu}{\omega_{ci} B_0} \nabla_\perp^4 \phi \tag{5.15}$$

By using Assumption 19 the $\frac{\mathrm{D}T_{e0}}{\mathrm{D}t}$ term in (5.12) may be expressed as

$$\frac{\mathrm{D}T_{e0}}{\mathrm{D}t} = T_{e0} \frac{\mathrm{D} \ln T_{e0}}{\mathrm{D}t} = T_{e0} \mathbf{v}_E \cdot \nabla \ln(T_{e0} e^{-\frac{x}{L_T}}) = T_{e0} \mathbf{v}_E \cdot (-\frac{1}{L_T}\mathbf{e}_x) = \frac{T_{e0}}{L_T B_0} \frac{\partial \phi}{\partial y}$$

By substituting this and $n_e = n_0 + n_1$ in (5.12) it is seen that all terms including $n_1$ is of second order. Omitting these, we may now write the temperature equation as

$$\frac{\mathrm{D}}{\mathrm{D}t}\frac{T_{e1}}{T_{e0}} = \frac{-1}{L_T B_0}\frac{\partial \phi}{\partial y} + \frac{2}{3}\frac{\kappa_\parallel}{n_0}\frac{\partial^2}{\partial z^2}\frac{T_{e1}}{T_{e0}} + \frac{2}{3}\frac{\hat{\alpha}}{e n_0}\frac{\partial J_\parallel}{\partial z} \tag{5.16}$$

Eliminating $J_\parallel$ by substituting (5.5) into (5.16) we obtain:

$$\frac{\mathrm{D}}{\mathrm{D}t}\frac{T_{e1}}{T_{e0}} + \frac{1}{L_T B_0}\frac{\partial \phi}{\partial y} - \frac{2}{3}\frac{\kappa_\parallel}{n_0}\frac{\partial^2}{\partial z^2}\frac{T_{e1}}{T_{e0}} = -\frac{2}{3}\frac{\hat{\alpha} T_{e0}}{\eta e^2 n_0}\frac{\partial^2}{\partial z^2}\left(\frac{e\phi}{T_{e0}} - \frac{n_1}{n_0} - \hat{\alpha}\frac{T_{e1}}{T_{e0}}\right) \tag{5.17}$$

We have now obtained the equations needed (5.14), (5.15) and (5.17). The equations are simplified and normalised to the order unity by transforming them to dimensionless variables by the following normalisations:

$$\tilde{x} = \frac{x}{\rho_s}, \quad \tilde{y} = \frac{y}{\rho_s}, \quad \tilde{z} = \frac{z}{L_\parallel}, \quad \tilde{t} = t\omega_{ci}\frac{\rho_s}{L_n}, \quad \tilde{n} = \frac{n_1}{n_0}\frac{L_n}{\rho_s},$$

$$\tilde{\phi} = \frac{e\phi}{T_{e0}}\frac{L_n}{\rho_s}, \text{ and } \tilde{T} = \frac{T_{e1}}{T_{e0}}\frac{L_n}{\rho_s}$$

The following model equations may thus be obtained (where the tildes have been omitted):

$$(\frac{\partial}{\partial t} + \mathbf{v}_E \cdot \nabla_\perp)n + \frac{\partial \phi}{\partial y} = \mathcal{C}\frac{\partial^2}{\partial z^2}(n + \hat{\alpha}T - \phi) + \nu\mathcal{D}^{2p} n \tag{5.18}$$

$$(\frac{\partial}{\partial t} + \mathbf{v}_E \cdot \nabla_\perp)(\nabla_\perp^2 \phi) = \mathcal{C}\frac{\partial^2}{\partial z^2}(n + \hat{\alpha}T - \phi) + \nu\mathcal{D}^{2p+2}\phi \tag{5.19}$$

$$(\frac{\partial}{\partial t} + \mathbf{v}_E \cdot \nabla_\perp)T + \frac{L_n}{L_T}\frac{\partial \phi}{\partial y} - \zeta\frac{\partial^2 T}{\partial z^2} = \chi\mathcal{C}\frac{\partial^2}{\partial z^2}(n + \hat{\alpha}T - \phi) + \nu\mathcal{D}^{2p} T \tag{5.20}$$

where $\hat{\alpha} = 1.71$, $\chi = \frac{2}{3}\hat{\alpha}$, and $\zeta$ and $\mathcal{C}$ are defined as

$$\mathcal{C} \equiv \frac{T_{e0} L_n}{\eta e^2 n_0 \omega_{ci} \rho_s L_\parallel^2} \tag{3.22}$$

and

$$\zeta = \frac{2}{3}\frac{\kappa_\parallel L_n}{n_0 \omega_{ci} L_\parallel \rho_s} = \frac{2}{3}\frac{\kappa_\parallel \eta e^2}{T_{e0}}\mathcal{C}$$

The parallel thermal conductivity, $\kappa_\parallel$, is given by:

$$\kappa_\parallel = 3.16\frac{n_e T_{e0}\tau_e}{m_e}$$

The kinematic viscosity term in (5.15) has been replaced by the hyperviscosity term of the form $\mathcal{D}^{2p} \equiv (-1)^{p+1}\nabla_\perp^{2p}$, which has additionally been included in each of the other equations for numerical reasons[1].
We have now a self-consistent closed set of equations describing drift waves driven by a density and an electron temperature background gradient.

[1] See the discussion of hyperviscosity in Section 3.1.5.

## 5.2 Analytical analysis of the equations

As for the Hasegawa-Wakatani system a full analytical solution of the partial differential equations (5.18-5.20) is not generally possible. However, important properties of the system may be found analytically, and in the present section we will derive the dispersion relation for the system and analyse the linear instability. Finally, we derive the temporal derivative of the energy, and determine the sources and sinks of the system.

### 5.2.1 Linear growth rate

Linear stability analysis of the model may be performed to obtain the growth rate of the drift waves. We assume that as long as $n$, $\phi$ and $T$ are small, they can locally be described as linear waves of the form

$$n = n_a e^{i(\mathbf{k}\cdot\mathbf{r}-\omega_t t)}, \quad \phi = \phi_a e^{i(\mathbf{k}\cdot\mathbf{r}-\omega_t t)}, \quad T = T_a e^{i(\mathbf{k}\cdot\mathbf{r}-\omega_t t)}$$

with $n_a$, $\phi_a$ and $T_a$ being small quantities. We substitute this in the equations (5.18-5.20) and omit the nonlinear terms ($\mathbf{v}_E \cdot \nabla_\perp n$, $\mathbf{v}_E \cdot \nabla_\perp \phi$ and $\mathbf{v}_E \cdot \nabla_\perp T$), since these are of second order. Hereby we get the Fourier decomposed linearised equations

$$-i\omega_t n_a + ik_y\phi_a = -\mathcal{C}k_z^2(n_a + \hat{\alpha}T_a - \phi_a) - \nu k_\perp^{2p} n_a \tag{5.21}$$

$$i\omega_t k_\perp^2 \phi_a = -\mathcal{C}k_z^2(n_a + \hat{\alpha}T_a - \phi_a) + \nu k_\perp^{2p+2}\phi_a \tag{5.22}$$

$$-i\omega_t T_a + i\frac{L_n}{L_T}k_y\phi_a + \zeta k_z^2 T_a = -\chi\mathcal{C}k_z^2(n_a + \hat{\alpha}T_a - \phi_a) - \nu k_\perp^{2p} T_a \tag{5.23}$$

where $k_\perp^2 = k_x^2 + k_y^2$ and $\omega_t = \omega_r + i\gamma$.
To obtain a nontrivial solution to this set of three equations with the unknowns $n_a$, $\phi_a$ and $T_a$, it is necessary to determine the $\omega_t$ values for which the determinant is zero. This necessitates the solution of the cubic dispersion relation found from the system of equations (5.21-5.23). Expressed in the form $\omega_t^3 + a_2\omega_t^2 + a_1\omega_t + a_0 = 0$, the coefficients may be written:

$$a_2 = i(e + 2\mu)$$

$$a_1 = -(2\mu e + \mu^2 + f)$$

$$a_0 = -(i\mu^2 e + i\mu f - bdk_y)$$

where the following abbreviations have been used:

$$b = \zeta k_z^2 \quad , \qquad c = k_y(1 + \hat{\alpha}\frac{L_n}{L_T}) \quad , \qquad d = \frac{\mathcal{C}k_z^2}{k_\perp^2} \quad , \qquad \mu = \nu k_\perp^{2p}$$

$$e = \frac{\mathcal{C}k_z^2}{k_\perp^2}(1 + k_\perp^2(1 + \frac{2}{3}\hat{\alpha}^2)) + \zeta k_z^2 + \nu k_\perp^{2p} \quad , \quad \text{and}$$

$$f = \frac{\zeta\mathcal{C}k_z^4}{k_\perp^2}(1 + k_\perp^2) + i\frac{\mathcal{C}k_z^2}{k_\perp^2}k_y(1 + \hat{\alpha}\frac{L_n}{L_T})$$

The general solution to a cubic equation may be written:

$$\omega_{t,1} = S_1 + S_2 - \frac{a_2}{3}$$

$$\omega_{t,2} = -0.5(S_1 + S_2) - \frac{a_2}{3} + i\frac{\sqrt{3}}{2}(S_1 - S_2)$$

$$\omega_{t,3} = -0.5(S_1 + S_2) - \frac{a_2}{3} - i\frac{\sqrt{3}}{2}(S_1 - S_2)$$

where $S_1$ and $S_2$ are:

$$S_1 = \sqrt[3]{R + \sqrt{Q^3 + R^2}}$$

$$S_2 = \sqrt[3]{R - \sqrt{Q^3 + R^2}}$$

The solutions of the cube roots have to be chosen so that $S_1$ and $S_2$ fulfill: $S_1 \cdot S_2 = -Q$. Q and R are calculated from the coefficients of the cubic equation as:

$$Q = a_1/3 - a_2^2/9$$

$$R = (a_1 a_2 - 3a_0)/6 - a_2^3/27$$

We are only interested in solutions with a positive imaginary part, since this corresponds to a growing wave. Solutions have been found by implementing the expressions for $\omega_t$ into *Mathematica*, and it appears that only one solution has a positive imaginary part corresponding to a positive growth rate $\gamma$. Since the solution is rather complicated, we only present $\gamma$ graphically in Figure 5.1, in which the parameters chosen are typical for the simulations. If the temperature gradient increases relative to the density gradient, i.e. $\frac{L_n}{L_T}$ increases, the growth rate $\gamma$ also increases. This may be observed in Figure 5.2, for which the parameters are the same as in Figure 5.1, except for $\frac{L_n}{L_T} = 1.0$ instead of 0.5. The maximum growth rate for $\frac{L_n}{L_T} = 0.5$ is $\gamma_{max} \approx \gamma(k_x = 0, k_y = 0.573, k_z = 0.277) \approx 0.154$, and for $\frac{L_n}{L_T} = 1.0$ the maximum growth rate is $\gamma(k_x = 0, k_y = 0.556, k_z = 0.316) \approx 0.220$. The maximum growth rate for the Hasegawa-Wakatani system with similar parameters (where applicable) is $\sim 0.15$. The increase in the growth rate for the present model relative to the Hasegawa-Wakatani case is to be expected, since the system is now driven by two gradients. If $\frac{L_n}{L_T}$ is set to zero, i.e. the drive of the temperature gradient is cancelled, then the maximum growth rate is $\gamma(k_x = 0, k_y = 1.1, k_z = 1.25) \approx 0.115$. This decrease compared to the Hasegawa-Wakatani system is due to the damping terms of the temperature equation, i.e. the heat conductivity and the viscous term. If further $\chi$ and $\zeta$ is set to zero, the Hasegawa-Wakatani equations are approximately retained from the model equations 5.18–5.20. In this case the maximum growth rate of $\gamma(k_x = 0, k_y = 1, k_z = 0.5) \approx 0.15$ is consistently obtained.

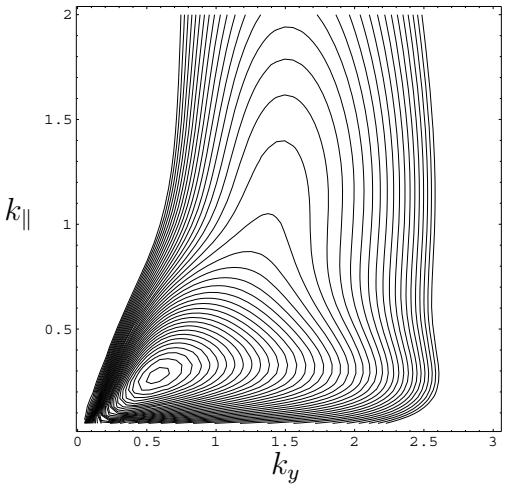


Figure 5.1: The growth rate as a function of $k_y$ and $k_z$, for $k_x = 0$, $\mathcal{C} = 1$, $\frac{L_n}{L_T} = 0.5$, $\zeta = 0.5$, $\nu = 2{\cdot}10^{-4}$, and order $2p = 6$. The contours are equally spaced and only positive values are plotted. $\gamma_{max} \approx \gamma(k_x = 0, k_y = 0.573, k_z = 0.277) \approx 0.154$.

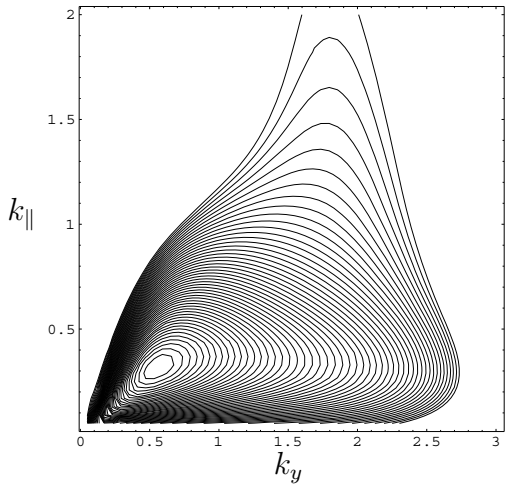


Figure 5.2: The growth rate as a function of $k_y$ and $k_z$, for $k_x = 0$, $\mathcal{C} = 1$, $\frac{L_n}{L_T} = 1.0$, $\zeta = 0.5$, $\nu = 2{\cdot}10^{-4}$, and order $2p = 6$. The contours are equally spaced and only positive values are plotted. $\gamma_{max} \approx \gamma(k_x = 0, k_y = 0.556, k_z = 0.316) \approx 0.220$.

### 5.2.2 Energy and flux

The total energy of the system may be expressed as

$$\mathcal{E} = \mathcal{E}_{kin} + \mathcal{E}_{pot} + \mathcal{E}_{thermal} = \frac{1}{2}\iiint \left[(\nabla_\perp \phi)^2 + n^2 + \frac{3}{2}T^2\right] \mathrm{d}x\,\mathrm{d}y\,\mathrm{d}z \quad (5.24)$$

The sources and sinks of energy of the system may be found by differentiation of (5.24) with respect to time. We assume that the solutions and their spatial derivatives are localised, i.e. vanish at infinity. Hence by partial integration we obtain:

$$\begin{aligned}\frac{\mathrm{d}\mathcal{E}}{\mathrm{d}t} = \iiint \; &- \; n\frac{\partial \phi}{\partial y} - \frac{3}{2}\frac{L_n}{L_T}T\frac{\partial \phi}{\partial y} - \mathcal{C}\left(\frac{\partial}{\partial z}(n + \hat{\alpha}T - \phi)\right)^2 - \frac{3}{2}\zeta\left(\frac{\partial T}{\partial z}\right)^2 \\ &- \; \nu((\nabla_\perp^p n)^2 + \frac{3}{2}(\nabla_\perp^p T)^2 + (\nabla_\perp^{p+1}\phi)^2)\,\mathrm{d}x\,\mathrm{d}y\,\mathrm{d}z \end{aligned} \quad (5.25)$$

The first two terms are the turbulent density and heat flux, respectively:

$$\Gamma_n = \iiint -n\frac{\partial \phi}{\partial y}\,\mathrm{d}x\,\mathrm{d}y\,\mathrm{d}z = \iiint n v_{E,x}\,\mathrm{d}x\,\mathrm{d}y\,\mathrm{d}z \quad (5.26)$$

$$\Gamma_T = \frac{L_n}{L_T}\iiint -T\frac{\partial \phi}{\partial y}\,\mathrm{d}x\,\mathrm{d}y\,\mathrm{d}z = \frac{L_n}{L_T}\iiint T v_{E,x}\,\mathrm{d}x\,\mathrm{d}y\,\mathrm{d}z \quad (5.27)$$

The next term is the Ohmic loss term, and the last terms are the heat conductivity loss term and the hyperviscous loss terms.
The only terms that may be positive are the two flux terms and thus the

only driving mechanisms are the density and the heat fluxes, which enter the equations through the background gradients. In analogy with the Hasegawa-Wakatani system the energy of the system is extracted from the background density gradient, and additionally for the $n\phi T_e$ model there is an electron temperature background gradient driving the turbulence.

## 5.3 Numerical results

The equations (5.18-5.20) are solved in a triply periodic geometry using the same numerical methods as those used in Chapter 3. First, we present the general behaviour of the $n\phi T_e$ model and compare to the Hasegawa-Wakatani model. Finally, we present a small investigation of the effect of the relative steepness of the density and temperature gradients.

### 5.3.1 General behaviour

It is naturally impossible to give an exhaustive description of the behaviour of the model, since the parameter space is multi-dimensional. However, in this paragraph we present the results of a simulation which appears typical for the investigated parameter space. Furthermore, for reasons of comparison the particular parameters used have been chosen to be similar to those of the simulations presented in Chapters 3 and 4. An exception is the viscosity parameter, which had to be higher in the present simulation in order to provide stability of the scheme. The following parameters were used: 96 modes in each of the perpendicular directions and 48 modes in the parallel direction. A domain size of $L_x = L_y = L_z = 12\pi$, a time step of $\mathrm{d}t = 0.002$, $\zeta = 0.5$, $\frac{L_n}{L_T} = 0.5$, a hyperviscosity of order $2p = 6$, and a viscosity parameter $\nu = 2 \cdot 10^{-4}$. The initial conditions were $\phi = n = T$ being low level random noise with zero mean divided by $k^2$.
The temporal evolution of the total energy and different energy components are presented in Figure 5.3. It may be seen that the energy grows exponentially until nonlinear effects dominate and the system evolves into a turbulent state, which is succeeded by a state where the main part of the energy is transfered into convective cells (flute-modes) having $k_\parallel = 0$. Thus, it appears - looking only at the energy - that the general behaviour of the $n\phi T_e$ model resembles that of the Hasegawa-Wakatani model to a very high degree.
The evolution of the turbulent fluxes is of particular interest in transport studies, and in Figure 5.4 the turbulent density flux, $\Gamma_n$, and the turbulent heat flux, $\Gamma_T$, are presented. There it may be seen that the correlation between $\Gamma_n$ and $\Gamma_T$ is quite high. This may be explained by the relatively high correlation of $n$ and $T$ (as it is presented in Figure 5.6.(c)) and the equal format of the expressions for the fluxes (5.26) and (5.27). The difference in amplitudes reflects mainly the difference in the steepness of the gradients expressed by $\frac{L_n}{L_T}$. This matter will be discussed further in Section 5.3.2.
In Figure 5.5 the spectral distribution of the energy is shown in $(k_\perp, k_\parallel)$–space at (a) $t = 40$ (during the exponential growth) and at (b) $t = 400$ (the

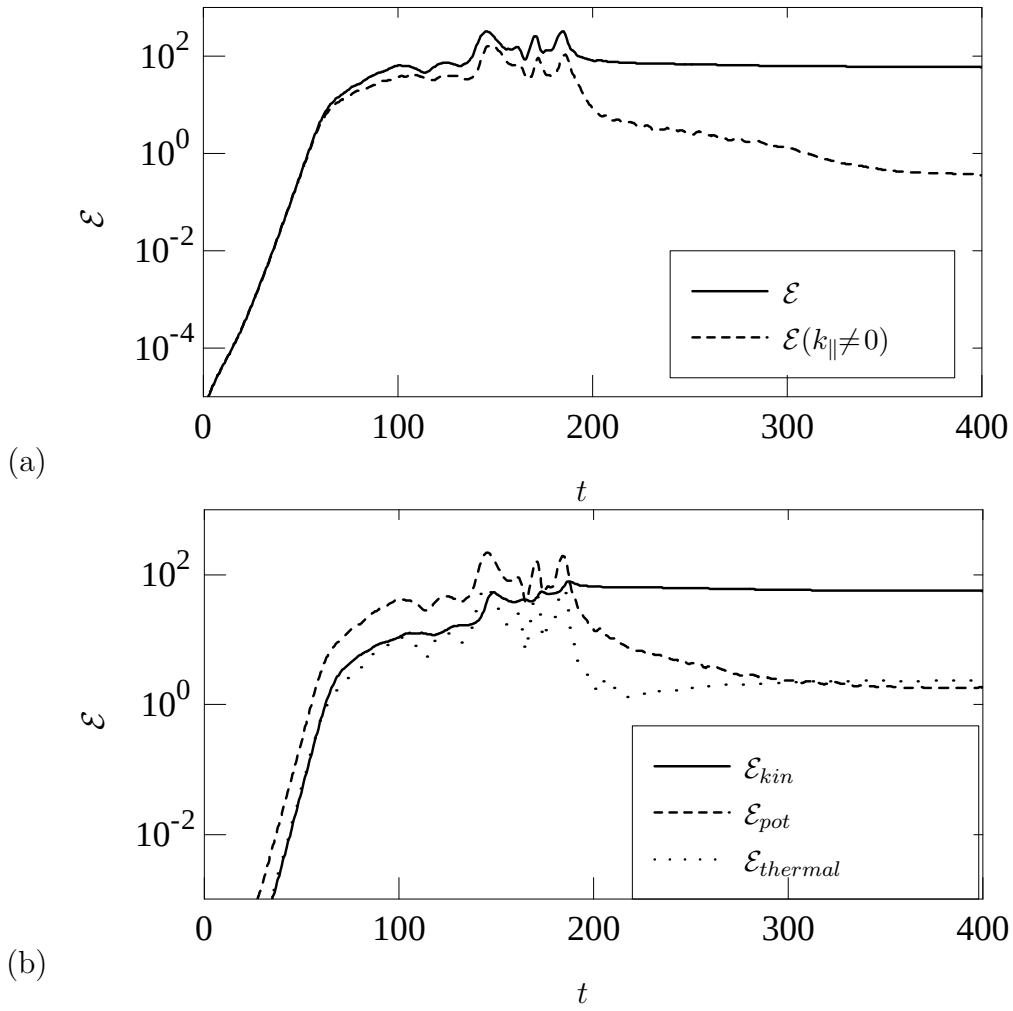


Figure 5.3: The temporal evolution of (a) the total energy $\mathcal{E}$, and the energy of the drift wave component $\mathcal{E}(k_\parallel \neq 0)$, and (b) the energy distributed on the kinetic, $\mathcal{E}_{kin}$, potential, $\mathcal{E}_{pot}$, and thermal energy, $\mathcal{E}_{thermal}$, components.

final state with a convective cell). One may compare Figure 5.5.(a) to that of the linear growth rate presented in Figure 5.1 taking into account that the initial conditions are scaled with $k^{-2}$.
The coupling and relation between $n$, $\phi$, and $T$ may become clearer by performing an analysis of the correlation of the fields. We have calculated the three-dimensional pointwise spatial correlations over the whole domain for the full fields, for the drift components of the fields ($k_\parallel \neq 0$), and for the convective cell modes of the fields ($k_\parallel = 0$). The analysis is presented in Figure 5.6 that shows the temporal evolution of the spatial correlation for zero time lag calculated as

$$\langle n\phi \rangle = \frac{\int n\phi \mathrm{d}\mathbf{r}}{\sqrt{\int n^2 \mathrm{d}\mathbf{r}} \sqrt{\int \phi^2 \mathrm{d}\mathbf{r}}}$$

Note that the correlation of $n$ and $\phi$ for the drift modes are relatively high,

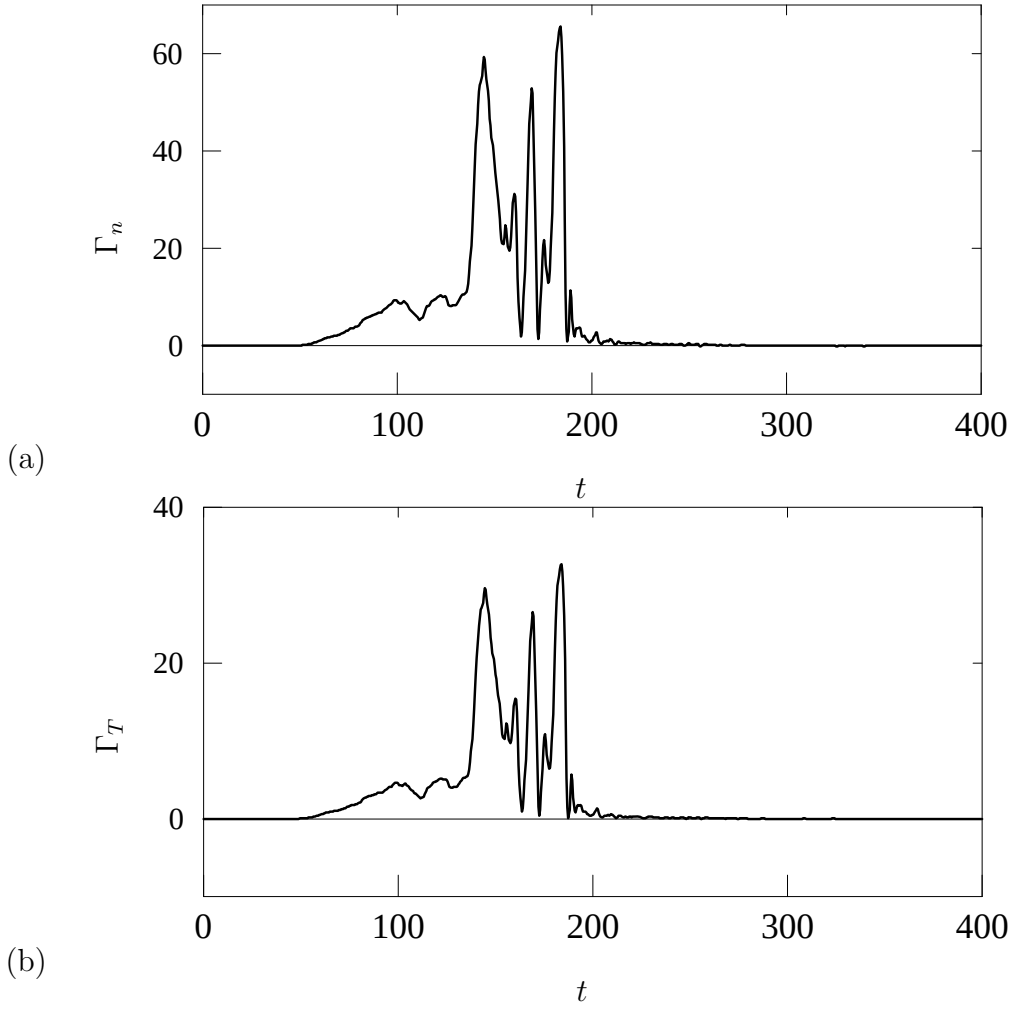


Figure 5.4: The temporal evolution of (a) the turbulent density flux, $\Gamma_n$, and (b) the turbulent heat flux, $\Gamma_T$.

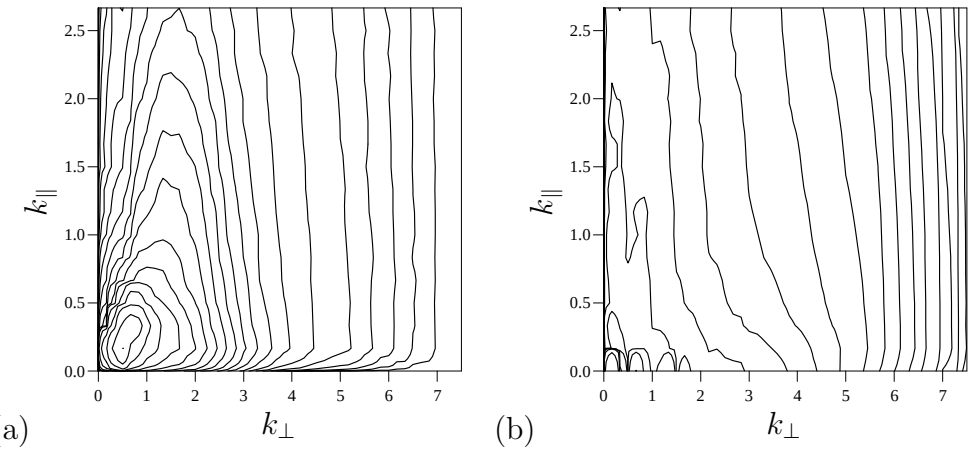


Figure 5.5: The energy power spectrum in $k_\perp, k_\parallel$–space. (a) $t = 40$ (exponential growth state), (b) $t = 400$ (convective cell dominated final state).

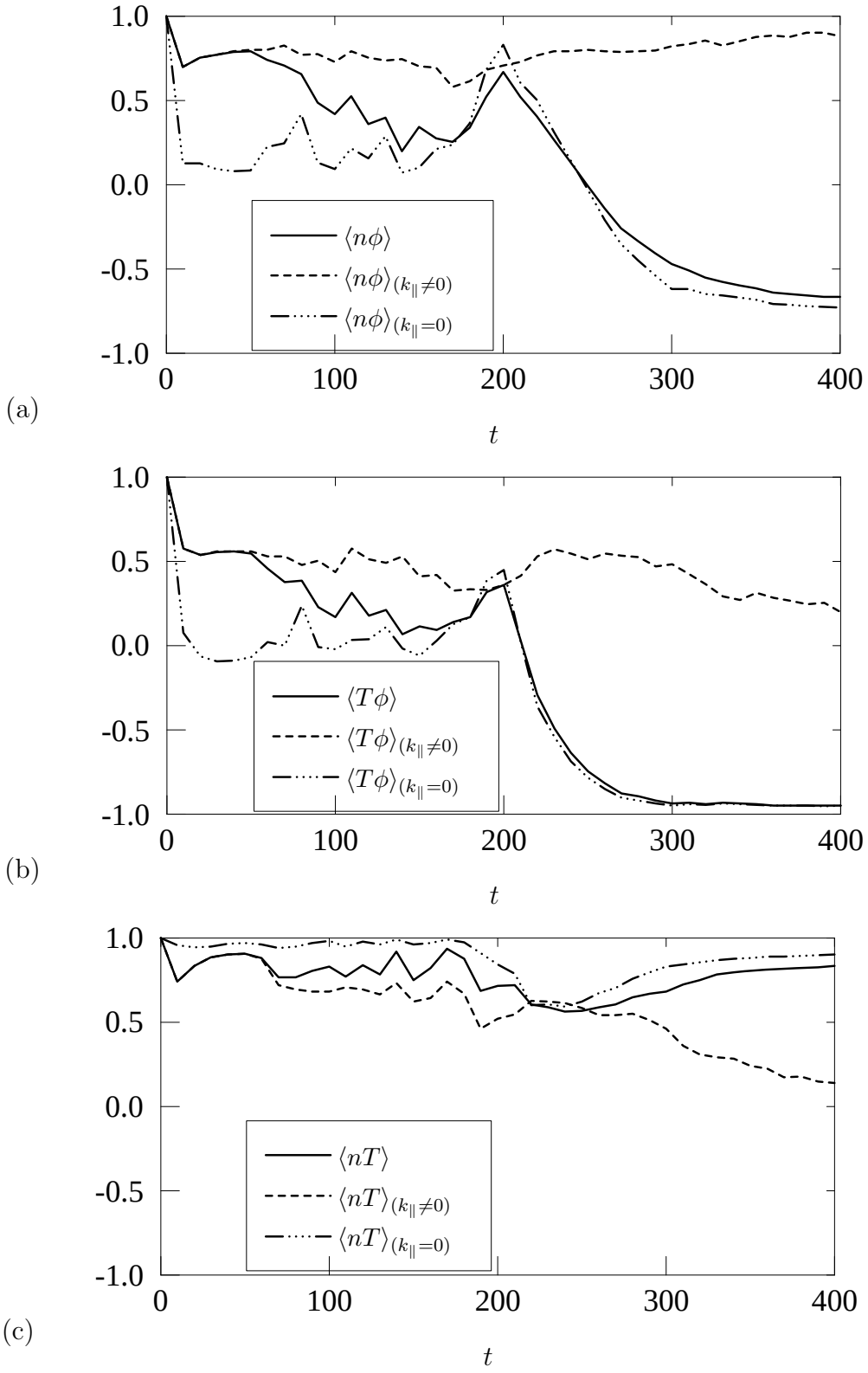


Figure 5.6: The temporal evolution of the three-dimensional spatial correlation for zero time lag of the fluctuations $n$, $\phi$ and $T$ in pairs (a) $n$ and $\phi$, (b) $T$ and $\phi$, and (c) $n$ and $T$. The correlation of the full fields as well as the drift ($k_\parallel \neq 0$), and convective cell components, ($k_\parallel = 0$).

whereas this is not the case for the drift modes of $n$ and $T$ oppositely to what one might have expected due to the common feature of the density and temperature being convected by the potential. On the contrary, one see a noteworthy strong correlation of the convective cell modes of $n$ and $T$, whereas the convective cell modes of $n$ and $T$, respectively, are nearly anti-correlated to those of $\phi$. Note again, as discussed in Chapter 3, that a phase difference of 90° of the fields would result in zero correlation in the plots above.
To shed a bit more light on the electron temperature dynamics the norms of the terms in the electron temperature equation are shown in Figure 5.7. It

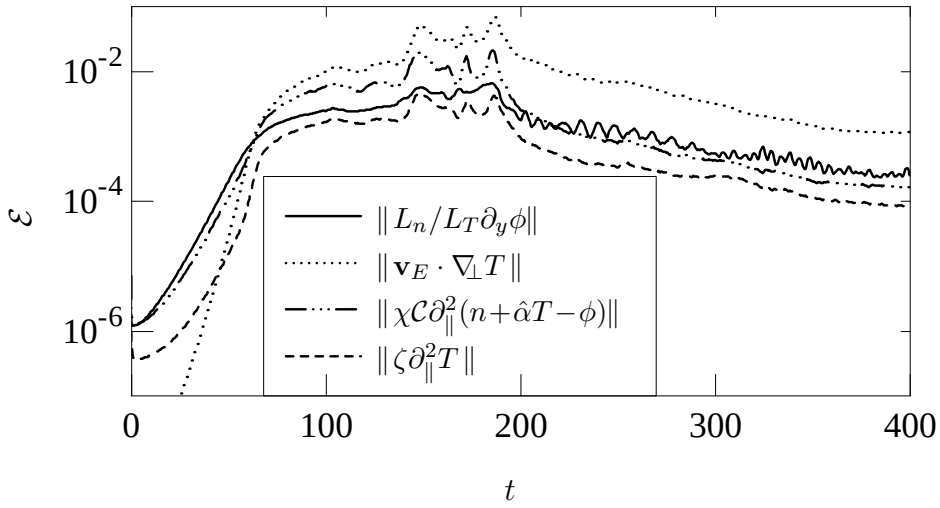


Figure 5.7: The norms of the terms in the electron temperature equation (5.19).

may be seen that the dominant term initially indeed is the temperature gradient term, which drives energy into the system. From $t \approx 60$ the nonlinear term is dominant, and we also note that during the most turbulent state the norm of the parallel coupling term, $\| \chi \mathcal{C} \partial_\parallel^2 (n + \hat{\alpha} T - \phi) \|$, is relatively high. This is an indication of the strong interaction between the drift waves of $n$, $\phi$, and $T$ in the turbulent regime.

### 5.3.2 Effect of variation of $\frac{L_n}{L_T}$

The particular feature of the $n\phi T_e$ model is - as described above - that it includes both potential, density, and temperature fluctuations as well as both a density and an electron temperature background gradient. The simulated transport of the system consists of both a turbulent density flux $\Gamma_n$ and a turbulent heat flux $\Gamma_T$. In this context, it seems relevant to study the dependence of the system - especially the transport fluxes - on the parameter $\frac{L_n}{L_T}$, which denotes the relative steepness of the temperature and density background gradients. Concerning this, a weakness of the model, as it is formulated in (5.18-5.20), is that the two gradients are bound together, so that, e.g., one cannot immediately switch off the density gradient and keep

the temperature gradient.
In the simulations we have varied $\frac{L_n}{L_T}$ over four different values: $0.1, 0.5, 1.0$, and 1.5, while keeping the other parameters constant at: 48 Fourier modes in each direction, a domain size of $L_x = L_y = L_z = 12\pi$, a time step of $\mathrm{d}t = 0.002$, $\zeta = 0.5$, a hyperviscosity of order $2p = 6$, and a viscosity parameter $\nu = 5 \cdot 10^{-4}$. The relatively high viscosity parameter was needed due to the limited number of Fourier modes.
The statistics of this investigation are based on 16 simulations: four series with the four $\frac{L_n}{L_T}$-values, where each series have a new set of random initial conditions. The initial conditions were $\phi = 0$, and $n = T$ being low level random noise with zero mean divided by $k^2$.
In Figures 5.8 and 5.9 we present plots of the evolution for the fluxes and energies for one of the four series. A clear tendency of the system is that the

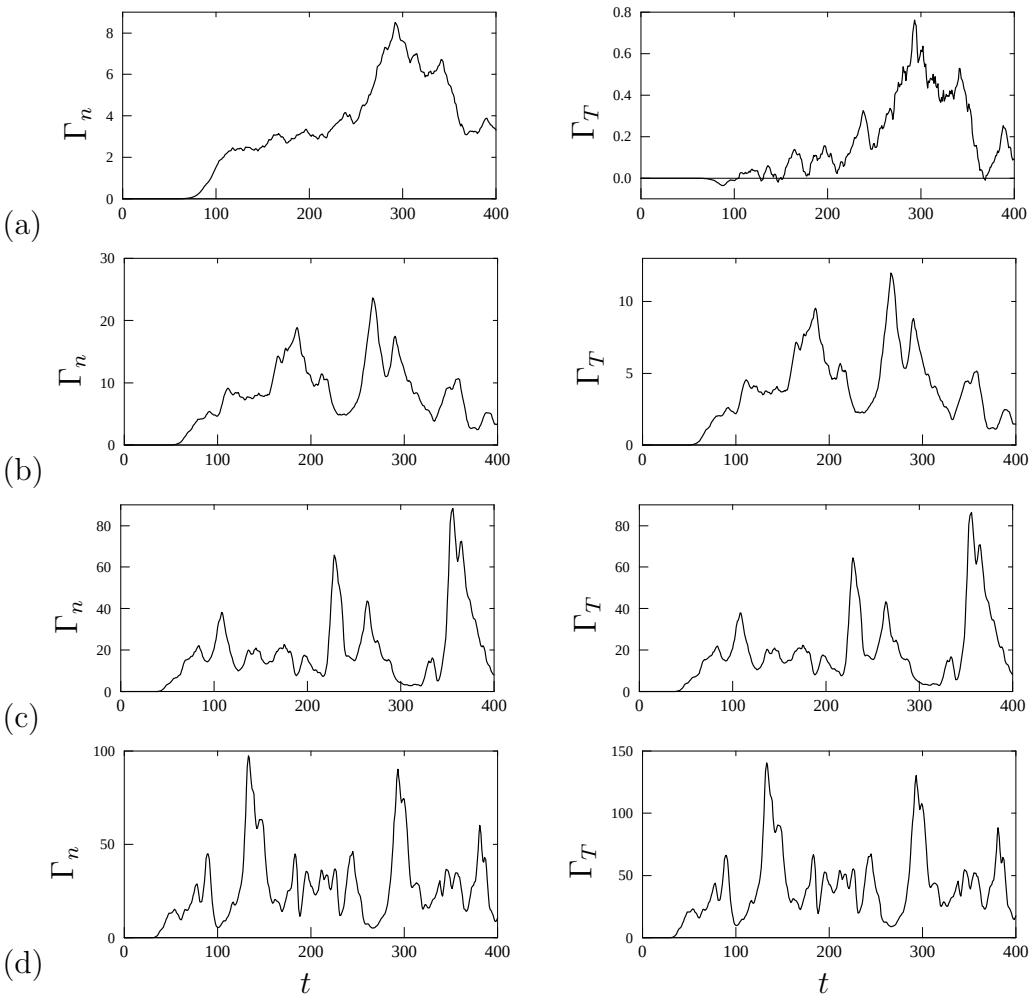


Figure 5.8: In the first column the turbulent density flux, $\Gamma_n$ is shown for increasing $\frac{L_n}{L_T}$ in each row: (a) 0.1, (b) 0.5, (c) 1.0, and (d) 1.5. In the second column we present the turbulent heat flux, $\Gamma_T$.

heat flux $\Gamma_T$ increases for increasing steepness of the temperature gradient, i.e. for increasing $\frac{L_n}{L_T}$ (see Figure 5.8). This may not be surprising, since the temperature drift wave fluctuations first extract their energy from the tem-

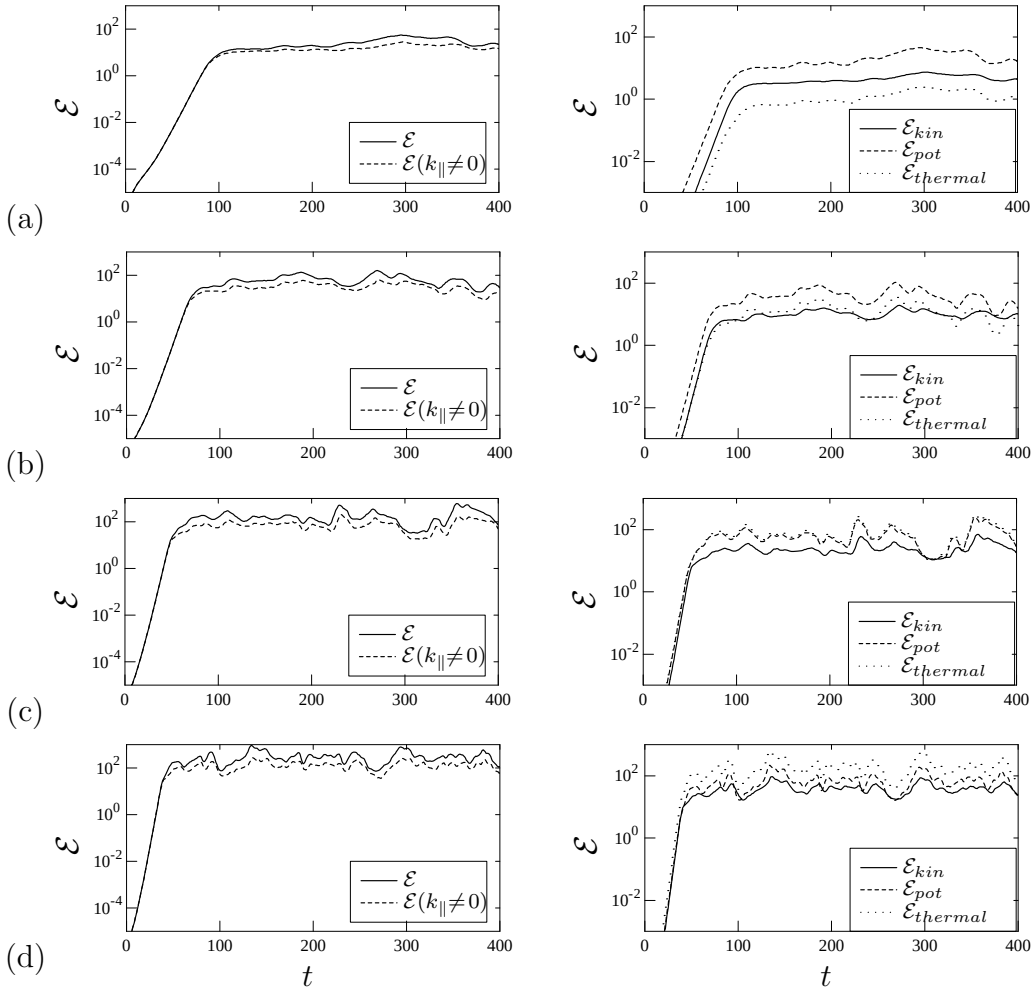


Figure 5.9: In the first column the total energy $\mathcal{E}$, and the energy of the drift wave component $\mathcal{E}(k_\parallel \neq 0)$ is shown for increasing $\frac{L_n}{L_T}$ in each row: (a) 0.1, (b) 0.5, (c) 1.0, and (d) 1.5. In the second column we present the energy distributed on the kinetic, $\mathcal{E}_{kin}$, potential, $\mathcal{E}_{pot}$, and thermal energy, $\mathcal{E}_{thermal}$, components.

perature gradient. On the other hand, it is also observed that the turbulent density flux $\Gamma_n$ is increased for increasing $\frac{L_n}{L_T}$ up to $\frac{L_n}{L_T} \approx 1.0$, where after the increase is less pronounced. The reason for the increase in the density flux is that the system contains more energy when the temperature gradient steepens and the density gradient is kept constant. The increase in total energy for increasing $\frac{L_n}{L_T}$ can also be seen in Figure 5.9. Observe furthermore that the correlation between $\Gamma_T$ and $\Gamma_n$ increases as $\frac{L_n}{L_T}$ is raised from 0.1 to 0.5. One may define an energy flux, i.e. the flow of heat carried by particles:

$$\Gamma_E = \frac{L_n}{L_T} \iiint -nT \frac{\partial \phi}{\partial y} \,\mathrm{d}x\,\mathrm{d}y\,\mathrm{d}z = \frac{L_n}{L_T} \iiint nT v_{E,x} \,\mathrm{d}x\,\mathrm{d}y\,\mathrm{d}z \tag{5.28}$$

which to first order may be written as [49]:

$$\Gamma_E = T_0 \Gamma_n + n_0 \Gamma_T \tag{5.29}$$

Within the ordering, $n_0$ and $T_0$ are of order unity, and we may approximate the energy flux by just adding the heat and density fluxes. Performing this operation further underlines the finding above that as the relative steepness of the temperature gradient increases, the system contains more energy, resulting in increased $\Gamma_n$, $\Gamma_T$ and also $\Gamma_E$ .
In consistence with the findings of Section 5.2.1 the exponential growth of the energy (due to the linear instability) is faster for increasing $\frac{L_n}{L_T}$ as seen in Figure 5.9, where we reveal the evolution of the energy for the four simulations presented in Figure 5.8.
In Figure 5.9 we also present the evolution of the kinetic, potential and thermal energy components. Not surprisingly, the thermal energy component increases with increasing $\frac{L_n}{L_T}$ - both in absolute and relative size. Interestingly, the thermal energy slightly exceeds the potential energy for $\frac{L_n}{L_T} = 1.0$, i.e. for the temperature and density gradients having equal slope.
A characteristic for most of the 16 simulations was that for the chosen parameters the system did not enter the quiet state dominated by convective cell modes before the simulations were stopped. However, it seems that the tendency of the system to transfer the energy into the convective cell modes is increased by increasing the steepness of the temperature gradient. This effect is seen in two of the four series (not including the one presented in Figures 5.8 and 5.9). We have no immediate explanation for this, since the increased temperature gradient first drives more drift waves in $T$, which is closely correlated to $n$ (see Section 5.3.1). The latter generally cascades energy towards higher wavenumbers [28], and this effect would thus not explain the observed feature. Naturally, the fluctuations in $T$ also couple to those in $\phi$ and in turn energy is cascaded to lower wavenumbers. However, this coupling is an effect of the complex nonlinear dynamics of the system, and it is not clear how the change of $\frac{L_n}{L_T}$ does affect the coupling between $T$ and $\phi$. United with the fact that the feature is only observed in two of four simulations, we must state that the observed dependency on $\frac{L_n}{L_T}$ may just be coincidental.
Conclusively, it may be stated that - as expected - the relative steepness of the temperature gradient to the density gradient has an effect on the quantitative measures of the whole system, and this is not only for the quantities tightly connected to the temperature fluctuations. This underlines the significance of including both temperature and density gradients when evaluating the turbulent transport of a given system influenced by drift waves.

## 5.4 Evaluation of the model

The evolution of the turbulence of the proposed model resembles that of the Hasegawa-Wakatani model, to a certain extent. This is mainly due to the temperature fluctuations being passively advected by the potential in the nonlinear turbulent state, analogous to the advection of the density. Hence the behaviour of $T$ is similar to that of $n$, although we found in Figure 5.6.(c) that the correlation of the drift components of $n$ and $T$ was particularly low.

Furthermore, we showed that temperature effects are important for the total transport quantities.
The combined effect of a density and an electron temperature gradient may be further investigated in the $n\phi T_e$ model, as well as correlations between $n$, $\phi$, and $T$ fluctuations, and the effect on the density, heat and energy transport fluxes. Thus the model is interesting to investigate. Additional simulations with the $n\phi T_e$ model could still be done to obtain better statistics, and finally, one should in future simulations investigate geometric effects.

# Chapter 6

# The Hasegawa-Wakatani model in a non-periodic geometry

This chapter contains a presentation of a wide variety of results obtained by simulations of the Hasegawa-Wakatani model in a non-periodic geometry. As we saw in Chapter 3, the use of a triply periodic geometry may cause the Hasegawa-Wakatani system to evolve into a final state that invalidates some of the underlying assumptions. Furthermore, the use of periodic boundary conditions may not be valid in most configurations, especially in the radial direction. Therefore, the simulation domain used in this chapter is non-periodic in the radial direction while still periodic in the $y$- and $z$-direction. This geometry also enable us to study the back-reaction of the fluctuations on the background density profile which is spatially fixed in the non-periodic geometry. The geometry and the back-reaction will be described and discussed in Section 6.1, and general results of the simulations will be presented in Section 6.2.

The use of a non-periodic geometry further enable us to study shear flow generation and the influence of this on turbulent transport etc. As written in Chapter 2 the generation mechanisms and the effects of shear flows are of great interest in relation to improvement of turbulent transport mitigation. In Section 6.3 we study the so-called Reynolds stress and the possibility to predict shear flow generation. We further explore an alternative method to estimate the Reynolds stress, and investigate the validity range of this quantity, which we term the pseudo-Reynolds stress. Finally, we look at the implications of misaligned probe arrays on the simulated experimental determination of Reynolds stresses.

In the last part of the chapter, Section 6.4, we investigate the performance of the system in a number of special cases, among these the case where we apply a constant external shear flow.

The contents of this chapter have in part been described in [50–52].

## 6.1 The non-periodic geometry

We still use the standard Hasegawa-Wakatani equations (3.23) and (3.24) with the background density of the form $n_0 = n_0(x) = N_0 \exp\{-x/L_n\}$. In the simulations presented in this chapter we do not use hyperviscosity, but we have added a kinematic viscosity/dissipation term (i.e. $2p = 2$) in each of the equations. In normalised dimensionless variables the equations appear as:

$$(\frac{\partial}{\partial t} + \mathbf{v}_E \cdot \nabla_\perp)n + \frac{\partial \phi}{\partial y} = \mathcal{C}\frac{\partial^2}{\partial z^2}(n - \phi) + \nu\nabla_\perp^2 n \tag{6.1}$$

$$(\frac{\partial}{\partial t} + \mathbf{v}_E \cdot \nabla_\perp)(\nabla_\perp^2\phi) = \mathcal{C}\frac{\partial^2}{\partial z^2}(n - \phi) + \nu\nabla_\perp^4\phi \tag{6.2}$$

It is necessary to use a two field, three-dimensional drift wave model to obtain the full interaction between the flow and the drift waves, since the dynamics are different for the flow components ($k_\parallel = 0$) and the drift waves ($k_\parallel \neq 0$). It is easy to check that for $k_\parallel = 0$ the equations decouple, and the vorticity equation (6.2) reduces to an Euler-type equation. Thus, the one-field model assumption of $\frac{n_1}{n_0} \sim \frac{e\phi}{T_e}$ - like that of Hasegawa-Mima - does not hold for the background flow. Finally, the Hasegawa-Wakatani model retains all parts of the $\mathbf{v}_E \cdot \nabla_\perp n$ term which is responsible for saturation of the turbulence as described in [53]. The Hasegawa-Wakatani equations thus include most of the dynamics important for the interaction between flow and turbulence, which makes it suitable for the present investigations.

In the Hasegawa-Wakatani model fluctuations and background can be evaluated simultaneously as the background and the fluctuations are separated, but the interaction between them is included. As discussed in Chapter 3 the constant background density gradient enters (6.1) via the $\frac{\partial \phi}{\partial y}$-term, since the second and third term at the left hand side of (6.1) is derived from $\mathbf{v}_E \cdot \nabla_\perp(n + n_0) = \mathbf{v}_E \cdot \nabla_\perp n + \frac{\partial \phi}{\partial y}$, when $n_0(x) = N_0 \exp\{-x/L_n\}$ is substituted (see Section 3.1.5). The average part of $n$ should contribute to the total density gradient. This back-reaction of the density fluctuations on the background density gradient, however, is not recoverable in previous Hasegawa-Wakatani simulations, due to the use of periodic geometries (see, e.g., [28, 30]).

In the present simulations we use a slab geometry - periodic in $y$ and $z$ (corresponding to the poloidal and toroidal directions, respectively), and with non-permeable walls in the radial direction, i.e. Dirichlet boundaries in $x$ ($\phi(x = 0) = \phi(x = L_x) = 0$ and $n(x = 0) = n(x = L_x) = 0$). This enables the back-reaction on the background density gradient from the density fluctuations. Factually, the system we are looking at will finally be, after the total gradient has adjusted itself, driven by the diffusive fluxes through the walls. Note that any three-dimensional system with Dirichlet boundary conditions on the density fluctuations will in the quasi-stationary saturated state be of the so-called "flux-driven" type (as opposed to "gradient-driven", where the background gradient is maintained constant artificially) [54, 55].

The density is normalised by a background density $n_{00}$, independent of $x$,

which can be seen as a pedestal density. Therefore, when $n_{00}$ is not added one may obtain negative densities as it is seen in Figure 6.5. The effective variation of the density gradient in the $x$-direction is $n_0(x) + \langle n \rangle_{y,z}(x)$, where $n_0$ is presented above and $\langle n \rangle_{y,z}$ is the averaged part of the fluctuations $n(x, y, z)$. $\langle \rangle_{y,z}$ denotes averaging over $y$ and $z$, i.e. $\langle f \rangle = \langle f \rangle_{y,z} = (L_y L_z)^{-1} \int f \mathrm{d}y \mathrm{d}z$. The variation of $n_0(x) + \langle n \rangle(x)$ can be large in amplitude, but varies only on large scales ($\nabla(n_0(x) + \langle n \rangle(x))$ is small). The fluctuations, however, are small but may have steep gradients, i.e. be fine-scaled in agreement with the drift scaling.
The simulations were performed by Fourier spectral methods using only sine transforms in the $x$-direction, since these, intrinsically, are zero at $x = 0$ and $x = L_x$, when $k_{x,min} = 2\pi/L_x$.

## 6.2 The evolution of the system

In this section we will present results from several simulations. However, the simulation primarily used is a finely resolved simulation with the following parameters: The number of modes is 256 in the perpendicular directions ($x$ and $y$) and 32 in the direction parallel to the magnetic field. The domain size is $L_x = L_y = 30$ and $L_z = 20$, and the time step $\mathrm{d}t = 3 \cdot 10^{-3}$. A viscosity parameter $\nu = 0.1$ was necessary for this number of modes to prevent the accumulation of energy in the short wavelengths. If nothing else is stated, this is the parameters used in the following.
In the simulations with Dirichlet boundary conditions the energy given via $\mathcal{E} \equiv \frac{1}{2} \int [(\nabla_\perp \phi)^2 + n^2] \, \mathrm{d}x \mathrm{d}y \mathrm{d}z$ does not grow to as high levels as for the case of triply periodic boundaries of, e.g., Chapter 3 or in [30]. In order to illustrate the difference between the Dirichlet and periodic domain simulations, we present in Figure 6.1 the evolution of the energy for two simulations with the same parameters being: $m = n = 64$, $o = 32$, $L_x = L_y = 30$, $L_z = 20$, $\mathrm{d}t = 4 \cdot 10^{-3}$, and the viscosity coefficient $\nu = 0.03$. The temporal evolutions

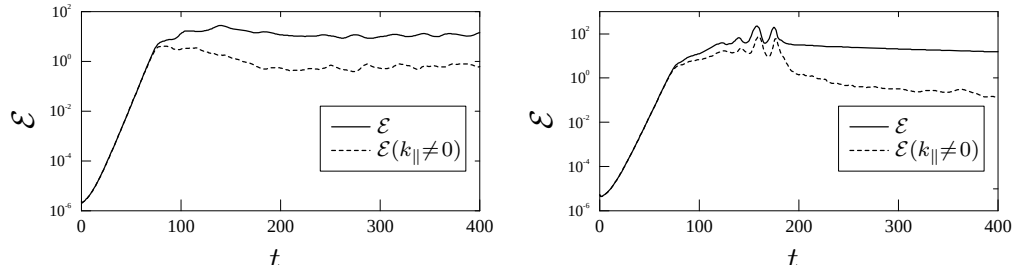


(a) Dirichlet case/Bounded domain (b) Triply periodic domain

Figure 6.1: The temporal evolution of the total energy $\mathcal{E}$ and the drift wave energy $\mathcal{E}(k_\parallel \neq 0)$ for two different geometries.

of the total energy and the energy of the drift modes ($k_\parallel \neq 0$) are presented in Figure 6.2 for the finely resolved simulation. The reduced maximum level also applies to the turbulent flux, which we present in Figure 6.3. In the

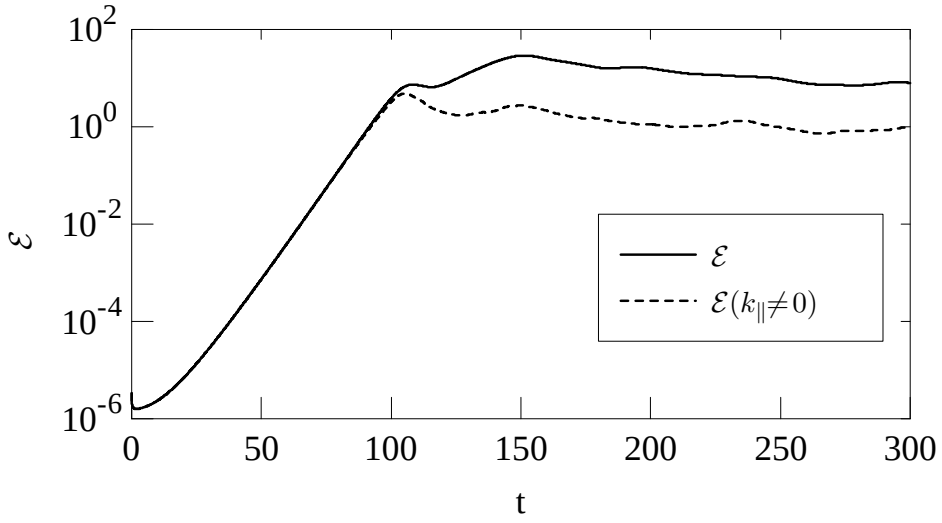


Figure 6.2: The temporal evolution of the total energy, $\mathcal{E}$, (full line), and the drift wave energy, $\mathcal{E}(k_\parallel \neq 0)$, (dashed line) for the Hasegawa-Wakatani model in a slab geometry with non-permeable walls in the radial direction.

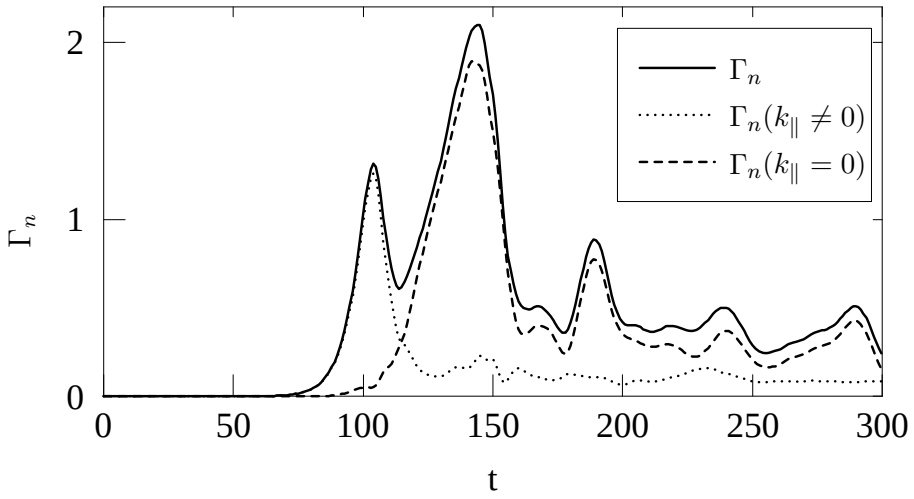


Figure 6.3: The temporal evolution of the turbulent flux, $\Gamma_n$, (full line), the drift wave component, $\Gamma_n(k_\parallel \neq 0)$, (dotted line), and the convective cell/flute mode component, $\Gamma_n(k_\parallel = 0)$, (dashed line) for the Hasegawa-Wakatani model in a slab geometry with non-permeable walls in the radial direction.

figure we plot the total turbulent flux, as well as the components of the flux having $k_\parallel \neq 0$ (the drift modes) and $k_\parallel = 0$ (the flute modes). It is seen that the drift component is almost the sole contributor to the turbulent flux when it starts to rise from $t \approx 75$. As the amplitudes of the normalised $\phi$ and $n$ approach unity, nonlinear effects start being important. Via nonlinear mode coupling (as described in, e.g., [22]) the energy is distributed over the whole mode space. Some rules of spectral transfer exist, however, and as described in [28] the potential exert an inverse cascade of energy from the drift modes

into the flute modes. Results of this transfer may actually be seen in Figure 6.3, where the $\Gamma_n(k_\parallel = 0)$ is rising from $t \approx 100$ as $\Gamma_n(k_\parallel \neq 0)$ is falling. It turn out that from $t \approx 120$ and onwards the main part of the turbulent flux is carried by convective cells. We should, additionally, note that before the $\Gamma_n(k_\parallel = 0)$ take over from $\Gamma_n(k_\parallel \neq 0)$ the total flux is decreased significantly. This tells us that the primary process immediately after the transition from the linear to the nonlinear state is that of distributing the energy from the linearly unstable modes over the whole mode space via nonlinear coupling, whereas the inverse cascade of energy into convective cells follows afterwards. The reason for the observed reduced growth of energy, flux, and fluctuation amplitude, is the back-reaction of the density fluctuations on the background density. The fluctuations organise to flatten the background profile, and the effective background density gradient is decreased. Consequently, the drive of the turbulence is quenched. Mathematically, the $\frac{\partial \phi}{\partial y}$-term in equation (6.1) originates from the convection of the background profile, and the back-reaction of the fluctuations on this is through the nonlinear convection term, where a $\frac{\partial n}{\partial x}\frac{\partial \phi}{\partial y}$-term occurs. As density and potential are closely coupled in the Hasegawa-Wakatani model to lowest order, the large scale variations in $n$ correspond to similar variations in $\phi$ leading to a sheared poloidal flow. Thus, the small-scale plasma turbulence organises into a poloidal shear flow having $k_y = 0$, hence the effect of the drive of the drift wave turbulence, the $\frac{\partial \phi}{\partial y}$-term, vanishes (see also [30]). The evolution of the total energy in two of the components of the flow is shown in Figure 6.4.

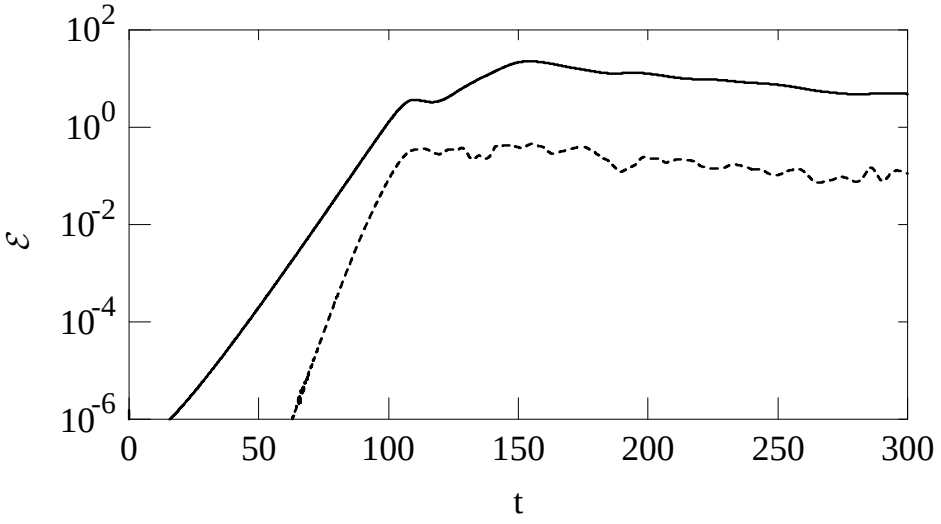


Figure 6.4: The temporal evolution of the energy in the background flow $\mathcal{E}(k_y = 0, k_\parallel = 0)$ (full line), and the zonal flow component of the drift waves: $\mathcal{E}(k_y = 0, k_\parallel \neq 0)$ (dashed line).

As the shear flow builds up, the effective gradient is decreasing in the main part of the profile and the fluctuation levels decrease. An exception is near the boundaries where steep gradients form due to the boundary conditions. The $yz$-averaged contribution of the fluctuations to the fixed background density appear in Figure 6.5, in which the effective total density gradient,

$n_0(x) + \langle n \rangle_{y,z}(x)$, and the variation of the constant background density gradient, $n_0$, are plotted. In this state the system is relatively quiescent and the

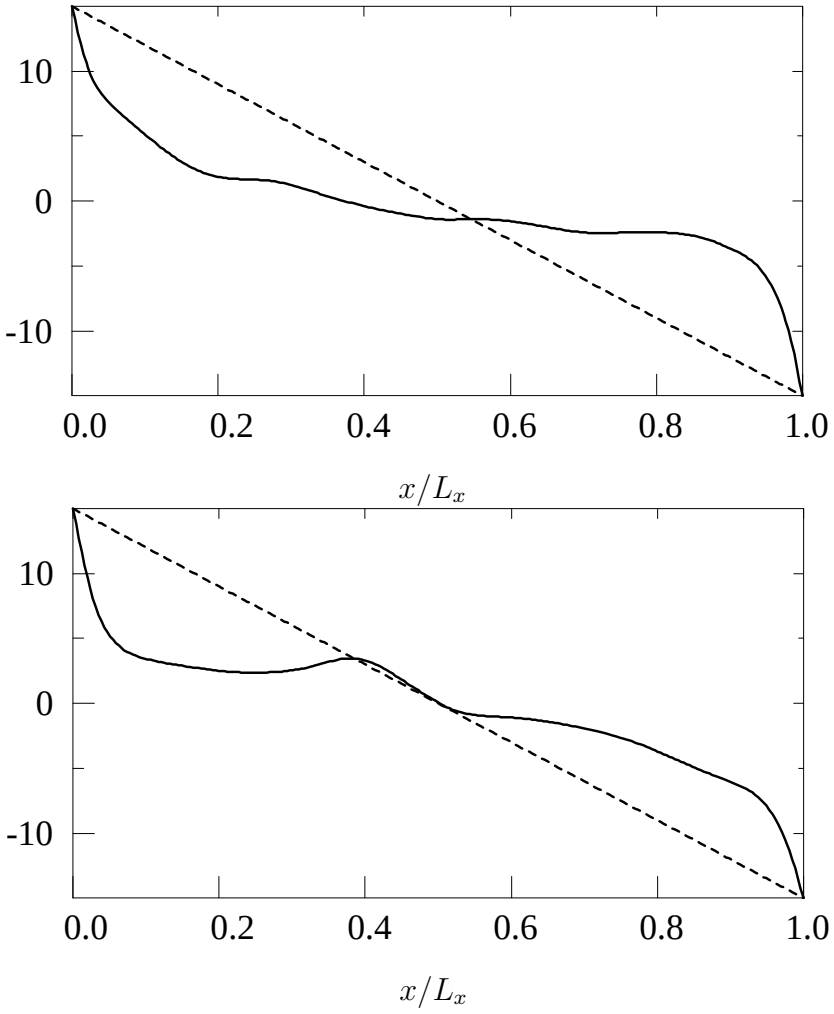


Figure 6.5: The radial profile of the constant background density gradient $n_0$ (dashed line), and the effective density gradient $n_0 + \langle n \rangle$ (full line) at the times (a) $t = 175$ and (b) $t = 200$. From the figure it may seem that negative background densities are used. This, however, is not the case in the model, and one may add a pedestal value of the density $n_{00}$.

main dynamics of the system is that the amplitude of the fluctuation-induced average profile is reduced by viscosity, which in turn leads to a build-up of the density gradient. Another view is that a diffusive in-flux at the high density side broadens the locally steep gradient of the combined background and mean fluctuation density. This flux is due to the $\nu\nabla_\perp^2 n$–term, and would normally be transported by the turbulence through the system along the radial profile. However, since the turbulent transport in this state is very low, the diffusive in-flux (at $x = 0$) causes the broadening of the locally steep gradient. The same effect occurs at the low density side (at $x = L_x$) except for this being an out-flux. Thus the global gradient is build up again, high amplitude fluctuations build up, and the radial flux increases until a poloidal

flow is generated again. The resulting behaviour of the system is one of separated flux bursts.
To illustrate the reoccurring flux burst behaviour of the system, we have performed simulations long enough to contain several periods of the system being quiescent, followed by a build-up of the global gradient, and reoccurrence of turbulent flux bursts. In order to limit the computation time for these simulations the resolution had to be kept quite low with the following parameters: $m = n = 32$, $o = 32$, $L_x = L_y = 25$, $L_z = 20$, $\mathrm{d}t = 4 \cdot 10^{-3}$, and a viscosity coefficient $\nu = 0.1$. The energy as a function of time is presented in Figure 6.6 and the turbulent flux in Figure 6.7. In Figure 6.8, the temporal

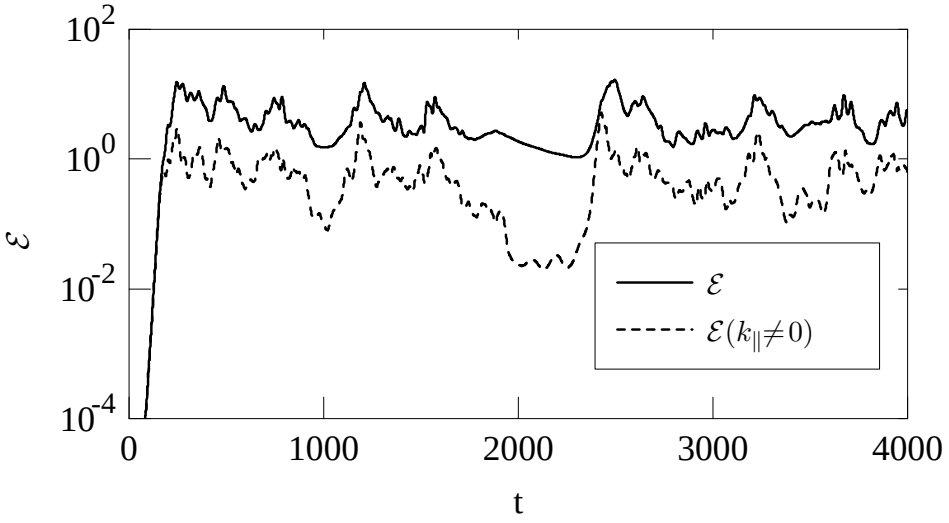


Figure 6.6: The evolution of the energy $\mathcal{E}$ for a long simulation in the non-periodic geometry.

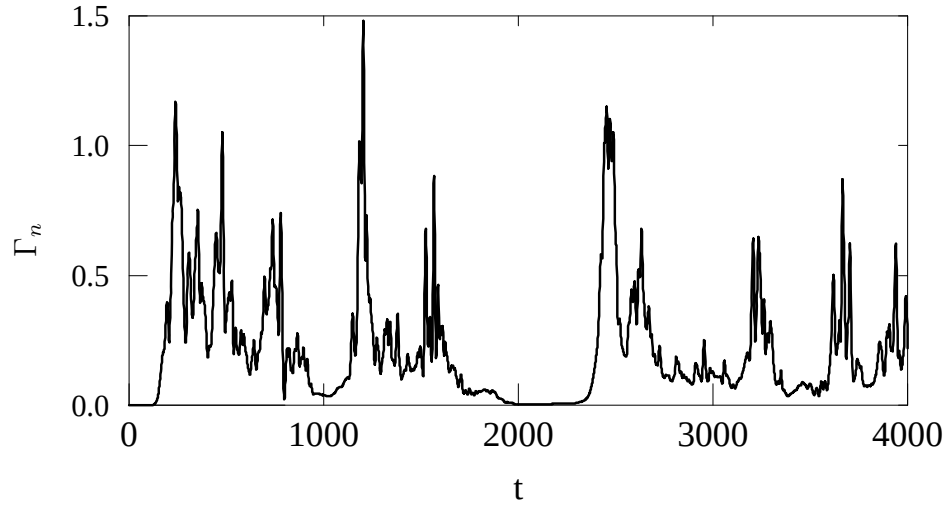


Figure 6.7: The evolution of the flux $\Gamma_n$ for a long simulation in the non-periodic geometry.

evolution of the maximum and minimum values of the density and potential

perturbations are presented. It is clear from these figures that the nature of

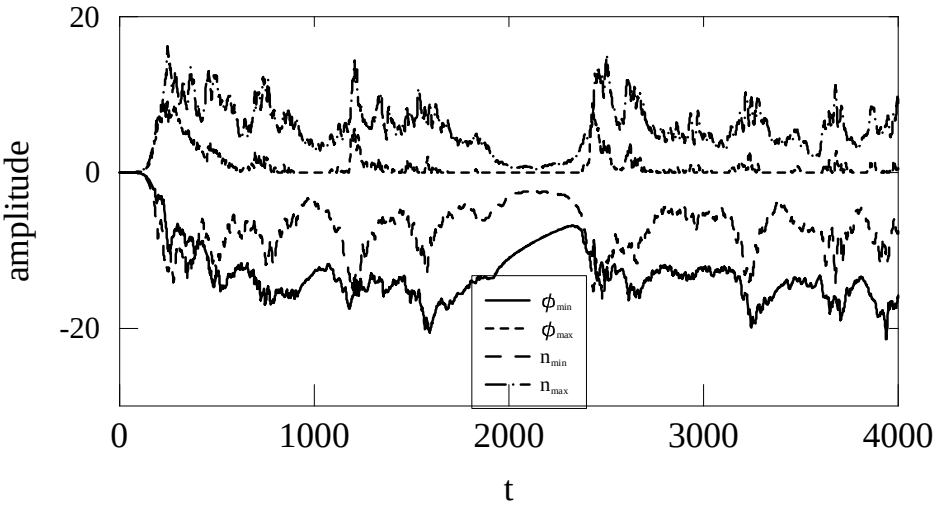


Figure 6.8: The evolution of the maximum and minimum values of the density and potential perturbations.

the fluctuations is very intermittent, and that the differences in amplitudes are significant from the quiescent to the turbulent periods.The duration of the rebuilding of the background gradient is expected to be dependent on the viscosity parameter $\nu$, in accordance with the explanation of the intermittent behaviour given above. Thus we have varied $\nu$ in a number of long simulations as the one above, and the results of this investigation have been gathered in Section 6.4.3.
The importance of the shear flow in limiting transport may be seen by comparing the turbulent flux to the maximum shearing rate of the poloidal flow, $\max\left(\frac{\partial v_y}{\partial x}\right)$. These are plotted in Figure 6.9, where it may be seen that as the shearing rate increases the turbulent flux is reduced and vice versa.
We may also see the importance of the shear flow from Figure 6.5.(b), where we see two regions with rapid transport (almost flat density profiles) separated by a transport barrier. In Figure 6.10.(a) we look at the poloidal flow profile superimposed the average profile of the density fluctuations. In Figure 6.10.(b) and (d) we present the root-mean-squared values of the fluctuations in $n$, and of the radial velocity, $v_r$, respectively. The latter determines in part the turbulent transport. From the figure we learn that the shearing rate of the shear flow is strong at the location of the transport barrier, and that the level of the density fluctuations and of the radial velocity are lowest in the region of the barrier. However, if we turn to Figure 6.10.(c) we may see that the radial profile of the potential fluctuations, $\phi$, has a maximum around the transport barrier. This $\phi$ also include the flute and shear flow modes and the location of the maximum of $\phi$ is thus not surprising.
The profiles as they occur in Figures 6.5 and 6.10 may be explained by the following heuristic arguments: The potential vorticity, $PV$, defined in Chapter 3, for a fluid element is conserved, and for the Hasegawa-Wakatani model

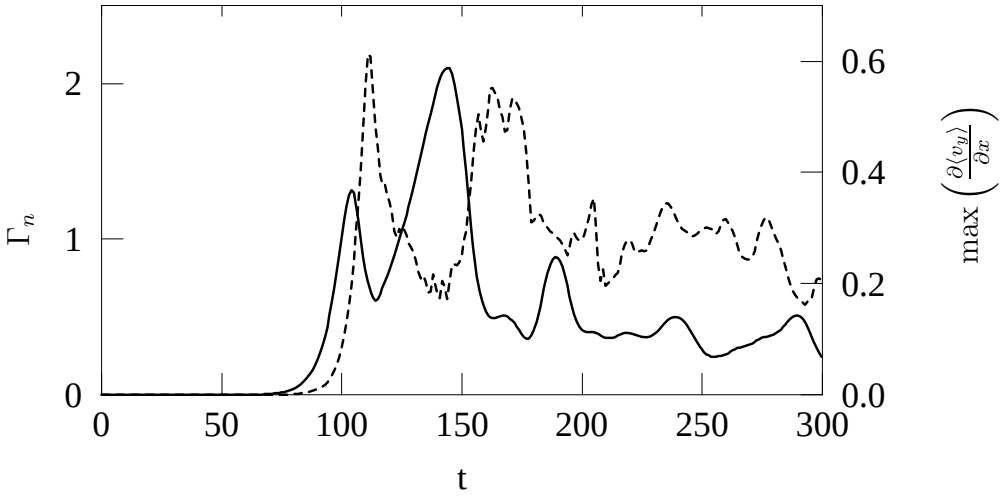


Figure 6.9: The temporal evolution of the turbulent flux $\Gamma_n = -\int n\frac{\partial\phi}{\partial y}\mathrm{d}\mathbf{x}$ (full line) and the maximum shearing rate $\max\left(\frac{\partial\langle v_y\rangle}{\partial x}\right)$ (dashed line).

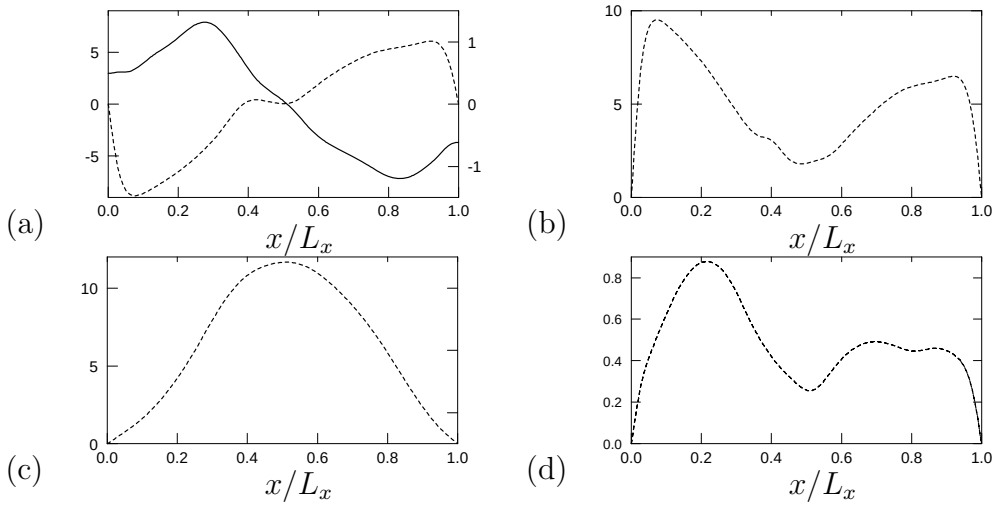


Figure 6.10: The radial profiles at time $t = 200$ of: (a) the poloidal velocity, $v_y$ (full line), and the mean of the density fluctuations, $\langle n\rangle$ (dashed line), (b) the root-mean-square of the density fluctuations, (c) the averaged profile of the potential fluctuations, $\langle\phi\rangle$, and (d) the root-mean-square of the radial velocity $v_r$.

this leads to (using (3.25)):

$$\frac{\mathrm{D}PV}{\mathrm{D}t} = 0 \quad \Rightarrow \quad \frac{\mathrm{D}(\nabla_\perp^2\phi - n + x)}{\mathrm{D}t} = 0$$

In a turbulent state with sufficient turbulent mixing invariants like the potential vorticity will be evenly distributed over the whole domain [56]. Assume for the moment that $n$ is distributing itself fastest: It will then fulfill $\langle n\rangle \propto x$, leading to the flat total density profile we see in Figure 6.5.(a). For the potential vorticity to be constant and evenly distributed $\phi$ has to fulfill: $\nabla_\perp^2\phi = constant \Rightarrow \phi \propto x^2$, which we see is the case in Figure 6.10.(c)

(this is also approximately the case at $t = 175$). This profile of $\phi$ leads to a poloidal shear flow, which suppresses the turbulence. This, in turn, causes the turbulent mixing to be insufficient to maintain $\frac{\mathrm{D}PV}{\mathrm{D}t} = 0$ for the domain, and thus the (partial) rebuilding of the gradient starts.
We assumed that $n$ is acting faster than $\phi$, and now we test if that is a fair assumption. By averaging the model equations (6.1) and (6.2) over $y$ and $z$ we obtain (except for the viscosity terms):

$$\frac{\partial \langle n \rangle}{\partial t} = -\frac{\partial \langle n v_x \rangle}{\partial x}$$

$$\frac{\partial \langle v_y \rangle}{\partial t} = -\frac{\partial \langle v_y v_x \rangle}{\partial x}$$

where the right hand side of the first expression is recognised as the derivative of the turbulent flux, and analogous to that one may call $\langle v_y v_x \rangle$ a momentum flux. In the following section the momentum flux will appear to be the so-called Reynolds stress. Assuming a local dispersion relation for the drift waves, $n$ is proportional to $\phi$ with a phase change, and it can be found that $\langle n v_x \rangle$ may be non-zero for three-wave-interactions. Similarly, it appears that four-wave-interactions are necessary for $\langle v_y v_x \rangle$ to be non-zero [57, 58]. Thus $\langle n v_x \rangle$ may be expected to be of lower order than $\langle v_y v_x \rangle$, and hence it follows from the expressions above that it is plausible that $n$ acts faster than $\phi$. Furthermore, by comparing Figures 6.3 and 6.12 presenting $\langle n v_x \rangle$ and $\langle v_y v_x \rangle$, respectively, we may get an idea of the order of the terms. This comparison further supports the assumption of $\frac{\partial \langle n \rangle}{\partial t} > \frac{\partial \langle v_y \rangle}{\partial t}$ since $\langle n v_x \rangle$ is generally an order of magnitude larger than $\langle v_y v_x \rangle$. Additionally, we see in Figure 6.9 that $\Gamma_n \sim \langle n v_x \rangle$ rise before $\frac{\partial v_y}{\partial x}$.
The explanation above is only hand-waving arguments, but it appears to be able to self-consistently explain the observed behaviour of the Hasegawa-Wakatani system in a domain with radial Dirichlet boundary conditions.

## 6.3 The Reynolds stress and shear flow generation

Diamond and Kim [59] presented a first theoretical approach to self-consistent flow generation in turbulent plasmas by small-scale turbulent fluctuations via the (electrostatic) Reynolds stress, which is defined as $R_\phi = R_\phi(x) = -\langle v_x v_y \rangle_{y,z} = B_0^{-2} \langle \partial\phi/\partial y \;\; \partial\phi/\partial x \rangle_{y,z}$, where $v_x$ and $v_y$ are the $x$- and $y$-components (radial and poloidal directions, respectively) of the $\mathbf{E} \times \mathbf{B}$–velocity. Measurements of the Reynolds stress can thus help to predict flows, e.g., shear flows in plasmas as demonstrated in [60,61]. In the latter reference it is found that the turbulence induced electrostatic Reynolds stress qualitatively accounts for the generation of a sheared poloidal flow. However, the determination of the Reynolds stress requires accurate measurements of the plasma potential $\phi$, a task that is difficult in general and nearly impossible in hot plasmas in large devices [60, 62].

Therefore, in Section 6.3.2 we look at an alternative way of estimating the Reynolds stress via the density fluctuations [63] (see also [64]), and we investigate the validity range of this quantity, which we term the pseudo-Reynolds stress. The advantage of such a quantity is that accurate measurements of density fluctuations are much easier to obtain. These measurements could be performed by probes, reflectometry, scattering and other methods, whereas measurements of potential fluctuations can only be performed by probes.
Prior to the treatment of the pseudo-Reynolds stress, we present in Section 6.3.1 analytical and numerical drift wave turbulence results which demonstrate the self-generation mechanism of shear flows via the Reynolds stress. Finally, in Section 6.3.3 we give an account of numerical investigations estimating the effect of misalignment on the experimental determination of the Reynolds stress.
The results presented in the following sections have been obtained by using the finely resolved simulation presented in the beginning of Section 6.2.

### 6.3.1 Shear flow generation by Reynolds stress in the Hasegawa-Wakatani model

By averaging the Hasegawa-Wakatani equation for the vorticity (6.2) over $y$ and $z$ we obtain

$$\frac{\partial \langle v_y \rangle}{\partial t} = \frac{\partial \left\langle \frac{\partial \phi}{\partial y} \frac{\partial \phi}{\partial x} \right\rangle}{\partial x} + \nu \frac{\partial^2 \langle v_y \rangle}{\partial x^2} \tag{6.3}$$

The Reynolds stress, defined in the preceding section, appears in normalised and dimensionless units as:

$$R_\phi = -\langle v_x v_y \rangle = \left\langle \frac{\partial \phi}{\partial y} \frac{\partial \phi}{\partial x} \right\rangle \tag{6.4}$$

and now the first term on the right hand side of (6.3) is identified as the divergence of the Reynolds stress, which is realised to be responsible for the generation of the poloidal flow.
The Reynolds stress is a measure of the anisotropy of the turbulent velocity fluctuations, since it is generated solely from inhomogeneous correlations between $v_x$ and $v_y$. As shown in [65] anisotropic velocity fluctuations produce a stress on the mean flow, and this causes an acceleration of the flow in the plasma, which, e.g., could be a poloidal flow ($y$-direction in the slab geometry). In other words, one may thus say that "the Reynolds stress describes the *exchange* of momentum between the mean flow and the turbulence" [11].
A self-consistent explanation of the flow generation is that the divergence of the Reynolds stress for drift wave turbulence can be seen as a flux of charge due to the nonlinear polarisation drift [66]. This creates a radial electric field, which combined with the toroidal magnetic field generates the poloidal flow. The flux of charge is solely a result of polarisation, and does thus not violate the assumption of quasi-neutrality.
As it appears from (6.3), it is the Reynolds stress that generates the poloidal flow in the Hasegawa-Wakatani model. This may be demonstrated (and used

as a consistency check for the simulations) by plotting the left and right hand side of (6.3) against each other, i.e. the acceleration of the poloidal flow versus the instant value of the divergence of the Reynolds stress including the viscous term. The results are shown for four different times in Figure 6.11, and it is seen that the correspondence is perfect to numerical accuracy. In an experimental setup one could perform a similar comparison to establish whether the flow is generated by turbulence, given one can measure the two quantities with sufficient accuracy.

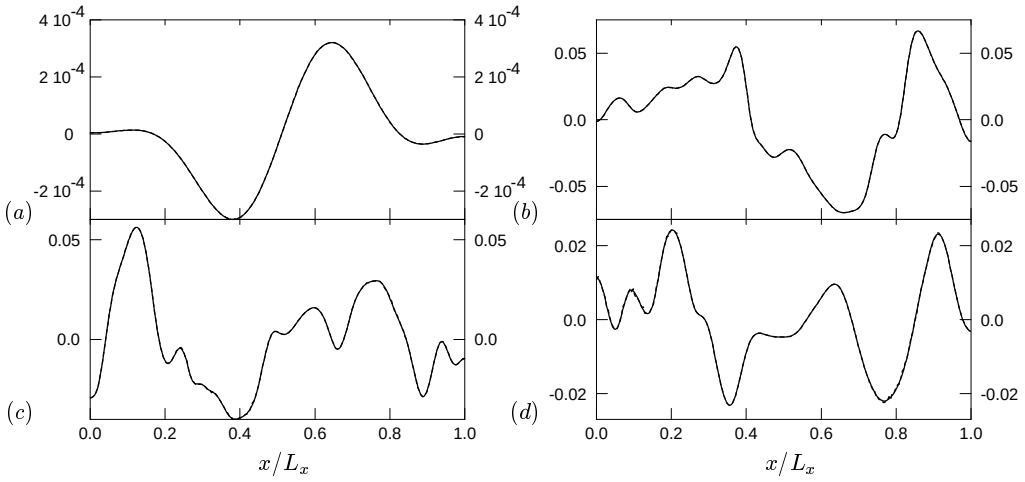


Figure 6.11: The acceleration of the mean poloidal flow, $\partial\langle v_y\rangle/\partial t$ (dashed line), compared to the right hand side of (6.3), $\partial R_\phi/\partial x + \nu\partial^2\langle v_y\rangle/\partial x^2$ (full line), at times (a) $t = 75$, (b) $t = 125$, (c) $t = 175$ and (d) $t = 250$.

While it is clear from the above that it is the Reynolds stress that generates the poloidal shear flow, it is not yet clear which modes that contribute to the Reynolds stress. Shear flow generation is seen in many models and may have different origin. In a paper by Drake et al. [67], shear flow generation is shown to emerge from convection cells in a simple 2D compressible fluid model, when an initial shear flow is applied as forcing.
In the case of the Hasegawa-Wakatani model, we have both flute modes (convection cells) and drift waves. We have calculated the separate contributions to the Reynolds stress from the flute modes and the drift modes, and present the temporal evolutions of these in Figure 6.12, where the Reynolds stress is integrated over the full domain. We see that the Reynolds stress is driven by the drift modes initially, and when the poloidal flow has been generated, the main contribution to the Reynolds stress comes from the flute modes. At later times - probably when the flow has stabilised and the system is quiescent - the contributions from the drift and flute modes to the Reynolds stress are equal. This means that the Reynolds stress is in part driven by a hydrodynamic instability, i.e. the flow is self-amplifying from a seed produced by the drift modes. One could express it differently: the drift waves drive the Reynolds stress directly, and also indirectly through the flute modes, into which the drift modes cascade energy.
Lastly, these results underline the importance of considering both the direct

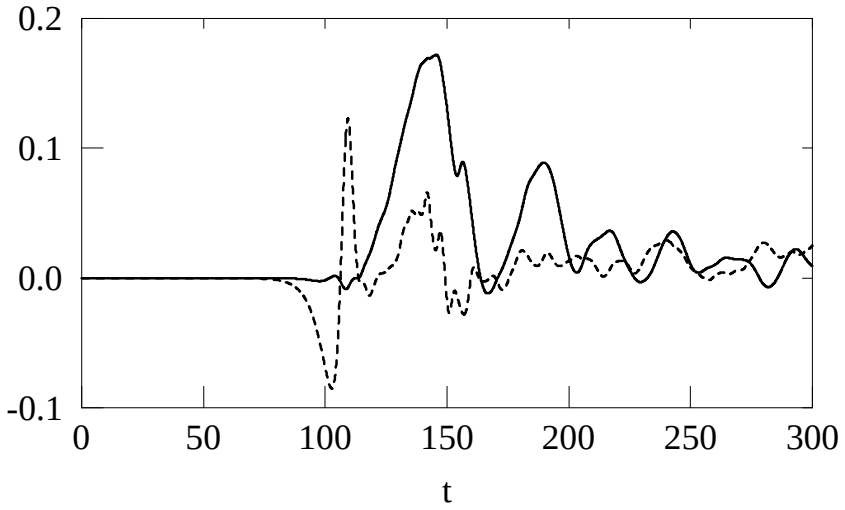


Figure 6.12: The temporal evolution of the flute mode ($k_\parallel = 0$) (full line) and drift mode ($k_\parallel \neq 0$) (dashed line) contributions to the Reynolds stress spatially integrated over the full domain.

contribution of the drift modes to the Reynolds stress, as well as the indirect contribution via the flute modes. The latter contribution is not retained when Hasegawa-Mima type models are used to evaluate the shear flow generation without considering the interaction between the flute and drift modes, as it is done in, e.g., [58, 68].

### 6.3.2 The pseudo-Reynolds stress

As demonstrated in the previous section, it is desirable to be able to measure or estimate the Reynolds stress in order to predict flow generation in experiments. The major problem of this measurement is, as stated above, that an experimental determination of the Reynolds stress demands an accurate measurement of the fluctuations in the electrostatic potential. This, unfortunately, is quite difficult, especially in large plasma devices. However, since the density and potential in drift wave type of turbulence are highly correlated quantities, it has been suggested that an approximate value of the Reynolds stress may be obtained from the density perturbations [63]. This density-based pseudo-Reynolds stress is defined as:

$$R_n = \left\langle \frac{\partial n}{\partial y}\frac{\partial n}{\partial x} \right\rangle \tag{6.5}$$

If a correlation between $R_n$ and $R_\phi$ exists, it will be sufficient to measure the density fluctuations, in order to estimate the Reynolds stress.
One may determine a relationship between $R_n$ and $R_\phi$ in the linear regime, and in the limit of near adiabaticity ($n \sim \phi$) the Hasegawa-Wakatani model (omitting viscosity) can be reduced to a single equation [69, 70]:

$$\frac{\mathrm{D}}{\mathrm{D}t}(1-\nabla^2)\phi + \frac{\partial}{\partial y}\phi = \delta\frac{\mathrm{D}}{\mathrm{D}t}\left(\frac{\partial}{\partial t} + \frac{\partial}{\partial y}\right)\phi \tag{6.6}$$

where $\delta = 1/k_\parallel^2 L_\parallel^2 < 1$ is the adiabaticity parameter and contains via the parallel scale length $L_\parallel = (L_n T_e/\eta e^2 n_0 \omega_{ci} \rho_s)^{1/2}$ the parallel resistivity. The density-fluctuations $n$ are computed from the electrostatic field $\phi$ through

$$n = \phi - \delta \left( \frac{\partial}{\partial t} + \frac{\partial}{\partial y} \right) \phi \tag{6.7}$$

From equation (6.7) we can determine the deviation of $R_n$ from $R_\phi$ in the linear regime, where formally $(\partial/\partial t + \partial/\partial y)\phi \approx \frac{\nabla^2 \partial_y}{1-\nabla^2}\phi$:

$$\begin{aligned} R_n &= \int \frac{\partial n}{\partial x}\frac{\partial n}{\partial y}\,\mathrm{d}x\mathrm{d}y = \int \frac{\partial}{\partial x}\left(\phi - \delta\frac{\nabla^2\partial_y}{1-\nabla^2}\phi\right)\frac{\partial}{\partial y}\left(\phi - \delta\frac{\nabla^2\partial_y}{1-\nabla^2}\phi\right)\,\mathrm{d}x\mathrm{d}y \\ &= R_\phi - 2\delta\int \frac{\partial\phi}{\partial x}\frac{\partial}{\partial y}\frac{\nabla^2\partial_y}{1-\nabla^2}\phi\,\mathrm{d}x\mathrm{d}y + \delta^2\int \frac{\partial}{\partial x}\frac{\nabla^2\partial_y}{1-\nabla^2}\phi\frac{\partial}{\partial y}\frac{\nabla^2\partial_y}{1-\nabla^2}\phi\,\mathrm{d}x\mathrm{d}y \end{aligned} \tag{6.8}$$

where $\partial_y = \partial/\partial y$. For $k \ll 1$ the $R_\phi$ term is dominant, while for $k \gg 1$ the only term contributing is proportional $\delta^2$, so that the term proportional to $\delta$ can generally be neglected. However, it is clear that small scales play a significant role in the exact determination of $R_n$. This will be most significant, when the whole non-linear relationship between density and potential fluctuations has to be considered.

Therefore, we performed numerical simulations, with the purpose of determining whether a density-based pseudo-Reynolds stress is in fact strongly correlated to the real Reynolds stress in the nonlinear regime. First, we look at the correlation between the density and potential, and the pointwise correlation of $n$ and $\phi$ in the whole domain is defined as

$$\langle n\phi \rangle = \frac{\int n\phi \mathrm{d}\mathbf{r}}{\sqrt{\int n^2 \mathrm{d}\mathbf{r}}\sqrt{\int \phi^2 \mathrm{d}\mathbf{r}}}$$

The correlation has been calculated for the full fields of $n$ and $\phi$, as well as for the drift waves ($k_\parallel \neq 0$), and for the convective cell ($k_\parallel = 0$) modes. This pointwise correlation as a function of time is presented in Figure 6.13, and it is seen that $n$ and $\phi$ are strongly correlated for the drift wave components, but nearly anti-correlated for the convective cell modes when the system reaches a state of saturated turbulence, as expected. In Figure 6.14 two-dimensional sections of the density and potential fields are presented for both the convective cell modes and for the drift modes for time $t = 175$, i.e. close to a state of saturated turbulence. From these figures it is clear that the drift components of $n$ and $\phi$ are strongly correlated. For the simulation presented here we chose the parallel coupling parameter to be $\mathcal{C} = 1$ ($\mathcal{C}$ is defined in (3.22)), but by choosing a higher value the electrons would become more adiabatic and the correlation between $n$ and $\phi$ would be even stronger.

The Reynolds stresses, calculated using (6.4) and (6.5) and averaged over $x$, are presented in Figure 6.15. This averaged Reynolds stress quantity is

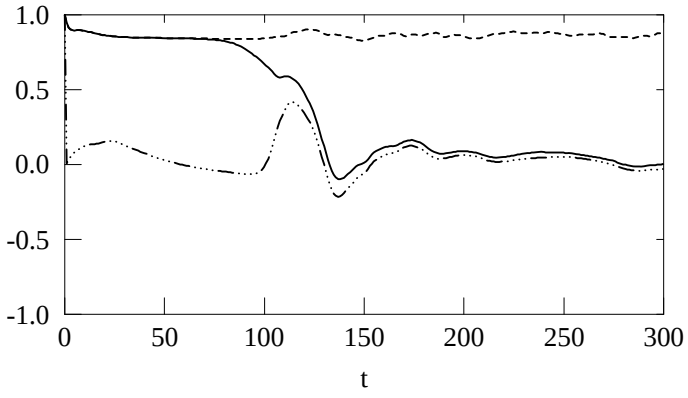


Figure 6.13: The temporal evolution of the correlation of $n$ and $\phi$ for all $k_\parallel$ (full line), for the convective cells ($k_\parallel = 0$, dash-dotted line), and for the drift modes ($k_\parallel \neq 0$, dashed line).

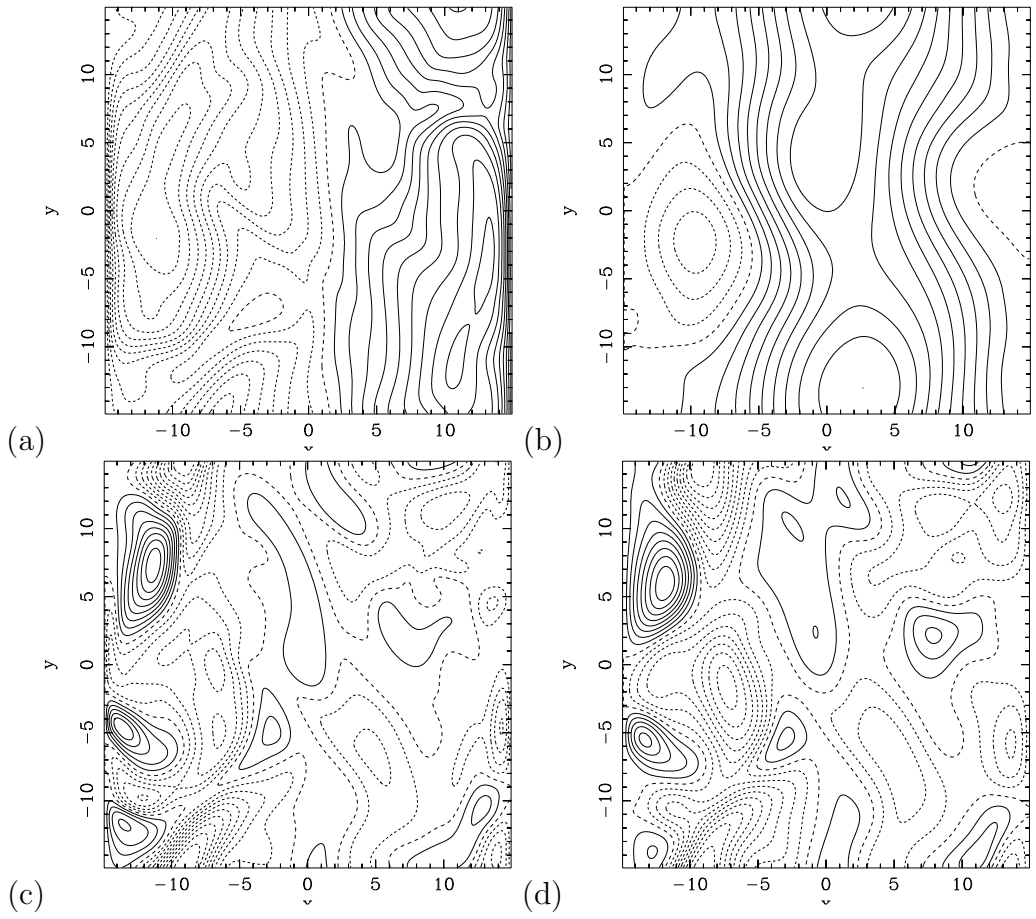


Figure 6.14: The density $n$ and the potential $\phi$ for the convective cells (a) and (b), respectively, and for the drift modes only (c) and (d), respectively, at the time $t = 175$.

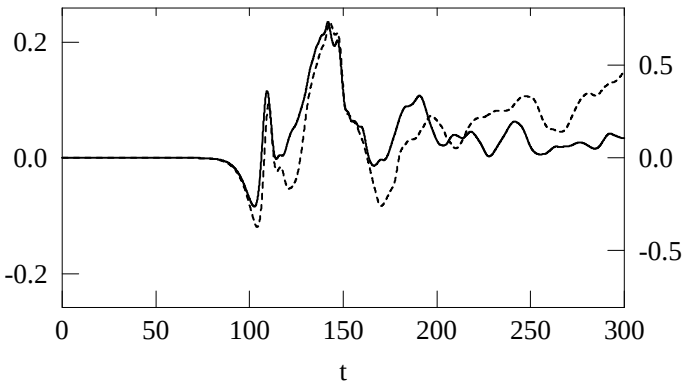


Figure 6.15: The temporal evolution of the Reynolds stress (full line) and the pseudo-Reynolds stress (dashed line) calculated using the full fields of $\phi$ and $n$. The graphs are differently scaled. The scale of $R_\phi$ is to the left, that of $R_n$ to the right.

not much use in predicting flows, since, e.g., a flow antisymmetric around the midpoint of the slab would result in the value zero. Here, however, the quantity is only used to give an impression of the similarity between the real and the pseudo Reynolds stresses. Since most of the energy is condensed into convective cells having $k_\parallel = 0$ (see Figure 6.2), the Reynolds stress is mainly the Reynolds stress of the convective cell for times $t \gtrsim 120$, as we saw in Figure 6.12. The correspondence between $R_n$ and $R_\phi$ is expected to be poor in this situation, since $n$ and $\phi$ are nearly non-correlated for the convective cell as seen in Figure 6.13. In Figure 6.16 we present the temporal evolution of the pointwise correlation of the velocity products calculated from the full fields of $\phi$ and $n$, $\frac{\partial\phi}{\partial y}\frac{\partial\phi}{\partial x}$ and $\frac{\partial n}{\partial y}\frac{\partial n}{\partial x}$, which are used to calculate the Reynolds stress and the pseudo-Reynolds stress, respectively. It is seen that the corre-

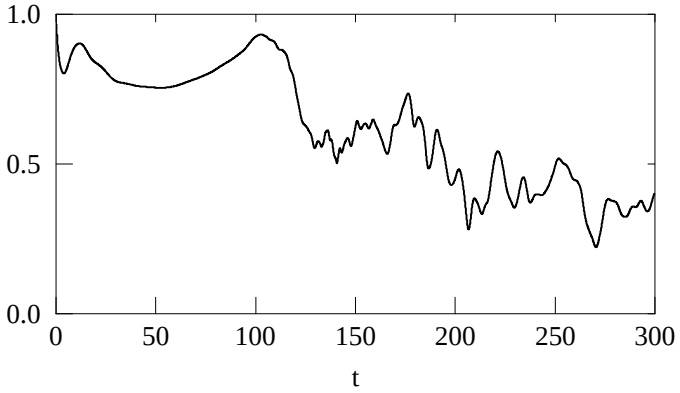


Figure 6.16: The temporal evolution of the correlation of the velocity products calculated from the full fields of $\phi$ and $n$, $\frac{\partial\phi}{\partial y}\frac{\partial\phi}{\partial x}$ and $\frac{\partial n}{\partial y}\frac{\partial n}{\partial x}$, and averaged over the full domain.

lation is quite high in the first part of the simulation, i.e., in the linear and quasi-linear regimes, where the turbulence is not yet fully developed.

In the plasmas confined by sheared magnetic fields, modes having $k_\parallel = 0$ exist only on resonant surfaces. Hence, it is reasonable to exclude the convective cell modes in the Reynolds stress calculations and only use the drift wave components. The results of calculating the Reynolds stresses using only the drift components are presented in Figure 6.17, and it is obvious that the correlation between $R_{n(k_\parallel \neq 0)}$ and $R_{\phi(k_\parallel \neq 0)}$ are stronger than that of $R_n$ and $R_\phi$. In Figure 6.18 we present the temporal evolution of the pointwise corre-

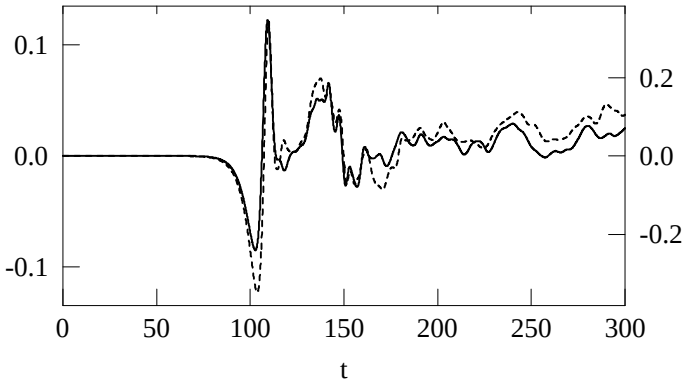


Figure 6.17: The Reynolds stresses calculated from the drift wave components only, $R_{\phi(k_\parallel \neq 0)}$ (full line) and $R_{n(k_\parallel \neq 0)}$ (dashed line). The graphs are differently scaled. The scale of $R_{\phi(k_\parallel \neq 0)}$ is to the left, and that of $R_{n(k_\parallel \neq 0)}$ is to the right.

lation of the velocity products calculated from the drift components of $\phi$ and $n$, $\frac{\partial \phi(k_\parallel \neq 0)}{\partial y}\frac{\partial \phi(k_\parallel \neq 0)}{\partial x}$ and $\frac{\partial n(k_\parallel \neq 0)}{\partial y}\frac{\partial n(k_\parallel \neq 0)}{\partial x}$, which are used to calculate the drift components of the Reynolds stress and the pseudo-Reynolds stress, $R_{\phi(k_\parallel \neq 0)}$ and $R_{n(k_\parallel \neq 0)}$, respectively. The correlation of these quantities is seen to be

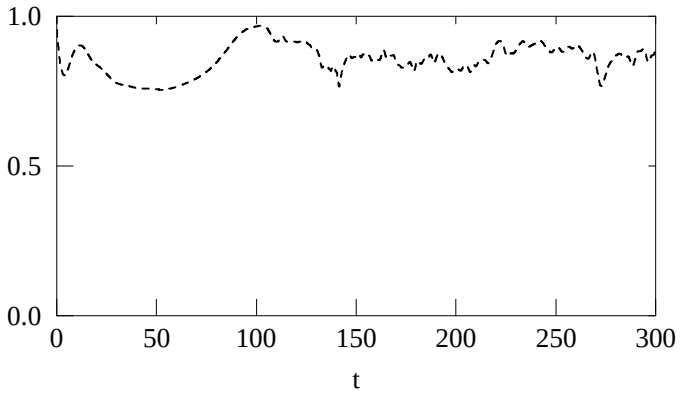


Figure 6.18: The temporal evolution of the correlation of the velocity products calculated from the drift components of $\phi$ and $n$, $\frac{\partial \phi(k_\parallel \neq 0)}{\partial y}\frac{\partial \phi(k_\parallel \neq 0)}{\partial x}$ and $\frac{\partial n(k_\parallel \neq 0)}{\partial y}\frac{\partial n(k_\parallel \neq 0)}{\partial x}$, and averaged over the full domain.

much higher than that of the full fields over the whole simulation.

To evaluate the usefulness of the pseudo-Reynolds stress we may compare the flow acceleration predicted by the pseudo-Reynolds stress calculated for the drift modes and the actual acceleration of the mean poloidal flow. This corresponds to the comparison for the Reynolds stress presented in Figure 6.11, and we present it for four different times in Figure 6.19. The correspondence

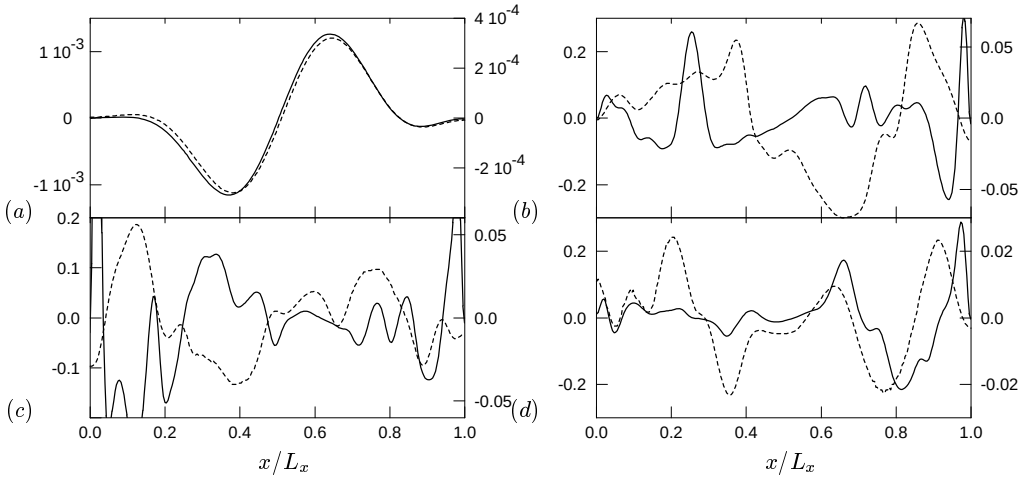


Figure 6.19: The acceleration of the mean poloidal flow, $\partial\langle v_y\rangle/\partial t$ (dashed line), compared to $\partial R_{n(k_\parallel\neq 0)}/\partial x + \nu\partial^2\langle v_y\rangle/\partial x^2$ (full line), at times (a) $t = 75$, (b) $t = 125$, (c) $t = 175$ and (d) $t = 250$. The graphs are differently scaled; the scale of the pseudo-Reynolds stress is to the left, that of the flow is to the right.

is fair at early times before the turbulence is fully developed $t \lesssim 120$, but even at later times the pseudo-Reynolds stress "diagnostic" captures many of the characteristics of the flow acceleration profile.
Alternatively, one may check the results by testing if the temporally integrated $\partial R_{n(k_\parallel\neq 0)}/\partial x$ (including viscosity) sums up to be the poloidal velocity, $v_y$. In Figure 6.20 the profile of the integral of the right hand side of (6.5) is compared to the velocity profile at four different instants in time. It is seen from the figures that the pseudo-Reynolds stress gives a good qualitative hint on the flow generation - at least for times before the turbulence is fully developed. The fact that the correspondence between the pseudo-Reynolds stress and the flow velocity degrades, could in part be explained by the density fluctuations being cascaded to smaller scales [28], which causes problems in properly resolving the gradient of the density field numerically. This causes the error in $\frac{\partial n}{\partial x}$ to grow, and since the quantity shown in Figures 6.19 and 6.20 is the divergence of a product of two derivatives, the error due to resolution becomes significant. The effect of the error is naturally most significant in the integrated profiles in Figure 6.20, since the error components are integrated as well. The error is not only dependent on the resolution, since it will not fully disappear by increasing the resolution. A higher number of modes will cause the density to be cascaded to even smaller scales, and a part of the problem is thus viscosity. However, it is not appropriate to increase the viscosity indefinitely, since this may cause important dynamics

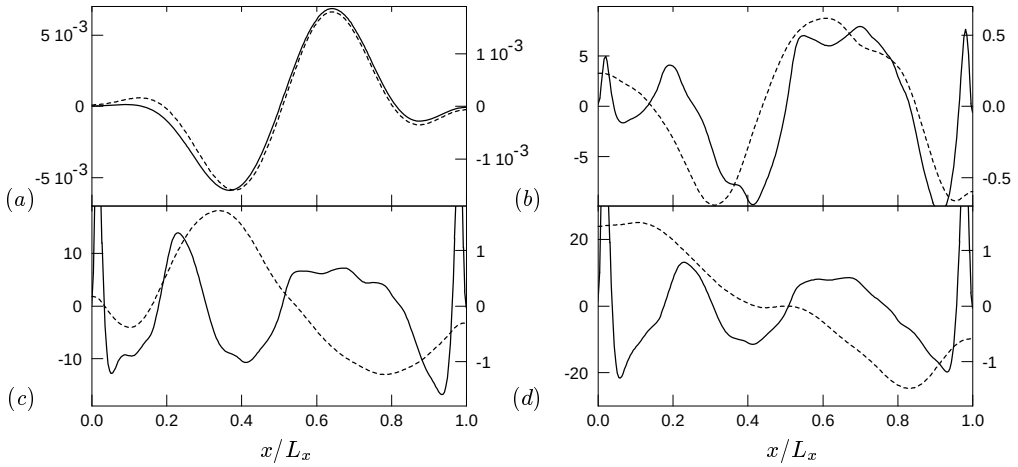


Figure 6.20: Comparison of the $\int(\partial R_{n(k_\parallel\neq 0)}/\partial x + \nu\partial^2\langle v_y\rangle/\partial x^2)\mathrm{d}t$ (full line) and $v_y$ (dashed line) profiles at different times (a) $T = 75$, (b) $T = 125$, (c) $T = 175$, and (d) $T = 250$. The graphs are differently scaled; the scale of the pseudo-Reynolds stress is to the left, that of the flow is to the right.

of the system to be suppressed. Thus the selection of correct parameters is a delicate balance between retaining the appropriate dynamics and properly resolving the desired quantities. The relation between the Reynolds stress and the pseudo-Reynolds stress may well be affected by changing the viscosity, and as seen from (6.3) the relation between shear flow generation and the Reynolds stress is also dependent on the viscosity. However, a full investigation of the parametric dependence on the viscosity is beyond the scope of the present work.

The quality of the pseudo-Reynolds stress was also evaluated for a resistive interchange turbulence model in [50]. The parameters used corresponded to those of the edge region of ATF ECH-heated plasmas [71]. For the case of L-mode the coherence between the Reynolds stress and the pseudo-Reynolds stress was found to be higher than 0.8, except at the radial positions close to low-order rational surfaces, where $k_\parallel$ is close to zero, i.e. when flute-like modes affect the dynamics. This corresponds nicely to the findings for the drift wave case above. Finally, for the case of H-mode for the resistive interchange model the coherence is much lower ($\sim 0.5$), and the reason given is that the averaged sheared flow dominates the system.

Finally, although the pseudo-Reynolds stress seems to have some validity from simulations with two different models, we should point out that there is many physical aspects of magnetically confined fusion plasmas, which are not included in the used models. Thus, the work presented above should be viewed as an initial approach to render probable the use of density measurements for prediction of shear flow generation via the pseudo-Reynolds stress.

### 6.3.3 Sensitivity of Reynolds stress measurements to probe alignment

We have looked into the effect of a misaligned probe array, when attempting to determine the Reynolds stress in an experiment. These investigations were performed with the Hasegawa-Wakatani model using the same parameters as in the previous sections. We imagine an array of five probes as illustrated in Figure 6.21, with fixed distances ($r$) and fixed (right) angles between the probes. This is the minimal array with which to obtain the divergence of the Reynolds stress from two independent measurements of the Reynolds stress as:

$$R_{\phi,1} = \frac{(\phi_2 - \phi_1)(\phi_4 - \phi_1)}{r^2} \qquad \text{and} \qquad R_{\phi,2} = \frac{(\phi_3 - \phi_2)(\phi_5 - \phi_2)}{r^2} \tag{6.9}$$

To obtain the Reynolds stress one should align the probes with the magnetic field to get the correct components of the perpendicular velocities, $-\partial\phi/\partial y$ and $\partial\phi/\partial x$. In an experiment, however, the magnetic topology might not be known precisely, and therefore we have simulated the effect of the probe being misaligned with respect to the magnetic field, by rotating it the angle $\alpha$ around the $z$-axis as shown in Figure 6.21, i.e. in the plane perpendicular to the magnetic field. The effect of misalignment along the magnetic field

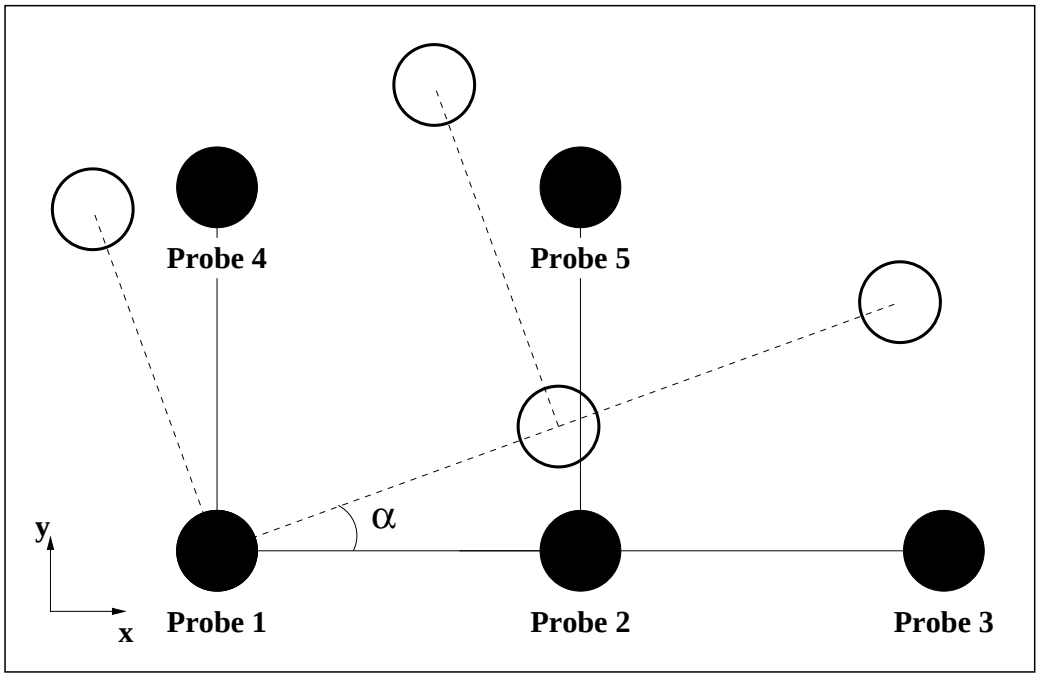


Figure 6.21: The probe array with five probes. The non-filled circles are the probe array after the array is rotated by the angle $\alpha$.

was also examined by rotating the probe around the $y$-axis. The probe array was located in the centre of the simulation domain, in order to minimise effects of the boundaries. The distance between the probes, $r$, was chosen to

be smaller than the autocorrelation length of the perturbations in order to calculate the Reynolds stress on a relevant scale. The values of $\phi$ between the grid points were found by spectral interpolation.
We present typical results for a given position of the probes, and the effect of a probe array misaligned in the plane perpendicular to the magnetic field is shown in Figure 6.22. The calculated Reynolds stresses change with the

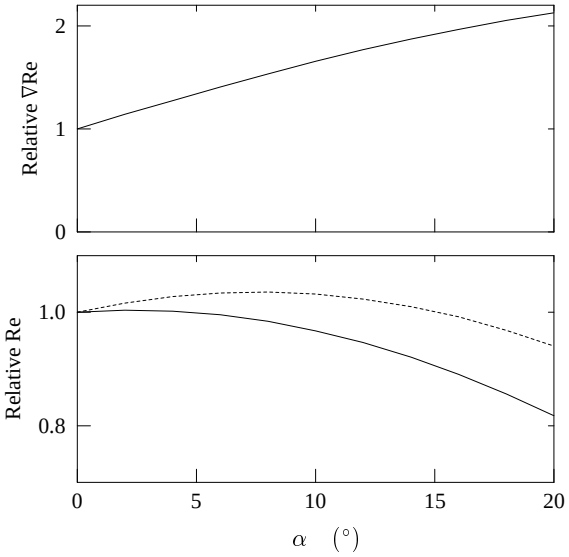


Figure 6.22: Rotated probe calculations at time $t = 176$ with the misalignment in the plane perpendicular to the magnetic field lines. Upper graph shows the difference of the "measured" divergence of the Reynolds stress and the value for perfect alignment relative to the latter as a function of the misalignment angle $\alpha$. The lower graph shows the change of the two Reynolds stresses.

angle $\alpha$, as it is seen in the lower part of the figure, whereas the calculated divergence of the Reynolds stress only changes by less than 30% if the misalignment in the plane perpendicular to the magnetic field is less than 5°.
The effect of a probe array misaligned in a plane parallel to the radial direction and parallel to the magnetic field is presented in Figure 6.23. The calculated divergence of the Reynolds stress only changes by less than 30% if the misalignment in the plane parallel to the magnetic field is less than 7°. However, for $\alpha > 7°$ the error in the determination of the divergence of the Reynolds stress rises quickly. Thus, the alignment of the probe array is important, but it is not crucial to have a perfect alignment to obtain a reasonably good estimate of the divergence of the Reynolds stress, and via this the acceleration of the mean shear flow. However, here we solely investigated the effect of alignment, and did not consider any probe effects - such as shadowing.

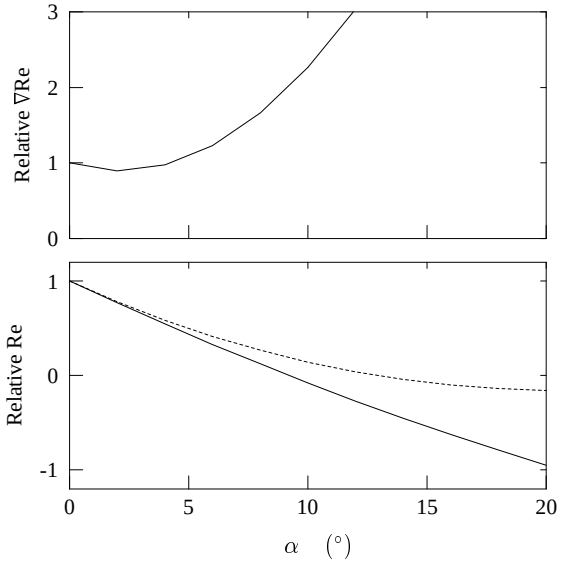


Figure 6.23: Rotated probe calculations at time $t = 176$ with the misalignment along the magnetic field lines. Upper graph shows the difference of the "measured" divergence of the Reynolds stress and the value for perfect alignment relative to the latter as a function of the misalignment angle $\alpha$. The lower graph shows the change of the two Reynolds stresses relative to the Reynolds stresses for perfect alignment.

## 6.4 Performance of the system for varying parameters and initial cases

The performance of the Hasegawa-Wakatani equations in a non-periodic slab domain, has been investigated for a number of cases. These include different initial conditions, variation of the aspect ratio ($L_x/L_y$) of the domain, variation of the size of the domain, variation of the viscosity, and investigation of the effect of an externally imposed shear flow. These cases do not give a full picture of the behaviour of the system, but they have been chosen to give some insight in the dynamics of the system for interesting setups.

### 6.4.1 Initial flat profile

The driving term of the Hasegawa-Wakatani system is the $\frac{\partial \phi}{\partial y}$-term of the density equation, which emulates the energy drive of the turbulence originating from a constant background density gradient. As we have seen in Section 6.2, the density perturbations build up as a back-reaction to this, and the total average density profile of the system becomes flat (see Figure 6.5).
An alternative to a gradient driven system is a flux driven system, in which a density source and sink are applied in the system and the density gradient is self-consistently evolved from the conditions imposed by the source and sink.

For the Hasegawa-Wakatani system one could set the background gradient to zero (i.e. omit the $\frac{\partial \phi}{\partial y}$-term in (6.1)), and add a density source and sink. However, in Section 6.1 it was briefly discussed that when the system with Dirichlet boundaries reaches a quasi-stationary saturated state, the system is, actually, effectively a flux-driven system, driven by the diffusive in- and out-fluxes, when the density gradient is effectively flat in the bulk of the domain.
As one special case, we performed simulations where the constant background density gradient was kept, while the initial condition of the density perturbations fulfilled that the total effective density profile was nearly flat. The initial situation is thus a flux-driven system, though, with one disadvantage being that the level of the flux drive, i.e. the source and sink rates, cannot be controlled.

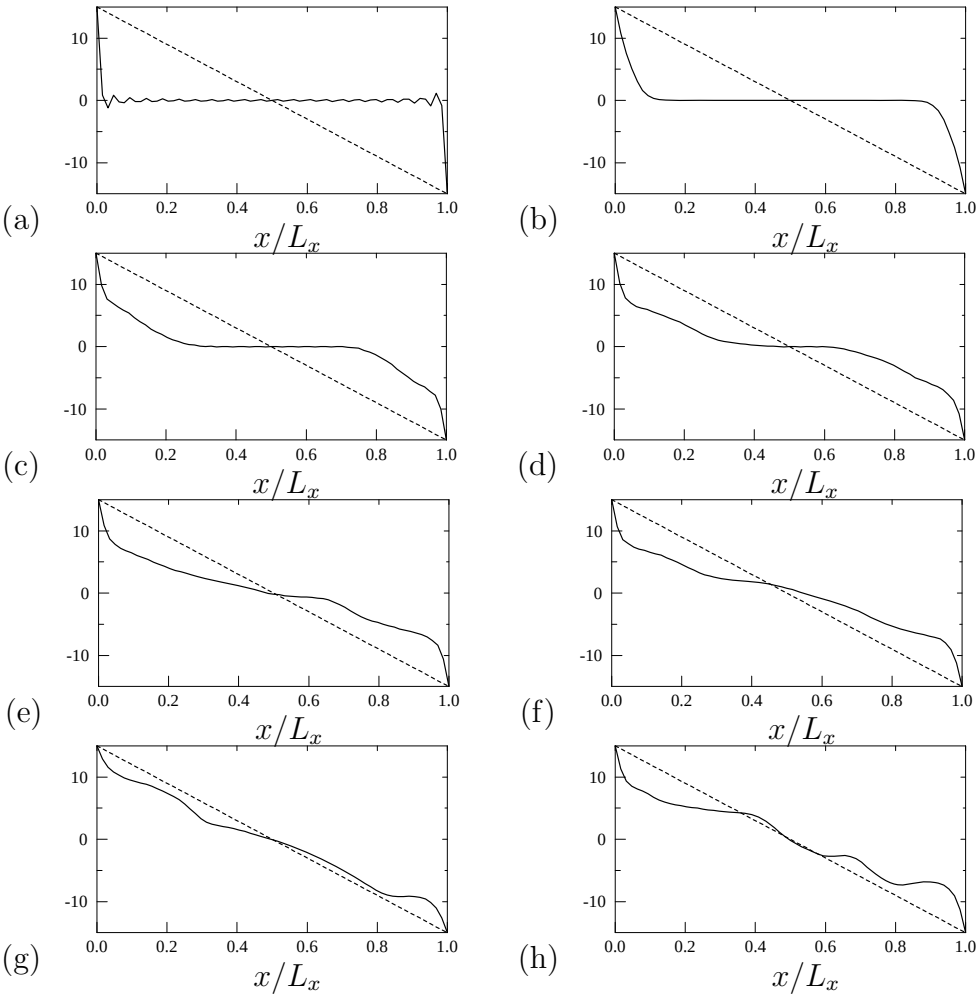


Figure 6.24: Plot of the total density profile, $n_0 + \langle n \rangle$ (full line), and the constant background gradient, $n_0$ (dashed line), for different times: (a) $t = 0$, (b) $t = 20$, (c) $t = 40$, (d) $t = 60$, (e) $t = 80$, (f) $t = 100$, (g) $t = 400$, and (h) $t = 500$.

The initial condition for the density perturbations was low level random noise

on top of the mean contribution that nearly flattened the background profile. The initial potential perturbations consisted in this case of low level random noise, only. The parameters for the simulation were: $m = n = 64$, $o = 32$, $L_x = L_y = 30$, $L_z = 20$, $\mathrm{d}t = 4 \cdot 10^{-3}$, and a viscosity coefficient $\nu = 0.05$. In Figure 6.24 we present the temporal evolution of the total density profile, and from this we see that the steep density gradients at the edges (in this case initially the source and sink areas) are smoothed, or are diffusing into the slab. This corresponds to the picture of diffusive fluxes over the boundaries as discussed in Section 6.1. The system evolves towards a build-up of the total density profile, and at $t = 400$ (Figure 6.24.(g)) the total profile is nearly following the constant background profile. This state is followed by building up of shear flows, and at $t = 500$, seemingly, two transport barriers exist, resulting in flat density profiles in three regions of the domain, as seen from Figure 6.24.(h).
The energy evolution of the simulation is shown in Figure 6.25, and it is seen

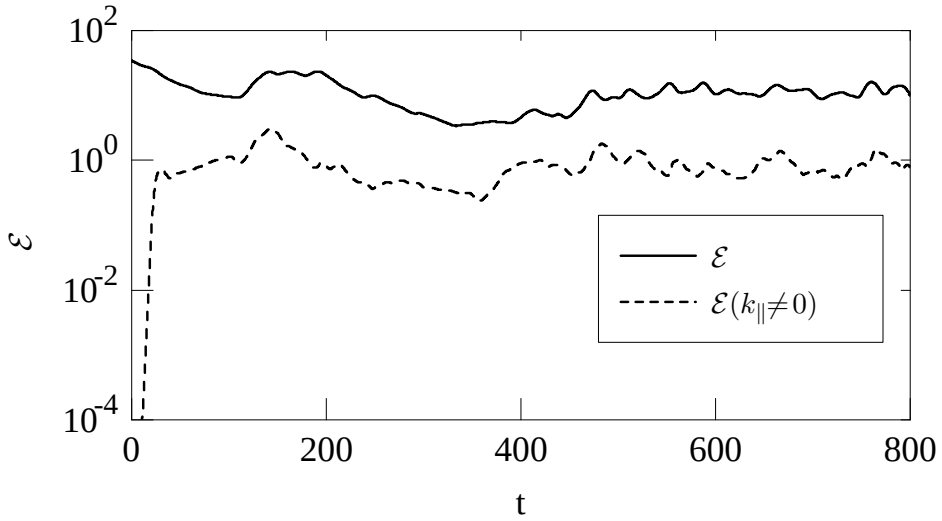


Figure 6.25: The temporal evolution of the total energy (full line) and the energy of the drift waves (dashed line) for a simulation initialised effectively with a flat total density profile.

that drift waves are building up from the initial perturbations on top of the large mean values of the density that cause the flute mode energy to be high.

### 6.4.2 Dependence on domain aspect ratio

The poloidal shear flow in the Hasegawa-Wakatani model in a periodic geometry is Kelvin-Helmholtz unstable if the aspect ratio of the simulation domain $\frac{L_y}{L_x}$ exceeds unity [28]. In that case, the poloidal shear flow does not build up, and is released by a radial flow enabled by the periodic boundaries in the $x$-direction [28]. The latter is not possible when we use Dirichlet boundary conditions, and here we present a brief study of the importance of the domain aspect ratio. We performed simulations with three different aspect ratios: $\frac{L_y}{L_x} = 1, 2, 4$. The other parameters were: $m = n = 64$, $o = 32$,

$L_x = 30$, $L_z = 20$, $\mathrm{d}t = 4 \cdot 10^{-3}$, and a viscosity coefficient $\nu = 0.05$.

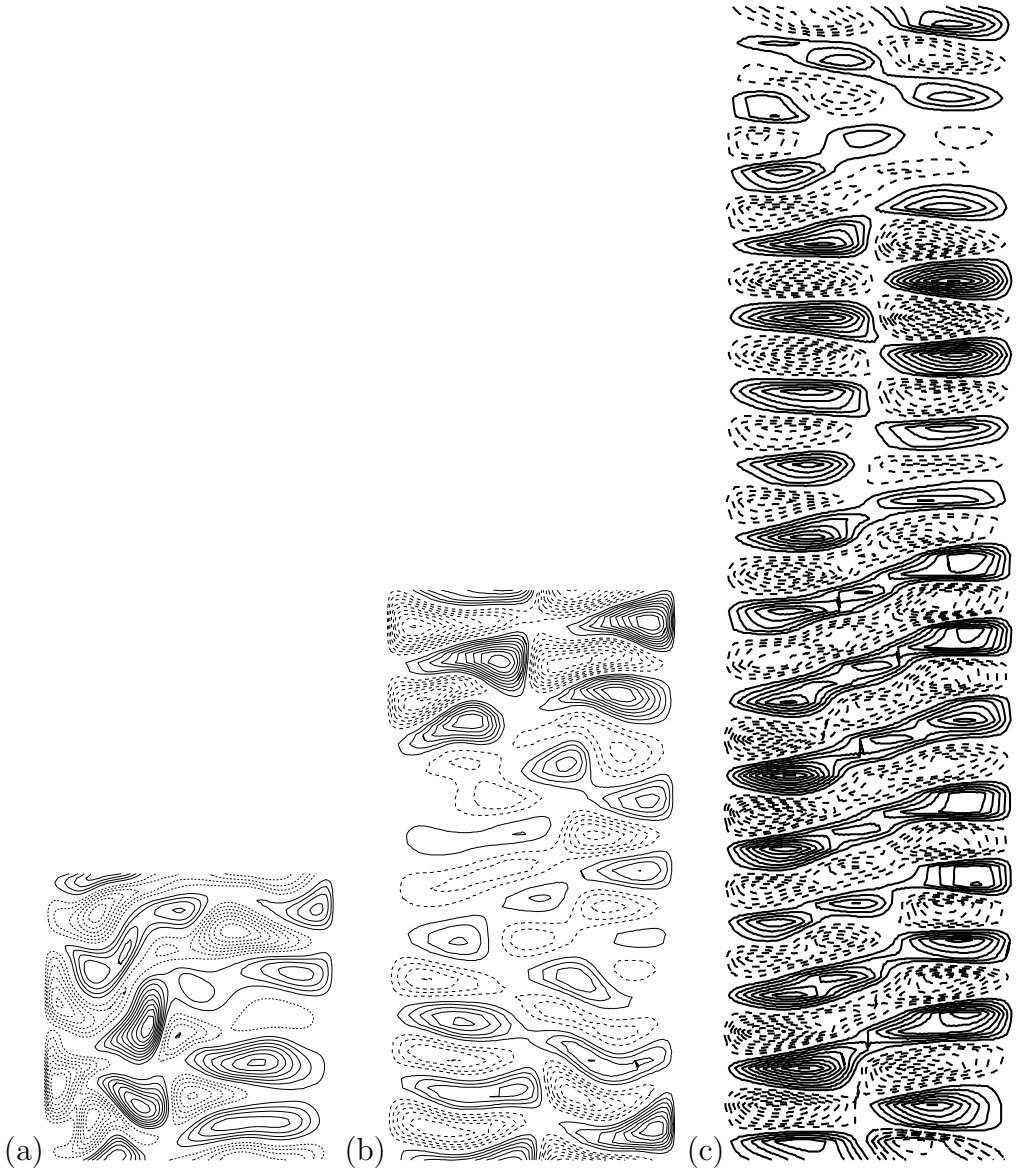


Figure 6.26: The density perturbation at $t = 110$ for three simulations with different $\frac{L_y}{L_x}$ aspect ratio. (a) $\frac{L_y}{L_x} = 1$, (b) $\frac{L_y}{L_x} = 2$, and (c) $\frac{L_y}{L_x} = 4$. The radial ($x$) direction is horizontal, and the poloidal ($y$) direction is vertical. The plots are presented in true relative sizes.

Within the tested range of aspect ratios, the overall performance of the system does not change: the instability drives energy into the turbulence, energy is transferred into the flute modes, a poloidal flow is build up, and the back-reaction from the density perturbations seeks to flatten the total density profile. Furthermore, the global parameters such as the energy and the flux are not significantly different in the three simulations, although there seems to be a tendency of the perturbations to grow to slightly higher levels for increasing aspect ratio.

Before the strong shear flow build up, a state with elongated structures in the radial direction occurs (these may be what some authors call streamers [72, 73]). In this state the number of structures are - not surprisingly - proportional to the box length in the $y$-direction. This can be realised in Figure 6.26, where we show the density perturbation at an intermediate time. The width in the $y$-direction of the individual structures is nearly the same in all three cases, as it appears from Figure 6.26. The Dirichlet boundary conditions prevent further development of the radial structures, and eventually a poloidal shear flow is build up, having approximately equal strength in all three cases.
The similarity of the simulations with three different aspect ratios may be a result of the tested aspect ratios being too small. In a recent paper [32], it is found that the shear flow is unstable for $k_y \lesssim \frac{0.6}{\alpha}$, where $\alpha$ is the width of the shear flow. Approximating $\alpha$ by $L_x$ we find that the aspect ratio should be $\frac{L_y}{L_x} \gtrsim 10$, in order for any $k_y$ to fulfil $k_y \lesssim \frac{0.6}{\alpha}$. One may thus anticipate different dynamics for rather large aspect ratios.
In order to test variations of the dynamics with domain size, we performed two simulations with parameters as the above, except for the domain size being $L_x = L_y = 20$ and $L_x = L_y = 30$. The results do not differ very much from each other, and one would be tempted to say that as long as a sufficient range of modes is included, including the most unstable modes (see Section 4.2.4 in [22]), the dynamics of the system is not significantly changed. However, the statistics are admittedly not great in this case.

### 6.4.3 The diffusive flux dependence on viscosity

In Section 6.2 we presented in Figures 6.6-6.8 a long simulation to illustrate the reoccurring flux burst behaviour of the system. The simulation was long enough to contain several periods of the system being quiescent, followed by a build-up of the global gradient, and turbulent flux bursts. The parameters for that simulation were: $m = n = 32$, $o = 32$, $L_x = L_y = 25$, $L_z = 20$, $\mathrm{d}t = 4 \cdot 10^{-3}$, and a viscosity coefficient $\nu = 0.1$.
We discussed in Section 6.2 that the dissipation damps the density fluctuations that have build up to flatten the total density profile, and is thus in turn responsible for the recreation of the density gradient. Thus the characteristic time-scale of the reoccurrence of flux bursts must be inversely proportional to the viscosity coefficient $\nu$. To clarify this point we performed a number of simulations with equivalent parameters, except for four different values of the viscosity parameter: $\nu = [0.025; 0.05; 0.075; 0.1]$. Plots of the energy and the flux for these simulations are presented in Figure 6.27, where we see that the dependence of the viscosity is at least two-fold. First, the increased viscosity may lead to generally lower fluctuation levels, and hereby lower energy and flux levels, as it is the case for $\nu = 0.1$. And secondly, the figure supports the main objective we aimed to illustrate, i.e. that the characteristic time of the cycle of flux bursts separated by quiescent periods of weak tubulence is inversely proportional to the viscosity.

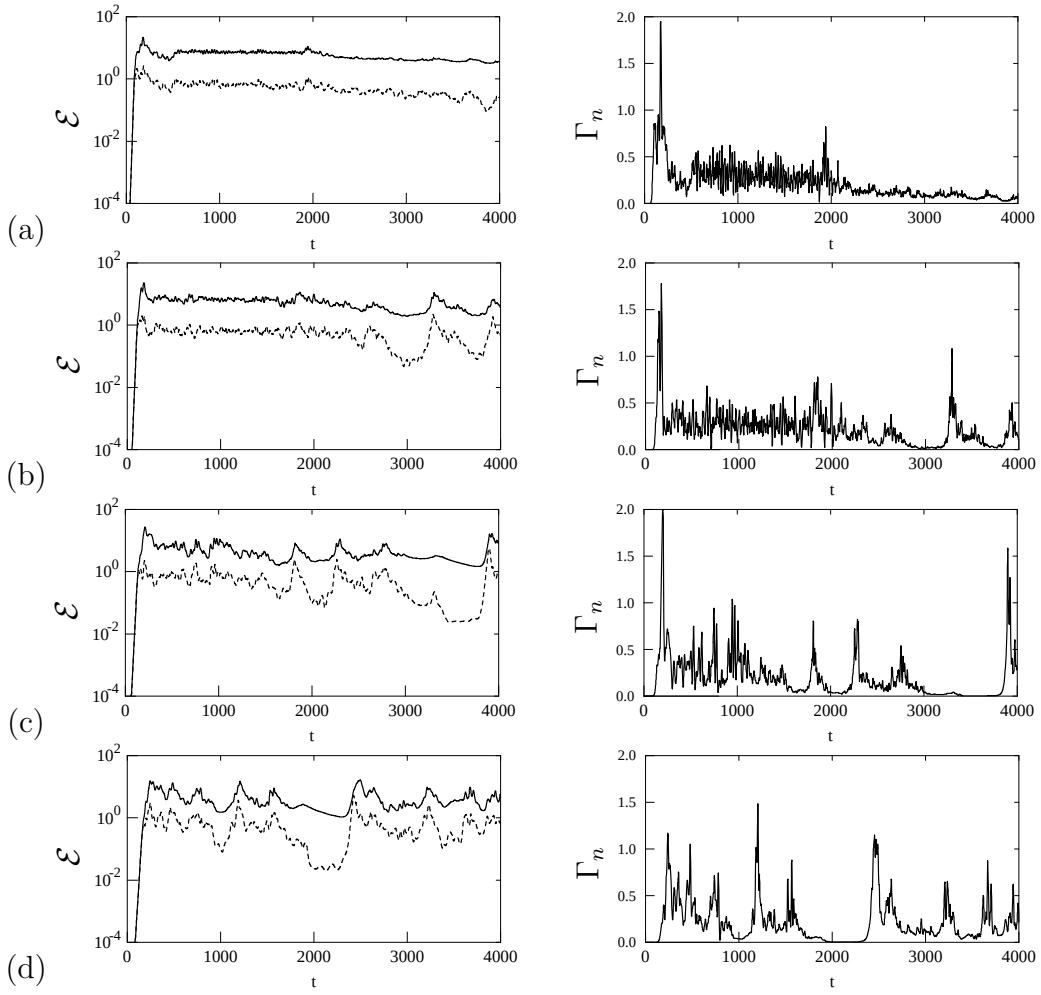


Figure 6.27: In the first column the total energy, $\mathcal{E}$ (full line), and the energy of the drift wave component, $\mathcal{E}(k_\parallel \neq 0)$ (dashed line), is shown for increasing $\nu$ in each row: (a) 0.025, (b) 0.05, (c) 0.075, and (d) 0.1. In the second column we present the corresponding turbulent fluxes.

### 6.4.4 Externally applied constant shear flow

In the previous sections we have described how the turbulence may generate a flow through the Reynolds stress. However, many other effects, such as neoclassical effects, trapped particles, ion orbit losses, and geometric asymmetries, may generate or accelerate a poloidal flow. Thus, one may not be able to predict the total flow by only considering the turbulent fluctuations. Nonetheless, the Reynolds stress can still be a good measure, since the external effects will influence the fluctuations, and in turn also the Reynolds stress. Thus, the Reynolds stress may - in time - contain not only the effect of the fluctuations alone, but also the effect of the otherwise generated flow. The non-turbulence induced poloidal flow may in this way also be thought of as a seed flow, since it affects the flow generated by the turbulent fluctuations. In this section we will look further into these effects by applying an external shear flow to the system. This may also help to clarify the role of the

self-generated shear flow on the development of the drift wave fluctuations and turbulent transport.
The implementation of the external poloidal shear flow, $\mathbf{v}_S \parallel \mathbf{e}_y$, is performed by replacing $\mathbf{v}_{E,y}$ by $\mathbf{v}_{E,y} + \mathbf{v}_S$ in (6.1) and (6.2). Note that in this way the fluctuations are not allowed to act back on $\mathbf{v}_S$, which is thus constant. The constant external shear flow is of the form

$$\mathbf{v}_S = \mathbf{v}_S(x) = \Theta \tanh\left(\frac{x - \frac{L_x}{2}}{\Delta}\right)\mathbf{e}_y$$

where $\Theta$ is a parameter giving the amplitude of the shear flow, and $\Delta$ is the width of the shear region. The radial profile of the flow is presented in Figure 6.28. One may discuss whether the back-reaction of the turbulence on

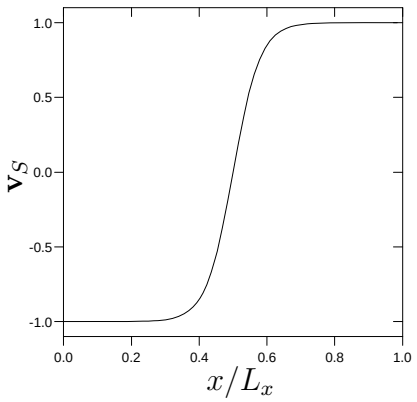


Figure 6.28: The shape of the externally applied poloidal shear flow. Here the amplitude $\Theta$ is unity.

the external shear flow should be included. In that case a term of the form $\mathbf{v}_E \cdot \nabla_\perp \nabla_\perp^2 \phi_S$ should be added to the left hand side of (6.2), where $\phi_S$ fulfills: $\mathbf{v}_S = \frac{\partial \phi_S}{\partial x}$ (this would enable a possibility for a Kelvin-Helmholtz instability). However, presently, we just want to study the reaction of the fluctuations on the constant shear flow.
We performed a number of simulations with different strengths and directions (parallel and anti-parallel to $\mathbf{e}_y$) of $\mathbf{v}_S$, i.e. for varying $\Theta$. The remaining parameters were: $m = n = 64$, $o = 32$, $L_x = L_y = 30$, $L_z = 20$, $\mathrm{d}t = 4 \cdot 10^{-3}$, and a viscosity coefficient $\nu = 0.05$. In Figure 6.29 we present the radial profiles of the self-generated poloidal shear flow, $\mathbf{v}_{E,y}$, and of the total poloidal shear flow, $\mathbf{v}_{E,y} + \mathbf{v}_S$, for different values of $\Theta$, in a quasi-stationary state. Figure 6.29.(a) shows only the self-generated shear flow, since $\Theta = 0$, and it can thus be used as a reference. In Figure 6.29.(b) we present the velocity profiles for a case with a very strong external shear flow $\Theta = 5$. For this case, the amplitude of the self-generated flow is reduced to approximately 10% of the reference. This is due to the external shear flow suppressing the fluctuations during the whole simulation, as we also see for the other cases with $\Theta = \pm 2$, only for $\Theta = 5$ it is more significant. Furthermore, a very

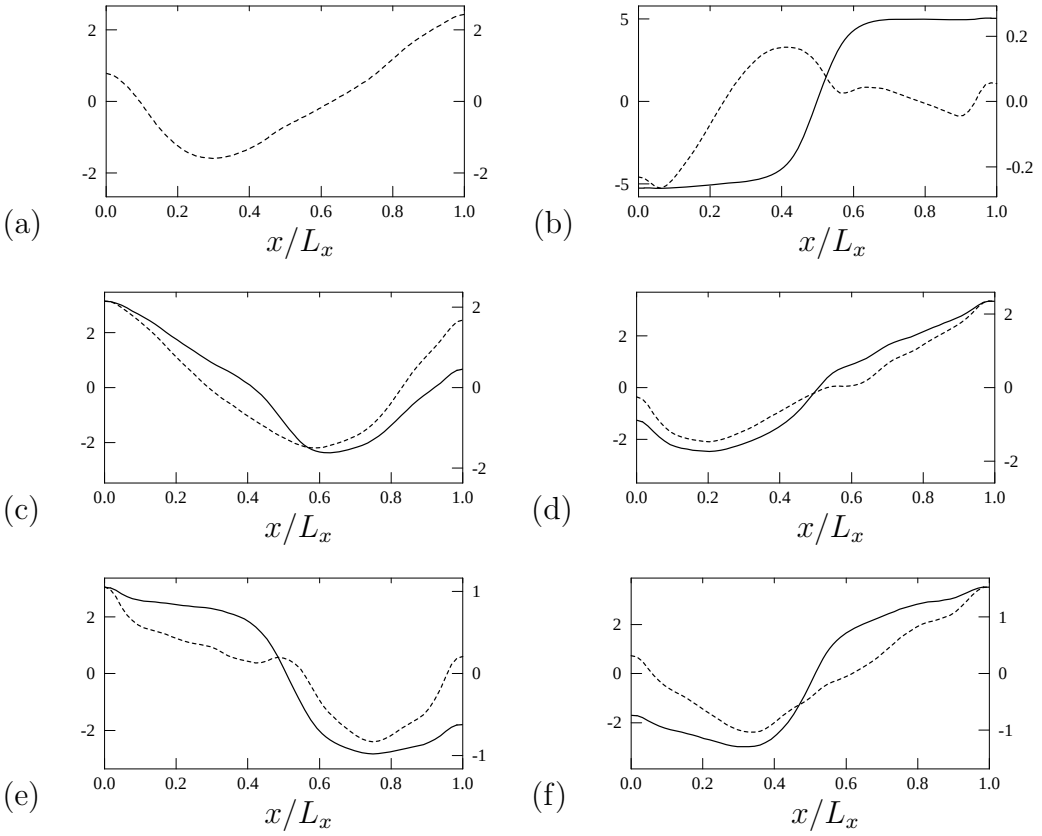


Figure 6.29: Self-generated $\mathbf{v}_{E,y}$ (dashed line) and $\mathbf{v}_{E,y} + \mathbf{v}_S$ (full line) shear flow profiles for (a) $\Theta = 0$, (b) $\Theta = 5$, (c) $\Theta = -1$, (d) $\Theta = 1$, (e) $\Theta = -2$, (f) $\Theta = 2$. The scale for the full line is to the left.

interesting detail is that the self-generated shear flow is counteracting the external shear flow, although the external shear flow is directed parallel to the self-generated shear flow in the reference case. From this we conclude that there is no seed flow effect of the external shear flow in this case of a very large amplitude. This is to be expected, since the strong external shear flow completely alter the domain and the conditions for the turbulence. Real space plots of the fluctuating quantities show that the inner and outer part of the domain are almost detached by the strong shear flow.

For more moderate amplitudes of the external shear flow it is seen in Figures 6.29.(c) and (d) that the self-generated shear flow is affected. For $\Theta = -1$ we see the minimum of the flow being shifted due to the external shear flow that have now acted as a seed flow. For these cases of moderate $\Theta$, we see that the amplitude of the self-generated flow is approximately maintained. For the case of $\Theta = 1$ one should note that despite the optimal direction of the moderate external shear flow, the amplitude of the minimum of the self-generated flow is reduced by nearly 10%. This indicate that the amplitude reduction mechanism is stronger than the seed flow mechanism. For the case of $\Theta = \mp 2$ in Figures 6.29.(e) and (f), the tendency of the amplitude reduction mechanism being dominant is more evident, and this results in a mere $\sim$ 15% increase in the amplitude of the minimum of the total shear

flow by the (100%) increase from $\Theta = 1$ to $\Theta = 2$.
The reduction in fluctuation amplitude, as described above, is most pronounced for the potential, but despite the general reduction, the density perturbations are able to severely affect the total density profile as it is presented in Figure 6.30. This figure contains in (a) the density profile, and in (b) the radial profile of the root-mean-square value of the radial velocity, $v_r$, for the case of a strong external shear flow $\Theta = 5$. It is seen from the density

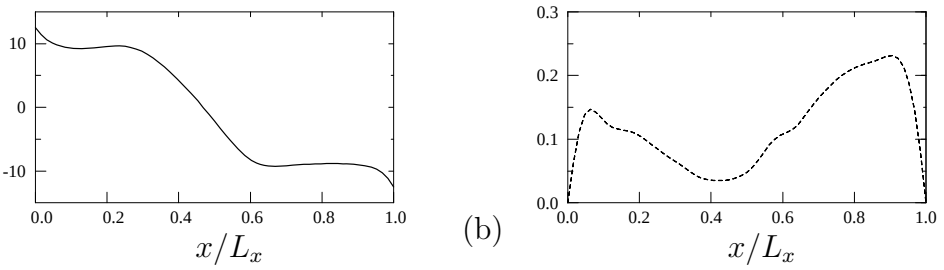


Figure 6.30: (a) The effective radial density profile, $n_0 + \langle n \rangle$, for the case of a shear flow with $\Theta = 5$, and (b) the radial profile of the root-mean-square value of the radial velocity, $v_r$.

profile that a transport barrier is formed around the location of maximum velocity shear. The observation of the formation of a transport barrier is further supported by Figure 6.30.(b), where we see a prominent depression of the radial velocity of the fluctuations around the supposed transport barrier. The transport in the areas inside and outside the barrier is higher, leading to the piece-wise flat density profile.
One could test how well the Reynolds stress captures the acceleration of the total shear flow, $\mathbf{v}_{E,y} + \mathbf{v}_S$, by a comparison as that of Figure 6.11. However, as $\mathbf{v}_S$ is constant in the present implementation, $\partial(\mathbf{v}_{E,y} + \mathbf{v}_S)/\partial t = \partial \mathbf{v}_{E,y}/\partial t$, and the comparison will be fulfilled as in the case of no external shear flow (which is the case to numerical accuracy).
A further investigation of the interplay between an external shear flow, the turbulence, and the self-generated shear flow could include: inclusion of back-reaction from the turbulence on the external shear flow (by including the term $\mathbf{v}_E \cdot \nabla_\perp \nabla_\perp^2 \phi_S$), temporal variation of the external shear flow (e.g., sudden switch on/off), effect of solely an external shear flow (by artificially neutralising the self-generated shear flow), and multiple transport barrier formation by an altered external shear flow profile.
Finally, regarding the generation and persistence of transport barriers, it would be interesting to see to what extent the self-generated shear flow, $\mathbf{v}_{E,y}$, is able to maintain a transport barrier that has first been initiated by an external shear flow, which is switched off at an instant after the barrier is formed. This idea is inspired by [74], in which it is stated about "Ohmic" H-modes in the START spherical tokamak: "The persistence of the H-mode following beam cutoff[1] in these discharges may be because the radial electric field generated by the beam is then maintained by the pressure gradient produced by the pedestal."

[1]Switch off of the Neutral Beam Injection (NBI) heating

# Chapter 7

# Reflectometry at MAST

During the authors stay at UKAEA-Fusion at Culham Science Centre near Abingdon, England, experimental fluctuation studies by reflectometry were performed at the Mega Amp Spherical tokamak (MAST). This was done by installing and setting up a homodyne one-channel reflectometer at MAST in collaboration with Dr. Cunningham. Such a reflectometer is useful for fluctuation studies, but is not able to measure density profiles. This will be possible with the future MAST multichannel reflectometer from the plasma physics group at IST Lisbon, Portugal.
This chapter will be introduced by a description of the general features of reflectometry techniques, and a brief literature study of reflectometry. Then the setup of the one-channel MAST reflectometer will be presented, and finally, following a section on data treatment, the results of the measurements will be presented and discussed.

## 7.1 Principles of reflectometry

Reflectometry is based on the fact that the refractive index of a plasma changes with the density and magnetic field. A microwave is launched into the plasma, and it is reflected if a *cut-off*[1] is present in the plasma. The reflected wave is then detected and mixed with the launched wave, and the resulting signal thus contains information on the phase delay and amplitude modulations caused by the plasma. A schematic diagram of this is presented in Figure 7.1. In order to obtain density profiles from reflectometry, one needs to calculate $\frac{\partial\varphi}{\partial\omega}$, where $\varphi$ is the phase delay, and $\omega$ is the reflectometer frequency. In order to calculate this, one needs measurements of $\varphi$ for several frequencies $\omega$, which then enable calculation of the spatial positions of the cut-offs, $x_{co}(\omega)$, by an Abel inversion expressed as [75]:

$$x_{co}(\omega) = a + \frac{c}{\pi}\int_0^{\omega}\frac{\partial\varphi}{\partial\omega}(\omega^2 - \omega'^2)^{-1/2}\mathrm{d}\omega' \tag{7.1}$$

If, however, only a single or a few frequencies are launched, this inversion is not possible, and only fluctuations of given density surfaces (corresponding

[1] At a cut-off the refractive index becomes imaginary.

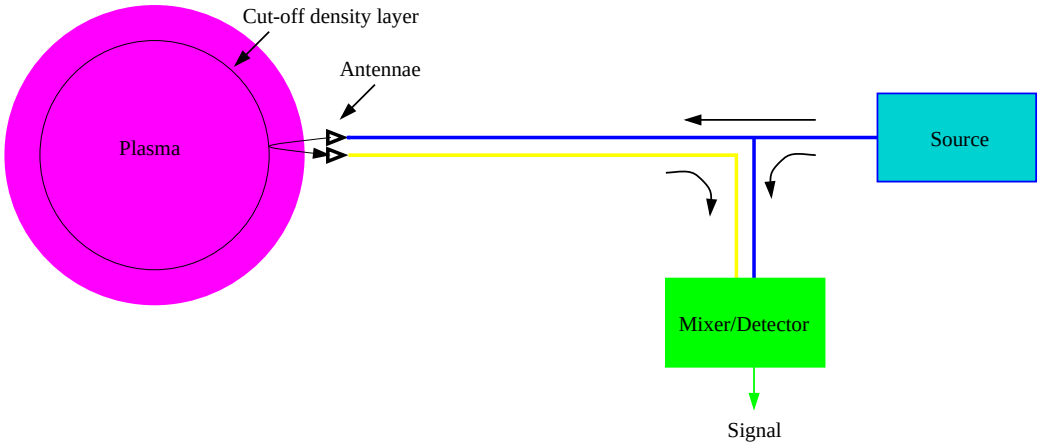


Figure 7.1: The principle of a reflectometer with a homodyne detection system, where the detector mixes the beam from the source and the reflected signal.

to the frequencies of the launched waves) may be measured.
The MAST fluctuation reflectometer system is of the latter kind and the cut-off densities and estimated locations of these will be described in Sections 7.2.2 and 7.2.3.

### 7.1.1 Brief look into the reflectometry literature

This brief look into the literature is mainly meant as a short reference guide for the reader who wants to know more about reflectometry. Laviron et al. [76] present a fine theoretical basis of reflectometry, and describe in some detail a number of reflectometer systems for profile measurements. They briefly discus the effect on the reflected signal of local density fluctuations during the transmission through the plasma before and after the reflection. A thorough description of a specific system for measuring edge density profiles (at TdeV) is given in [77].
Mazzucato presents in [78] a good review on both fluctuation and profile reflectometry. The article considers the wave theory, and contains a thorough description of the theoretical background of reflectometry. It also contains a discussion of the effect of fluctuations on profile measurements, and of the validity of fluctuation measurements.
In [79] Bretz gives a general review of diagnostics for measurements of microturbulence in tokamaks. Firstly, this puts fluctuation reflectometry into a context, secondly, the section on reflectometry has some nice points. He is relatively optimistic regarding the possibilities of reflectometry, however, he concludes that no consensus on the interpretation of correlation reflectometry exists. Correlation reflectometry works by having more reflectometer channels at different frequencies. These reflect at different densities and radii, and by this it may be possible to estimate correlation lengths of turbulent structures, provided the frequencies are sufficiently close. A final point

in [79] is that the effect of poloidal structures is important in especially correlation reflectometry studies. The validity of correlation reflectometry is severely challenged in [80, 81], where the problem, of the density fluctuations interfering with the reflectometer signal during transmission before and after reflection, is thoroughly treated.
Kramer et al. [82] present multichannel reflectometry results of density fluctuations in JET. The article contains a nice description of the behaviour of the homodyne detection system in use, discusses various data treatments, and finally presents the results of a number of topical studies. In this way the article provides a practical view on some of the possibilities of fluctuation reflectometry.

## 7.2 The MAST fluctuation reflectometer

The MAST fluctuation reflectometer is set up to be a single channel, 33.1GHz, X-mode system with homodyne detection. The frequency corresponds to a cut-off density of approximately $1.01 \cdot 10^{19}\mathrm{m}^{-3}$ for the lower X-mode cut-off (see Section 7.2.2). In order to get the reflection as far in the edge as possible the system has been operated in X-mode only; however, nothing prevents operation in O-mode if desired. The reflectometer is located next to the interferometer port and is probing in the horizontal mid-plane. The radial location of the cut-off surface is generally $r/a = 70 - 90\%$.
We term the system 'the MAST fluctuation reflectometer', since the system produces fluctuation spectra – not density measurements. Since the movements of a given density surface is observed, the spectra could be seen as velocity fluctuation spectra of that given density surface. The second reason for the 'fluctuation' term is to avoid confusion with the future density profile reflectometer to be installed by the IST group in Lisbon, Portugal.

### 7.2.1 The Mega Ampere Spherical Tokamak

As described in Chapter 1 many fusion reactor concepts are being investigated in fusion research programmes over the world. One of the newest concepts is the *spherical tokamak* (ST), in which the aspect ratio (major radius to minor radius) is very low, so that the shape of the vessel is approaching a sphere with a central rod through it.
The worlds first high temperature spherical tokamak START (Small Tight Aspect Ratio Tokamak) was designed and build at Culham Science Centre, and was operating from 1991 to 1998. The results of the machine (e.g., a plasma $\beta$ upto 40%) were so promising that a number of STs have been build around the world. A recent account of the status and implications of ST research may be found in [83].
The machine succeeding START at Culham is MAST (Mega Ampere Spherical Tokamak), which in linear dimensions is nearly three times as large as its predecessor. Together with NSTX (National Spherical Torus Experiment) at Princeton, USA, MAST is the largest ST in the world, and it is further de-

scribed in [84]. General results obtained in the MAST spring 2000 campaign are described in [85].

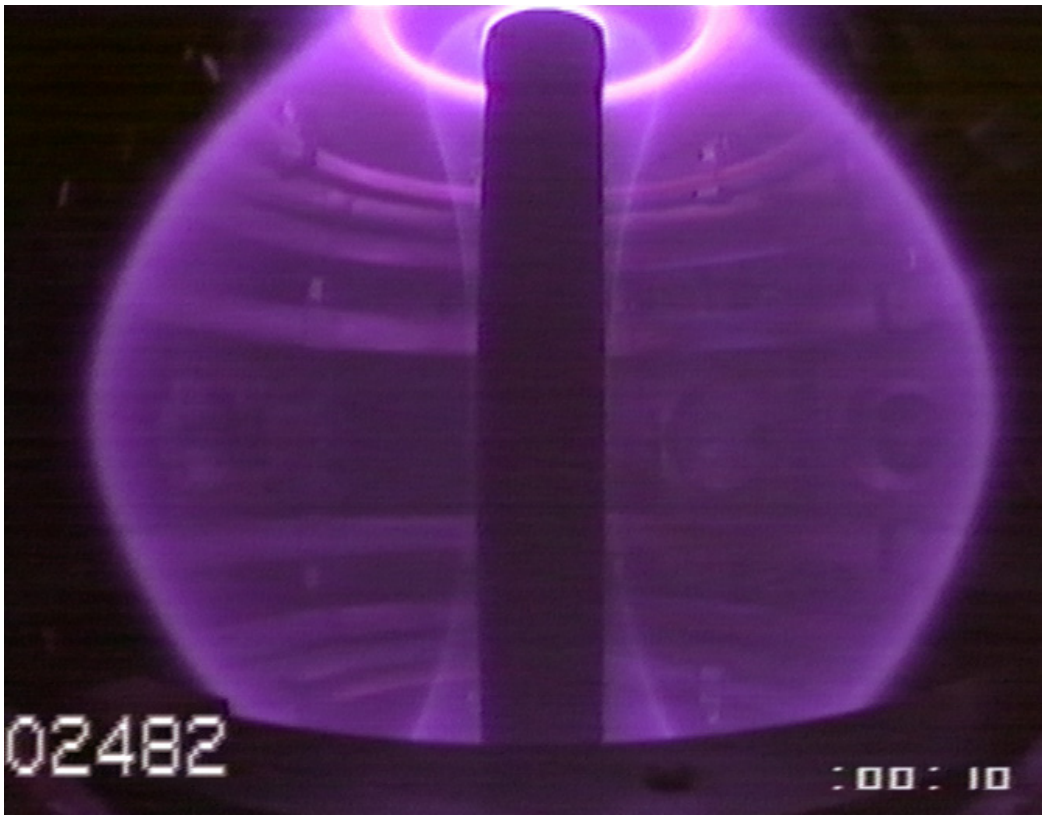


Figure 7.2: Photograph of the first MAST plasma (shot 2482) that reached more than 1MA of plasma current.

Typical parameters for the MAST plasmas during the spring 2000 campaign are: plasma current $I_p$ =0.6-1MA, central electron temperature $T_e(R) \gtrsim$ 1keV, central electron density $n_e(R) \approx 4 \cdot 10^{19}\mathrm{m}^{-3}$, toroidal magnetic field $B_T(R) \approx 0.52\mathrm{T}$, poloidal magnetic field $B_p(a) \approx 0.15\mathrm{T}$, minor plasma radius $a \approx 0.55\mathrm{m}$, and major radius $R \approx 0.75\mathrm{m}$. The plasma pulse length is typically in the order of $150 - 350\mathrm{ms}$, and the energy confinement time for an H-mode discharge is estimated to be 28ms [85].
When estimating typical scale lengths of turbulence in numerical turbulence studies, the ion gyro radius at the electron temperature $\rho_s = \sqrt{T_e m_i}/eB$ is often used (see Chapter 3). For MAST $\rho_s$ is in the range of 3-6mm depending on the exact temperature and magnetic field.

### 7.2.2 Calculation of cut-off densities

Since the refractive index of the plasma changes with density, the incoming reflectometer wave will be reflected when the density is such that the refractive index goes to zero. This cut-off density, $n_{co}$, is dependent on the polarisation of the wave. For an O-mode wave the cut-off is not dependent

on the magnetic field, and the cut-off density may be expressed as:

$$\frac{\omega_{pe}^2}{\omega^2} = 1 \qquad \Leftrightarrow \qquad n_{e,co} = \frac{m_e \epsilon_0 \omega^2}{e^2} \tag{7.2}$$

where $\omega_{pe}$ is the electron plasma frequency, and $\omega = 2\pi f$ is the frequency of the incoming wave.
For X-mode waves the expression is more complicated, since it is dependent on the magnetic field:

$$\frac{\omega_{pe}^2}{\omega^2} \frac{\omega^2 - \omega_{pe}^2}{\omega^2 - \omega_{pe}^2 - \omega_{ce}^2} = 1 \tag{7.3}$$

where $\omega_{ce} = \frac{eB}{m_e}$ is the electron Larmor radius. Two solutions to (7.3) can be found, which we call XL-mode for left hand polarised X-mode, and XR-mode for right hand polarised X-mode. For the XL-mode the cut-off density is:

$$\frac{\omega_{pe}^2}{\omega^2 - \omega\omega_{ce}} = 1 \qquad \Leftrightarrow \qquad n_{e,co} = \frac{m_e \epsilon_0}{e^2} \left( \omega^2 - \omega \frac{eB}{m_e} \right) \tag{7.4}$$

and for the XR-mode:

$$\frac{\omega_{pe}^2}{\omega^2 + \omega\omega_{ce}} = 1 \qquad \Leftrightarrow \qquad n_{e,co} = \frac{m_e \epsilon_0}{e^2} \left( \omega^2 + \omega \frac{eB}{m_e} \right) \tag{7.5}$$

In the edge region of the MAST plasma the magnetic field is approximately $B = 0.3\text{T}$, and for the frequency of the reflectometer channel, $f = 33.1\text{GHz}$, the cut-off densities are:

$$\begin{aligned} \text{O-mode} &: n_{co} = 1.35 \cdot 10^{19}\text{m}^{-3} \\ \text{XL-mode} &: n_{co} = 1.01 \cdot 10^{19}\text{m}^{-3} \\ \text{XR-mode} &: n_{co} = 1.70 \cdot 10^{19}\text{m}^{-3} \end{aligned}$$

### 7.2.3 Calculation of cut-off position

The determination of where the plasma density, $n$, equals the cut-off density, $n_{co}$, of the reflectometer wave is very difficult if not impossible with the current setup. We have estimated it by using the line-integrated density taken from the interferometer data (see [75] for a description of a interferometer), and then calculating the density profile by assuming a parabolic shape. This calculation is done by an IDL routine we call `densprof`, which uses this expression:

$$n(r) = -\frac{3S_{intf}}{16a^3} r^2 + \frac{3S_{intf}}{16a} \tag{7.6}$$

where $r$ is the radial position in the plasma ($r = 0$ at the centre axis), and $a$ is the minor radius of the plasma, which is typically 0.55m. By this expression it is assumed that $n(r) = 0$ for $|r| \geq a$. $S_{intf}$ is the interferometer signal, which is the line-integrated density of four passes through the plasma diameter at the horizontal mid-plane, which is also the position of the reflectometer.

By input of frequency and polarisation of the reflectometer wave as well as an estimated density profile, the IDL routine `reflpos` calculates the approximate cut-off position. The calculated positions of the cut-offs relative to the minor radius (so that 100% means at the outer edge of the plasma) are presented in Table 7.1 for various line-integrated densities for a launched 33.1GHz wave.
Since the line-integrated density usually is in the order of $1 \cdot 10^{20}\mathrm{m}^{-2}$ or less, it is seen from Table 7.1 that the reflection does not usually occur in the outermost regions of the plasma. Therefore, the magnetic field is not constant while the wave travels in the plasma. If the toroidal field is assumed to be the major component of the magnetic field (an assumption that gets better when moving into the plasma), the field can be assumed to evolve as:

$$B(r) = B_T(r) = \frac{B_0 R_0}{R_0 + r} \tag{7.7}$$

where $B_0$ is the toroidal magnetic field at the toroidal axis, which is at the major radius $R_0$.
The expression (7.7) can be put into (7.4) and (7.5) and new expressions for $n_{co}$ – now dependent on $r$ – is found. Now, the equation to solve to find the cut-off position is $n(r) = n_{co}(r)$. Since the XL-mode is most interesting due to a lower cut-off density, we only treat that here. By combining (7.4), (7.6), and (7.7) and simplifying one obtains:

$$\frac{m_e \epsilon_0}{e^2}\omega^2 - \frac{3S_{intf}}{16a} = \frac{\epsilon_0}{e}\omega\frac{B_0 R_0}{R_0 + r} - \frac{3S_{intf}}{16a^3}r^2 \tag{7.8}$$

This equation has been solved for a number of interferometer signals, and the result is presented in the last column of Table 7.1 for the parameters $B_0 = 0.52\mathrm{T}$ at the toroidal axis (corresponding to $B(-a) = 1.95\mathrm{T}$ and $B(a) = 0.3\mathrm{T}$), and $a = 0.55\mathrm{m}$ and $R = 0.75\mathrm{m}$ (corresponding to an aspect ratio of 1.36).
In Table 7.1 it is seen that for line-integrated densities of $6 \cdot 10^{19}\mathrm{m}^{-2}$ and above, the difference of the XL-mode and the $B$-corrected XL-mode is insignificant. The use of O-mode reflectometry is generally preferable, since no concern has to be paid to the magnetic field, except for the alignment. However, as seen from Table 7.1 the interferometer signal needs to be larger than approximately $1.2 \cdot 10^{20}\mathrm{m}^{-2}$ in order for the cut-off position to be in the same range as the one for the XL-mode. Therefore, the XL-mode has been used until now.
A better estimate of where the reflectometer wave is reflected may be found using the density profile measurements from the Thomson scattering (TS) system. A major disadvantage of the MAST TS system at the time of these experiments, though, was that the profile was only measured at one given instance during each shot.

### 7.2.4 The reflectometer system setup

The MAST fluctuation reflectometer system as it is mounted at MAST is shown in Figure 7.3. The system consists of a Gunn oscillator (the right most

| $S_{intf}$ ($10^{19}\mathrm{m}^{-2}$) | Est. $n_0$ ($10^{19}\mathrm{m}^{-3}$) | Cut-off pos. O-mode (% of $a$) | Cut-off pos. XL-mode $B = 0.3T$ (% of $a$) | Cut-off pos. XL-mode $B$-corr (% of $a$) |
|---|---|---|---|---|
| 1.0 | 0.34 | – | – | -66.7 |
| 2.0 | 0.68 | – | – | -21.3 |
| 3.0 | 1.0 | – | 9.1 | 36.4 |
| 4.0 | 1.4 | 5.8 | 50.6 | 56.0 |
| 5.0 | 1.7 | 45.0 | 63.6 | 66.2 |
| 6.0 | 2.0 | 57.9 | 71.0 | 72.5 |
| 7.0 | 2.4 | 65.6 | 75.8 | 76.9 |
| 8.0 | 2.7 | 70.8 | 79.3 | 80.0 |
| 9.0 | 3.1 | 74.6 | 81.8 | 82.4 |
| 10.0 | 3.4 | 77.5 | 83.8 | 84.2 |
| 11.0 | 3.8 | 79.8 | 85.4 | 85.8 |
| 12.0 | 4.1 | 81.7 | 86.7 | 87.0 |
| 13.0 | 4.4 | 83.3 | 87.8 | 88.1 |
| 14.0 | 4.8 | 84.6 | 88.7 | 88.9 |
| 15.0 | 5.1 | 85.7 | 89.5 | 89.7 |
| 16.0 | 5.5 | 86.7 | 90.2 | 90.4 |
| 17.0 | 5.8 | 87.5 | 90.8 | 91.0 |
| 18.0 | 6.1 | 88.2 | 91.4 | 91.5 |
| 19.0 | 6.5 | 88.9 | 91.8 | 91.9 |
| 20.0 | 6.8 | 89.4 | 92.3 | 92.3 |
| 21.0 | 7.2 | 90.0 | 92.6 | 92.7 |
| 22.0 | 7.5 | 90.5 | 93.0 | 93.1 |
| 23.0 | 7.8 | 90.9 | 93.3 | 93.4 |
| 24.0 | 8.2 | 91.3 | 93.6 | 93.7 |
| 25.0 | 8.5 | 91.7 | 93.8 | 93.9 |

Table 7.1: Position of cut-offs for 33.1 GHz reflectometer wave for O-mode and XL-mode polarisations. A parabolic density profile with minor radius of $a = 0.55$m is assumed. For the $B$-corrected XL-mode cut-off calculations a major radius of $R = 0.75$m (corresponding to an aspect ratio of 1.36), and a toroidal magnetic field of a strength $B_0 = 0.52$T at the toroidal axis (corresponding to $B(-a) = 1.95$T and $B(a) = 0.3$T) were used. Fields marked '–' indicate that the wave is not reflected by the plasma, and fields marked with negative values indicate that the wave is reflected at the inside of the major radius.

part) with an output frequency of 33.1GHz, a directional coupler waveguide (the black waveguide), a transmitting and a receiving antenna (green horns), and a mixer/detector (the left-most unit with a cable connected to it). The signal from the detector runs through a pre-amplifier (not shown) with amplification of 40dB for all frequencies up to 6MHz, before entering the data acquisition card. The sampling frequency of the data acquisition card has been 500kHz and 250kHz for the results presented here.

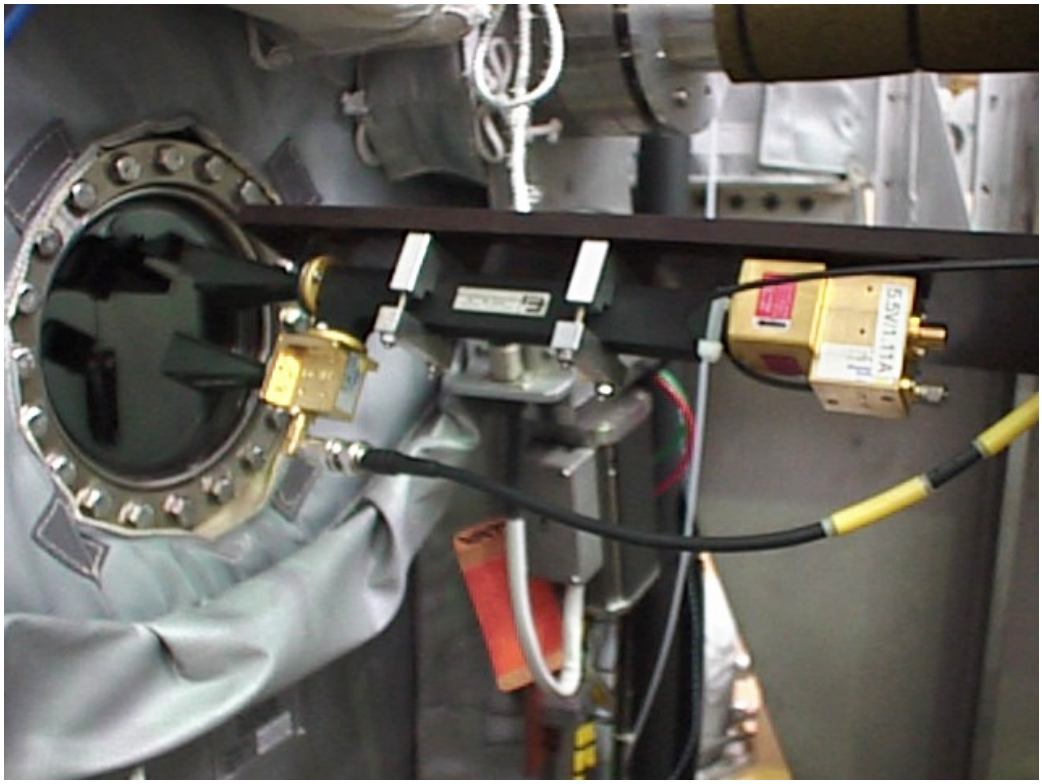

Figure 7.3: The MAST fluctuation reflectometer. In order to have pure X-mode reflections the reflectometer system is mounted at 30° to the horizontal mid-plane due to the pitch angle of the magnetic field. This pitch angle is dependent on $I_p$ and $B_T$ for each shot, but 30° is generally a good estimate for the present studies.

From Figure 7.3 it is seen that the reflectometer is mounted in an angle to horizontal. In most tokamaks the toroidal field is much stronger than the poloidal field and therefore $\mathbf{B} \sim \mathbf{B}_T$. However, since the toroidal field is relatively weak for spherical tokamaks, this assumption is not necessarily valid. Therefore, the reflectometer must be mounted in an angle in order to avoid mixing of signals of different (O and X) polarisation. This pitch angle $\alpha$ is the angle between $\mathbf{B}(a)$ and $\mathbf{B}_T$, where the former is the superposition of the toroidal and poloidal magnetic field at $r = a$. The relative polarisation of an incoming beam to the magnetic field in the plasma stays constant, as the wave propagates into the plasma, where the angle between $\mathbf{B}(r)$ and $\mathbf{B}_T$ naturally changes due to the magnetic shear. An explanation for this could be

that inside the plasma the magnetic field determines the frame of reference. Thus, the pitch angle $\alpha$ can be expressed as

$$\tan(\alpha) = \frac{B_P(a)}{B_T(a)} \qquad \Rightarrow \qquad \alpha = \tan^{-1}\left(\frac{B_P(a)}{B_T(a)}\right) \tag{7.9}$$

The toroidal field is expressed by (7.7), and the poloidal magnetic field can be found via Ampère's law. Since we want to find the magnetic field at $r = a$, the current threading the circuit of the line integral is the total plasma current $I_p$. However, other contributions to the poloidal magnetic field exist, e.g. the P4 and P5 coils of MAST (see [85] for a description of the coils of MAST). In the following calculations it is assumed that the extra contribution cancels, and that $B_p$ can be found from the full $I_p$:

$$\frac{1}{\mu_0}\oint_{r=a} B_P(r)\mathrm{d}s = I_p \qquad \Rightarrow \qquad B_P(a) = \frac{\mu_0}{L(a_1, a_2)} I_p \tag{7.10}$$

The length of the perimeter of a poloidal cross section of the plasma is called $L(a_1, a_2)$, where $a_1$ and $a_2$ are the major radii of an ellipse. Since the MAST plasma is quite elongated, it affects the result significantly if the cross section is assumed circular (in the order of 50%). Therefore, we use:

$$L(a, \kappa a) \approx \pi a(1+\kappa)\left(1 + \frac{1}{8}\left(\frac{1-\kappa}{1+\kappa}\right)^2\right)^2 \tag{7.11}$$

where $a_1 = a$ and $a_2 = \kappa a$ [86], and $\kappa$ is the elongation. Combining equations (7.9)-(7.11), we can now calculate $\alpha$ as

$$\alpha = \tan^{-1}\left(\frac{\mu_0 I_p(R_0 + a)}{L(a, \kappa a) B_{T0} R_0}\right) \tag{7.12}$$

In Figure 7.4 $\alpha$ is plotted as a function of the plasma current for two values of $\kappa$. From the figure it may be seen that for the plasma shots with $I_p \approx 0.5$MA, the pitch angle $\alpha$ is approximately 20°, but $\alpha$ increases with $I_p$ for a given toroidal magnetic field.

The angle may not seem very large, nonetheless, the fraction of O-mode in a signal assumed to be in X-mode for a setup, where the reflectometer is mounted horizontally is $\sin(20°)/(\sin(20°) + \cos(20°)) \approx 26.7\%$. Since O- and X-mode are reflected at different densities, the signals received in that case is, firstly, a mixture of signals, and secondly, even from different regions of the plasma. This underlines the necessity of adjusting the reflectometer in the angle $\alpha$.

Optimally, the pitch angle of the reflectometer to the magnetic field should be adjusted continually, i.e. for changing $I_p$. This is naturally not practical, and the angle should ideally be adjusted on a daily basis depending on the expected currents and fields.

Finally, regarding the sign of $\alpha$, the plasma current is counter-clockwise on MAST, when observed from above, and the toroidal magnetic field $B_T$ is

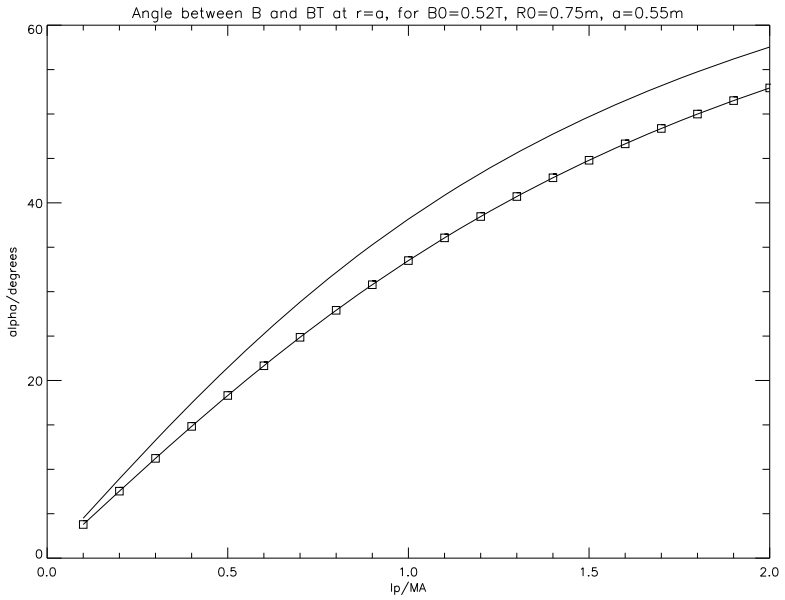


Figure 7.4: The dependence of the pitch angle, $\alpha$, between $B(a)$ and $B_T(a)$, on the plasma current $I_p$. The clear line curve is for an elongation $\kappa = 2.0$, while the "boxed" line curve is for $\kappa = 2.5$. The other parameters are $B_{T0} = 0.52$T, $R_0 = 0.75$m, $a = 0.55$m.

parallel to $I_p$ [87], although it does not have to be parallel for stability. From this the pitch angle is found to be up to down for left to right, when viewed from the outside of the plasma.
A few assumptions were made in the calculations above, and to obtain a better estimate for the pitch angle $\alpha$, an equilibrium code written by Dr. Cunningham was used. A plasma current of $I_p = 600$kA, a minor radius of $r \approx 0.55$m, and a major radius of $R = 0.8$m was used. The pitch angle at $r = R+a$ was $\alpha \approx 30.5°$. Since the plasma often enlarges with increasing currents, we may assume that this value of $\alpha$ does not change much. Hence, the angle chosen for mounting the reflectometer has been 30° to the horizontal plane.

### 7.2.5 Limitations of the reflectometer

Some events in the plasma are not detected (or detectable) by the reflectometer. As mentioned in Section 7.1, no density profile measurements can be made – only fluctuations of a given density surface; generally being well to the low field side of the core region. Therefore, events occurring in the core or at the high field side are not seen. This has been the case in some shots, where strong mode activity was seen in the interferometer signal, while it was not detected by the reflectometer. Likewise, MARFEs [88], which are located close to the centre column, are not seen by the reflectometer.
The reflectometer sees fluctuations of density, and therefore does not see electromagnetic turbulence directly, as it will be discussed in Section 7.4.1.

The sampling frequency of the data acquisition card has been from 250kHz to 500kHz giving a Nyquist frequency down to 125kHz. As it will appear in Section 7.4.3 this is insufficient to obtain all of the relevant spectrum, and a higher sampling frequency is desired for future experiments.
The nonlinear nature of the homodyne detection system also limits the ability to distinguish higher harmonics of the signal being due to an artifact of the detection system or a physical presence in the plasma. An unambiguous demonstration that the harmonics are of physical origin would require a heterodyne detection system.
According to [78] reflectometer measurements of fluctuations do not make sense if the assumption of geometrical optics is not fulfilled, since the resolution of the spectrum of plasma fluctuations degrades. Since the reflectometer frequency is $f = 33.1$GHz, the wave length is $\lambda = 9.06$mm, and according to the assumption of geometrical optics this requires the observable wavelengths to be in the order of at least 2-3cm. As shown in Section 7.2.1, a typical length scale of turbulence $\rho_s$, is in the order of 3-6mm, i.e. we cannot see turbulent structures smaller than $\sim 5\rho_s$, according to [78].

## 7.3 Data treatment

A couple of data analysis codes have been used to analyse the obtained reflectometer data. The program mainly used is the IDL program `vlad_00`, which was provided by Dr. Shevchenko, Culham Science Centre. The main functionality of the program is the original, while some effort has been put in improving the appearance of the hard copies, and adding new ways of presenting the reflectometer data.
Various treatments of raw data are applied in order to produce power spectra and other figures. These include smoothing, apodisation and sometimes filtering. These different techniques will be described in the following.

### 7.3.1 Apodisation

A data trace has a finite length, and if a Fourier transform of the raw data trace is made, some effects of the abrupt start and end of the trace will affect the spectrum. An example of this is a signal of white noise from $t = -a$ to $t = a$, which is equal to the multiplication of a white noise signal of infinite length and a top-hat function:

$$f(t) = \begin{cases} 1 & \text{if } |t| \leq a \\ 0 & \text{if } |t| > a \end{cases}$$

The Fourier transform of $f(t)$ is $\sin(a\omega)/\omega$, and artificial frequencies will arise, related to $f(\omega)$ rather than to the data trace. An example of an artificial signal like this is the Airy pattern observed, when looking through an aperture.
A way of avoiding the artificial frequencies is using apodisation. By this the data is smoothly attenuated, so that the amplitude of the signal is zero

at the beginning and end of the trace. The data presented in this chapter has been multiplied by a triangular apodisation function before the Fourier transforms have been performed. An example of such triangular apodisation can be seen in Figure 7.5, where a white noise (random) signal is presented in (a), and in (b) the signal has been multiplied by the same triangular apodisation function, which is used in the present data analysis. In Figure

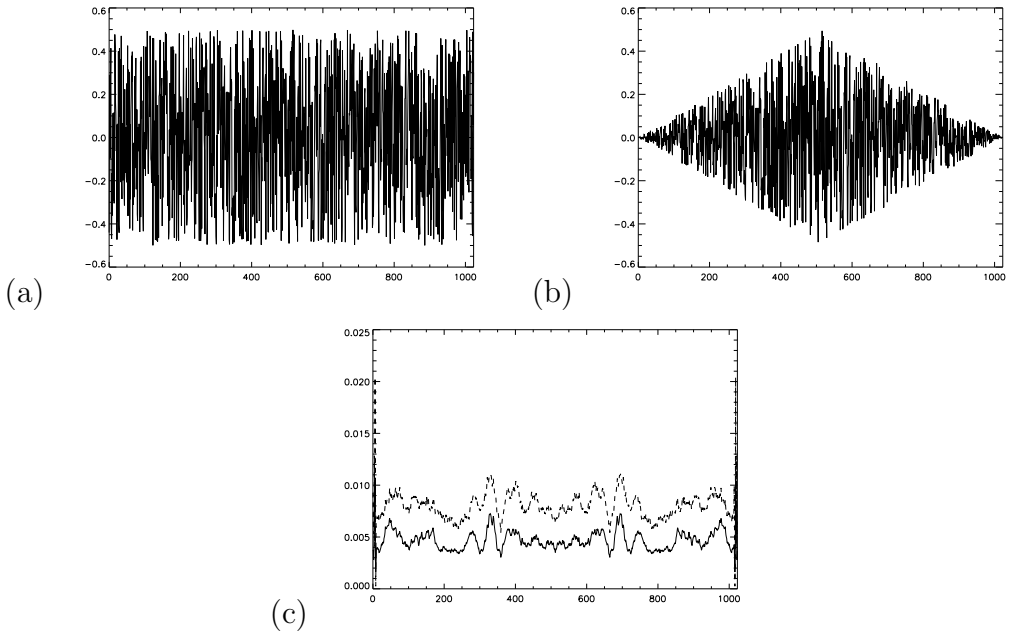


Figure 7.5: (a) A random noise trace, (b) the same trace after apodisation, and (c) the (smoothed) Fourier transform of the two traces (a) and (b). The dashed line is for trace (a) and the full line is for trace (b).

7.5.(c) the Fourier transforms of the two traces are presented, and it is seen that the main difference of the two traces is the level and not the shape. This is naturally due to lesser "energy" in the apodised trace. The effect of the abrupt start and end of the trace of the non-apodised signal is more significant for a higher resolution, since the spectrum of an infinite white noise signal should be flat, whereas the non-apodised signal will vary due to the "top-hat" effect described above.
As seen in Figure 7.5 some information is lost due to the damping of the trace, but this is the cost of using apodisation. The most serious loss of information is in the case where the spectral properties of the signal change during the time slice chosen for calculation of the spectrum. This effect can be tested and/or avoided by choosing a suitable time slice. Finally, other apodisation functions exist, e.g., a Gaussian function, but this is somewhat harder to implement.

### 7.3.2 Smoothing

Smoothing of the spectrum is often included, when power spectra are calculated, since otherwise the main trend of the spectra would be hard to obtain. An example of this is seen in Figure 7.6.(a) and (b). The smoothing used in

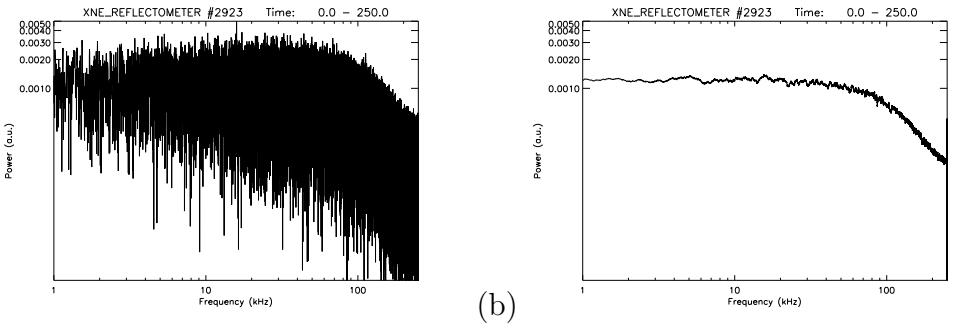


(a) (b)

Figure 7.6: Example of the effect of smoothing of reflectometer data of shot 2923, (a) non-smoothed and (b) smoothed spectrum.

the present work is done with a boxcar average of a specified width, and is of the form:

$$R_i = \begin{cases} \frac{1}{w}\sum_{j=0}^{w-1} A_{i+j-w/2} & \text{for } i = w/2, \ldots, N-w \\ A_i & \text{otherwise} \end{cases}$$

where $w$ is the width of the average, and $N$ is the number of elements in $A$. The disadvantage of smoothing is that the original data is modified, so that variations on fine scales may be lost.

### 7.3.3 Data presentation

The different ways the obtained data is treated in this work will briefly be described below. A common way to present experimental data is to produce a power spectrum. A power spectrum is calculated by:

$$P(f) = 2\,|F(f)|^2$$

where $F(f)$ is the Fourier transform of the data trace.
For the high frequency part of the power spectrum the power level decays as a power law (see Figure 7.6.(b)), and we define the exponent, $s$, of the decay by: $P(f) \propto f^s$. Plots of the exponent of the decaying part of the power spectra as a function of time have been calculated, and an example may be seen in Figure 7.22. This has been made by calculating the power spectrum of a time slice, and finding the gradient of the decaying part by fitting.
A measure of the coherence of a signal can be given by calculating the auto-

correlation function of the signal. The autocorrelation is defined by

$$A(\tau) = \frac{\sum_{t=0}^{T-\tau-1} \Big(s(t) - \bar{s}\Big)\Big(s(t+\tau) - \bar{s}\Big)}{\sum_{t=0}^{T-1} \Big(s(t) - \bar{s}\Big)^2}$$

where $\tau$ is the time lag, $\bar{s}$ is the mean of the data trace $s(t)$, and $T$ is the final time. Plots of the evolution of the width of the autocorrelation have been made (see Figure 7.12), and these may give information of the turbulence in different states.
Finally, spectrograms have been made and will be presented. These are pseudo three-dimensional plots, showing the frequency spectrum of the signal as a function of time. The size of the time slice used for calculating the spectrum can be varied, and this affects the resolution of the spectrograms along the frequency and time axis.

## 7.4 Results

This main section of the present chapter encompasses selections of results found by analysis of the MAST fluctuation reflectometer. The analysis has been divided into three topics: effects of Internal Reconnection Events (IREs), effects of Neutral Beam Injection (NBI), and finally H-mode detection. The main emphasis will be put on the last topic, since it links well to the rest of this thesis.

### 7.4.1 IREs

In a plasma different events may occur, leading to an increased transport or a change of state. In MAST the most important class is Internal Reconnection Events (IREs), where magnetic flux surfaces in the plasma reconnect, leading to a partial loss of confinement. A suitable initial test of the fluctuation reflectometer is to detect large events like IREs. After an IRE the density often drops, causing the reflecting surface to move, and this has to be taken into account when interpreting the results.
In Figures 7.7.(a) and (b) the traces of the line-integrated density, the plasma current, NBI input, and the reflectometer signal are presented for shots 2410 and 2574, respectively. In the traces of the reflectometer signal an effect of the IREs is seen. The clear effect is especially seen in shot 2574 that was made after the angle of the reflectometer (Section 7.2.4) had been changed from 20° to 30°.
The effect of the IREs may be even clearer, when looking at the spectrograms in Figures 7.8.(a) and (b). For the case of shot 2410 it is seen that the IRE causes a sort of change of state for the plasma. Take for instance the signal at $t = 40$ms and $t = 105$ms (before and after the IRE), where the density, plasma current, and NBI power are the same. Between the two

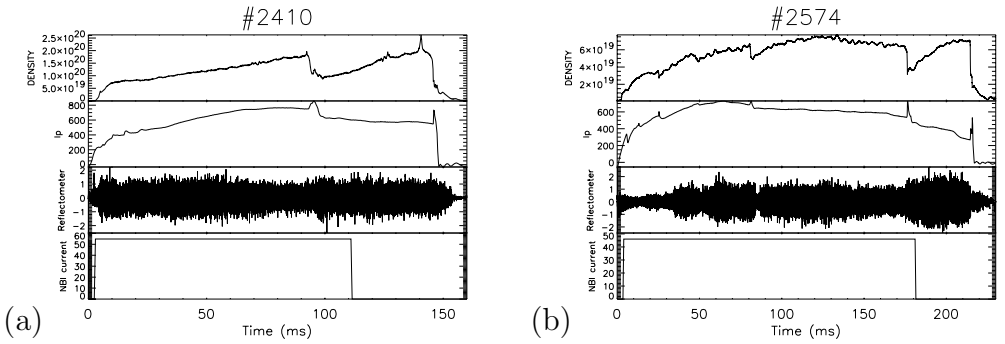


Figure 7.7: The temporal evolution of the (line-integrated) density (in $m^{-2}$), the plasma current (in kA), the reflectometer signal (in V), and the NBI current (in A) for two shots with major IREs, (a) 2410 and (b) 2574.

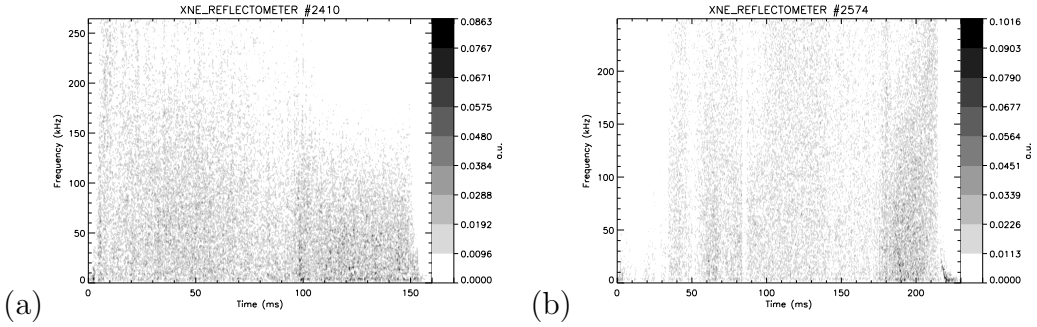


Figure 7.8: Spectrograms for two shots with major IREs, (a) 2410 and (b) 2574.

instants the slope of the spectrum has changed. The effect may be clearer in the trajectory graph presented in Figure 7.9, which shows the exponent of the power spectrum as a function of the line-integrated density for a number of points in time. The line connects the time points, and the points in the lower part of the graph correspond to times after the IRE. It is clear from this graph that the plasma is in two different states before and after the IRE, and that this has nothing to do with different densities of the plasma. Such a 'bifurcation' has been searched for in other shots, but shot 2410 is until now the most pronounced example.

The effect might be explained by the plasma changing to or from DND[2]-configuration from or to a limiter configuration. The $D_\alpha$ diagnostic (see description in Section 7.4.3) could indicate whether that was the case, but, unfortunately, it was not running during shot 2410.

The explanation for the behaviour could be as simple as different configurations. However, a similar bifurcation has been seen in JET [89], where abrupt changes in the confinement have been observed after a so-called $X$-event occurs, while the macroscopic plasma parameters remain the same. Therefore, the findings at MAST (shot 2410) could be a subject of further investigation.

[2]DND is an abbreviation for Double-Null-Divertor and is the state where the plasma has X-points in both the upper and lower divertors.

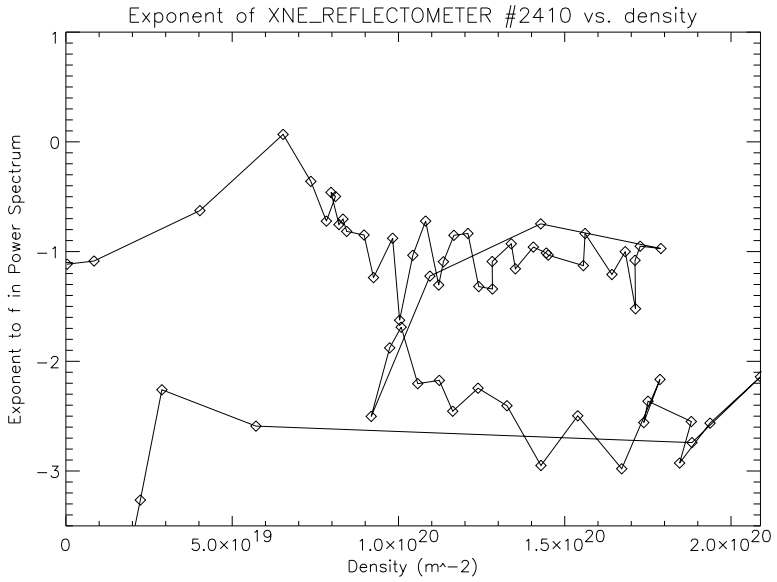


Figure 7.9: Trajectory graph for shot 2410 showing the exponent of the power spectrum as a function of the line-integrated density. Each scatter point is 2.5ms apart. The upper part is for early times.

Conclusively, it is clear that the reflectometer signal is influenced (both in amplitude and frequency) by the IREs.

### Precursors to IREs

One interesting application of the reflectometer would be, if it could trace precursors to IREs. But, the search for IRE precursors in the reflectometer data, has brought no decisive conclusions, yet. Though, there seems to be an increase in the width of the autocorrelation before some of the IREs. These observed increases may be just occasional, and the quantitative value of the autocorrelation is only significant for a few cases[3]. Those IREs in question may in fact be a large IRE following a small IRE. The increase in autocorrelation can in this case be due to the first IRE, since an increase in autocorrelation is seen after IREs, although not in all cases. The increase in autocorrelation after an IRE can be explained by the plasma relaxing into a more quiet state.
The lack of IRE precursors in the reflectometer data may not be surprising, since the IREs are mainly magnetic configuration instabilities, i.e. the mode-locking and reconnection of magnetic flux surfaces. Furthermore, this may happen on a very fast time-scale that might not be properly resolved by the reflectometer data. On the other hand, *if* these reconnections were to show up indirectly in the reflectometer data, it would most probably be as an

[3]However, it must be pointed out that the autocorrelation time is generally not much more than the data sampling interval, so these tests should be repeated, when a faster sampling is available.

increase in the autocorrelation.

### 7.4.2 Effect of NBI on turbulence

A common way of heating a plasma is to inject an energetic beam of neutral atoms - typically hydrogen or deuterium. During the first MAST campaign the power input from the Neutral Beam Injection (NBI) was 250-800kW, compared to an Ohmic heating of approximately 250-4000kW [85].
We would expect the NBI to influence the flows and turbulence in the plasma, and therefore we compare two nearly identical shots without (shot 2405) and with (shot 2413) NBI in Figures 7.10.(a) and (b). The large spikes in the

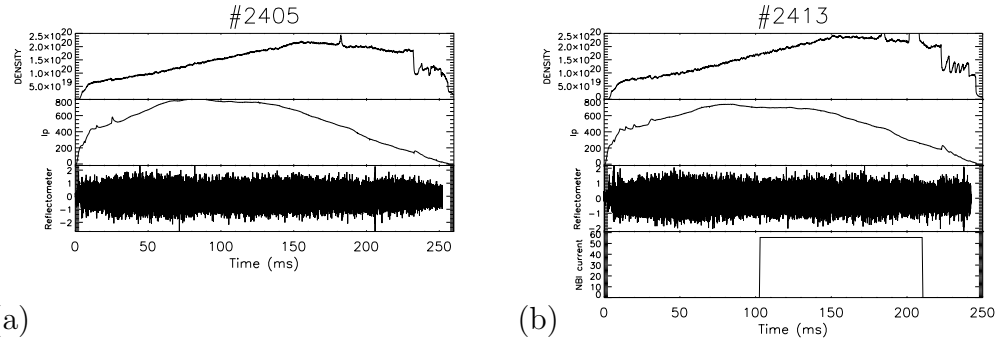


Figure 7.10: The temporal evolution of the (line-integrated) density (in $m^{-2}$), the plasma current (in kA), the reflectometer signal (in V), and the NBI current (in A) for a shot without (2405) and a shot with NBI (2413).

line-averaged density signal of 2413 are MARFEs, and these are not picked up by the reflectometer, since they are located at the high field side of the plasma.
In the spectrograms in Figures 7.11.(a) and (b) it is seen that the NBI indeed influences the turbulence, since during NBI pulses the fluctuation spectrum steepens, i.e. high frequency turbulence decreases. Consistent with this it

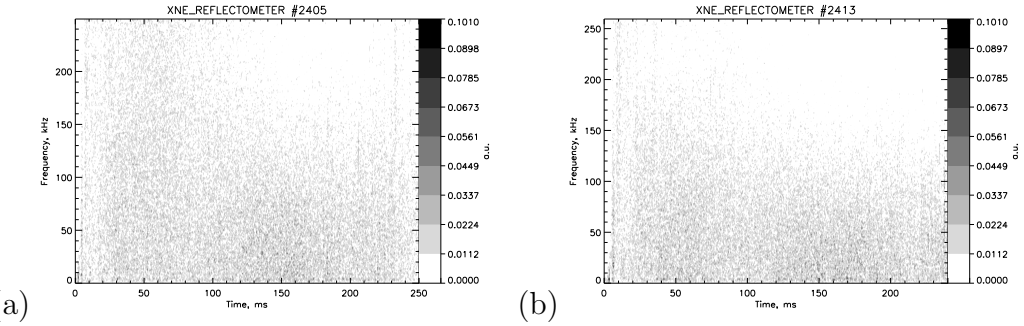


Figure 7.11: Spectrograms for a shot without (2405) and a shot with NBI (2413).

seems that the width of the autocorrelation of the reflectometer signal broadens as it may be seen in Figure 7.12. In linear devices it is possible to make

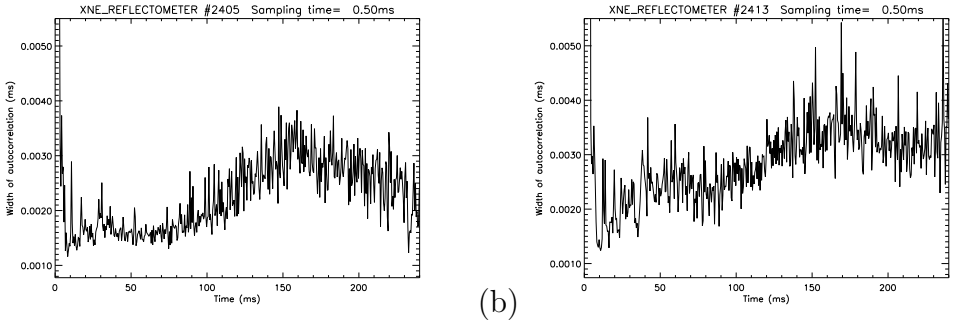


(a) (b)

Figure 7.12: The temporal evolution of the width of the autocorrelation function calculated in time intervals of 0.5ms, for a shot without (2405) and a shot with NBI (2413).

mode selective control of drift wave turbulence [90,91]. This is performed by externally imposing given frequencies by electrodes, and it is observed that the broad band drift wave turbulence in the plasma, with time, synchronizes to the few imposed frequencies. Analogous to this, it may be thought that the reason for the alteration of the turbulence by the NBI, could be that the existing turbulence synchronizes with the turbulent field imposed by the NBI. For the MAST case the frequencies of the NBI induced turbulence is not known, and it may not be a very narrow band. However, the effect of turbulence synchronizing to a strong and steadily imposed signal could be the same as that seen in [90,91]. In the linear device case the synchronization is tested by sweeping the electrode frequencies, whereas a similar test is not immediately possible for the MAST NBI case.

### 7.4.3 H-mode detection

#### H-modes

In magnetic confinement plasma devices several operational regimes exist, and in 1982 the high confinement mode or H-mode was discovered on ASDEX in Garching, Germany [31]. During an H-mode the radial shape of the plasma density is box-like, as opposed to the peaked profile in the ordinary low confinement mode (L-mode). The particle and energy confinement times are increased, and generally, a decrease in the turbulence levels is observed.
No single explanation of the H-mode has yet been proven, but during H-modes strong poloidal sheared flows are observed in the edge region. The shear flow is thought to cause the turbulence levels to decrease, and the anomalous transport to be reduced - an effect well-known from theory (see Chapters 2 and 6). The poloidal flow is probably an $E \times B$-flow caused by a radial electric field, which may be set up by the turbulence itself, as it is discussed in Chapter 6. Alternatively, in order to assist the generation of the $E \times B$-flow, experiments have been performed in TEXTOR, where a radial electric field is imposed by an inserted electrode [92, 93]. One of

the conclusions from these experiments is that the changes in the electric field, govern the changes in the density gradient [93], i.e. confirming that the $E \times B$-flow helps improving confinement.

In the later part of the MAST spring 2000 campaign more than 10 H-mode shots were obtained, and some of these are described in [94], where results from the reflectometer are also included. Corresponding H-mode results from NSTX are presented in [95].
The reflectometer obtained data from seven of the MAST H-mode shots: 2941, 2942, 2948, 2949 (brief), 2950, 2951, and 2952. The H-mode of shot 2949 was so brief that it has not been included in the analysis.
As an example of an H-mode shot we present the line-integrated density, the $D_\alpha$ signal (see the description in the next paragraph), and the raw data of the reflectometer in Figure 7.13. We see that when the plasma is in H-mode, the density rises, and the signal of the reflectometer drops, a fact we return to shortly. To give a clearer impression of the significance of the H-modes,

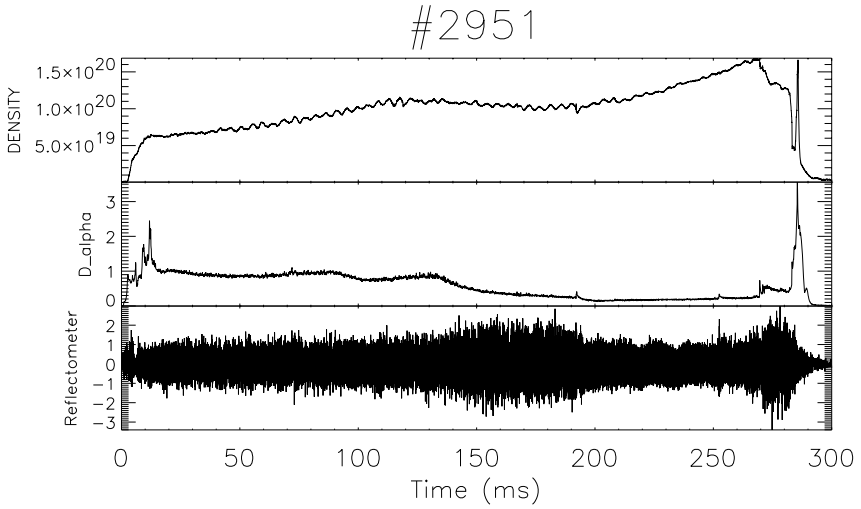


Figure 7.13: The line-integrated density, the $D_\alpha$ signal and the reflectometer trace of MAST discharge 2951, where the H-mode transition occur at $t \approx$ 194ms.

a series of three pictures (made by the fast video camera), demonstrating the difference between L-mode and H-mode, is shown in Figure 7.14. In the L-mode the plasma radiates a lot, and the edges are very fuzzy. This is in great contrast to the H-mode, which has very sharp edges and only little radiation in the visible spectrum. Note that both the L- and the H-mode presented are in the DND-configuration.

### Diagnostics

During the H-modes the density fluctuation levels were expected to decrease and the frequencies to drop, and indeed,this was seen by the reflectometer as presented in Figure 7.15. The shots containing the H-modes were rather long (up to 380ms), and in order to contain the full data trace, the sampling

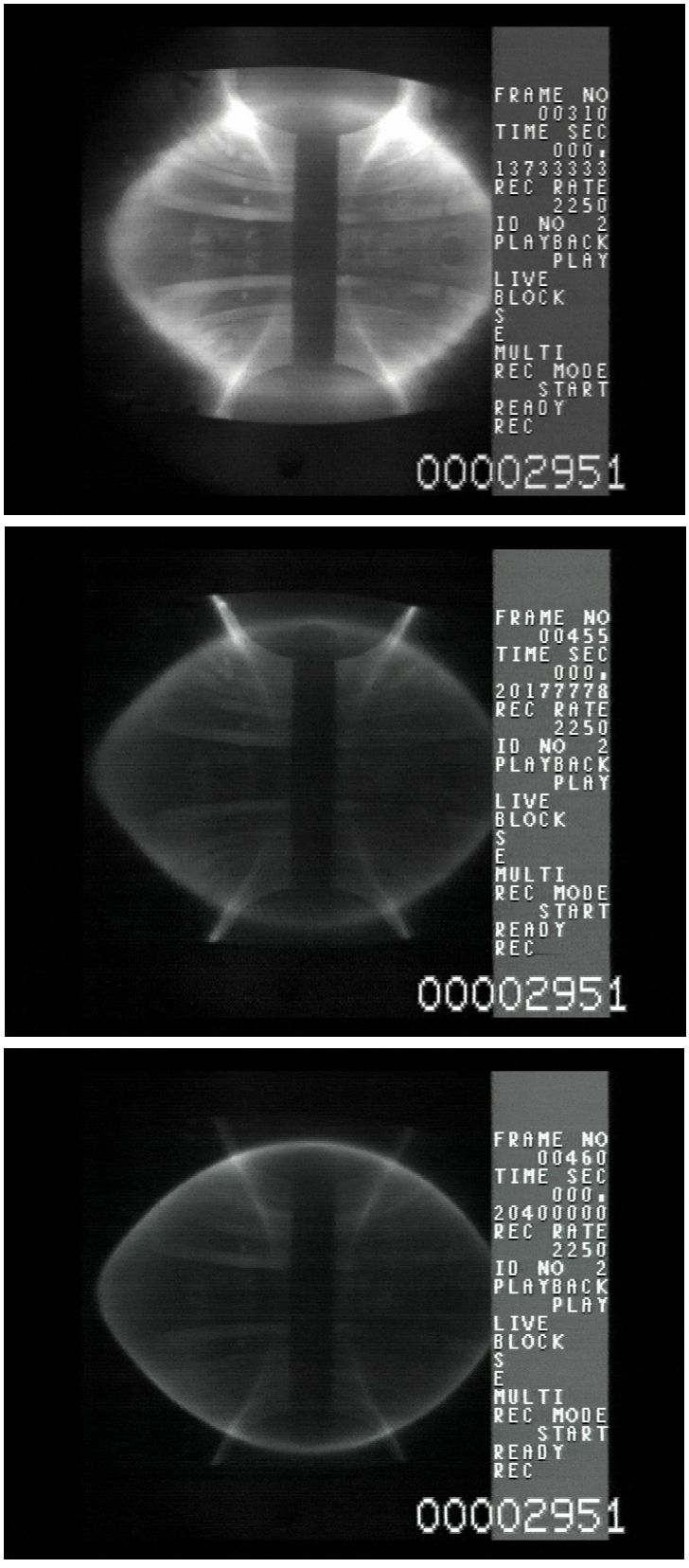


(a)

(b)

(c)

Figure 7.14: Snapshots by the fast video of MAST discharge 2951 (a) in L-mode, (b) just 1ms before/during L-H transition, and (c) in H-mode. Notice the very sharp edges of the plasma in H-mode.

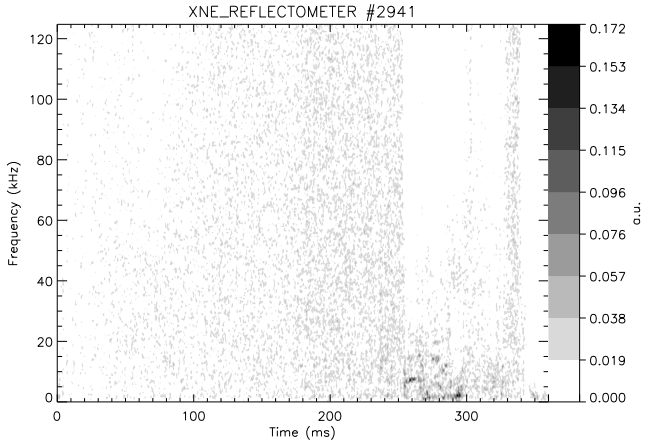


Figure 7.15: Spectrogram showing the evolution of the density fluctuation spectrum seen by the reflectometer over shot 2941. Note the sharp L-H transition at $t \approx 254$ms.

frequency of the reflectometer was lowered to 250kHz, so that the Nyquist frequency in the spectra is only 125kHz.
In order to assess the performance of the reflectometer during the H-mode, the fast video and a $D_\alpha$ signal were used to compare the timing of ELMs (edge localised modes) and transitions between L- and H-mode. The fast video had a $D_\alpha$ filter mounted for the H-mode shots presented here.
The $D_\alpha$ signal trace used is `XIM_DA/HM10/R/F`, since it is located in the horizontal midplane as the reflectometer, though, directly opposite. The $D_\alpha$ signal is obtained by a photomultiplyer that detects line radiation for neutral deuterium being excited in the plasma edge. Particles leaving the plasma are transported in the scrape-off-layer (SOL) to the divertor, where the ions and electrons recombine. The resulting atom is then recycled into the plasma causing $D_\alpha$ emission. The time-scale for this recycling proces is estimated to be 100$\mu$s [96]. During the H-mode this transport in the SOL is reduced, and the $D_\alpha$ signal drops, since less recombination takes place. This can be seen in Figure 7.13, and will be clearer from some of the following figures.
Finally, data from the spectrometer Celeste has been used in the form of the evolution of the poloidal flow velocity.

### Timing

It is difficult to give a precise timing of the start, end, and events of the H-modes; firstly, because the diagnostics have a limited temporal resolution, secondly, because there is no very well-defined criterion for the time of the exact transition. The latter is somewhat subjective, and it is important to state which criterion has been used.
The fast video had for the shots presented here a sampling time of 0.4444ms, which is a severe limitation in the timing. For the shots treated here the transition into H-mode was apparently triggered by a sawtooth-like event. The duration of the L-H transition used in the present analysis is the time

period between this event and the first quiet H-mode picture.
The $D_\alpha$ trace has a sampling time of 77$\mu$s, but due to the exponential decay shape of the trace in a L-H transition (see Figure 7.16.(d)), it may be difficult to establish the precise timing of the transition. The transition may be argued to happen when the exponential decay starts, or when the value of the $D_\alpha$ signal is below a characteristic level of the signal hitherto. Here the transition has been assumed to start at the former and end at the latter.
The reflectometer has a sampling time of 4$\mu$s, however, the shortest practical time-slice for calculating a spectrum is in the order of 50$\mu$s. The criterion for the L-H transition time used here, is the time when the spectrum changes from being broad band ($f \geq 125$kHz) to narrow band ($f \lesssim 60$kHz). By this definition the timing of the L-H transition may well be affected, if the bandwidth of the reflectometer is increased, since turbulence with frequencies above 125kHz may be damped earlier.

### The L-H transition results

The L-H transition has been studied for all the H-mode shots, and the timing has been compared between the reflectometer signal, the $D_\alpha$ signal, and the video. In Figure 7.16 the full H-mode and a zoom on the L-H transition for shot 2941 are presented. From the figure it is seen that the transition

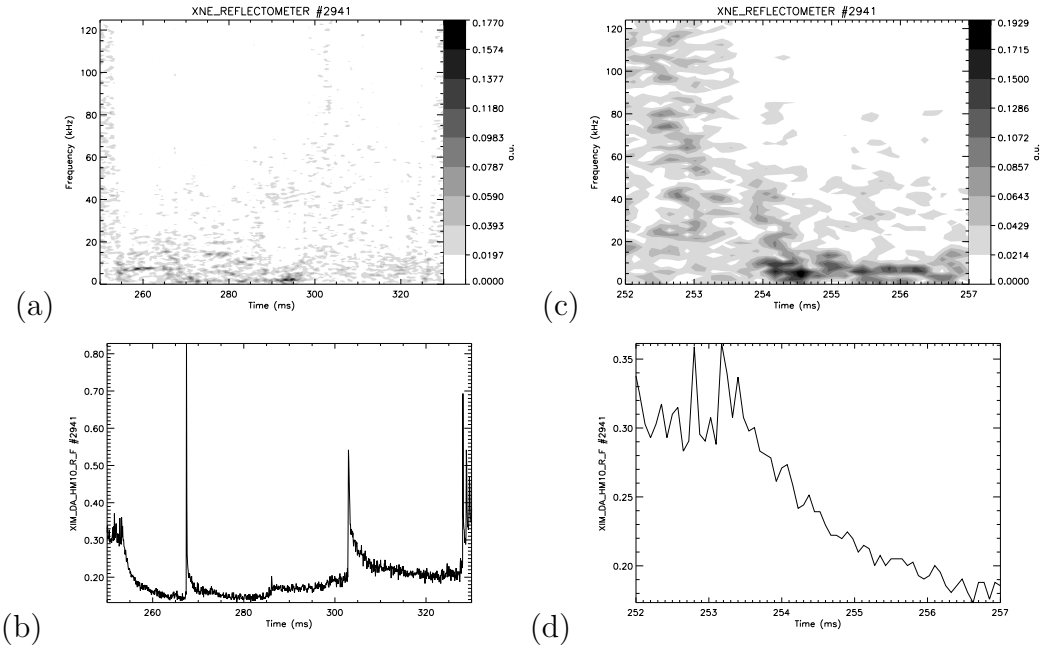


Figure 7.16: The evolution of the H-mode of shot 2941 as seen by (a) the reflectometer and (b) the $D_\alpha$ signal. And a zoom on the start of the H-mode as seen by (c) the reflectometer and (d) the $D_\alpha$ signal.

starts approximately at the same time for the reflectometer and the $D_\alpha$ signal ($t = 253.5$ms), while the transition is shorter for the reflectometer, due to the relatively slow decay of the $D_\alpha$ signal. According to the reflectometer

(and the definitions given above) the L-H transition time is in the order of 0.2ms for shot 2941, while the transition time is generally in the order of 0.5ms. An equivalently precise determination of the transition time is hard to obtain for the fast video and $D_\alpha$ signal, and the transition times obtained for those are generally in the order of 0.5-2.0ms.

### ELMs

ELMs are instabilities in the edge region of a plasma in H-mode. They cause brief, drastic increases in the energy and particle fluxes out of the plasma. The physical background of ELMs is not yet fully understood, but a thorough description of experimentally observed ELMs can be found in [97]. In all of the H-mode shots treated here ELMs occur, and these are generally seen in all three diagnostics. An example of this is presented in Figure 7.17, where the ELMs are perfectly timed between the reflectometer and the $D_\alpha$ signal. However, the reflectometer does sometimes see events not detected

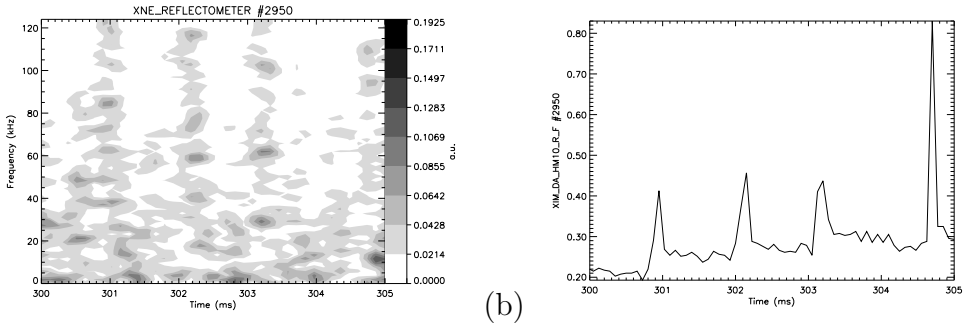


(a) (b)

Figure 7.17: ELMs at the end of the H-mode of shot 2950 as seen by (a) the reflectometer and (b) the $D_\alpha$ signal.

by the fast video or the $D_\alpha$ diagnostic. These events are probably low amplitude fluctuations that do not affect the H-mode confinement sufficiently to influence the D recycling process. An example of this is shown in Figure 7.18, where the video (not shown), the $D_\alpha$ diagnostic, and the reflectometer all detect an ELM at $t = 267.4$ms, whereas only the reflectometer detects the event at $t = 264$ms. This first event, which is not as broad band as the ELM, is purely a density fluctuation event, and may be the cause of the following ELM. Generally, it is seen that most ELMs are preceded by small broader frequency events, or more often an increasing broadening of the frequency spectrum. The frequency spectrum between the ELMs in Figure 7.17 is also broader than in the rest of the H-mode, which is presented in Figure 7.19. This indicates that the turbulence is less coherent in this state, an effect that will be discussed shortly. An explanation of the preceding broadening of the spectrum could be that the strong flow is gradually weakening, which then allows a sudden strong burst of turbulent fluctuations. These are then damped by a reoccurrence of the flow (or organised into a flow again), which is relatively easily obtained, since the plasma is in a state optimised for H-mode. This cycling process of intermittent bursts of flux damped by shear

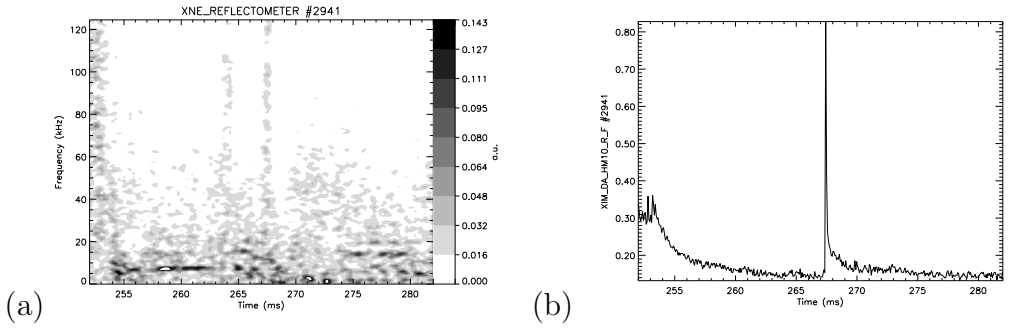


Figure 7.18: ELMs in the early part of the H-mode of shot 2941 as seen by (a) the reflectometer and (b) the $D_\alpha$ signal.

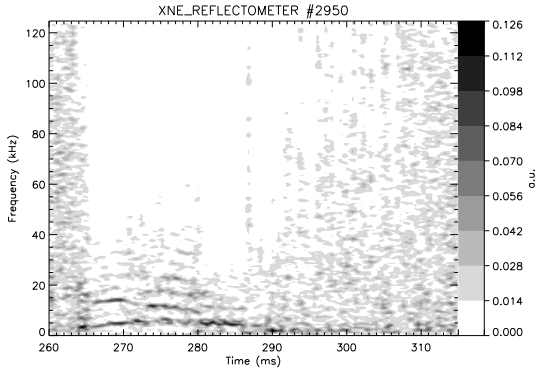


Figure 7.19: The H-mode of shot 2950 as seen by the reflectometer. Note the broadening of the frequency band towards the end of the shot.

flows is often seen in numerical modeling of turbulence. Examples of this is found in Chapter 6, although the models presented there are probably too simple to really explain the physics of ELMs.
If we look further at the spectrogram in Figure 7.18 before the ELMy events, it is seen that a very strong low frequency mode ($f \approx 7$kHz) forms just after the transition into H-mode. At around $t = 261.5$ms the mode starts to decay and is no longer dominant when the first broad band frequency event occur. Generally, it is seen in the reflectometer results that strong low frequency modes tend to damp the formation of ELMs, and this can also be seen in the spectrogram of the H-mode of shot 2950 presented in Figure 7.19. Other examples of the suppression of broad band frequency events are seen in shot 2951 and 2952, two quite similar shots, of which only the latter is presented here in Figure 7.20. An interesting feature of the spectrogram of shot 2952 is that a very large number of harmonics of a strong $\sim$ 4kHz fundamental mode occur. At $t = 250$ms up to the $11^{\text{th}}$ harmonic can be distinguished, all being below 40kHz. The presence of the harmonics, though, could well be an artifact of nonlinear effects of the homodyne detection system as discussed in Section 7.2.5. However, at some instants the lower harmonics disappear, while the higher harmonics persist, and this would indicate that the harmon-

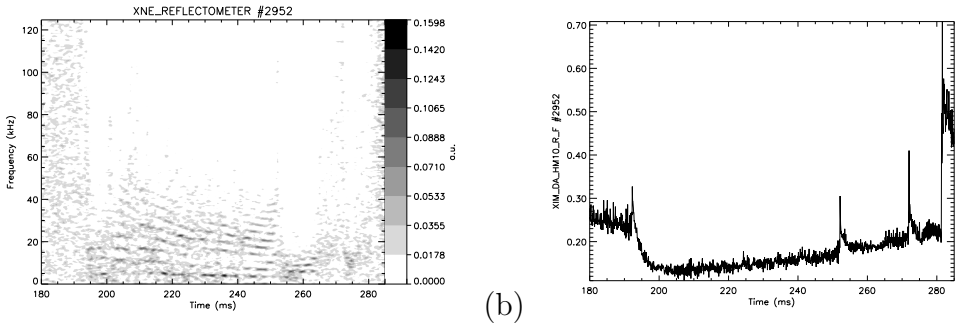


(a) (b)

Figure 7.20: The H-mode of shot 2952 as seen by (a) the reflectometer and (b) the $D_\alpha$ signal. Note the strong low frequency mode and its harmonics.

ics may be of physical origin. It is also worth noting that the strong modes are chirping down in frequency.
In order to take a closer look at the evolution of the modes, a number of power spectra each calculated over 5ms are presented in Figure 7.21. It is clear that the level of the higher frequencies is reduced, when the level of low frequencies increases. From Figure 7.22 we see that the total energy of the density fluctuation power spectrum does not change much over the H-mode. This illustrates that an almost constant energy is distributed between the lower and the higher frequencies, and the energy does not just disappear when the level of the low frequency fluctuations decrease. In Figure 7.21 it is further seen that the fundamental mode chirps from approximately 5kHz to 3.5kHz. The level of the fundamental mode is not always higher than the harmonics, which further suggests that the harmonics are not artifacts of the homodyne detection system. The disappearance of some of the lower harmonics is also clearly seen.
Finally, in recent numerical simulations of turbulence in MAST, performed by Dr. Thyagaraja's CUTIE code, an H-mode is reached, and the spectrum is dominated by a strong (1,1)-electromagnetic mode with a frequency of approximately 4kHz [98]. In the edge region a mode with $\sim$ 20kHz also occurs. The agreement between the reflectometer data and the CUTIE results on the 4kHz mode is interesting, but may be coincidental.

### H-L transition

We saw in the previous section that a certain broadening of the frequency spectrum of the density fluctuations is seen prior to events like ELMs. This is also the case for the final H-L transition, which in more cases seems to be induced by ELMs, and this would in part explain the observed broadening. However, for some shots the build-up phase where the frequency spectrum broadens up to a H-L transition can be in the order of 10ms. An example of this is presented in Figure 7.23, where the full H-mode and a zoom on the last part of the H-mode are presented.
The mechanism is probably that the poloidal flow decreases towards the end of the H-mode, and therefore the width of the density fluctuation spectrum

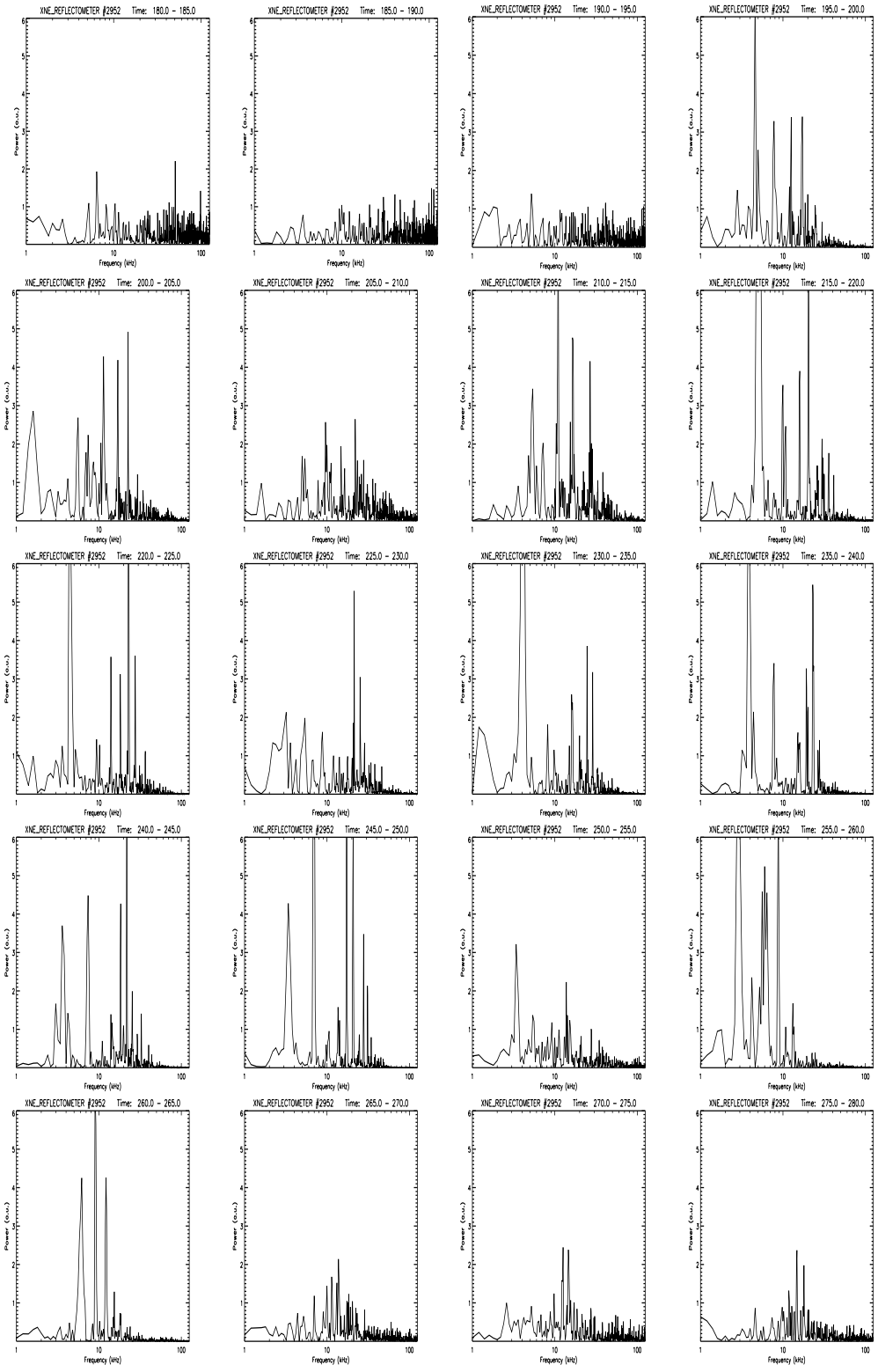


Figure 7.21: Power spectra over 5ms time-slices covering the H-mode of shot 2952. Note the strength and spectral location of the harmonics.

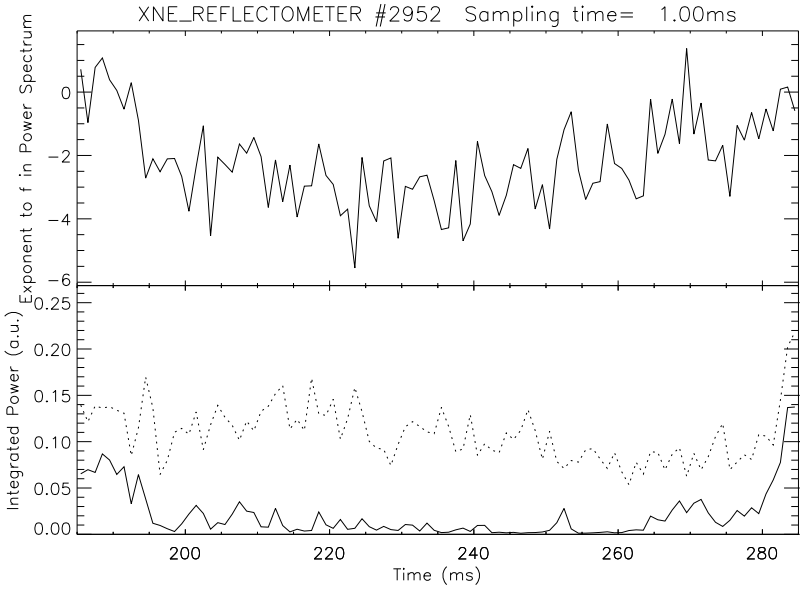


Figure 7.22: The upper graph shows the exponent of the high frequency part (50-110kHz) of the power spectrum for the H-mode of shot 2952. The lower graph shows the energy in the high frequency modes (full line), and the total energy in the fluctuation spectrum (dotted line).

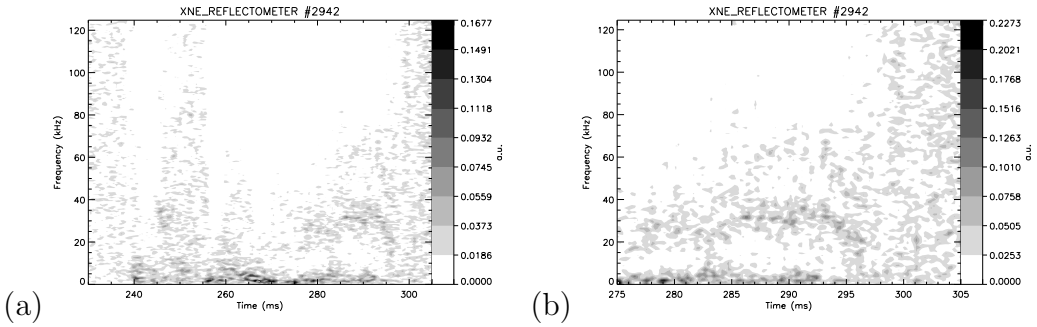


Figure 7.23: Spectrogram of reflectometer data for shot 2942 for (a) the full H-mode and (b) the last part before the H-L transition.

increases, since the fluctuations are not depressed as much. An equally consistent picture is that of the energy of the flow being transferred into turbulent fluctuations, as the opposite process of that described for the L-H transition.

### Conclusion

For several of the H-mode shots the transition from broad band spectra (here $f \geq 125$kHz) to low frequency spectra seems to be at the same time as, but somewhat faster than, the L-H transition detected by the $D_\alpha$ signal and the fast video (see, e.g., Figure 7.16). This drop in high frequency turbulence may very well start a little earlier for the higher frequencies, but this will only be apparent if the bandwidth of the reflectometer is increased as discussed

in Section 7.2.5. But even the present results suggest that it may be the turbulence level that decreases before the H-mode occurs, as the turbulence is possibly being organised into a poloidal shear flow, followed by the L-H transition. This interpretation may be disputed, especially because the poloidal flow velocity measurements (Celeste) seem to indicate that the major changes in the flow velocities occur just after the L-H transition is indicated by the $D_\alpha$ signal. A first rough estimate of the evolution of the poloidal flow velocity for a part of shot 2952 is shown in Figure 7.24. It may be, though, that only a small change in the poloidal velocity is needed to initiate the H-mode, and that the major change is due to a self-amplifying process after the L-H transition has occurred [99]. Although the interpretation of the

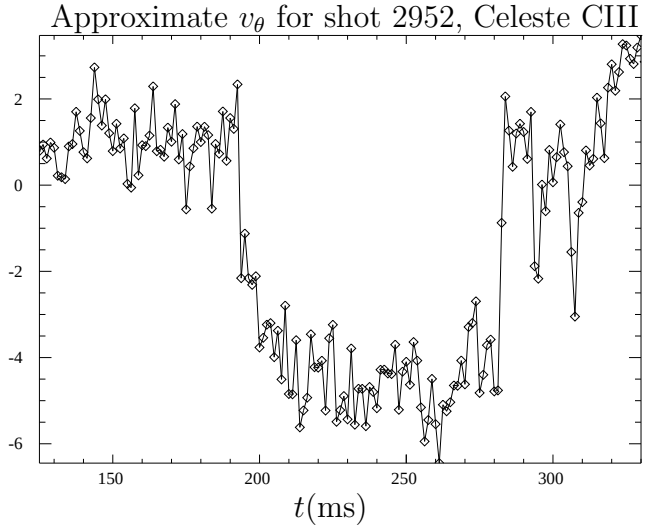


Figure 7.24: The evolution of the poloidal velocity for shot 2952 measured by Celeste. The graph presented is only a rough estimate and the absolute values are not exact but in the correct range [99].

precursor of the L-H transition seen by the reflectometer may be disputed, it is clear from the results presented that both ELMs and H-L transitions are preceded by a broadening of the fluctuation spectrum. This gives further encouragement to increase the sampling frequency to detect probable clear precursors to the L-H transitions.

## 7.5 Discussion and conclusion of the MAST fluctuation reflectometer

The MAST fluctuation reflectometer has proven to work as intended, and the best performance has been in the area of diagnosing H-modes. One outcome has been very interesting results, which strongly suggest that a prior increase in the density fluctuation level is responsible for or strongly connected to ELMs in H-mode and the H-L transition. The H-mode detection

by the reflectometer has also proven to be a good supplement to the $D_\alpha$ diagnostic.
One desired requirement for further investigations with the reflectometer is to increase the sampling frequency to at least 1MHz. This will primarily enable more firm conclusions on the H-mode data, not the least on the topic of precursors to the transition. A further possibility for development is to install more reflectometer channels. An advantage of having more frequencies is that correlation lengths of turbulent structures might be estimated by correlating signals from two reflectometer channels, provided the frequencies are sufficiently close. In Table 7.2 the estimated spatial distances between the cut-offs belonging to the 4 Gunn oscillators in stock are listed. These are calculated assuming a parabolically shaped density profile. As shown in Section

| Model number | $f_{min}$ (GHz) | $f_{max}$ (GHz) | $r_{co}(f_{max})$ (m) | $r_{co}(f_{min})$ (m) | $(\Delta r_{co})_{max}$ (m) |
|---|---|---|---|---|---|
| 917 | 32.54 | 33.53 | 0.4579 | 0.4647 | |
| | | | | | 0.0314 |
| 918 | 37.57 | 38.57 | 0.4177 | 0.4265 | |
| | | | | | 0.0405 |
| 919 | 42.58 | 43.61 | 0.3653 | 0.3772 | |
| | | | | | 0.0472 |
| 920 | 47.17 | 48.55 | 0.2966 | 0.3181 | |

Table 7.2: Table of frequency ranges and spatial distances for the 4 available Gunn oscillators. The radial positions of the cut-offs were calculated using a line-integrated density of $1 \cdot 10^{20}\mathrm{m}^{-2}$, $a = 0.55$m, and an X-mode signal. During H-modes the $(\Delta r_{co})_{max}$ will be significantly smaller than presented here. The number of significant digits is not as high as presented.

7.2.1 the typical length scale of the turbulence, $\rho_s$, is in the order of $3-6$mm depending on the actual temperature and magnetic field. If this is compared to the differences in Table 7.2 it is seen that the channels are $\sim 5-10\rho_s$ apart, which may be too far to see any correlation. However, the geometrical optics considerations of Section 7.2.5 indicated that the resolution of the reflectometer is in the order of $\sim 5\rho_s$, and nevertheless, it might be possible to see some large structures. Furthermore, the $(\Delta r_{co})_{max}$ presented in Table 7.2 is based on the assumption of a parabolically shaped (L-mode) density profile. For H-modes the $(\Delta r_{co})_{max}$ will be significantly smaller providing the pedestal density is sufficiently high. However, one should not forget the problems of correlation reflectometry signals being dominated by multiple small angle scattering processes, occurring on the path towards the cut-off surfaces, as mentioned in Section 7.1.1. These problems, however, may not be significant in the case of H-mode, since the steep density gradient will cause the separation of the cut-off positions to be in the order of millimeters, and since the launched wave does not travel far in the plasma, the effects of multiple scattering may be much less pronounced, and thus, correlation measurements may be feasible.

Finally, we should mention that recently two additional reflectometer channels have been installed at MAST, and the first results are anticipated in the next campaign.

# Chapter 8

# Discussion of hollow $T_e$ profiles at MAST

During the MAST spring 2000 campaign hollow electron temperature, electron density and electron pressure profiles were observed. The profiles were obtained by the Thomson scattering (TS) system, which provided one profile (of each quantity) per shot. An example of TS measured electron temperature, density and pressure profiles is presented in Figure 8.1, where $T_{e,max} \approx 600$ and $T_{e,centre} \approx 150$.
In the spring 2000 campaign the hollow profiles were not made intentionally, and the collection of shots exhibiting hollow profiles was thus spread over the whole campaign. Some of the shots exhibited hollow electron temperature profiles, and some hollow electron density profiles. Additionally, for a majority of the hollow profile shots, features that may be described as transport barriers were observed. The hollow profile shots have been categorised by Dr. Meyer and I. Lehane [101], and the categorisation is presented in Table 8.1.

| Name | $T_e$ | $n_e$ | Impurities | Time in shot | Regime |
|---|---|---|---|---|---|
| Ears | normal | sort of hollow | no indication | late | H-mode |
| Enh. imp. | hollow | peaked | enh. FeXVi | $< 100$ms | start-up |
| Transport | hollow | flat or hollow | no indication | $< 100$ms | start-up |

Table 8.1: Categorisation of the hollow profile shots observed in the spring 2000 MAST campaign [101]. Enh. is an abbreviation for enhanced.

## 8.1 Possible explanations of the hollow profiles

After the end of the spring 2000 campaign three explanations for the hollow temperature profiles have been proposed:

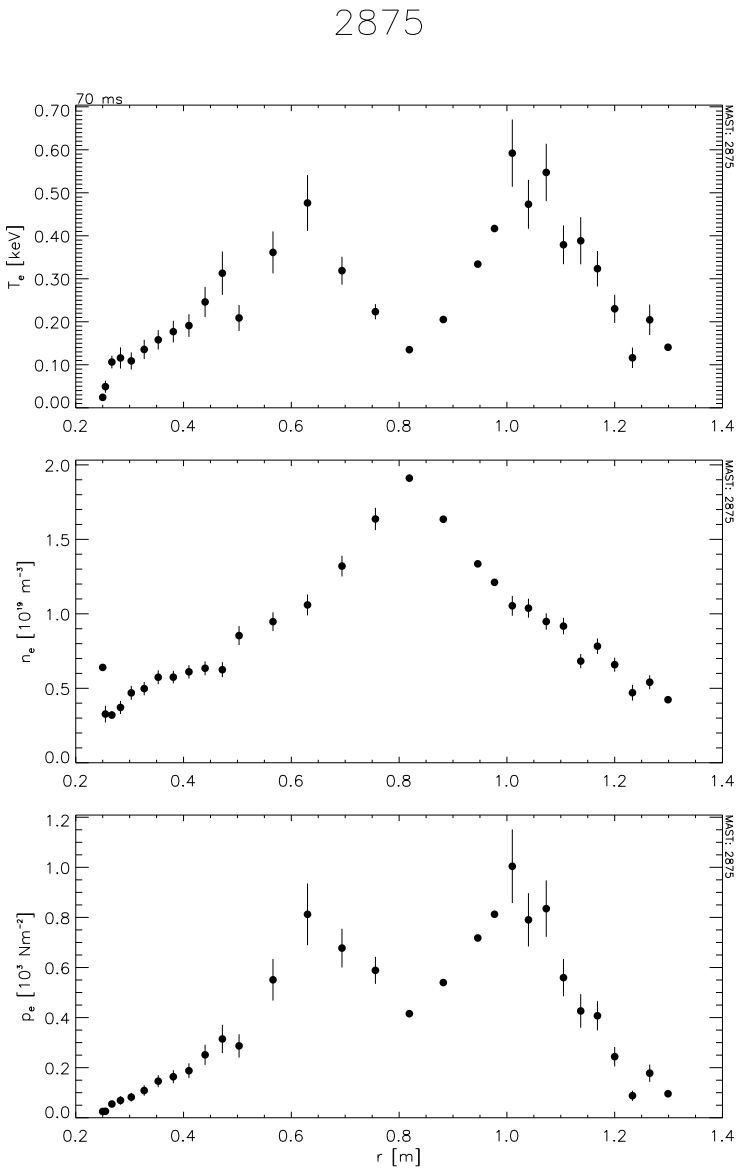


Figure 8.1: The electron temperature, electron density, and electron pressure of MAST shot 2875 obtained by Thomson Scattering [100].

a) slow current penetration

b) high-Z impurity radiation cooling

c) turbulent advection and creation of transport barriers

All three effects could in theory contribute to the observed hollow profiles, and yet a fourth explanation could still arise.
Regarding a), the slow current penetration explanation is connected to the effect of the current penetrating the (almost perfectly) conducting plasma in a time of order $\mu_0 a^2/\eta$, where $\mu_0$ is the permeability, $a$ is the minor radius, and $\eta$ is the resistivity of the plasma. If the rate of current rise is faster than the penetration time, a skin current may be formed [88], with the result

of dominant off-axis heating. The importance of the current profile on the temperature profile is described in [102]. However, it is unlikely that such hollowness as seen in the $T_e$-profiles for, e.g., shot 2875 in MAST could be caused by slow current penetration, and even if it was, it would be transient due to inward heat transport down the gradients. Furthermore, the "violent" initiations of the MAST plasmas by the merging-compression scheme [85], will most likely cause a large part of the current to penetrate the plasma initially.
Regarding b), the radiation by impurities is the most straightforward explanation, and it could in theory be responsible for low core temperatures. High-Z impurities like iron (Fe) may enter the plasma after the plasma has touched the wall, for instance. There may be an inward pinch on the Fe ions that accumulate in the centre, and they are cooling the plasma core by line radiation. This effect is identified for one of the classifications in Table 8.1. Similar scenarios has been seen in other machines such as START where the explanation of impurity radiation was shown to be the most likely [103]. Recent analysis of MAST data performed by I. Lehane, and presented in [104], promote the explanation of impurities being responsible for some of the hollow profiles. It has been found that the on-axis impurity accumulation trigger so-called Spontaneous Snakes which is a density instability. This snake mode is also observed by other diagnostics at MAST [104].
Regarding c), the picture could be a low $(m, n)$-mode advecting heat out from the core and at the same time creating a poloidal flow, which gives rise to a transport barrier. Of the three explanations, this is the only one that self-consistently explains the hollow $T_e$ profiles and the apparent transport barriers. There may be some trouble in explaining the simultaneously peaked density profiles, but it could be explained by transport of cold particles into the core. Simulations with the CUTIE code of MAST-like plasmas show a (1,1)-mode generating a transport barrier and an H-mode, and also slightly hollow temperature profiles [98].
Finally, it should be mentioned that the hollow electron density profiles seen in some shots cannot be explained by either explanation a) or b). This is a further argument to consider (turbulent) transport processes in the future investigations of the hollow profiles observed in some MAST discharges. The prospect of c) being the explanation, is that it seems that the MAST plasma self-generates an advanced scenario with central reversed magnetic shear and a hollow current and q-profile.

## 8.2 Further experiments

To further elucidate the interesting phenomenon of hollow profiles one may propose the following experiments: hollow profiles and relation to impurity radiation (such analysis has recently been performed by I. Lehane as mentioned above), hollow profiles in the initial phase (in connection with current penetration), hollow profiles in connection with sawtooth crashes (MHD activity), and the connection between turbulence, transport and hollow profiles.

Concerning the investigation of *Turbulent transport related to hollow $T_e$ profiles*, we would propose the immediate goals of: seeking to reproduce the hollow $T_e$ profiles, to investigate the time evolution of the hollow profiles, of the internal transport barriers, and of the turbulence observed, e.g., by the reflectometer and magnetic pick-up coils. Furthermore, we would propose a parameter scan to evaluate the persistence of the hollow profiles, and an investigation of the relation between flows, turbulence and the hollow profiles. The obtained experimental results, including both the profiles, flows, and fluctuation statistics, may then be compared to simulation results from, e.g., CUTIE.

# Chapter 9

# Conclusion

In the present thesis, we have sought to expand the insight in the dynamics of drift wave turbulence and turbulent transport in the context of fusion plasmas. The work has been divided into two parts: a numerical and theoretical treatment of models describing electrostatic drift wave turbulence, and an experimental part, mainly focusing on reflectometry measurements of fluctuations in the edge region of the Mega Amp Spherical Tokamak in Culham Science Centre, UK.

In Chapter 1, we put the work in a context of fusion energy research, and motivated the development of fusion power, as well as research in the field of turbulence and transport.
In the second introductory chapter, Chapter 2, general concepts of turbulence models, shear flows, and transport, were introduced with emphasis on electrostatic drift wave turbulence models.

In Chapter 3, we reviewed the derivation of the Hasegawa-Wakatani model as well as simulation results. The purpose was to present a background for comparison, since the models treated in Chapters 4-6 are derived on the basis of the Hasegawa-Wakatani model. The general behaviour of the model found by the simulations may be summarised as: Drift waves grow from low level noise due to a linear instability, and having obtained sufficiently large amplitudes, the drift waves excite convective cells (structures having $k_{\|} = 0$) through nonlinear interactions. A turbulent state, in which the amplitudes of both the drift waves and the convective cells increase, is sustained by nonlinear processes. Eventually, a poloidal flow builds up, and suppresses the supply of energy to the drift waves. This results in a final stable state with nearly all the energy condensed into large convective cells of the size of the domain. Additionally, we see that the turbulent particle flux is intermittent and is strongest during the turbulent state, while the flux level reduces to $\sim$ 1% of the maximum in the quasi-steady weakly turbulent state.
In the last part of Chapter 3, we presented results showing that the coupling and the transfer of energy between drift waves and convective cells, are dependent on the drive of the drift wave dynamics, i.e. the phase shift

between the density and potential fluctuations, and in turn the resistivity of the plasma.

In Chapter 4, we derived a model which is a generalisation of the standard Hasegawa-Wakatani model, with finite ion temperature corrections retained to lowest order[1]. The behaviour of this ion temperature modified Hasegawa-Wakatani model resembles that of the original model to a high degree. However, for some parameters the tendency of the system to condensate the energy into the $k_{\|} = 0$ modes, is affected by the finite ion temperature. It is anticipated that this is caused by the ion temperature term causing a relatively larger part of the energy to be kinetic energy, and the dominant cascading direction of the kinetic energy is from high to low $k_{\|}$-values.

The $n\phi T_e$ model was derived and presented in Chapter 5. The model is derived in the frame of the Hasegawa-Wakatani model, but is additionally containing a background electron temperature gradient and electron temperature fluctuations derived from the Braginskii electron temperature equation. Simulations are performed with this $n\phi T_e$ model, and we observe that for some parameters, the evolution of the turbulence of the model resembles that of the Hasegawa-Wakatani model, to a certain extent. This is mainly due to the temperature fluctuations being passively advected by the potential in the nonlinear turbulent state, analogous to the advection of the density. Hence, the general behaviour of $T$ is expected to be similar to that of $n$. Nevertheless, we found in Figure 5.6.(c) that the correlation of the drift components (only) of $n$ and $T$ is particularly low. The origin of this could be a subject for further investigations.
Chapter 5 was finalised by an investigation of the effect of varying the relative steepness of the temperature and density gradients. We found that the relative steepness of the temperature gradient to the density gradient has an effect on the quantitative measures of the whole system. This is not only for the quantities tightly connected to the temperature fluctuations. This underlines the significance of including both temperature and density gradients when evaluating the turbulent transport of a given system influenced by drift waves.

Chapter 6 contained a wide variety of results obtained by simulations of the Hasegawa-Wakatani model in a non-periodic geometry, i.e. in a slab geometry with Dirichlet boundary conditions in the radial ($x$) direction. We first investigated the general behaviour of the model in this new geometry, and it was shown that on key points the system behaves markedly different from the periodic domain case. The source of the differences should mainly be found in the fact that the fluctuations are now able to react back on the background density gradient, and it so happens that the fluctuations

[1] 2011 update: Regrettably: As described in the footnotes in Chapter 4 a term was left out in the original derivation of the equations.

organise to flatten the total effective density gradient. This tendency of the density fluctuations was explained by heuristic arguments concerning conservation of potential vorticity, $PV$. The flattening limits the drive of the drift wave instability, and combined with the simultaneously generated poloidal shear flow, it follows that the potential and density fluctuations are reduced. It was also discovered that the shear flow may create a transport barrier that divides the domain into two regions with strong fluxes and flat gradients.

The general description of the model in a non-periodic geometry was succeeded by an exploration of the subject of shear flow generation and the Reynolds stress. The Reynolds stress is a measure of the anisotropy of the turbulent velocity fluctuations that produce a stress on the mean flow, and it was found analytically that for the Hasegawa-Wakatani model the poloidal ($y$) flow generation is solely attributed to the Reynolds stress including viscosity. This was confirmed numerically, and an investigation into the origin of the Reynolds stress reveals that it is driven by the drift modes initially, while after the poloidal flow has been generated, the main contribution to the Reynolds stress comes from the flute modes.

The succeeding subject was the evaluation of the usefulness of the pseudo-Reynolds stress, which is based on density measurements, as opposed to potential measurements leading to the Reynolds stress. It was tested against the observed flow generation, and it was found that the pseudo-Reynolds stress gives a good qualitative hint on the flow generation - at least before the turbulence is fully developed.

A numerical study of the effect of misalignment of a simple probe array for experimentally measuring the Reynolds stress was performed. We concluded from the investigations that the alignment of the probe array with respect to the magnetic field is important, but it is not crucial to have a perfect alignment to obtain a reasonably good estimate of the divergence of the Reynolds stress, and from this the acceleration of the mean shear flow.

The final section of Chapter 6 concerned the behaviour of the system for various initial states and parameters. One of the subjects was the diffusive flux dependence on the viscosity, where we saw that the characteristic time of the cycle of turbulent flux bursts separated by quiescent periods of weak turbulence is inversely proportional to the viscosity. We also examined the effect of applying an external shear flow, and it was found that strong shear flows may decouple parts of the domain by creating a prominent transport barrier. Simultaneously, it was found that strong external shear flows mainly suppress the fluctuations, and hence inhibit the self-generated shear flows, as opposed to work as seed flows. For weaker external shear flows a constructive interaction between the external and self-generated shear flow may occur, but it appeared that generally the turbulence reduction mechanism is stronger than the seed flow mechanism.

Concluding the part on numerical simulations of drift wave turbulence we may suggest a few opportunities for further studies. This could be to apply the Dirichlet boundary conditions to the $n\phi T_e$ model, and investigate

and compare the back-reactions of the density and temperature fluctuations on their respective background gradients. For the Hasegawa-Wakatani model in the non-periodic geometry one may look further into the correlation of the shearing rate and the flux as a function of increasing coupling parameter, $\mathcal{C}$, and also correlate this to the local shear of the drift waves. One may also consider using a more advanced geometry to include effects of magnetic shear and/or curvature, but then we are "crossing the line" towards the more advanced models, for which a clear distinction of effects is not easy.

In Chapter 7, we presented the setup and first results of the MAST fluctuation reflectometer that was mounted in the spring of 2000 at Culham Science Centre, UK. The reflectometer was proven to work as intended, and a number of topical studies were presented. We looked, e.g., at the apparent decrease of levels of high frequency turbulence during NBI heating pulses, and found a possible explanation in the experimental and theoretical method of mode selective control of drift wave turbulence.
The reflectometer proved to be particularly good at diagnosing H-modes, and a number of interesting results appeared. Some of these strongly suggested that a prior increase in the width of the density fluctuation frequency band is responsible or strongly connected to the ELMs in the H-mode and the H-L transition. Finally, the H-mode detection by the reflectometer was proven to be a good supplement to the $D_\alpha$ diagnostic. In some cases, the reflectometer may even capture events not seen by the $D_\alpha$ diagnostic.

In Chapter 8, we briefly presented the interesting phenomenon of hollow electron temperature and electron density profiles observed in MAST. We discussed three possible explanations, and stated that no firm conclusions on the cause of the hollow profiles have been found yet. Though, some of the hollow profiles are likely to be related to impurity radiation from the core of the plasma. One of the explanations we forwarded was one incorporating shear flows and transport barriers resulting from MHD mode activity. Further experiments are needed to study and describe the phenomenon.

# Appendix A

# Chaotic behaviour

The chaotic behaviour of the Hasegawa-Wakatani model in a two-dimensional periodic geometry was investigated and described in [105]. We have not performed such detailed study of the model in a three-dimensional geometry, but have observed the differences in the results, caused by using different initial conditions or different numerical schemes. This appendix briefly describes some of the observed chaotic features of the Hasegawa-Wakatani model.

## A.1 Effect of numerical scheme

One might oppose to the fact that, e.g., the choice of FFT affect the behaviour of the system, even if the same initial conditions are maintained. However, since each FFT routine does not come out with exactly the same error, the system will be perturbed a little by each FFT (the typical numerical error of one forward and one inverse FFT is in the order of $10^{-15}$). If the system is very sensitive to noise, this will affect the evolution of the system. If the term "sensitivity to initial conditions" is more tractable, one could imagine each of the tiny perturbations of the FFT to be transformed back to the initial state, which then would be modified. In Figure A.1 we present the evolution of the energy for three simulations having identical parameters, but using different FFTs in the numerical scheme. The figure clearly illustrates that the evolution of the system is severely affected by the choice of numerical scheme.

## A.2 Effect of initial conditions

To illustrate the extreme sensitivity of initial conditions, simulations were performed using the same parameters, the same numerical methods, and the same initial conditions, except for performing one forward and one inverse FFT on the initial data set, i.e. introducing a difference of the initial conditions in the order of $10^{-15}$.
The result is presented in Figure A.2, where we see that the main differences start occurring in the nonlinear turbulent regime.

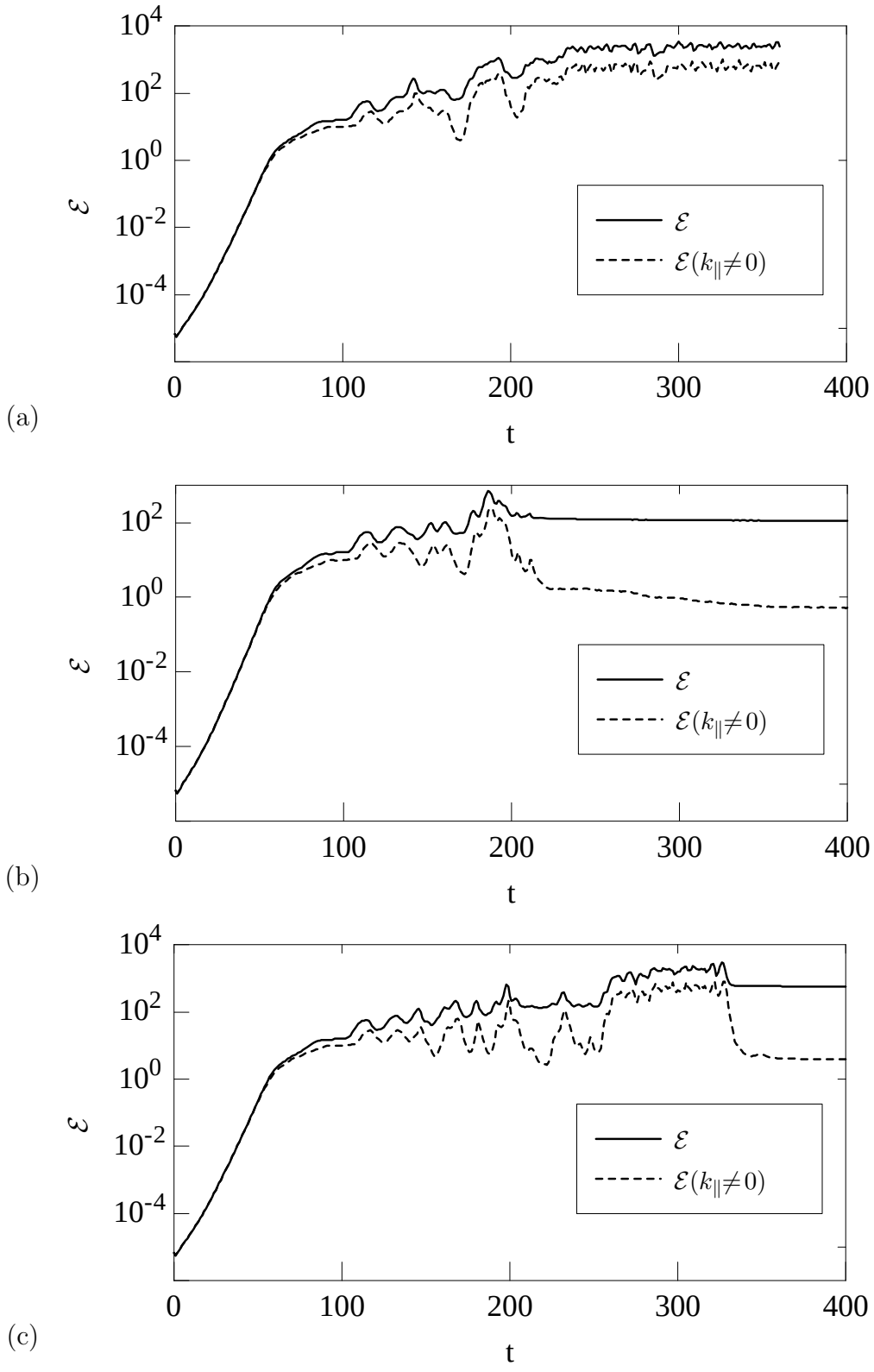


(a)

(b)

(c)

Figure A.1: Plots of the evolution of energy for three simulations with the same initial conditions and parameters, but using three different FFT routines. (a) 3x1D Singleton, (b) 2D "vectorised" + 1D Singleton, and (c) 3D "vectorised".

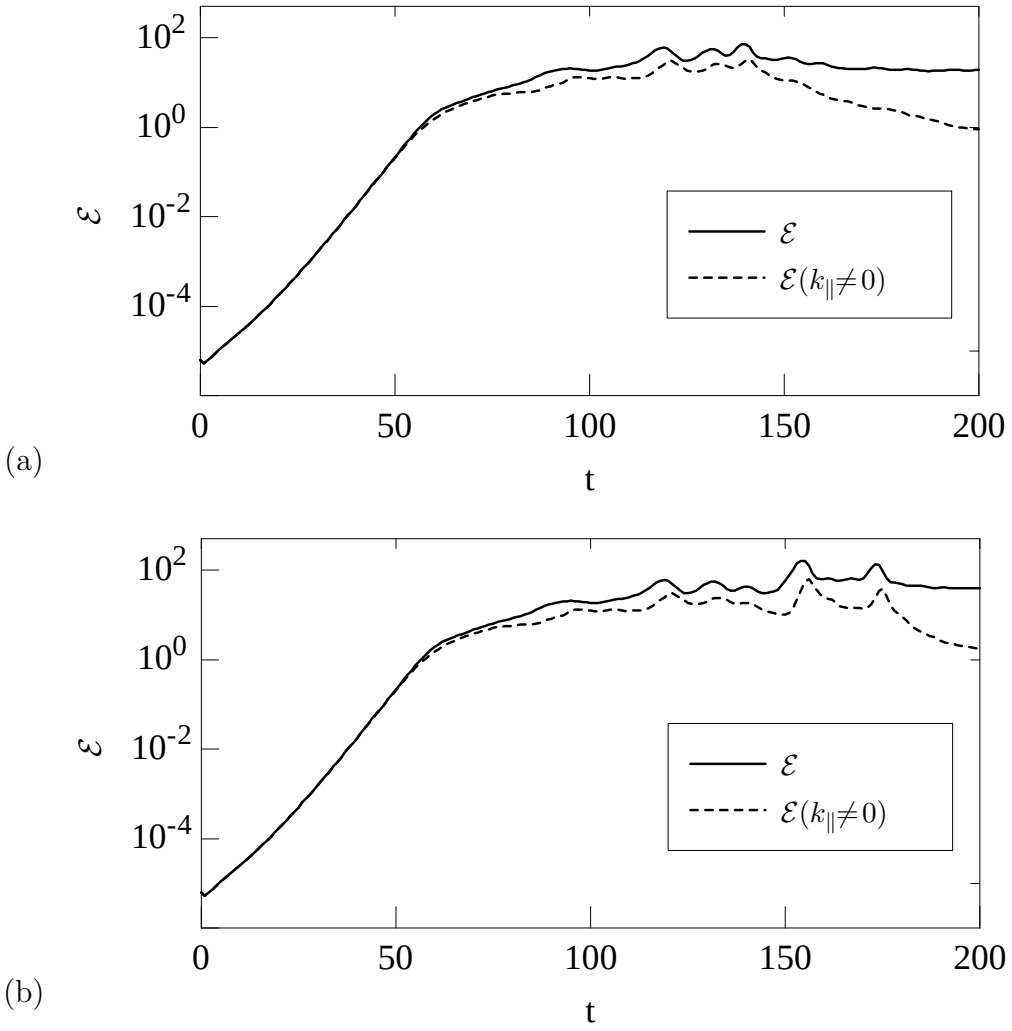


(a)




(b)

Figure A.2: Plots of the evolution of the energy for two simulations with the same parameters, using the same numerical methods, but with slightly different initial conditions, i.e. the initial fields of (b) have been Fourier transformed back and forth.

# Appendix B

# List of notation

| | | |
|---|---|---|
| $\phi$ | | electrostatic potential |
| $n_i$ | | ion density |
| $n_e$ | $n_0 + n_1$ | electron density |
| $n_0$ | | background density |
| $n_1 = n$ | | fluctuating density |
| $T_e$ | $T_{e0} + T_{e1}$ | electron temperature |
| $T_{e0}$ | | background electron temperature |
| $T_{e1} = T$ | | fluctuating electron temperature |
| $T_i$ | | ion temperature |
| $\theta$ | $T_i/2T_e$ | temperature ratio |
| $L_n$ | $n_0(x) = N_0 e^{-\frac{x}{L_n}}$ | characteristic density gradient length scale |
| $L_T$ | $T_0(x) = T_0 e^{-\frac{x}{L_T}}$ | characteristic temperature gradient length scale |
| $\bar{\bar{\mathrm{P}}}_i$ | $\bar{\bar{\Pi}}_i + p_i \bar{\bar{\mathrm{I}}}$ | total ion pressure |
| $\bar{\bar{\Pi}}_i$ | | anisotropic ion pressure |
| $p_i$ | $n_i T_i$ | isotropic ion pressure |
| $p_e$ | $n_e T_e$ | isotropic electron pressure |
| $B_0$ | | constant magnetic field |
| $B_P$ | | poloidal magnetic field |
| $B_T$ | | toroidal magnetic field |
| $\alpha$ | see (7.12) | pitch angle of the magnetic field |
| $v_i$ | | ion velocity |
| $v_e$ | | electron velocity |
| $\mathbf{v}_E$ | $-\nabla\phi \times \mathbf{e}_z/B_0$ | $\mathbf{E} \times \mathbf{B}$-velocity |
| $v_r$ | $v_{E,x}$ | radial velocity |
| $\mathbf{v}_S$ | $\Theta \tanh\left(\frac{x-\frac{L_x}{2}}{\Delta}\right) \mathbf{e}_y$ | external poloidal shear flow |
| $\Theta$ | | amplitude of external shear flow |
| $\boldsymbol{\omega}$ | $(\nabla \times \mathbf{v}_i)$ | ion vorticity |
| $\omega$ | $\nabla_\perp^2 \phi/B_0$ | parallel component of the ion vorticity |
| $\frac{\partial v_y}{\partial x}$ | | shearing rate |
| $t$ | | time |
| $\omega_t$ | $\omega_r + i\gamma$ | frequency of turbulent fluctuations |
| $\gamma$ | | growth rate of linear instabilities |
| $\frac{\mathrm{D}}{\mathrm{D}t}$ | $\frac{\partial}{\partial t} + \mathbf{v}_E \cdot \nabla$ | total convective derivative |

| | | |
|---|---|---|
| $\mu$ | | viscosity parameter |
| $\nu$ | | viscosity parameter |
| $\mathcal{D}^{2p}$ | $(-1)^{p+1}\nabla_\perp^{2p}$ | hyperviscosity of order $2p$ |
| $k_\perp$ | $\sqrt{k_x^2+k_y^2}$ | wavenumber perpendicular to $B_0$ |
| $k_\parallel$ | $k_z$ | wavenumber parallel to $B_0$ |
| $\delta$ | $1/k_\parallel^2 L_\parallel^2$ | adiabaticity parameter |
| $m_i$ | | ion mass |
| $m_e$ | | electron mass |
| $\mu_0$ | | vacuum permeability |
| $\epsilon_0$ | | vacuum permittivity |
| $I_p$ | | plasma current |
| $\eta$ | | plasma resistivity |
| $J_\parallel$ | | parallel plasma current |
| $\tau_e$ | | electron collision time |
| $\mathbf{q}_e$ | | electron heat flux |
| $\kappa_\parallel$ | $3.16 n_e T_{e0} \tau_e / m_e$ | parallel thermal conductivity |
| $\omega_{ci}$ | $eB_0/m_i$ | ion cyclotron frequency |
| $\omega_{ce}$ | $eB_0/m_e$ | electron cyclotron frequency |
| $\omega_{pe}$ | $n_e e^2/\epsilon_0 m_e$ | electron plasma frequency |
| $\rho_s$ | $\sqrt{T_{e0} m_i}/eB_0$ | ion Larmor radius at $T_{e0}$ |
| $\mathcal{C}$ | $T_e L_n / \eta e^2 n_0 \omega_{ci} \rho_s L_\parallel^2$ | parallel coupling factor |
| $L_\parallel$ | $(T_e L_n / \eta e^2 n_0 \omega_{ci} \rho_s \mathcal{C})^{1/2}$ | typical parallel length scale |
| $\zeta$ | $\frac{2}{3}\kappa_\parallel \eta e^2 \mathcal{C}/T_{e0}$ | constant |
| $\hat{\alpha}$ | 1.71 | constant |
| $x_{co}$ | see (7.1) | reflectometer cut-off position |
| $n_{co}$ | see Section 7.2.2 | cut-off density |
| $R_\phi$ | $\left\langle \frac{\partial\phi}{\partial y}\frac{\partial\phi}{\partial x} \right\rangle$ | Reynolds stress |
| $R_n$ | $\left\langle \frac{\partial n}{\partial y}\frac{\partial n}{\partial x} \right\rangle$ | pseudo-Reynolds stress |
| $\mathcal{E}$ | $\mathcal{E}_{pot} + \mathcal{E}_{kin} + \mathcal{E}_{thermal}$ | total energy |
| $\mathcal{E}_{pot}$ | $\frac{1}{2}\int n^2 \, \mathrm{d}\mathbf{x}$ | potential energy |
| $\mathcal{E}_{kin}$ | $\frac{1}{2}\int (\nabla_\perp \phi)^2 \, \mathrm{d}\mathbf{x}$ | kinetic energy |
| $\mathcal{E}_{thermal}$ | $\frac{1}{2}\frac{3}{2}\int T^2 \, \mathrm{d}\mathbf{x}$ | thermal energy |
| $\Gamma_n$ | $-\int n \frac{\partial\phi}{\partial y} \, \mathrm{d}\mathbf{x}$ | density flux |
| $\Gamma_T$ | $-\frac{L_n}{L_T}\int T \frac{\partial\phi}{\partial y} \, \mathrm{d}\mathbf{x}$ | heat flux |
| $\mathcal{W}$ | $\frac{1}{2}\int (n - (\nabla_\perp^2 \phi))^2 \, \mathrm{d}\mathbf{x}$ | generalised enstrophy |
| $PV$ | see (3.25) | potential vorticity |

# Bibliography


[1] European Commission, *Green Paper - Towards a European strategy for the security of energy supply*, Number 769 in COM(2000), European Commission, Bruxelles, final edition, 2000.

[2] J. P. H. E. Ongena and G. Van Oost, *Energy for future centuries. Will fusion be an inexhaustible, safe and clean energy source?*, Fusion Technology **37** (2000).

[3] V. O. Jensen, *Fusionsenergi - hvor langt er vi nået?*, Naturens Verden **4** (1999) 14–25.

[4] J. Houghton, *Global Warming – The complete briefing*, Cambridge University Press, Cambridge, UK, 2nd edition, 2000.

[5] C. D. Lin, editor, *Review of Fundamental Processes and Applications of atoms and ions*, chapter Atomic and Molecular Processes in Muon-Catalyzed Fusion by J. S. Cohen, World Scientific Pub, 1993.

[6] R. L. McCrory, R. E. Bahr, R. Betti, T. R. Boehly, T. J. B. Collins, R. S. Craxton, J. A. Delettrez, W. R. Donaldson, R. Epstein, J. Frenje, V. Y. Glebov, V. N. Goncharov, O. V. Gotchev, R. Q. Gram, D. R. Harding, D. G. Hicks, P. A. Jaanimagi, R. L. Keck, J. H. Kelly, J. P. Knauer, C. K. Li, S. J. Loucks, L. D. Lund, F. J. Marshall, P. W. McKenty, D. D. Meyerhofer, S. F. B. Morse, R. D. Petrasso, P. B. Radha, S. P. Regan, S. Roberts, F. Seguin, W. Seka, S. Skupsky, V. A. Smalyuk, C. Sorce, J. M. Soures, C. Stoeckl, R. P. J. Town, M. D. Wittman, B. Yaakobi, and J. D. Zuegel, *OMEGA ICF experiments and preparation for direct drive ignition on NIF*, Nucl. Fusion **41** (2001) 1413–1422.

[7] R. Balescu, *Transport Processes in Plasmas*, North-Holland, Amsterdam, 1988.

[8] J. Weiland, *Collective Modes in Inhomogeneous Plasma*, Institute of Physics Publishing, Bristol, Philadelphia, 2000.

[9] W. Horton, *Drift waves and transport*, Rev. Mod. Phys. **71** (1999) 735–778.

[10] J. A. Krommes, *Systematic statistical theories of plasma turbulence and intermittency: Current status and future prospects*, Phys. Rep. **283** (1997) 5–48.

[11] P. W. Terry, *Suppression of turbulence and transport by sheared flow*, Rev. Mod. Phys. **72** (2000) 109–165.

[12] B. Scott, *$E \times B$ shear flows and electromagnetic gyrofluid turbulence*, Phys. Plasmas **7** (2000) 1845–1856.

[13] F. Jenko and W. Dorland, *Nonlinear electromagnetic gyrokinetic simulations of tokamak plasmas*, Plasma Phys. Control. Fusion **43**(Suppl. 12A) (2001) A141–A150.

[14] W. M. Tang, *Microinstability theory in tokamaks*, Nucl. Fusion **18** (1978) 1089–1160.

[15] R. Hazeltine and J. Meiss, *Plasma Confinement*, Addison-Wesley Publishing Company, Redwood City, 1992.

[16] B. D. Scott, *Three Dimensional Computation of Drift Alfvén Turbulence*, Plasma Phys. Control. Fusion **39** (1997) 1635–1668.

[17] A. J. Wootton, H. Y. W. Tsui, and S. Pranger, *Edge turbulence in tokamaks, stellarators and reversed field pinches*, Plasma Phys. Contr. Fus. **34** (1992) 2023–2030.

[18] M. Endler, L. Giannone, K. McCormick, H. Niedermeyer, A. Rudyj, G. Theimer, N. Tsois, S. Zoletnik, ASDEX Team, and W7-AS Team, *Turbulence in the SOL of ASDEX and W7-AS*, Physica Scripta **51** (1995) 610–616.

[19] V. Naulin, S. B. Korsholm, and P. K. Michelsen, *Three-dimensional Simulations of Drift Wave Turbulence*, in *Theory of Fusion Plasmas*, edited by J. W. Connor, E. Sindoni, and J. Vaclavik, pages 505–510, Editrice Compositori, Bologna, 1998.

[20] F. F. Chen, *Introduction to Plasma Physics and Controlled Fusion*, Plenum-Press, New York, London, 1984.

[21] R. J. Goldston and P. H. Rutherford, *Introduction to Plasma Physics*, Institute of Physics Publishing, Bristol, Philadelphia, 1995.

[22] S. B. Korsholm, *Resistive Drift Wave Turbulence*, Master's thesis, Risø National Laboratory, Roskilde, Denmark, 1998, Risø-I-1280(EN).

[23] A. Hasegawa and M. Wakatani, *Plasma Edge Turbulence*, Phys. Rev. Lett. **50** (1983) 682–686.

[24] A. Hasegawa and K. Mima, *Pseudo-three-dimensional turbulence in magnetized nonuniform plasma*, Phys. Fluids **21** (1978) 87–92.

[25] J. Pedlosky, *Geophysical Fluid Dynamics*, Springer Verlag, New York, 1987.

[26] W. Horton and A. Hasegawa, *Quasi-two-dimensional dynamics of plasmas and fluids*, Chaos **4** (1994) 227–251.

[27] T. S. Pedersen, P. K. Michelsen, and J. J. Rasmussen, *Resistive coupling in drift wave turbulence*, Plasma Phys. Control. Fusion **38** (1996) 2143–2154.

[28] D. Biskamp and A. Zeiler, *Nonlinear Instability Mechanism in 3D Collisional Drift-Wave Turbulence*, Phys. Rev. Lett. **74** (1995) 706–709.

[29] S. B. Korsholm, P. K. Michelsen, and V. Naulin, *Three Dimensional Study of the Hasegawa-Wakatani Drift-Wave Model*, in *Proceedings of the 1998 International Congress on Plasma Physics*, volume 22C of *Europhysics Conference Abstracts*, pages 2378–2381, European Physical Society, Prague, 1998.

[30] S. B. Korsholm, P. K. Michelsen, and V. Naulin, *Resistive Drift Wave Turbulence in a Three Dimensional Geometry*, Phys. Plasmas **6** (1999) 2401–2408.

[31] F. Wagner et al., *Regime of Improved Confinement and High Beta in Neutral-Beam-Heated Divertor Discharges of the ASDEX Tokamak*, Phys. Rev. Lett. **49** (1982) 1408–1412.

[32] E. S. Benilov, V. Naulin, and J. J. Rasmussen, *Does a sheared current stabilize inversely stratified flows in the ocean and plasma?*, Phys. Fluids **14** (2002) 1674–1680.

[33] A. Ekedahl, Y. Baranov, J. A. Dobbing, B. Fisher, C. Gormezano, T. T. C. Jones, M. Lennholm, V. Parail, F. Rimini, J. A. Romero, P. Schild, A. C. C. Sips, F. X. Söldner, and B. Tubbing, *Profile Control Experiments in JET using Off-axis Lower Hybrid Current Drive*, Jet Report JET-P(97)47, Abingdon, UK, 1997.

[34] V. O. Jensen, *Fusionsplasmafysik*, Risø National Laboratory, Roskilde, Denmark, 1989.

[35] G. E. Karniadakis, M. Israeli, and S. A. Orszag, *High-Order Splitting Methods for the Incompressible Navier-Stokes Equations*, J. Comp. Phys. **97** (1991) 414–443.

[36] E. A. Coutsias, F. R. Hansen, T. Huld, G. Knorr, and J. P. Lynov, *Spectral Methods in Numerical Plasma Simulation.*, Physica Scripta **40** (1989) 270–279.

[37] S. J. Camargo, D. Biskamp, and B. D. Scott, *Resistive drift-wave turbulence*, Phys. Plasmas **2** (1995) 48–62.

[38] T. S. Pedersen, *Resistive Drift Wave Turbulence*, Master's thesis, Risø National Laboratory, Roskilde, Denmark, 1995.

[39] C. Z. Cheng and H. Okuda, *Formation of Convective Cells, Anomalous Diffusion, and Strong Plasma Turbulence Due to Drift Instabilities.*, Phys. Rev. Lett. **38** (1977) 708–711.

[40] H. L. Pécseli, *Electrostatic Drift Waves*, Lecture notes. University of Oslo, Norway, 1997.

[41] S. B. Korsholm, P. K. Michelsen, and H. L. Pécseli, *Nonlinear Dynamics of Resistive Electrostatic Drift Waves*, Physica Scripta **T82** (1999) 12–16.

[42] P. K. Michelsen, S. B. Korsholm, and H. L. Pécseli, *Three Dimensional Studies of a Modified Hasegawa-Wakatani Model*, in *Proceedings of the EPS 26th Conference on Controlled Fusion and Plasma Physics*, European Physical Society, Maastricht, 1999, Contribution P1.119.

[43] C. Hidalgo, J. H. Harris, T. Uckan, G. R. Hanson, J. D. Bell, M. A. Meier, C. P. Ritz, and A. J. Wootton, *Experimental evidence of edge turbulence driven by multiple mechanisms in AFT*, Nucl. Fusion **33** (1993) 146–149.

[44] S. B. Korsholm and P. K. Michelsen, *Density and Temperature Gradient Driven Drift Waves*, in *Proceedings of the EPS 26th Conference on Controlled Fusion and Plasma Physics*, European Physical Society, Maastricht, 1999, Contribution P1.118.

[45] P. K. Shukla, G. Murtaza, and J. Weiland, *Electron-temperature-gradient-driven drift waves and anomalous electron energy transport*, J. Plasma Phys. **44** (1990) 393–404.

[46] B. D. Scott, *The mechanism of self-sustainment in collisional drift wave turbulence*, Phys. Fluids B **4** (1992) 2468–2494.

[47] A. Zeiler, F. F. Drake, and D. Biskamp, *Electron temperature fluctuations in drift-resistive ballooning turbulence*, Phys. Plasmas **4** (1997) 991–1001.

[48] S. I. Braginskii, *Transport processes in a plasma*, Rev. Plasma Phys. **1** (1965) 205–311.

[49] A. H. Nielsen, H. L. Pécseli, and J. J. Rasmussen, *Turbulent transport in low-$\beta$ plasmas*, Phys. Plasmas **3** (1996) 1530–1544.

[50] S. B. Korsholm, P. K. Michelsen, V. Naulin, J. J. Rasmussen, L. Garcia, B. A. Carreras, and V. E. Lynch, *Reynolds stress and shear flow generation*, Plasma Phys. Control. Fusion **43** (2001) 1377–1395.

[51] S. B. Korsholm, P. K. Michelsen, V. Naulin, and J. J. Rasmussen, *Reynolds stress and shear flow generation*, in *Proceedings of the EPS 27th Conference on Controlled Fusion and Plasma Physics*, European Physical Society, Budapest, 2000, Contribution P3.075.

[52] S. B. Korsholm, P. K. Michelsen, V. Naulin, and J. J. Rasmussen, *Analysis of Determination of Reynolds Stress in Drift Wave Turbulence*, in *Proceedings of the EPS 28th Conference on Controlled Fusion and Plasma Physics*, European Physical Society, Madeira, 2001, Contribution n. 1000654.

[53] V. Naulin, K. H. Spatschek, S. Musher, and L. I. Piterbarg, *Properties of a two-nonlinearity model for drift-wave turbulence*, Phys. Plasmas **2** (1995) 2640–2652.

[54] P. H. Diamond and T. S. Hahm, *On the dynamics of turbulent transport near marginal stability*, Phys. Plasmas **2** (1995) 3640–3649.

[55] X. Garbet and R. E. Waltz, *Heat flux driven ion turbulence*, Phys. Plasmas **5** (1998) 2836–2845.

[56] V. Naulin, J. Nycander, and J. J. Rasmussen, *Equipartition and transport in two-dimensional electrostatic turbulence*, Phys. Rev. Lett. **81** (1998) 4148 – 4151.

[57] V. Naulin, *Physics of Turbulent Plasma - An Introduction*, Lecture script, 1st draft, 2002.

[58] C. N. Lashmore-Davies, D. R. McCarthy, and A. Thyagaraja, *The nonlinear dynamics of the modulational instability of drift waves and the associated zonal flows*, Phys. Plasmas **8** (2001) 5121–5133.

[59] P. H. Diamond and Y.-B. Kim, *Theory of mean poloidal flow generation by turbulence*, Phys. Fluids B **3** (1991) 1626–1633.

[60] C. Hidalgo, C. Silva, M. A. Pedrosa, E. Sánchez, H. Fernandes, and C. A. F. Varandas, *Radial Structure of Reynolds Stress in the Plasma Boundary of Tokamak Plasmas*, Phys. Rev. Lett. **83** (1999) 2203–2205.

[61] Y. H. Xu, C. X. Yu, J. R. Luo, J. S. Mao, B. H. Liu, J. G. Li, B. N. Wan, and Y. X. Wan, *Role of Reynolds Stress-Induced Poloidal Flow in Triggering the Transition to Improved Ohmic Confinement on the HT-6M Tokamak*, Phys. Rev. Lett. **84** (2000) 3867–3870.

[62] B. LeBlanc, R. Bell, S. Bernabei, J. Hosea, R. Majeski, M. Ono, C. Phillips, J. Rogers, G. Shilling, C. Skinner, and J. Wilson, *Direct observation of ion-Bernstein-wave-induced poloidal flow in TFTR*, Phys. Rev. Lett. **82**(2) (1999) 331–334.

[63] C. Hidalgo, Private communication.

[64] P. H. Diamond, M. N. Rosenbluth, E. Sanchez, C. Hidalgo, B. van Milligen, T. Estrada, B. Brañas, M. Hirsch, H. J. Hartfuss, and B. A. Carreras, *In Search of the Elusive Zonal Flow Using Cross-Bicoherence Analysis*, Phys. Rev. Lett. **84** (2000) 4842–4845.

[65] D. J. Tritton, *Physical Fluid Dynamics*, Clarendon Press, Oxford, 2nd edition, 1988.

[66] V. Naulin, *Turbulent transport by higher order particle drifts*, Europhys. Lett. **43** (1998) 533 – 538.

[67] J. F. Drake, J. M. Finn, P. Guzdar, V. Shapiro, V. Shevchenko, F. Waelbroeck, A. Hassam, C. S. Liu, and R. Sagdeev, *Peeling of convection cells and the generation of sheared flow*, Phys. Fluids B **4** (1992) 488–491.

[68] A. I. Smolyakov, P. H. Diamond, and V. I. Shevchenko, *Zonal flow generation by parametric instability in magnetized plasmas and geostrophic fluids*, Phys. Plasmas (2000) 1349–1351.

[69] J. Crotinger and T. H. Dupree, *Trapped structures in drift wave turbulence*, Phys. Fluids B **4** (1992) 2854–2870.

[70] V. Naulin and K. H. Spatschek, *Nonlinear drift-wave structures and their influence on particle transport*, Phys. Rev. E **55** (1997) 5883–5893.

[71] L. Garcia, B. A. Carreras, V. E. Lynch, J. N. Leboeuf, and D. E. Newman, *Resistive pressure gradient-driven turbulence at stellarator plasma edge*, Phys. Plasmas **4** (1997) 3282–3292.

[72] G. Manfredi, C. M. Roach, and R. O. Dendy, *Zonal flow and streamer generation in drift turbulence*, Plasma Phys. Control. Fusion **43** (2001) 825–837.

[73] S. Champeux and P. H. Diamond, *Streamer and zonal flow generation from envelope modulations in drift wave turbulence*, Phys. Lett. A **288** (2001) 214–219.

[74] A. Sykes, R. Akers, L. Appel, P. Carolan, J. Connor, N. Conway, G. Counsell, A. Dnestrovskij, Y. Dnestrovskij, M. Gryaznevich, P. Helander, M. Nightingale, C. Ribeiro, C. Roach, M. Tournianski, M. Walsh, and H. Wilson, *H-mode operation in the START spherical tokamak*, Phys. Rev. Lett. **84** (2000) 495–498.

[75] I. H. Hutchinson, *Principles of Plasma Diagnostics*, Cambridge University Press, Cambridge, UK, 1990.

[76] C. Laviron, A. J. H. Donné, M. E. Manso, and J. Sanchez, *Reflectometry techniques for density profile measurements on fusion plasmas*, Plasma Phys. Control. Fusion **38** (1996) 905–936.

[77] D. Pinsonneault, B. Quirion, J.-L. Lachambre, and C. Legros, *Edge density profile measurements in TdeV using amplitude modulation reflectometry*, Rev. Sci. Instrum. **68** (1997) 990–993.

[78] E. Mazzucato, *Microwave reflectometry for magnetically confined plasmas*, Rev. Sci. Instrum. **69** (1998) 2201–2217.

[79] N. Bretz, *Diagnostic instrumentation for microturbulence in tokamaks*, Rev. Sci. Instrum. **68** (1997) 2927.

[80] E. Z. Gusakov and M. A. Tyntarev, *The two-dimensional theory of reflectometry diagnostics of plasma fluctuations*, Fusion Engineering and Design **34-35** (1997) 501–505.

[81] E. Z. Gusakov and B. O. Yakovlev, *Two dimensional theory of correlation reflectometry scattering diagnostics*, in *Proceedings of the EPS 27th Conference on Controlled Fusion and Plasma Physics*, European Physical Society, Budapest, 2000, Contribution P1.114.

[82] G. J. Kramer, A. C. C. Sips, and N. J. Lopes Cardozo, *Electron density fluctuation in JET measured with multichannel reflectometry*, Plasma Phys. Control. Fusion **35** (1993) 1685–1699.

[83] A. W. Morris, R. J. Akers, J. W. Connor, G. F. Counsell, R. J. Fonck, M. P. Gryaznevich, V. Gusev, T. C. Hender, S. M. Kaye, G. P. Maddison, R. Majeski, T. J. Martin, K. G. McClements, S. Medvedev, Y. K. M. Peng, C. M. Roach, D. C. Robinson, S. Sharapov, A. Sykes, M. Valovic, M. J. Walsh, and H. R. Wilson, *The role of the spherical tokamak in clarifying tokamak physics*, Plasma Phys. and Control. Fusion **41** (1999) B191–B207.

[84] A. Sykes, the START, NBI, MAST, and Theory teams, *The spherical tokamak programme at Culham*, in *17th IAEA Fusion Energy Conference, 19-24 October 1998 in Yokohama, Japan.*, IAEA, 1998, IAEA-CN-69/OV2/5.

[85] A. Sykes, R. J. Akers, L. C. Appel, E. Arends, P. Carolan, N. Conway, G. Counsell, G. Cunningham, A. Dnestrovskij, Y. Dnestrovskij, A. Field, S. Fielding, M. Gryaznevich, S. Korsholm, E. Laird, R. Martin, M. Nightingale, C. Roach, M. Tournianski, M. Walsh, C. Warrick, H. Wilson, and S. You, *First results from MAST*, Nucl. Fusion **41** (2001) 1423–1433.

[86] B. C. Berndt, *Ramanujan's Notebooks - Part III*, Springer Verlag, New York, 1991.

[87] G. Cunningham, *MAST OPS Note 00.13: Direction of the toroidal field in MAST*, Technical report, UKAEA, Culham Science Centre, 2000.

[88] J. Wesson, *Tokamaks*, Oxford University Press, Oxford, 2nd edition, 1997.

[89] J. A. Wesson and B. Balet, *Abrupt Changes in Confinement in the JET Tokamak*, Phys. Rev. Lett. **77** (1996) 5214–5217.

[90] C. Schröder, T. Klinger, D. Block, A. Piel, G. Bonhomme, and V. Naulin, *Mode selective control of drift wave turbulence*, Phys. Rev. Lett. **86** (2001) 5711–5714.

[91] T. Klinger, C. Schroder, D. Block, F. Greiner, A. Piel, G. Bonhomme, and V. Naulin, *Chaos control and taming of turbulence in plasma devices*, Phys. Plasmas **8** (2001) 1961–1968.

[92] R. R. Weynants, G. van Oost, G. Bertschinger, J. Boedo, P. Brys, T. Delvigne, K. Dippel, F. Durodie, H. Euringer, K. Finken, D. Gray, J. Hey, D. Hillis, J. Hogan, L. Konen, R. Leners, A. Messiaen, A. Pospieszczyck, U. Samm, R. Schorn, B. Schweer, G. Telesca, R. van Nieuwenhove, and P. Vandenplas, *Confinement and profile changes induced by the presence of positive or negative radial electric fields in the edge of the Textor tokamak*, Nucl. Fusion **32** (1992) 837–853.

[93] S. Jachmich, G. Van Oost, R. R. Weynants, and J. A. Boedo, *Experimental investigations on the role of $E \times B$ flow shear in improved confinement*, Plasma Phys. Control. Fusion **40** (1998) 1105–1113.

[94] R. J. Akers, G. F. Counsell, A. Sykes, L. C. Appel, E. R. Arends, C. Byrom, P. G. Carolan, N. J. Conway, G. Cunningham, A. Dnestrovskij, Y. N. Dnestrovskij, A. R. Field, S. J. Fielding, M. Gryaznevich, P. Helander, A. Kirk, S. B. Korsholm, R. Martin, H. Meyer, M. P. S. Nightingale, C. M. Roach, V. Shevchenko, M. Tournianski, M. J. Walsh, C. D. Warrick, The MAST Team, and The NBI Team, *L-H Transition in the Mega-Amp Spherical Tokamak*, Phys. Rev. Lett. **88**(3) (2002).

[95] R. Maingi, M. G. Bell, R. E. Bell, C. E. Bush, E. D. Fredrickson, D. A. Gates, S. M. Kaye, H. W. Kugel, B. P. LeBlanc, J. E. Menard, D. Mueller, S. A. Sabbagh, D. Stutman, G. Taylor, D. W. Johnson, R. Kaita, R. J. Maqueda, M. Ono, F. Paoletti, S. F. Paul, Y.-K. M. Peng, A. L. Roquemore, C. H. Skinner, V. A. Soukhanovskii, and E. J. Synakowski, *Characteristics of the First H-Mode Discharges in the National Spherical Torus Experiment*, Phys. Rev. Lett. **88**(3) (2002).

[96] A. Field, Private communication, 2000.

[97] A. L. Colton, *Experimental Investigation of Edge Localised Modes in JET*, PhD thesis, Risø National Laboratory, Roskilde, Denmark, 1993.

[98] A. Thyagaraja, Private communication, 2000.

[99] N. Conway, Private communication, 2000.

[100] E. Arends, Private communication, 2000.

[101] H. Meyer and I. Lehane, Private communication, 2000.

[102] R. J. Hawryluk, K. Bol, N. Bretz, D. Dimock, D. Eames, E. Hinnov, J. Hosea, H. Hsuan, F. C. Jobes, D. Johnson, E. Meservey, N. Sauthoff, G. L. Schmidt, S. Suckewer, M. Ulrickson, and S. von Goeler, *The effect of current profile evolution on plasma-limiter interaction and the energy confinement time*, Nucl. Fusion **19** (1979) 1307–1317.

[103] C. M. Roach, *START OPS Note 97.6: Hollow $T_e$ Profiles on START: Could it be Chlorine?*, Technical report, UKAEA, Culham Science Centre, 1997.

[104] I. Lehane, M. W. D. Mansfield, M. G. O. Mullane, E. R. Arends, S. Korsholm, H. Meyer, P. G. Carolan, A. Sykes, M. Gryaznevich, and R. Buttery, *Impurity Radiation and Transport in the MAST Tokamak*, Poster at the $43^{rd}$ Meeting of the APS Division of Plasma Physics, Long Beach, California, USA, 2001.

[105] T. S. Pedersen, P. K. Michelsen, and J. J. Rasmussen, *Lyapunov exponents and particle dispersion in drift wave turbulence*, Phys. Plasmas **3** (1996) 2939–2950.

Risø DTU is the National Laboratory for Sustainable Energy. Our research focuses on development of energy technologies and systems with minimal effect on climate, and contributes to innovation, education and policy. Risø has large experimental facilities and interdisciplinary research environments, and includes the national centre for nuclear technologies.

**Risø DTU**
**National Laboratory for Sustainable Energy**
**Technical University of Denmark**

Frederiksborgvej 399
PO Box 49
DK-4000 Roskilde
Denmark
Phone +45 4677 4677
Fax +45 4677 5688

www.risoe.dtu.dk